UNIVERSITAT POLITÈCNICA DE CATALUNYA BARCELONATECH

Station keeping analysis and design for new floating offshore wind turbines

by

Pau Trubat Casal

ADVERTIMENT La consulta d'aquesta tesi queda condicionada a l'acceptació de les següents condicions d'ús: La difusió d'aquesta tesi per mitjà del repositori institucional UPCommons (http://upcommons.upc.edu/tesis) i el repositori cooperatiu TDX (http://www.tdx.cat/) ha estat autoritzada pels titulars dels drets de propietat intel·lectual **únicament per a usos privats** emmarcats en activitats d'investigació i docència. No s'autoritza la seva reproducció amb finalitats de lucre ni la seva difusió i posada a disposició des d'un lloc aliè al servei UPCommons o TDX. No s'autoritza la presentació del seu contingut en una finestra o marc aliè a UPCommons (*framing*). Aquesta reserva de drets afecta tant al resum de presentació de la tesi com als seus continguts. En la utilització o cita de parts de la tesi és obligat indicar el nom de la persona autora.

ADVERTENCIA La consulta de esta tesis queda condicionada a la aceptación de las siguientes condiciones de uso: La difusión de esta tesis por medio del repositorio institucional UPCommons (http://upcommons.upc.edu/tesis) y el repositorio cooperativo TDR (http://www.tdx.cat/?locale-attribute=es) ha sido autorizada por los titulares de los derechos de propiedad intelectual **únicamente para usos privados enmarcados** en actividades de investigación y docencia. No se autoriza su reproducción con finalidades de lucro ni su difusión y puesta a disposición desde un sitio ajeno al servicio UPCommons No se autoriza la presentación de su contenido en una ventana o marco ajeno a UPCommons (*framing)*. Esta reserva de derechos afecta tanto al resumen de presentación de la tesis como a sus contenidos. En la utilización o cita de partes de la tesis es obligado indicar el nombre de la persona autora.

WARNING On having consulted this thesis you're accepting the following use conditions: Spreading this thesis by the institutional repository UPCommons (http://upcommons.upc.edu/tesis) and the cooperative repository TDX (http://www.tdx.cat/?locale-attribute=en) has been authorized by the titular of the intellectual property rights **only for private uses** placed in investigation and teaching activities. Reproduction with lucrative aims is not authorized neither its spreading nor availability from a site foreign to the UPCommons service. Introducing its content in a window or frame foreign to the UPCommons service is not authorized (framing). These rights affect to the presentation summary of the thesis as well as to its contents. In the using or citation of parts of the thesis it's obliged to indicate the name of the author.

STATION KEEPING ANALYSIS AND DESIGN FOR NEW FLOATING OFFSHORE WIND TURBINES

PhD Dissertation by

Pau Trubat Casal

Supervised by

Climent Molins i Borrell

and

Xavi Gironella i Cobos

Doctorat en Enginyeria de la Construcció

AGRAÏMENTS

En aquestes línies voldria agrair a tota aquella gent que d'una manera o altre m'heu ajudat i acompanyat en aquest viatge llarg anomenat doctorat. Primer de tot a la meva mare, en Jordi i la meva parella, l'Anna, per tot recolzament que m'heu donat.

La meva major gratitud a en Climent com a director de la Tesi per la dedicació aportada, ajuda i guia en aquesta camí. Sense l'oportunitat de participar en el projecte AFOSP, el meu desenvolupament en el món de l'enginyeria marina per a molins flotants no que va desencadenar en els estudis de doctorat, no hagués estat possible. Durant aquests anys, hem treballat conjuntament en diferents projectes que m'han donat un nou punt de vista de l'enginyeria en general i dels molins flotants en particular. Moltes gràcies per tot. També vull agrair profundament a en Xavi com a co-director per la dedicació i ajuda a l'hora de treure endavant els articles i la Tesi del doctorat.

Els inicis mai són fàcils, i encara més quan estàs davant d'un projecte de recerca que ha de començar posant els fonaments per a uns objectius ambiciosos. Sense dubte, aquest projecte no hagués estat possible sense els companys i amics del grup de recerca, l'Alexis i en Dani. De l'Alexis només puc dir que és un tot-terreny amb una dedicació i força enormes que va ser el meu principal referent des dels inicis fins que va marxar, mai és tard per tornar. Amb en Dani hem aconseguit continuar la feina de l'Alexis amb treball mutu, llimant les diferències, i superant els obstacles que ens anàvem trobant. Moltes gràcies als dos, sense vosaltres crec difícil que haguéssim arribat tant lluny.

SUMMARY

In the framework of the reduction of the emissions of greenhouse gases, the renewable energies have a key role as they are an endless and non-contaminant energy source. FOWT will be the technology that will exploit the wind resources in deep seas. In order to achieve a commercial deployment of this technology, a cost reduction is necessary through the optimization of the whole floating platform by detailed studies to reduce its design uncertainties. One important aspect is the mooring system, which commonly represents between a 10 to 15 % of the capex.

The present research aims to increase the knowledge of the design and analysis of the station keeping systems for floating offshore wind turbines. One of the most important aspects for a correct analysis and design of the mooring system is the simulation of the lines coupled with the floating structure and the wind turbine. The main loads over the mooring systems are due to the motion of the top end of the line, which is imposed by the platform motion. At the same time, the platform motion is due to the wind, the turbine and the wave loads but is also influenced by the mooring response. Therefore, the coupling of the floating wind turbine components is very important.

In this dissertation, two different mooring line models coupled to a finite element model for the analysis of floating platforms are presented. The first model is a finite element model based on a slender rod approach that considers the axial extensibility of the element for small strains and the bending stiffness. The model is extended to consider the rheological damping in the axial and bending direction within the constitutive equations of the problem. This model allows the simulation of different types of elements such as chains, wire ropes or dynamic cables, a critical element due to its lower resistance. The implementation of material damping allows to consider the damping of the coating elements with viscous-elastic behavior, or an approximation of the friction between internal wires. The second model is a new approach named quasi-dynamic model. The model assesses the static solution of the catenary equation but updates the line tension based on the external hydrodynamic forces and the inertial forces from the theoretical motion of the mooring line. This simplified model allows assessing a large amount of simulations due to its low computational cost and producing accurate mooring line fatigue assessments. In addition, it can be used to considerer the dynamics of large arrays of mooring systems in floating wind farms.

In the design of mooring lines is important to consider and foresee the different phenomena and loads that can act along on the life span of these elements. Within these phenomena there are the vortex induced motions of the platform, the vortex induced vibration of the cylindrical elements of the line, the second order wave forces that affect to the low frequency range, the slack-snap phenomenon or the wave hydrodynamic forces over the mooring lines. In this dissertation, the effects of the waves forces over the mooring lines over a semisubmersible and a spar platform have been studied. The study analyzes the contribution of the wave forces over the mooring lines and the results are compared if these forces are disregarded in order to determine when it is an important source of damage for the fatigue strength.

Finally, new floating platform concepts need to be tested and analyzed in controlled conditions in order to validate the models used for the final designs. To carry on these tests, it is important that all the FOWT components are well scaled and represented, such as the wind turbine, the platform and the mooring system. It is common that pool and flume basins do not present enough size for the catenary shape mooring systems because they cover a large extension. In this area, an optimization model for a truncated mooring system is presented. The truncated mooring system is formed by two types of chains to emulate the actual prototype mooring system of a scale spar platform in a narrow flume.

RESUM

En el marc de la reducció de les emissions de gasos d'efecte hivernacle, les energies renovables jugaran un paper clau, ja que són una font d'energia inesgotable i no contaminant. L'energia eòlica marina flotant serà la tecnologia que explotarà els recursos eòlics marins a gran profunditat. Per tal d'aconseguir un desenvolupament a escala comercial d'aquesta tecnologia és necessari una reducció dels costos a través de l'optimització dels aerogeneradors marins gràcies a estudis i anàlisis molt detallats per tal de reduir-ne les incerteses. Un dels aspectes importants és el sistema d'amarratge, el qual pot representar entre un 10 i 15 % del cost total d'una instal·lació.

La present recerca aprofundeix en el disseny i anàlisis dels sistemes d'amarratge per a molins de vent flotant. Un dels aspectes més importants per a al correcte disseny i anàlisis dels sistemes d'amarratge és la simulació de les amarres conjuntament amb el sistema flotant. Els esforços a que es veuen sotmesos els sistemes d'amarres són degut principalment als moviments del cap de l'amarra imposats pel moviment de la plataforma. A la mateixa vegada, el moviment de la plataforma es deu principalment a les forces del vent i de l'onatge però que també es influenciat per la resposta de les amarres. Aquest fet fa molt important tenir en compte la interacció entre els dos sistemes (plataforma-amarres).

En aquesta dissertació es presenten dos models d'amarres diferents acoblats a un model d'elements finits per a l'anàlisi d'estructures flotants. El primer model, és un model d'elements finits per a línies d'amarres basat en un model de vareta esvelta. Aquest model es basa en funcions polinòmiques, té en compte l'extensibilitat de l'element per petites deformacions i la rigidesa a flexió. El model s'ha ampliat per tenir en compte l'esmorteïment material degut als esforços en les direccions axial i de flexió dins de les equacions constitutives dels problema. Aquest model permet la simulació d'elements com les cadenes, cables o els cables elèctrics, uns elements crítics degut a la seva baixa resistència. Aquesta implementació permet considerar l'esmorteïment que provoca els elements protectors amb un comportament viscoelàstic o una aproximació del fregament entre els cables interns. El segon model es tracta d'un model quasi-dinàmic, el qual es basa en la solució estàtica de les amarres però actualitza la tensió de l'amarra en funció de les forces inercials i hidrodinàmiques externes calculades a partir del moviment teòric de l'amarra. Aquest model simplificat permet realitzar gran número de simulacions gràcies al seu baix cost

computacional i obtenir el disseny a fatiga de les amarres. A més a més, es pot utilitzar per a considerar la dinàmica de grans conjunts de sistemes d'amarres en parcs eòlics flotants.

En el disseny de les amarres també s'ha de tenir en compte i preveure els diferents fenòmens i accions que poden influir en la vida útil d'aquests elements. Dins d'aquests fenòmens podem trobar els moviments induïts per despreniment de vòrtex de la plataforma, les vibracions induïdes per despreniments de vòrtex dels elements cilíndrics de les amarres, les forces de segon ordre de l'onatge que afecta als rangs de baixes freqüències, el fenomen de distensió i tensió sobtada o les forces hidrodinàmiques de l'onatge sobre les amarres. En aquesta tesi, s'ha aprofundit en l'anàlisi dels efectes de les forces de l'onatge sobre les amarres per a una plataforma tipus semi-submergible i per una tipus *spar*. En aquest sentit es fa una comparació entre la consideració o no d'aquestes forces sobre les amarres pe tal de determinar en quins casos poden suposar una font important de dany per a la seva resistència a la fatiga.

Per últim, els nous conceptes de plataformes flotants s'han d'assajar i analitzar en condicions controlades per tal de validar els models utilitzats en el disseny final. Per portar a terme aquests assajos, és important que tots els elements que conformen els FOWT estiguin ben escalats i representats, des de la de turbina, passant per l'estructura i el sistema d'amarratges. És freqüent que les piscines i canals d'assaig no presentin les dimensions adequades per a l'experimentació dels sistemes d'amarres en forma de catenària, ja que poden ocupar una gran extensió d'espai. En aquest àmbit es presenta un model d'optimització d'unes amarres truncades. Les amarres truncades estan formades per dos tipus de cadena diferents per tal d'emular el disseny d'amarres del prototip a escala real de la plataforma WindCrete en un canal d'assaig estret.

TABLE OF CONTENTS

TABLE OF FIGURES

LIST OF TECHNICAL NAMES

ALS	Accidental Limit State
CFD	Computational Fluid Dynamics
FEM	Finite Element Method
FLS	Fatigue Limit State
FOWT	Floating Offshore Wind Turbines
IEA	International Energy Agency
IPCC	Intergovernmental Panel on Climate Change
ULS	Ultimate Limit State
O&G	Oil and Gas

1 INTRODUCTION

Nowadays global warming is a fact, and human activities are estimated to specifically the cause of warming about 0.8 to 1.2 ºC of the mean temperature relative to the pre-industrial period (1850-1900) (IPCC, 2018). Scientifics believe that anthropogenic emissions from pre-industrial period are unlikely to increase more than 0.5 ºC the global temperature (Allen et al., 2018, IPCC, 2018), that will limit the total rise to 1.5ºC as set in the 21st Conference of Parties (COP21) in December 2015 (United Nations, 2015). Then, anthropogenic emissions causing world warming will have to decrease to zero to achieve this agreement.

The main impact of the climate change is the temperature increase of the atmosphere and oceans. Other impacts are the changing of precipitation or melting snow and ice, which alter the hydrological systems and thus, the quality and quantity of water resources. Also, the mean sea level rose about 0.19 m over the period 1901-2010. Moreover, the ocean has absorbed about the 30 % of the emitted CO_2 causing acidification of oceans that reduces the calcium carbonate saturation with adverse consequences for many calcifying organisms like corals (Fabry et al., 2008); IPCC, 2014). Furthermore, an increase of extreme weather and climate events have been observed like the reduction of cold days and nights, the increase of the heat-related human mortality, the increase of heavy precipitations, and other impacts like heat waves, floods, droughts, cyclones and wildfires (IPCC, 2014).

One of the main causes of the global warming is the increase of the emissions of anthropogenic greenhouse gasses like CO2 or CH4, which mainly comes from the combustion of coal, gas and petrol of the transportation sector, industries and combustion power plants to produce energy and electricity.

Society and Scientifics are pushing the Governments around all over the globe to apply changes on the regulations to become a low-carbon economy and society and defining a cost-effective decarbonization process. Renewable energy market will play a big role in the decarbonization pathway, and it is expected to reach the 30 % of the power production worldwide by 2022, and wind and solar will represent the 80 % of the renewable capacity growth (OECD/IEA, 2017).

The wind energy resources can be found in onshore and offshore sites. The wind energy capacity placed in feasible locations in the year 2030 scenario is about 253 GWatts for onshore sites, and 66.5 GW for offshore locations. However, the installed capacity of the wind energy plants in 2014 was of 121 GW onshore wind plants, and 8 GWs offshore ones (Corbetta, 2015). The evolution of the wind energy industry has followed the logic path from onshore to offshore due to the increase of the complexity of the location and technology readiness. Moreover, placing wind turbines in offshore locations will allow the use of larger rotors as the environmental impacts are lower and the scale economies imply a more efficient turbines.

The technology used in offshore locations below 60 m sea depths is bottom fixed, with three different foundations, the monopiles, the gravity base and the jacket structures. These technologies are economically viable up to 60 m depth, (WindEurope, 2018). Larger depths imply larger structures which increase the Capital Expenditure (CAPEX) and the Operating Expenses (OPEX) reducing the economic margins. Then, the Floating Offshore Wind Turbines (FOWT) has highlighted as the unique reliable technology for depths larger than 60 m to take advantage of this resource in deep waters. However, the technology readiness level of FOWTs is not already mature for a commercial use and more research and innovations are required as well as economies of scale to reduce the overall costs.

There are three dominant classifications of wind turbines structures: 1) the Semi-submersible platform, 2) the Spar-buoy and 3) the Tension leg platform (TLP). A sketch of the structure typologies are shown in Figure 1-1. Some of the FOWT already launched in a full scale size are 7 spars: the Hywind demo in Norway (Driscoll et al., 2016), the 6 Hywind 2 (Equinor, 2019) in Scotland. Also, three semisubmersibles were launched, the WindFloat in Portugal (Peiffer, 2018), the V-Shape Semi-Sub (Komatsu et al., 2016) and the Floatgen platform in France (Choisnet et al., 2018).

FOWT is one of the industrial solutions that will contribute to the reduction of the emissions of greenhouse gasses because of offshore sites present larger wind resources and, then, FOWT capacity factors will be high. FOWTs are currently the solution that will leverage the high and constant winds of the offshore deep sea sites due to the lack of obstacles. However, FOWT technology still needs research and development for a full deployment in a commercial stage (IEA, 2018).

European Commission (2020), James & Costa (2015) and IEA WindEurope (2018) defined the targets for the FOWT technology to be competitive at a commercial scale. These objectives are a reduction of the total costs of the platform, of the maintenance operations and of the mooring system, electrical cable and grid connections. Within these objectives, the cost reduction of station keeping systems must outcome from new optimized mooring systems and as well from new advanced modelling tools which allow to predict more accurately the internal forces in all the stages of the life cycle of the FOWT and, particularly, the reliability of the mooring and cable systems (James & Costa, 2015; Matha et al., 2011).

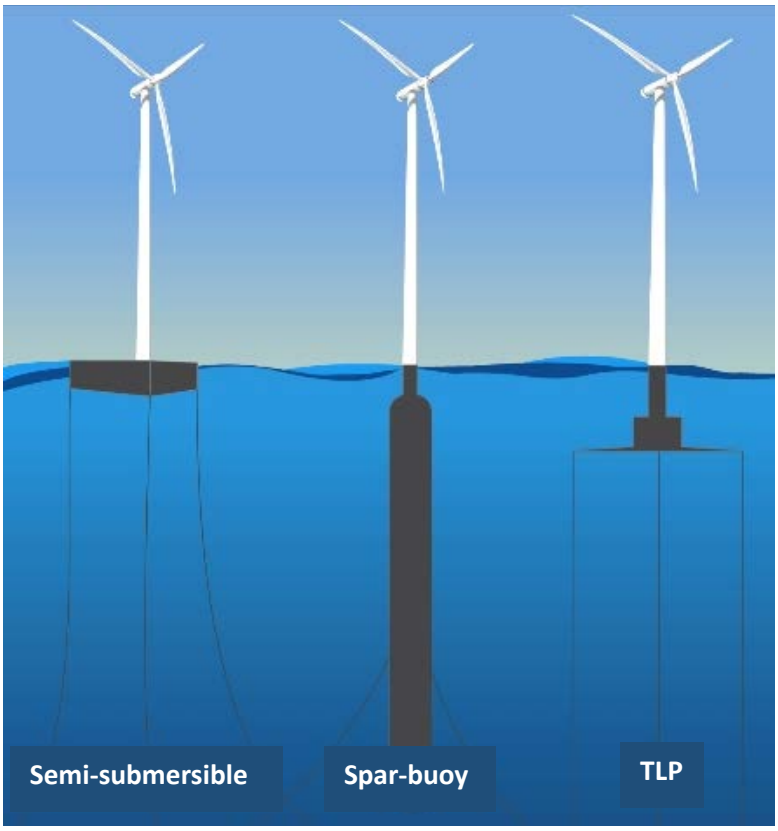

*Figure 1-1: Floating wind turbines types (*Woodward, 2011)

Within the research of Offshore Structures at the Civil and Environmental Department at UPC, a new floating concept named WindCrete was developed. Windcrete is a monolithic concrete spar floating platform for wind turbines developed and conceptually proved in the AFOSP innovation project with KIC-InnoEnergy (Molins et al., 2013; Molins et al., 2014; Campos et al., 2016).

The spar prototype is designed as a monolithic concrete structure from the top of the tower to the bottom of the buoy, thus joints are avoided to ensure water-tightness and a good fatigue behavior. The structure for a 5 MW wind turbine, is composed of three parts: first, the buoy, composed of a cylinder with a diameter of 13 m and a height of 120 m; second, the transition piece, which is a cone of 10 m high, these two parts are the submerged ones, therefore the total draft of the structure is 130 m. The third part is the emerged tower that reaches 87.6 m above the mean sea level. The moorings system is connected to the platform at the fairleads located at a depth of 70 m, near the center of gravity to reduce the coupling motions between the surge and pitch. Further research, will define the WindCrete characteristics for a 15 MW wind turbine within the Corewind Project (Corewind, 2019), funded by the European Commission.

Moreover, in order to assess the behavior of the FOWT platforms (semi-submersible, spars or TLP), and bottom fixed platforms (monopiles, jacket or gravity based), a numerical model named FloaWDyn is under development. The FloaWDyn model is an aero-hydro-servo-elastic tool that analyses the whole structure, platform and tower using the finite element method.

The FloaWDyn is based on a co-rotational Finite Element Model that couples the overall dynamics of the whole platform with its deformation at each time step (Campos et al., 2017). The FEM allows either truss, beam and shell elements. The aerodynamics are assessed by the FAST AeroDyn model (Jonkman & Jonkman, 2016). The hydro forces are divided in hydrostatic forces that accounts for the buoyancy of the structure and the wave forces. The mooring system models are based on the work presented in this Thesis. The mooring system can be modeled with a quasi-static model, with a quasi-dynamic model and with a dynamic finite element model. The quasi-dynamic model is an upgrade of the quasi-static model which uses the static solution of the catenary line, but updates the tension of the line based on an approximation of the dynamics of the line. The FEM model is based on the slender rod model, (Garrett, 1982), with the addition of the material stiffness, small strain assumption and material damping for both axial and bending deformations (Trubat & Molins, 2019) Both models are further detailed in this Thesis.

Further details of the FloaWDyn model are presented in the Appendix 3 because is the frame model used for the simulations within this Thesis.

1.1 RESEARCH OBJECTIVES

The aim of the research presented in this Thesis is to increase the knowledge related to the station keeping analysis and design for floating offshore wind turbines. The proper achievement of the main goals is planned through the accomplishment of the next partial objectives:

- Develop a state of the art of the existing numerical models and design procedures for station keeping systems for FOWT's.
- Develop a new dynamic mooring model to couple it with FloaWDyn, the aero-hydro-servo-elastic model.
- Improve the dynamic mooring model upgrading the design capabilities to assess different type of materials and cables, clump weights, buoys and shared mooring lines.
- Develop a fast and reliable mooring model improving the current quasi-static models to allow an affordable and accurate mooring fatigue assessment.
- Contribute to the design procedure of mooring lines for FOWTs by assessing the influence on the wave loads on the lines.

1.2 DISERTATION OUTLINE

The present Thesis is organized as a compilation of four research journal papers and a conference paper. The Thesis is composed of six chapters and one appendix chapter. The 1st chapter is the introduction; the 2nd chapter is the state of the art of the analysis and design of the station keeping systems; the 3rd to 6th chapters are composed from the body of the journal papers submitted and extended to give a wider

explanation of the research. The appendix exposes the FloaWDyn model as the model used for the simulations and the contribution of the author in the hydrodynamics and wave forces implementation. Each paper has been edited and presented as a chapter in a Thesis format.

Chapter 2 presents the state of the art review of the methods for the analysis and design of station keeping systems. It is based on the introduction and states of the art of the research papers.

Chapter 3 presents an extension of the slender rod model (Garrett, 1982) that takes into account the internal viscous damping through a rheological model in the axial and bending directions. This approach allows to assess in a more realistic way the damping contribution of the line elements due to its deformation and can be applied to chains, wire ropes and electrical cables.

Chapter 4 proposes a new model for catenary mooring line analysis which approaches the dynamic behavior of the line from the quasi-static solution updating the fairlead tension by multiplying it with a quasi-dynamic factor. The model allows a fast and reliable mooring analysis for fatigue assessment in the time domain.

Chapter 5 shows the influence of the wave loads over the mooring lines. The research appraises the tension variation in the mooring lines due to waves for two different types of FOWTs and the influence of the depth of the fairlead position. The load variation is studied for peak tension and fatigue analysis.

Chapter 6 presents an optimization problem for the characterization of the mooring system for the Windcrete platform scale test prototype. The scale mooring system has to be design to emulate the prototype mooring system but with large space constraints because it has to be installed in a narrow wave flume.

Appendix 1 provides the hydrodynamic wave kinematics and loads implemented in the FloaWDyn model. The main characteristics of the theory are presented as well as the main parameters that are used to define and assess the waves hydrodynamics over the bar and shell elements of the model. The appendix also contains a new approach to assess the diffraction phenomenon in cylinder elements by only modifying the higher frequency range of the wave elevation.

1.3 PUBLICATIONS

1.3.1 Publications conforming the present dissertation

The research papers presented as chapters of the thesis are listed in the following.

Chapter 3:

- '*Rheological damping for slender rods',* published in Marine Structures, 67 (2019) 102639

  Authors: Pau Trubat and Climent Molins

Chapter 4:

- '*Quasi-dynamic mooring line model',* submitted to Marine Structures

Authors: Pau Trubat, Climent Molins and Xavi Gironella

Chapter 5:

- '*Wave hydrodynamic forces over mooring lines on floating offshore wind turbines',* published in Ocean Engineering (2019)

Authors: Pau Trubat, Climent Molins and Xavi Gironella

Chapter 6:

- *Design Optimization for a Truncated Catenary Mooring System for Scale Model Test,* published in Journal of Marine Science and Engineering, 2015, 3(4), 1362-1381

Authors: Climent Molins, Pau Trubat and Xavi Gironella, Alexis Campos

1.3.2 Other publications developed in the framework of the thesis

Appendix 1:

- *'Application of Morison equation in irregular wave trains with high frequency waves ',* presented in the Proceedings of the ASME 2018 37th Intenational Conference, Offshore and Artic Engineering, OMAE 2018-77913

Authors: Pau Trubat, Climent Molins, Philipp Hufnagel, Daniel Alarcón, Alexis Campos

2 STATE OF THE ART

Main efforts to reduce the uncertainties of the design of FOWT are focused on the improvement of the simulation tools as remarked by IEA (2018); James & Costa (2015); Matha et al. (2011). There are two typologies of models, the high-fidelity models and the engineering models. The formers are based on CFD models which solves the fluid dynamics in the time domain and the interaction with the floating platforms. The CFD models are also high computational cost but can achieve a high accuracy and more understanding of the fluid-structure interaction phenomenon (Robertson & Jonkman, 2019; Borisade et al., 2016). The engineering models are more simplified models but can perform lager analysis and allow coupling many models, like the structure, the wind turbine, the aerodynamics, and the mooring lines. The engineering models can be based on the frequency domain (Pegalajar-Jurado et al., 2018), or in the time domain (Jonkman & Jonkman, 2016; A Campos et al., 2017) and the motion of the platform are usually assessed by rigid body, multibody or FEM formulations. The engineering tools are based on the coupling of the numerical models of the different components that make up the FOWT such as the blade aerodynamics, the platform hydrodynamics, the mooring loads, and the overall structural response. Then, uncertainties can come from many sources due to the complexity of the models. However, these tools are the only way to perform all the design load cases that the standards require with a reasonable computational cost. IEA Tasks 23 and 30, also known as Offshore Code Comparison Collaboration Projects (OC3, OC4 and OC5), are international collaborative projects with the aim of assessing the accuracy and reliability of these sophisticated tools and identifying research and development needs (Jonkman & Musial, 2010).

Within the different FOWT components, the mooring system design and its cost reduction are highlighted (James & Costa, 2015) as a key factor for ensuring a future commercialization of the technology.

Moreover, the “Secure, clean and efficient energy work program” of the UE Horizon2020 (European Commission, 2020), specifies a reliable, sustainable and cost efficient mooring system in the scope for the floating wind technology. The improvement of the mooring systems may come from new mooring solutions like the use of advanced materials to reduce weight and costs, the sharing of mooring system between adjacent FOWTs, but also from a more deeply understanding of the mooring design by increasing the fidelity of the models as well as the development of fast and reliable models to use in macro models for wind farms.

In the following sections, the state of the art of the mooring and the station keeping systems is presented with special focus in the different station keeping systems; the numerical models currently used for design purpose; the design process and main phenomena related with the design, such as slack-snap phenomenon; and the scale mooring systems used in the scale model tests.

2.1 MOORING CONFIGURATIONS

The main function of a station keeping system is to restrain the position of a floating platform in an acceptable range inside its initial equilibrium position. The surge and sway offset for FOWTs are limited due to the dynamic cables that transmits the electrical power to the sub-station. These limitation aims to reduce the total stress that the cable has to resist to avoiding the failure of the electrical system (Young et al., 2018). These cables cannot resist large loads, then they must be compliant at any position of the platform and, thus, platform motions must avoid large excursions. Moreover, the station keeping system also contributes to the restraint of the orientation of the platform, providing the needed yaw stiffness to the FOWT.

The station keeping systems can be divided in three groups, 1) catenary moorings; 2) semi-taut or taut moorings; and 3) tendon lines, and can be shown in Figure 2-1.

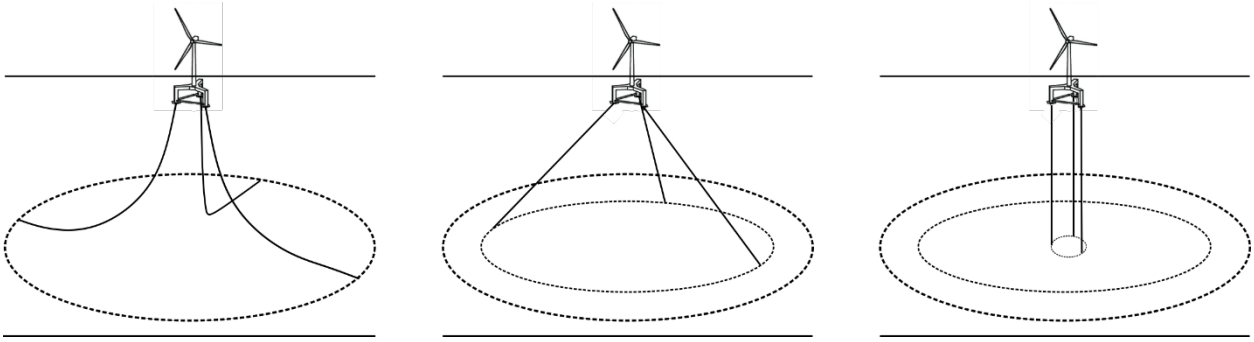

Figure 2-1: Station keeping system types

2.1.1 Catenary moorings

The catenary mooring system is the most common used station keeping system in the offshore industry because its simplicity, the easy installation and the design knowledge. Catenary mooring systems can be installed independently of the sea depth, but the actual applicability is for shallow waters and up to not very deep seas. Larger sea depths increase the length of the catenary lines which increase the total

suspended weight, and also increases the foot print that takes up in the seabed. Thus, this solution is less economically feasible and reduce the working payload of the floating structures.

The catenary line usually presents a horizontal span of 5-20 times the vertical dimension (S. Chakrabarti, 2005). It is common to be composed by three different segment types as shown in Figure 2-2. The first one attached to the platform is a chain which avoids bending moments in the connection due to its lack of bending stiffness. The middle segment is usually composed by a steel wire rope, that allows to reduce the suspended weight maintaining the breaking strength of the line. The bottom section attached to the anchor and supported on the seabed is also a chain. The use of a chain in this region helps to avoid the wear on the line due to the contact with the seabed. Catenary lines are designed to transmit only horizontal forces to the anchor. Then, a segment of the bottom chain has always to rest over the seabed even for the worst load case to ensure that no vertical force acts on the anchor.

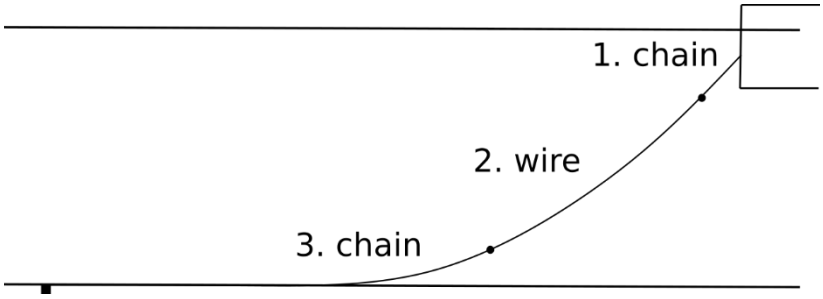

Figure 2-2: Catenary mooring shape sketch

The FOWT concepts designed with catenary mooring systems for the station keeping are the Hywind Demo, (Driscoll et al., 2016) , the Hywind 2 pilot park in Scotland (Equinor, 2019), the VolturnUS (Habib Dagher et al., 2017), the V-Shape Semi-Sub (Komatsu et al., 2016), and the WindCrete (Campos et al., 2016; Molins et al., 2014).

2.1.2 Semi-taut and taut lines

In deeper seas where catenary mooring systems are not feasible, the semi-taut and taut mooring systems are commonly used in the O&G industry. The lines used are mainly synthetic fiber ropes of polyester, but wire ropes can be also used. These systems allow to reduce the total suspended weight of the mooring lines, and provide the restoring forces by the stretching of the lines. Then, the main parameter that characterize the lines is the axial stiffness. However, the mooring lines have to present enough elasticity to resists the overloads due to the wave motions of the platform.

The semi-taut mooring systems present a short chain segment connected to the anchor that lies on the sea-bed at its static initial configuration. However, if the platform is loaded by either wind or waves forces, achieving a certain surge offset, the mooring line becomes taut and the anchor have to resist vertical loads. Then, anchors have to be driven piles, suction piles, plate anchors or special drag embedded anchors that restrain loads in vertical and horizontal directions (Müller et al., 2018), the Figure 2-3 shows the principal anchor types.

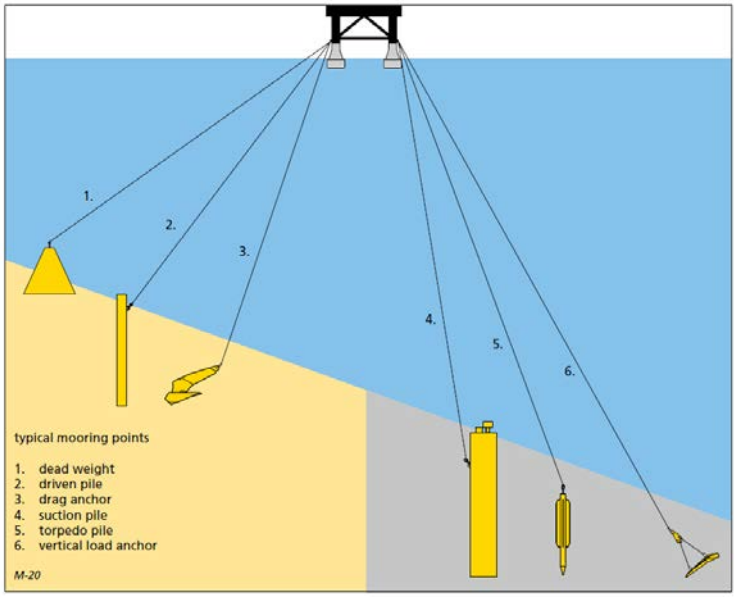

Figure 2-3: Principal anchor types (Vryhof, 2015)

The main advantage of the taut mooring system is the reduction of the suspended line weight and the reduction of the footprint in very deep seas.

Some concepts of FOWT designed with semi-taut mooring systems are the WindFloat from Principle Power (Peiffer, 2018), and the Floatgen from IDEOL (Choisnet et al., 2018).

2.1.3 Tendon legs

Restrained floaters are equipped with a station keeping system that restrain one or more modes of motion. These floaters are usually attached to the seabed by vertical steel tendons. The restrained motions are the heave, for systems with one or two tendon, and pitch/roll if the station keeping system has more than two tendons.

Restrained floaters are also known as tension leg platforms, which have an extra buoyancy that is cancelled out by the force exerted by the tendons. The motions of the platform have to be studied in a wider frequency range: 1) the high frequency response is governed by the tendons; 2) the wave frequency response; 3) the low frequency range due to wind and low frequency wave range.

These type of floaters also need pile type anchors, and present the lower footprint because they raise vertically. There are some FOWT concepts with tendon legs like the TLPWind (Amate et al., 2014), the GICON-TLP, (Großmann et al., 2014) and the Blue-H (Blue H Engineering, 2017).

2.1.4 Station keeping connections

Mooring system can be attached to the platform in two ways: 1) as a spread mooring system, or 2) as a single point mooring (SPM) system shown in Figure 2-4.

The spread mooring system presents all the lines distributed along the platform edge through the fairleads. This type of connection gives a yaw restoring moment to the platform that can be increased by

the use of crowfoots also known as delta lines. Many examples of spread mooring systems can be found within the FOWT concepts as, the WindFloat (Peiffer, 2018), the Hywind (Driscoll et al., 2016), the FLOATGEN (Choisnet et al., 2018), the V-Shape Semi-Sub (Komatsu et al., 2016), and the WindCrete platform (Campos et al., 2016).

In the SPM systems all the mooring lines are attached at the same point. This allows the floating platform to weathervane to the main wind direction. Some examples can be found in the FOWT concepts like the X1Wind (X1Wind, 2019), the Hystoh platform (Manjock & Starr, 2019), and the Eolink platform (Guyot et al., 2019).

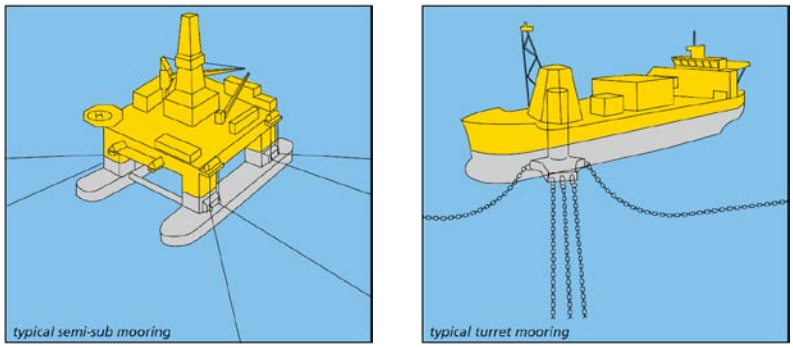

*Figure 2-4: Spread (left) and SPM (right) mooring systems (*Vryhof, 2015)

2.1.5 Wind Farm configurations

Floating offshore wind farms will be composed of between 50 and 100 FOWT depending on the size of the farm. Several strategies are being studied to reduce the costs related to the installation process. Lerch et al. (2019) presented a model to optimize the collection grid to reduce the total costs and decreasing the energy losses. Also current research is done in order to design shared anchors between adjacent FOWTs in order to reduce the costs of the station keeping systems of the wind farm as shown in (Hallowell et al., 2018; Fontana et al., 2016).

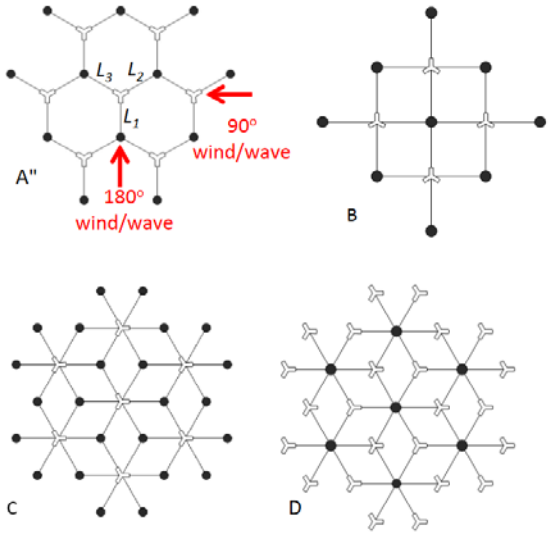

*Figure 2-5: Shared anchor geometric designs (*Fontana et al., 2016)

2.2 MODELS FOR THE ANALYSIS OF MOORING LINE AND CABLE

The analysis of the mooring systems is performed by numerical models that compute the forces that the mooring lines apply to the platform. These forces are assessed by the position of the fairlead and its motion that are updated at each time step. The numerical models for mooring analysis can be divided in linearized, quasi-static and dynamic models. The formers are the simplest because assesses the response of the mooring system as a linear stiffness and are mainly used in frequency domain models (Hegseth & Bachynski, 2019). Time domain models use either quasi-static or dynamic mooring line models. The quasi-static models apply the catenary equation to assess the forces of the mooring line top end point, at the fairlead, from the actual fairlead position. The dynamic models assess the line behavior by solving the equations of motion of the mooring lines by considering the inertial forces, the internal forces, and the external forces as the wet weight, the seabed contact, the hydrodynamic forces and the reaction forces as shown in Figure 2-6.

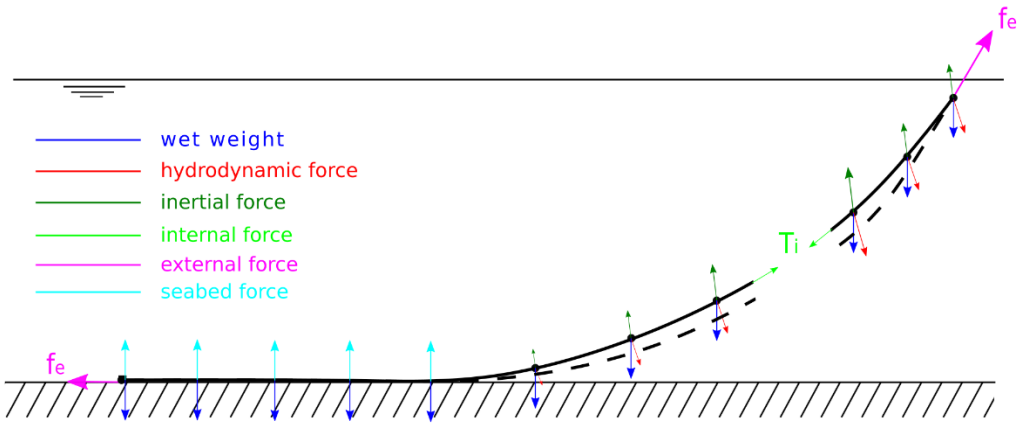

Figure 2-6: Mooring line forces

2.2.1 Quasi-static models

The quasi-static models are based on the catenary equation which have to be solve using nonlinear equation systems (Faltinsen, 1990). The nonlinearities come from the unknown portion of the line suspended and the interaction with the line axial stiffness. Improved analytical models allow to consider the loads applied to the line at the touch down point. Lenci & Callegari (2005) presented a model that considers the soil stiffness, sthe bending stiffness and continuity of shear loads at the touch down point for cables named the three-fields model. The coupling of the quasi-static mooring line models with the platform dynamics gives good results for the platform motions, but the mooring tensions results are incorrectly because the dynamic forces of the line cannot be considered. However, the dynamics of the mooring lines can be estimated by analytical and empirical solutions. Jason I. Gobat & Grosenbaugh (2001) proposed an empirical model to assess the dynamic tension of a mooring line due the vertical motion of it upper end and Aranha & Pinto (2001) proposed an algebraic approximation to assess the dynamic

tension in risers and mooring lines for harmonic excitation in the direction of the cable's tangent. However, dynamic mooring line models are becoming more popular due to their better accuracy.

2.2.2 Dynamic models

The first dynamic model for mooring lines was the lumped mass method (Walton & Polachek, 1959). The lumped mass method divides the mooring line in a number of elements, where its mass, internal forces and external forces are lumped in the nodes of the elements. Later, material elasticity was included by a spring system that connects consecutive lumped masses and the floor contact was also added by Nakajima et al. (1982). On the other hand, line characteristics such as internal damping, bending and torsional stiffness were neglected. The equations of motions were derived by applying dynamic equilibrium and stress-strain deformations on each node, which were solved in the time domain using finite difference schemes.

A second approach to the spatial discretization of the mooring line is based on the finite differences. The main difference between the finite differences and the lumped mass method is the initial assumption of the element description for deducing the equations. Finite differences are based on a small differential element while lumped mass method uses a finite discrete element. Ablow & Schechter (1983) proposed a method that discretizes the problem in both space and time using finite differences. This method uses a second-order implicit scheme centered in space and time, the so-called box-method. These first approaches were unstable when the line reaches null tension at any point of the line. Howell (1992) proposed to take into account the bending stiffness of the cable to overcome the zero tension cable problems with good results. J.I. Gobat & Grosenbaugh (2001) presented a generalized α-method for time integration of the cable dynamics retaining the box-method for the spatial discretization.

FEM for dynamic analysis of slender rods or mooring lines are currently widely used and thoroughly validated within the offshore industry. FEM describe the cable line as a continuous system, but the displacement field is discretized into a number of nodes. The method uses interpolation functions to describe the displacement in the internal points between nodes as well as the tangent, the curvature or the tension; and constitutive equations to describe the strain-stress relationship of the material. Three families of slender rod FEM models can be found in the literature. A first group uses linear interpolation shape functions to describe the cable node global position (Lindahl, 1985; Aamo & Fossen, 2000; Azcona, 2016). These models can only take into account axial deformation and require a fine discretization of the line to accurately simulate large variations of the curvature or slack events. The second family uses larger order finite elements, from cubic to high-order polynomial elements. They allow to model properly the change of curvature of the line and also enable to take into account the bending and the torsional stiffness to improve accuracy in the slack events. They reduce the required discretization at the cost of having a larger number of nodal variables. Some models that use larger order finite elements are Garrett (1982), Buckham (2003), Kim (2003) and Palm et al. (2017). The third family of FEM comes from 3D beam finite element models applied for mooring lines (Petrone et al., 2016) where classic 3D beam formulations are extended for large displacements and rotations, these formulations also include more variables as the spin of the element in addition to the spatial three DOF.

Most of the models use variations of the Newmark's time scheme integration, like the HHT alpha-method presented by Hilber et al. (1977), or the generalized-α method presented by Chung & Hulbert (1993) which applies numerical damping dissipation to overcome numerical instabilities applied (Gobat & Grosenbaugh 2006; Chen & Basu 2018).

The increase of the interest in fiber ropes for mooring systems in deep waters has promoted the extension and the appearance of new mooring line models that deal with high-extensible cables and nonlinear stress-strain relationship. Tahar & Kim (2008) implemented nonlinear stress-strain relationship for polyester mooring lines using Garrett (1982) FEM formulation, but small strain assumption was considered. Lin & Sayer (2015) implemented a second order approximation for the strain to deal with large deformations. Tjavaraas et al. (1998) proposed a finite difference model that considers large strain and nonlinear stress-strain relation. Bai & Niedzwecki (2018) implemented a meshfree formulation using a Local Radial Pint Interpolation Method (LRPIM) that allow to deal with large deflections for slender rods.

The mooring line models use Hooke-s law constitutive equations for describing the elastic behavior of the line in axial direction. More complex models use internal viscous damping to represent energy dissipation from axial velocity deformation due to tether friction between the layers of conductors and polymer coatings (Buckham, 2003; Azcona 2016). On the other hand, stranded cable damping source comes mainly from the sliding between wires during flexural vibrations (Claren & Diana, 1969). The stick-slip frictional behavior of strand cables was first described by Hardy (1990) and extended by Goudreau et al. (1998) which is modelled using classic Amontons-Coulomb friction law. More detailed models assess the stick-slip behavior of each wire of the strand to account for the non-linear section bending response of the cable cross section (Foti et al., 2016). Recently, the research in visco-elastic materials leads to new models to take into account the viscous-elastic rheological damping of beams in bending (Di Paola et al., 2013; Oliveto & Sivaselvan, 2015; Martin, 2017). Moreover, Petrone et al. (2016) presented an extension of a beam FEM to a mooring line model that takes into account both the axial and the bending damping for mooring cables.

2.3 MOORING DESIGN ON FOWTS

The engineering models for analyzing FOWTs, e.g. FAST by Jonkman & Jonkman (2016) and FloawDyn by Campos et al. (2017), are models for design purpose that must be fast and reliable. However, they have to consider a large number of factors that takes part in the design of a FOWT like the Wind Turbine (WT), the tower vibrations, the platform hydrostatics, the mooring behavior, all the possible met-ocean conditions and the service sate of the FOWT. All these factors increase the computational cost, which has to include the large amount of simulations that have to be performed in order to fulfil all the requirements for the Ultimate Limit State, Accidental Limit State and Fatigue Limit State of the current standards.

From the point of view of the loads over the platform dynamics and its final design, the mooring dynamics are of little importance and have a very limited effect on the overall behavior of the floating wind turbine. However, in mooring analysis design, the dynamics effects can be very important and can increase significantly the design tensions from the simulations as stated by Masciola et al. (2013) and Robertson et al. (2017). This difference, is also stated on the safety factor of the mooring line design prescribed in the

design standards such as DNVGL (2015), which is lower if dynamic analyses are performed. On the other hand, mooring dynamic models increase the degrees of freedom of the numerical model and thus, the computational cost for the FOWT analysis.

Currently only dynamic models are capable to reproduce in a good degree of accuracy the tension range of a mooring system for design purpose. To proper model the mooring line by using dynamic models, the line should be divided into several elements, with multiple degrees of freedom as the position and the tension of the line. This leads to high computational cost models as main disadvantage.

The design of the mooring systems for FOWTs is highly influenced by the conditions of the actual particular location of the FOWT. The main parameters that will effect are the depth and the seabed type, but also the met ocean condition, the FOWT typology, the service life of the mooring system and the availability to perform maintenance inspections. Campanile et al. (2018) suggested the use of six mooring lines to ensure redundancy to avoid problems with the fail of one mooring line, and the design parameters should ensure a high fatigue safety factors to avoid onshore inspections. Current station keeping designs are based on optimization tools, which use simplified frequency domain models to predict the ULS, FLS and ALS for the different analyzed cases, and find for the most economical solution. Fylling & Berthelsen (2011) presented a tool for optimizing a spar platform design as well as the mooring system and the dynamic cable. Brommundt et al. (2012) used an optimization problem to design the length of the mooring line and found that the wind spectrum is an important constrain due to the high energy in the low frequency range that affects to the mooring system. Brommundt et al. (2012) also found that the linearization of the mooring system that frequency domain analyses use lead to a more conservative designs due to the non-vertical load constraint at the anchors is more easily violated. Benassai et al. (2014) studied the optimization problem for a tri-floater wind turbine under ULS and ALS design and found that the mooring line weight is substantially independent of the depth in the range between 100 and 200 m, but increases for below and above that range. Benassai et al. also found that the optimum mooring system solutions were found for a platform maximum admissible offset of the water depth of 24 % for 50 m depths, and about 15 % for depths larger than 100 m.

Moreover, long term mooring design for FOWT has become a tough challenge due to the difficulties to assess the dynamics of mooring lines with a low computational cost that balances out the large number of simulations that have to be performed in fatigue analysis. Furthermore, quasi-static models do not represent the total cyclic forces at the most tensioned point of the lines, generally the fairlead, so large safety factors should be applied. This problem is also stated for the design of steel catenary risers of the O&G industry. Quéau et al. (2014) and Sedghi & Kimiaei (2018) used dynamic amplification factors to adjust the static tension to improve the fatigue response of catenary risers and mooring lines respectively. However dynamic of mooring lines are also important for fatigue analysis (Azcona et al., 2017). Barrera et al. (2020) proposed the assessment of the fatigue life of the mooring system of a FOWT from a selected subset of sea states and rebuilding for the full life time using a radial basis function interpolation technique.

Another important mooring line phenomenon is the snap loads. This phenomenon can cause large tensions and be the worst loading condition case in the service life of the mooring line. Snap loads occur due to an over excitation of the fairlead motion. Then, the line gets slack and is retensionded suddenly

producing the peak load. Niedzwecki & Thampi (1991) presented a method to predict the slack region as a function of the frequency ratio, the displacement ratio and the damping ratio for a hanging cable. Suhara et al. (1981) presented an analytic formulation to predict the slack phenomena for catenary mooring lines as a function of a dimensionless acceleration that depends on the mooring characteristics and the fairlead motion amplitude and frequency. Palm et al. (2017) presented a hp-adaptative FEM that changes the size of the mesh and the polynomial order to capture snap loads with high accuracy. Hsu et al. (2017) proposed a composite Weibull distribution to better predict tension distribution for a semi-submersible platform which suffers slack-snap process during experimental tests under a design irregular wave.

2.4 MOORING SCALE MODEL

Truncated mooring systems are a common solution in order to scale the mooring systems used in the O&G industry (Fan et al., 2012; Qiao & Ou, 2014; Stansberg et al., 2001; Zhang et al., 2014). Since the tank basins sizes do not allow performing tests in the common scales for the upcoming ultra-deep waters, new systems have to be conceived to manage this challenge, as shown in Figure 2-7. The truncated passive system is the most widely used and feasible method of the hybrid model testing methods, which uses a combination of physical model tests and numerical models. In the passive method, all the model characteristics like platform properties, wave height, current velocity, *etc.*, are well scaled except the working depth and the mooring shape. This method uses an equivalent truncated mooring system for the scale tests and the results are used to interpret and adjust the model in order to perform a full depth numerical model.

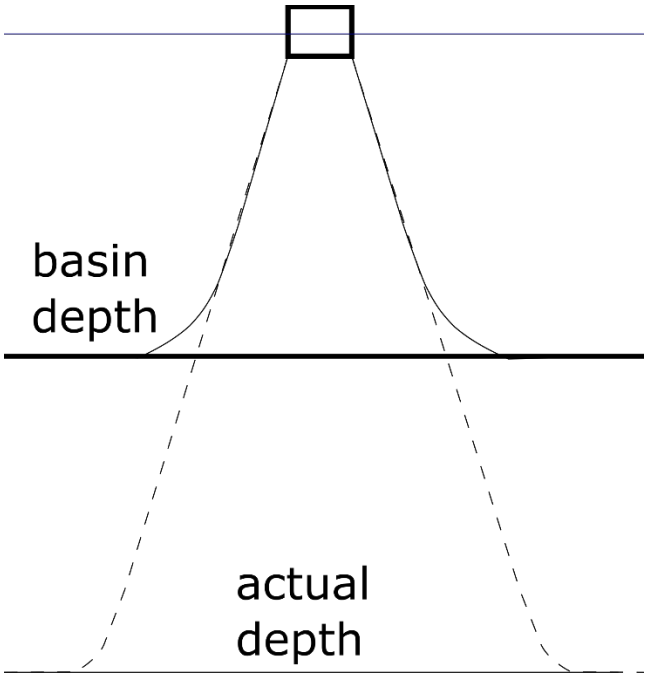

Figure 2-7: Basin vs actual depth and scaled platform setup

Stansberg et al. (2001) state the challenges for the development of the truncated passive methods. The new truncated mooring system set-up has to guarantee the following aspects: (1) the motion response should have the same behavior as the results of the full-depth mooring system and (2) the truncated mooring system should present the most similar physical properties as the full-depth system. To achieve the correct design of the truncated mooring system, Stansberg presents the following rules ordered by priority.

- Model the total horizontal restoring force
- Model the quasi-static coupling between vessel responses
- Model a “representative” level of mooring and riser system damping, and current force
- Model a “representative” single line tension characteristics (at least quasi-static)

In the field of the truncated mooring system design, optimization models to better adjust the truncated system approach to the real one are commonly used to solve the problem. Zhang et al. (2014) proposed an annealing simulation algorithm for hybrid discrete variables to optimize the static response of a single catenary and the whole catenary system static response in one direction. Further investigations propose an optimization model that accounts for the mooring-induced damping generated by the transverse motion of the mooring line due to the low-frequency surge oscillation using a genetic algorithm (Fan et al., 2012). In order to improve the behavior of the truncated mooring line, Qiao & Ou (2014) propose the connection of viscous dampers joined to the mooring line to simulate the whole damping of the real mooring line. These models have been validated and widely used, but the quasi-static approach could underestimate the tension in the mooring lines due to dynamics when those are important (Stansberg et al., 2004). On the other hand, new methods have recently been developed to take into account the line dynamics and obtain a more realistic system behavior using the real scaled mooring line in the upper sections, where the line dynamics are more relevant, and using external actuators that replicate the truncated line segments behavior (Argyros et al., 2011).

3 MOORING DYNAMIC MODEL

3.1 INTRODUCTION

In this chapter, a new extension of the FEM model proposed by Garrett (1982) adding rheological damping material is presented. The model takes advantage of high order shape functions which describe more accurately the line shape and the addition of a visco-elastic term for accounting the damping behavior of the line due to the deformation of the element. This approach allows to assess in a more realistic way the damping contribution of the line elements due to its deformation and can be applied to chains, wire ropes and power cables. The chain elements have no bending stiffness and present higher corrosion and friction resistance than wire ropes, and are commonly used in the bottom and upper segments of the moorings lines. Wire ropes are mainly used in middle sections of long mooring lines, between chains, to reduce the total weight. Electrical wires are one of the most sensitive elements of FOWT because they export the energy produced. Then, they deserve accurate simulation to assess its performance along their service life (James & Costa, 2015).

The model is based on the Garret's formulation, a FEM model for slender rods which assumes large displacements and rotations, but small strains, by including the extensibility of the line as proposed by Kim (2003). The model is extended by accounting for internal viscous damping trough a rheological model and assessing correctly the contribution of the curvature of the rod within the strain-stress constitutive equations. The rheological damping is based on the Kelvin-Voigt model (Christensen, 1982), which proper defines the behavior of visco-elastic materials as used for wire and electrical cable protection and synthetic ropes (Flory et al., 2004). The Kelvin-Voigt model is a proper model for assessing creep and

relaxation which contributes for the internal damping stresses of sudden incremental loads. However, instantly stress-strain relation is conceptually not verified. Moreover, in some cases such as strand cables, the damping source is amplitude dependent instead of frequency dependent. Then, the friction damping due to the stick-slip phenomenon has to be considered as an equivalent viscous damping evaluated for an estimated critical damping ratio, which does not fulfils exactly the physical phenomenon (Rao, 2011). However, the use of a rheological model is more computationally efficient compared with the cross section fiber damping analysis. The proposed rheological model is applied to the axial and the bending internal forces. Derivation of the axial and bending damping forces are presented and assessed in terms of the critical damping ratio for both forces. The curvature of the rod is precisely included by a Lagrange multiplier, which relates the tension and the derivative of the moment. This Lagrange multiplier is included in the strain-stress constitutive equation to combine correctly the equations of motion and deformation. The use of the Lagrange multiplier implies the addition of a new variable. Thus, the number of degrees of freedom of the problem is also increased. Otherwise, the main advantage is the direct relation of the stress-strain relation equation with the equations of motions of the slender rod. Then, both system of equations can be solved jointly in a larger system of equations in a matrix way. In the other case, the internal stress would be an explicit term and should be assessed at the end of each iteration. Using the internal stresses as an explicit term would increase the number of iterations to get a proper tolerance of the solution.

The chapter presents the differential equations of motion of the slender rods, the finite element integration, the initial static configuration and the time integration schemes of the proposed model.

The accuracy of the model is appraised with three examples of verification followed by two validation cases. The verification analyses consist in the numerical simulation of the vibration of a rod in axial and bending forces with different values of the critical damping. The validation examples are more complex and consist in, first, comparing the experimental results of the free fall of a dynamic cable presented by Koh et al. (1999) and, second, the simulation of the experimental results of a mooring chain with a cyclic imposed motion at one end (Lindahl, 1985; Palm et al., 2013).

3.2 RHEOLOGICAL DAMPING MATERIAL

The rheological behaviour of viscoelastic solids may be described by the Kelvin-Voigt model which includes a spring and a dashpot in parallel as depicted in Figure 3-1, (Christensen, 1982). The strain-stress relation of the material for a constant initial stress presents a creep behavior transforming all stress to the spring at infinite time. However, instant stress-train relation behavior is not presented as certain time is needed to achieve the elastic tension. This time is related with the retardation time.

The time retardation (Mezger, 2014) is the ratio between $\frac{\eta}{E}$ and in the cases dealt in this research is between 1 and 4 % of the vibration period, where E and η are the Young modulus and the material viscosity respectively.

The differential equation that defines the strain-stress behavior in the Kelvin-Voigt model can be expressed by Eq. (3.1), where σ is the normal tension of the cross section of the line, ε is the axial strain

of a line section. In all the following development, direct proportion between stress and strains is assumed (Hooke's law).

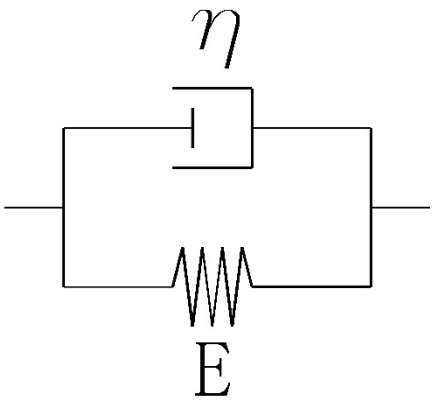

Figure 3-1: Kelvin-Voigt rheological model

$$\sigma = \mathrm{E}\varepsilon + \eta\frac{\partial \varepsilon}{\partial t} \tag{3.1}$$

Then, in absence of bending, the axial force (N) is obtained directly by integrating the uniform axial stress across the section A:

$$\mathrm{N} = \int \sigma \, \mathrm{dA} = \mathrm{EA}\varepsilon + \eta\mathrm{A}\frac{\partial \varepsilon}{\partial t} \tag{3.2}$$

From Eq. (3.1), the internal bending moment can be obtained by the integration of the stress multiplied by the distance to the neutral axis of the cross section, in this case the centerline. Assuming the Euler-Bernoulli beam approach, the strain-curvature relation can be expressed as $\varepsilon \cong \kappa \cdot z$, where z is the transverse distance with origin at the neutral axis and normal to axial coordinate in the osculating plane, and κ is the cable curvature. Then, the curvature velocity can be approximate from the axial strain velocity as follows $\frac{\partial \varepsilon}{\partial t} \cong \frac{\partial \kappa}{\partial t} z$. Thus, the moment is expressed in Eq. (3.3), where I is the second moment of area of the cross section.

$$\mathrm{M} = \int \sigma \cdot \mathrm{z} \, \mathrm{dA} = \int \left(\mathrm{E}\varepsilon + \eta\frac{\partial \varepsilon}{\partial t}\right) \cdot z \, dA = \int \left(\mathrm{E}\kappa + \eta\frac{\partial \kappa}{\partial \mathrm{t}}\right) \cdot z^2 \, dA = I\left(\mathrm{E}\kappa + \eta\frac{\partial \kappa}{\partial t}\right) \tag{3.3}$$

3.3 ROD MODEL ADDING RHEOLOGICAL DAMPING

The adopted rod model is a FEM model based on the formulation presented by Garrett (1982) which is derived from the translational and rotatory equations of motions of a slender rod for large displacements and rotations. Also the material stiffness and the small strain assumption is accounted as proposed by Kim

Kim (2003). The model is extended to apply the material damping for both axial and bending deformations, the normal strains.

The cable is defined by the centreline position $\mathbf{r}(s,t)$ as a function of the arc-length parameter "s" and the time "t", as is shown in Figure 3-2. The centreline position defines the deformed shape of the line. At any point of the line the tangent vector of the curve $\mathbf{t}$ is defined as the unit vector of the derivative of the centreline position respect to the arc-length parameter, where the norm of the derivative of the centreline is equal to the strain plus the unit. The normal vector $\mathbf{n}$ is defined as the unit vector of the derivative of the tangent vector, and can also be expressed as the second derivative of the line position divided by the curvature (k). The tangent and the normal vectors define the osculating plane at each point. The binormal vector $\mathbf{b}$ is defined as the cross product of $\mathbf{t}$ and $\mathbf{n}$. The tangent, normal and binormal vectors are defined in Eq. (3.4), where prime denotes differentiation respect to "s". The global coordinates is such as the z direction is pointing against the gravity. The unitary global vectors are defined as $[\boldsymbol{e_x}, \boldsymbol{e_y}, \boldsymbol{e_z}]$.

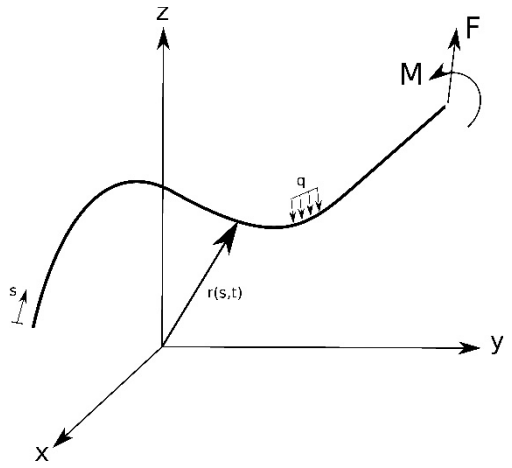

Figure 3-2: cable centerline sketch

$$\begin{aligned}
\mathbf{t} &= \frac{\frac{\partial \mathbf{r}}{\partial s}}{\left\|\frac{\partial \mathbf{r}}{\partial s}\right\|} = \frac{\mathbf{r}'}{\|\mathbf{r}'\|}\ ; \\
\mathbf{n} &= \frac{1}{\kappa}\frac{d\mathbf{t}}{ds} = \frac{1}{\kappa}\frac{d}{ds}\left(\frac{\mathbf{r}'}{\|\mathbf{r}'\|}\right) = \frac{1}{\kappa}\frac{\mathbf{r}''}{\|\mathbf{r}'\|}\ ; \\
\mathbf{b} &= \mathbf{t} \times \mathbf{n}
\end{aligned} \tag{3.4}$$

where:

$\|\mathbf{r}'\| = (1+\varepsilon)$, ε is the strain

κ is the curvature and is defined as $\kappa = \frac{\|\mathbf{r}''\|}{\|\mathbf{r}'\|}$

$$\frac{d}{ds}\left(\frac{\mathbf{r}'}{\|\mathbf{r}'\|}\right)=\frac{\mathbf{r}''(\mathbf{r}'\cdot\mathbf{r}')^{\frac{1}{2}}-\mathbf{r}'\frac{1}{2}(\mathbf{r}'\cdot\mathbf{r}')^{-\frac{1}{2}}\cdot 2(\mathbf{r}'\cdot\mathbf{r}'')}{\mathbf{r}'\cdot\mathbf{r}'}=\frac{\mathbf{r}''}{\sqrt{\mathbf{r}'\cdot\mathbf{r}'}}$$

3.3.1 Derivation of the equation of motion

Conservation of the linear and angular momenta of a differential cable element leads to the translational equation of motion Eq. (3.5) and to the static rotatory equation of motion Eq. (3.6) by neglecting the rotatory inertia and the shear deformation. $\mathbf{F}$ and $\mathbf{M}$ are the resultant force and moment respectively of the internal stress state at one point acting on the centreline, $\mathbf{q}$ and $\mathbf{m}$ are the external applied force and moment per unit length, ρ_m is the line density, A is the cross section of the line, and the superposed dot denotes differentiation with respect to time.

$$\mathbf{F}'+\mathbf{q}=\rho_m A\,\ddot{\mathbf{r}} \tag{3.5}$$

$$\mathbf{M}'+\frac{\mathbf{r}'}{\|\mathbf{r}'\|}\times\mathbf{F}+\mathbf{m}=0 \tag{3.6}$$

The resultant moment for an elastic rod according to Euler-Bernoulli theory with equal principal stiffness, adding rheological damping material and disregarding the torsional component of the stress is expressed in Eq. (3.7). This equation is derived from the moment Eq. (3.3) in terms of $\mathbf{t}$ and $\mathbf{n}$.

$$\mathbf{M}=EI\kappa\mathbf{b}+\eta I\dot{\kappa}\mathbf{b}=\frac{\mathbf{r}'}{\|\mathbf{r}'\|}\times\left(\left(EI+\eta I\frac{\dot{\kappa}}{\kappa}\right)\frac{\mathbf{r}''}{\|\mathbf{r}'\|}\right)=\frac{\mathbf{r}'}{\|\mathbf{r}'\|}\times\left(EI\frac{\mathbf{r}''}{\|\mathbf{r}'\|}+\eta I\left(\frac{\mathbf{r}''\cdot\dot{\mathbf{r}}''}{\mathbf{r}''\cdot\mathbf{r}''}-\frac{\mathbf{r}'\cdot\dot{\mathbf{r}}'}{\mathbf{r}'\cdot\mathbf{r}'}\right)\frac{\mathbf{r}''}{\|\mathbf{r}'\|}\right) \tag{3.7}$$

The curvature velocity $(\dot{\kappa})$ is obtained by the derivative of the curvature respect to time, as is shown in Eq. (3.8). The equation states the relation between the curvature velocity and the difference between the normal and tangent velocities. In a simplified way, it means that if the velocity of the normal vector increases in a given proportion with the tangent velocity, the curvature remains constant and then, the curvature velocity is zero.

$$\dot{\kappa}=\frac{(\mathbf{r}''\cdot\dot{\mathbf{r}}'')}{(\mathbf{r}'\cdot\mathbf{r}')^{\frac{1}{2}}\cdot(\mathbf{r}''\cdot\mathbf{r}'')^{\frac{1}{2}}}-\frac{(\mathbf{r}''\cdot\mathbf{r}'')^{\frac{1}{2}}\cdot(\mathbf{r}'\cdot\dot{\mathbf{r}}')}{(\mathbf{r}'\cdot\mathbf{r}')^{\frac{3}{2}}} \tag{3.8}$$

Then, the ratio of the curvature velocity respect to the curvature found in Eq. (3.7) can be expressed as:

$$\frac{\dot{\kappa}}{\kappa}=\frac{\mathbf{r}''\cdot\dot{\mathbf{r}}''}{\mathbf{r}''\cdot\mathbf{r}''}-\frac{\mathbf{r}'\cdot\dot{\mathbf{r}}'}{\mathbf{r}'\cdot\mathbf{r}'} \tag{3.9}$$

In order to expand the Eq. (3.6), the derivative of the resultant moment from Eq. (3.7) respect to the arc length has the form of Eq. (3.10).

$$\mathbf{M}' = \left(\frac{\mathbf{r}'}{\|\mathbf{r}'\|}\right)' \times \left(\left(EI + \eta_B I\left(\frac{\mathbf{r}''\cdot\dot{\mathbf{r}}''}{\mathbf{r}''\cdot\mathbf{r}''} - \frac{\mathbf{r}'\cdot\dot{\mathbf{r}}'}{\mathbf{r}'\cdot\mathbf{r}'}\right)\right)\frac{\mathbf{r}''}{\|\mathbf{r}\prime\|}\right) + \frac{\mathbf{r}'}{\|\mathbf{r}'\|} \times \left(\left(EI + \eta_B I\left(\frac{\mathbf{r}''\cdot\dot{\mathbf{r}}''}{\mathbf{r}''\cdot\mathbf{r}''} - \frac{\mathbf{r}'\cdot\dot{\mathbf{r}}'}{\mathbf{r}'\cdot\mathbf{r}'}\right)\right)\frac{\mathbf{r}''}{\|\mathbf{r}'\|}\right)' = \frac{\mathbf{r}''}{\|\mathbf{r}'\|} \times \left(\left(EI + \eta_B I\left(\frac{\mathbf{r}''\cdot\dot{\mathbf{r}}''}{\mathbf{r}''\cdot\mathbf{r}''} - \frac{\mathbf{r}'\cdot\dot{\mathbf{r}}'}{\mathbf{r}'\cdot\mathbf{r}'}\right)\right)\frac{\mathbf{r}''}{\|\mathbf{r}\prime\|}\right) + \frac{\mathbf{r}'}{\|\mathbf{r}'\|} \times \left(\left(EI + \eta_B I\left(\frac{\mathbf{r}''\cdot\dot{\mathbf{r}}''}{\mathbf{r}''\cdot\mathbf{r}''} - \frac{\mathbf{r}'\cdot\dot{\mathbf{r}}'}{\mathbf{r}'\cdot\mathbf{r}'}\right)\right)\frac{\mathbf{r}''}{\|\mathbf{r}'\|}\right)' = \frac{\mathbf{r}'}{\|\mathbf{r}'\|} \times \left(EI\frac{\mathbf{r}''}{\|\mathbf{r}\prime\|} + \eta_B I\left(\frac{\mathbf{r}''\cdot\dot{\mathbf{r}}''}{\mathbf{r}''\cdot\mathbf{r}''} - \frac{\mathbf{r}'\cdot\dot{\mathbf{r}}'}{\mathbf{r}'\cdot\mathbf{r}'}\right)\frac{\mathbf{r}''}{\|\mathbf{r}\prime\|}\right)' \tag{3.10}$$

Next, substituting Eq. (3.10) into Eq. (3.6) and neglecting the applied linear moment per unit length $\mathbf{m}$ leads to:

$$\frac{\mathbf{r}'}{\|\mathbf{r}'\|} \times \left(\left(EI\frac{\mathbf{r}''}{\|\mathbf{r}'\|} + \eta I\left(\frac{\mathbf{r}''\cdot\dot{\mathbf{r}}''}{\mathbf{r}''\cdot\mathbf{r}''} - \frac{\mathbf{r}'\cdot\dot{\mathbf{r}}'}{\mathbf{r}'\cdot\mathbf{r}'}\right)\frac{\mathbf{r}''}{\|\mathbf{r}'\|}\right)' + \mathbf{F}\right) = 0 \tag{3.11}$$

The Eq. (3.11) shows the relationship between $\mathbf{r}$, $\mathbf{F}$ and $\mathbf{M}'$. Then, $\mathbf{F}$, and $\mathbf{M}'$ must be proportional to the tangent vector $\mathbf{t}$, and this relationship can be expressed as follows.

$$\left(EI\frac{\mathbf{r}''}{\|\mathbf{r}'\|} + \eta I\left(\frac{\mathbf{r}''\cdot\dot{\mathbf{r}}''}{\mathbf{r}''\cdot\mathbf{r}''} - \frac{\mathbf{r}'\cdot\dot{\mathbf{r}}'}{\mathbf{r}'\cdot\mathbf{r}'}\right)\frac{\mathbf{r}''}{\|\mathbf{r}'\|}\right)' + \mathbf{F} = \lambda\frac{\mathbf{r}'}{\|\mathbf{r}'\|} \tag{3.12}$$

Where $\lambda(s,t)$ is a scalar, and can be identified as the Lagrange multiplier. Then, the force $\mathbf{F}$ is of the form of:

$$\mathbf{F} = -\left(EI\frac{\mathbf{r}''}{\|\mathbf{r}'\|} + \eta I\left(\frac{\mathbf{r}''\cdot\dot{\mathbf{r}}''}{\mathbf{r}''\cdot\mathbf{r}''} - \frac{\mathbf{r}'\cdot\dot{\mathbf{r}}'}{\mathbf{r}'\cdot\mathbf{r}'}\right)\frac{\mathbf{r}''}{\|\mathbf{r}'\|}\right)' + \lambda\frac{\mathbf{r}'}{\|\mathbf{r}'\|} \tag{3.13}$$

The scalar product of Eq. (3.13) with $\frac{\mathbf{r}'}{\|\mathbf{r}'\|}$ leads to an expression that defines the Lagrange multiplier in Eq. (3.14).

$$\lambda = \left(\mathbf{F} + \left(EI\frac{\mathbf{r}''}{\|\mathbf{r}'\|} + \eta_B I\left(\frac{\mathbf{r}''\cdot\dot{\mathbf{r}}''}{\mathbf{r}''\cdot\mathbf{r}''} - \frac{\mathbf{r}'\cdot\dot{\mathbf{r}}'}{\mathbf{r}'\cdot\mathbf{r}'}\right)\frac{\mathbf{r}''}{\|\mathbf{r}'\|}\right)'\right)\frac{\mathbf{r}'}{\|\mathbf{r}'\|} = \mathbf{F}\frac{\mathbf{r}'}{\|\mathbf{r}'\|} + \left(EI\frac{\mathbf{r}''}{\|\mathbf{r}'\|} + \eta_B I\left(\frac{\mathbf{r}''\cdot\dot{\mathbf{r}}''}{\mathbf{r}''\cdot\mathbf{r}''} - \frac{\mathbf{r}'\cdot\dot{\mathbf{r}}'}{\mathbf{r}'\cdot\mathbf{r}'}\right)\frac{\mathbf{r}''}{\|\mathbf{r}'\|}\right)'\frac{\mathbf{r}'}{\|\mathbf{r}'\|} = T - \left(EI + \eta_B I\left(\frac{\mathbf{r}''\cdot\dot{\mathbf{r}}''}{\mathbf{r}''\cdot\mathbf{r}''} - \frac{\mathbf{r}'\cdot\dot{\mathbf{r}}'}{\mathbf{r}'\cdot\mathbf{r}'}\right)\right)\kappa^2 \tag{3.14}$$

Since:

$$\begin{cases} \lambda\frac{\mathbf{r}'}{\|\mathbf{r}'\|}\cdot\frac{\mathbf{r}'}{\|\mathbf{r}'\|} = \lambda\frac{\|\mathbf{r}'\|^2}{\|\mathbf{r}'\|^2} = \lambda \\ \mathbf{F}\frac{\mathbf{r}'}{\|\mathbf{r}'\|} = \mathbf{F}\cdot\mathbf{t} = \mathbf{T} \\ \left(X\frac{\mathbf{r}''}{\|\mathbf{r}'\|}\right)'\frac{\mathbf{r}'}{\|\mathbf{r}'\|} = \left(EI\frac{\mathbf{r}''}{\|\mathbf{r}'\|}\cdot\frac{\mathbf{r}'}{\|\mathbf{r}'\|}\right)' - X\frac{\mathbf{r}''}{\|\mathbf{r}'\|}\cdot\left(\frac{\mathbf{r}'}{\|\mathbf{r}'\|}\right)' = -X\frac{\mathbf{r}''}{\|\mathbf{r}'\|}\cdot\frac{\mathbf{r}''}{\|\mathbf{r}'\|} = -X\frac{\|\mathbf{r}''\|^2}{\|\mathbf{r}'\|^2} = -X\kappa^2 \end{cases}$$

Where $X = EI + \eta_B I\left(\frac{\mathbf{r}''\cdot\dot{\mathbf{r}}''}{\mathbf{r}''\cdot\mathbf{r}''} - \frac{\mathbf{r}'\cdot\dot{\mathbf{r}}'}{\mathbf{r}'\cdot\mathbf{r}'}\right)$

If the Eq. (3.13) is substituted in the Eq. (3.5) the following translational equation of motion is obtained:

$$-\left(EI\frac{\mathbf{r}''}{\|\mathbf{r}'\|}+\eta I\left(\frac{\mathbf{r}''\cdot\dot{\mathbf{r}}''}{\mathbf{r}''\cdot\mathbf{r}''}-\frac{\mathbf{r}'\cdot\dot{\mathbf{r}}'}{\mathbf{r}'\cdot\mathbf{r}'}\right)\frac{\mathbf{r}''}{\|\mathbf{r}'\|}\right)''+\left(\lambda\frac{\mathbf{r}'}{\|\mathbf{r}'\|}\right)'+\mathbf{q}=\rho_m A\ddot{\mathbf{r}} \tag{3.15}$$

3.3.2 Inclusion of the constitutive equation

The constitutive equation of a rod relates the axial strain with the tension. The derivative of the position of the rod is equal to the unity plus the strain, $\|\mathbf{r}'\|=1+\varepsilon$. Then, if the stretch of the rod is assumed to be linear and small, then the next equation is obtained and further approximated as:

$$\mathbf{r}'\cdot\mathbf{r}'=(1+\varepsilon)^2=1+2\varepsilon+O(\varepsilon^2) \tag{3.16}$$

Then, isolating ε we obtain:

$$\varepsilon=\frac{1}{2}(\mathbf{r}'\cdot\mathbf{r}'-1) \tag{3.17}$$

The relation between tension and strain for each element is described in Eq. (3.18) from the internal axial force of Eq. (3.2).

$$T=N=\ AE\varepsilon+\eta A\dot{\varepsilon} \tag{3.18}$$

From the strain (ε) defined in Eq. (3.17), the following approximation of the strain velocity by the derivative respect to time is obtained:

$$\dot{\varepsilon}=\frac{\partial}{\partial t}\varepsilon=\frac{\partial}{\partial t}\left(\frac{1}{2}(\mathbf{r}'\cdot\mathbf{r}'-1)\right)=\ \mathbf{r}'\cdot\dot{\mathbf{r}}' \tag{3.19}$$

Then, substituting Eq. (3.17) and Eq. (3.19) into Eq. (3.18), the Eq. (3.14) can be expressed as follows, which relates the strain with the Lagrange multiplier:

$$\begin{aligned}0=\ T-\left(EI+\eta_B I\left(\frac{\mathbf{r}''\cdot\dot{\mathbf{r}}''}{\mathbf{r}''\cdot\mathbf{r}''}-\frac{\mathbf{r}'\cdot\dot{\mathbf{r}}'}{\mathbf{r}'\cdot\mathbf{r}'}\right)\right)\kappa^2-\lambda=\varepsilon+\frac{\eta_A}{E}\dot{\varepsilon}-\left(\frac{EI}{EA}+\frac{\eta_B I}{EA}\left(\frac{\mathbf{r}''\cdot\dot{\mathbf{r}}''}{\mathbf{r}''\cdot\mathbf{r}''}-\right.\right.\\ \left.\left.\frac{\mathbf{r}'\cdot\dot{\mathbf{r}}'}{\mathbf{r}'\cdot\mathbf{r}'}\right)\right)\kappa^2-\frac{\lambda}{EA}=\frac{1}{2}(\mathbf{r}'\cdot\mathbf{r}'-1)+\frac{\eta_A}{E}(\mathbf{r}'\cdot\dot{\mathbf{r}}')-\left(\frac{EI}{EA}+\frac{\eta_B I}{EA}\left(\frac{\mathbf{r}''\cdot\dot{\mathbf{r}}''}{\mathbf{r}''\cdot\mathbf{r}''}-\frac{\mathbf{r}'\cdot\dot{\mathbf{r}}'}{\mathbf{r}'\cdot\mathbf{r}'}\right)\right)\kappa^2-\frac{\lambda}{EA}\end{aligned} \tag{3.20}$$

The dynamics of a slender rod with rheological damping material is fully described by Eq. (3.15) and Eq. (3.20). The Eq. (3.15) is the equation of motion of the centreline and the Eq. (3.20) fulfils the constitutive equations relating the strain and the curvature of the line to its equation of motion by the Lagrange multiplier.

3.3.3 Critical Damping assessment

The damping term (c) of the dynamic equation of a vibrating system, Eq. (3.21), is usually characterized by critical damping coefficient (c_{cr}) through the damping ratio ξ by $c=\xi\cdot c_{cr}$. The critical damping coefficient and the natural frequency is defined by Eq. (3.22) and Eq. (3.23) respectively Inman (2001).

$$m\ddot{x}(t) + c\dot{x}(t) + kx(t) = 0 \tag{3.21}$$

$$c_{cr} = 2\sqrt{km} \tag{3.22}$$

$$\omega_d = \omega_n\sqrt{1-\xi^2}, \text{ where } \omega_n = \sqrt{\frac{k}{m}} \tag{3.23}$$

The critical viscosity, which implies a critical damping behavior for each force, are derived in the next equations for the axial force and the bending moment. This characterization is obtained assuming that the rod is only subjected to a pure axial load or pure bending moment in each case. This procedure allows to assess the viscosity of a loaded rod with its boundary conditions for a given damping ratio. Then, using a simple vibration test of a rod and assessing its damping behavior the related viscosity can be obtained.

For a better comprehension of the following partial differential equations of next sections, derivatives respect to the time and to the rod axial direction are expressed by subscripts t and x respectively.

3.3.3.1 Axial Critical Damping

Considering only the elongation of a rod without any other external force excluded the axial force, the translational equation of motion Eq. (3.5) can be reformulated in terms of the displacement of the rod (u) and the Kelvin-Voigt rheological model for the axial stress-strain relation is expressed as Eq. (3.24). The strain as a function of the rod axial displacement is expressed as $\varepsilon = u_x$.

$$\rho_m A\frac{\partial^2 u}{\partial t^2} - \frac{\partial(T)}{\partial x} = \rho_m A\frac{\partial^2 u}{\partial t^2} - \frac{\partial(EA\varepsilon+\eta A\varepsilon_t)}{\partial x} = \rho_m A\, u_{tt} - AEu_{xx} - \eta A u_{xxt} = \rho_m u_{tt} - Eu_{xx} - \eta u_{xxt} = 0 \tag{3.24}$$

Assuming the separation of variables $(x,t) = \phi(x)h(t)$, Eq. (3.24) yields in:

$$\rho_m \phi h_{tt} - Eh\phi_{xx} - \eta h_t \phi_{xx} = 0 \tag{3.25}$$

Eq. (3.25) can be rewritten in Eq. (3.26), where the right side depends of t and the left side of x. Then, the unique solution is a scalar defined as $-\beta_A^2$, (Inman, 2001).

$$\frac{\rho_m}{(\eta h_t + Eh)}h_{tt} = \frac{1}{\phi}\phi_{xx} = -\beta_A^2 \tag{3.26}$$

Then, the left side of Eq. (3.26) can be rewritten as a temporal ordinary differential equation (ODE) as shown in Eq. (3.27).

$$\rho_m h_{tt} + \eta\beta_A^2 h_t + E\beta_A^2 h = 0 \tag{3.27}$$

Then, the critical damping behavior of an axially deformed rod is produced by the critical viscosity:

$$\eta_{A,Critic} = \frac{2}{\beta_A\sqrt{\rho_m \cdot E}} \tag{3.28}$$

For a cantilever rod with a free end motion, β_A can be assessed from the next boundary conditions: no motion of the fixed point, $u(0,t)=0$, and no tension on the free end, thus $u_x(L,t)=0$. Then, applying these assumptions to the ODE of the left side of Eq. (3.26), $\phi_{xx}+\beta_A^2\phi=0$, the mode shapes obtained of the rod are $\beta_{A,n}=\frac{\left(n\pi-\frac{\pi}{2}\right)}{L}$, whereby the first mode is $\beta_{A,1}=\frac{\pi}{2L}$.

3.3.3.2 Bending Critical Damping

Following the same procedure as for the axial critical damping, the Eq. (3.29) represents the partial differential equation of motion the transverse vibration due to a bending moment of an Euler-Bernoulli beam.

$$\rho_m A\frac{\partial^2\omega}{\partial t^2}+\frac{\partial^2}{\partial x^2}\left(EI\frac{\partial^2\omega}{\partial x^2}+\eta I\frac{\partial^3\omega}{\partial x^2\partial t}\right)=\rho_m\frac{\partial^2\omega}{\partial t^2}+EI\frac{\partial^4\omega}{\partial x^4}+\eta I\frac{\partial^5\omega}{\partial x^4\partial t}=0 \tag{3.29}$$

Assuming again the separation of variables, ω can be defined as a product $\omega(x,t)=\phi(x)h(t)$, then:

$$\rho_m A\phi h_{tt}+EIh\phi_{xxxx}+\eta Ih_t\phi_{xxxx}=0 \tag{3.30}$$

In Eq. (3.30), there are different terms depending on t and on x, then, the unique solution is a scalar defined as $-\beta_B^4$.

$$\frac{\rho_m A}{(\eta h_t+EIh)}h_{tt}=-\frac{1}{\phi}\phi_{xxxx}=-\beta_B^4 \tag{3.31}$$

Considering the left part of Eq. (3.31), the equation can be rewritten as an ODE as shown in Eq. (3.32).

$$\rho_m Ah_{tt}+\eta I\beta_B^4h_t+EI\beta_B^4h=0 \tag{3.32}$$

Then, the critical damping behavior of a bending deformed rod is achieved by the critical viscosity:

$$\eta_{B,Critic}=\frac{2}{\beta_B^2\sqrt{\rho_m A\cdot\frac{E}{I}}} \tag{3.33}$$

For a cantilever beam with a free end motion, the β_A can be assessed from the next boundary conditions: no deflection and straight direction of the bam at the fixed point, $\omega(0,t)=0$ and $\frac{\partial\omega}{\partial x}(0,t)=0$, and no moment and no shearing force at the free end, $\frac{\partial^2\omega}{\partial x^2}(L,t)=0$ and $\frac{\partial^3\omega}{\partial x^3}(L,t)=0$. Then, applying these assumptions to the ODE $\phi_{xxxx}-\beta_B^4\phi=0$, the first bending mode is expressed as $\beta_{B,1}=\frac{0.59686\pi}{L}$, Inman (2001).

3.4 FINITE ELEMENT METHOD IMPLEMENTATION

The Eq. (3.15) and Eq. (3.20) that represent the dynamics of the system including the constitutive behavior in axial and bending, respectively, are unified in Eq. (3.34). Both equations will be treated jointly to apply the finite element Garlekin method.

$$\left.\begin{aligned} \rho_m A\ddot{\mathbf{r}} + \left(EI\frac{\mathbf{r}''}{\|\mathbf{r}'\|} + \eta_B I\left(\frac{\mathbf{r}''\cdot\dot{\mathbf{r}}''}{\mathbf{r}''\cdot\mathbf{r}''} - \frac{\mathbf{r}'\cdot\dot{\mathbf{r}}'}{\mathbf{r}'\cdot\mathbf{r}'}\right)\frac{\mathbf{r}''}{\|\mathbf{r}'\|}\right)'' - \left(\lambda\frac{\mathbf{r}'}{\|\mathbf{r}'\|}\right)' &= \mathbf{q} \\ \frac{1}{2}(\mathbf{r}'\cdot\mathbf{r}'-1) + \frac{\eta_A}{E}(\mathbf{r}'\cdot\dot{\mathbf{r}}') - \left(\frac{EI}{EA} + \frac{\eta_B I}{EA}\left(\frac{\mathbf{r}''\cdot\dot{\mathbf{r}}''}{\mathbf{r}''\cdot\mathbf{r}''} - \frac{\mathbf{r}'\cdot\dot{\mathbf{r}}'}{\mathbf{r}'\cdot\mathbf{r}'}\right)\right)\kappa^2 - \frac{\lambda}{EA} &= 0 \end{aligned}\right\}\text{v} \tag{3.34}$$

Consider a single element of length L, the position of the centerline of the rod element (r), and the Lagrange multiplier (λ) are expressed as the sum of the approximate values of the nodes multiplied by its shape functions as is shown in Eq. (3.35) and, Eq. (3.36) where N_l, P_m are the shape functions, and U_{il}, λ_m are the unknown coefficients, where $0 \le s \le L$ and the subscript $i = 1,2,3$ that denotes the 3 DOF of the node position.

$$r_i(s,t) = \sum_l N_l(s)U_{il}(t) \tag{3.35}$$

$$\lambda(s,t) = \sum_m P_m(s)\lambda_m(t) \tag{3.36}$$

The Hermite interpolation shape functions are used to define the rod position vector (N_l), and the quadratic shape functions are used to interpolate the Lagrange multiplier (P_m), shown in Eq. (3.37) where $\xi = \frac{s}{L}$.

$$\left.\begin{aligned} N_1 &= 1 - 3\xi^2 + 2\xi^3 \\ N_2 &= L(\xi - 2\xi^2 + \xi^3) \\ N_3 &= 3\xi^2 - 2\xi^3 \\ N_4 &= L(-\xi^2 + \xi^3) \end{aligned}\right\} \qquad \left.\begin{aligned} P_1 &= 1 - 3\xi + 2\xi^2 \\ P_2 &= 4\xi(1-\xi) \\ P_3 &= \xi(2\xi - 1) \end{aligned}\right\} \tag{3.37}$$

Then, the position (r_i), the tangent (r_i') and the Lagrange multiplier(λ) are evaluated at each node. The parameters U_{il} and λ_m are thus:

$$\left.\begin{aligned} U_{i1} &= r_i(s_i,t) \\ U_{i2} &= r_i'(s_i,t) \\ U_{i3} &= r_i(s_{i+1},t) \\ U_{i4} &= r_i'(s_{i+1},t) \end{aligned}\right\} \qquad \left.\begin{aligned} \lambda_1 &= \lambda(s_i) \\ \lambda_2 &= \lambda\left(s_i + \frac{L}{2}\right) \\ \lambda_3 &= \lambda(s_{i+1}) \end{aligned}\right\} \tag{3.38}$$

Applying the Garlekin method to the weak form of the Eq. (3.34) by multiplying the shape function by its respective equation, the Eq. (3.39) is obtained.

$$\begin{aligned}&\int_0^L N_l\left(\rho\ddot{\mathbf{r}}+\rho_w AC_a\ddot{\mathbf{r}}^n+\left(EI\frac{\boldsymbol{r}''}{\|\boldsymbol{r}'\|}+\eta_B I\left(\frac{\boldsymbol{r}''\cdot\dot{\boldsymbol{r}}''}{\boldsymbol{r}''\cdot\boldsymbol{r}''}-\frac{\boldsymbol{r}'\cdot\dot{\boldsymbol{r}}'}{\boldsymbol{r}'\cdot\boldsymbol{r}'}\right)\frac{\boldsymbol{r}''}{\|\boldsymbol{r}'\|}\right)''-\left(\lambda\frac{\boldsymbol{r}'}{\|\boldsymbol{r}'\|}\right)'-\mathbf{q}\right)ds=0\\&\int_0^L P_m\left(\frac{1}{2}(\boldsymbol{r}'\cdot\boldsymbol{r}'-1)+\frac{\eta_A}{E}(\boldsymbol{r}'\cdot\dot{\boldsymbol{r}}')-\left(\frac{EI}{EA}+\frac{\eta_B I}{EA}\left(\frac{\boldsymbol{r}''\cdot\dot{\boldsymbol{r}}''}{\boldsymbol{r}''\cdot\boldsymbol{r}''}-\frac{\boldsymbol{r}'\cdot\dot{\boldsymbol{r}}'}{\boldsymbol{r}'\cdot\boldsymbol{r}'}\right)\right)\kappa^2-\frac{\lambda}{EA}\right)ds=0\end{aligned}\tag{3.39}$$

The integration of the Eq. (3.39) leads to the dynamic system of equations expressed in Eq. (3.40):

$$\left.\begin{aligned}M_{ijlk}\,\ddot{U}_{jk}+\left(K^1_{ijlk}+K^{1,Damp}_{ijlk}+\lambda_n K^2_{nijlk}\right)U_{jk}-F^e_{il}=0\\A_{mil}U_{jl}U_{jk}-B_m+D_{mn}U_{kl}\dot{U}_{lk}-E_{mil}(U,\dot{U})-C_{mn}\lambda_n=0\end{aligned}\right\}\tag{3.40}$$

where:

$$M_{ijlk}=\int_0^L\rho N_l N_k\delta_{ij}ds\tag{3.41}$$

$$K^1_{ijlk}=\int_0^L\frac{EIN_l''N_k''}{\sqrt{(N_s'U_{js})^T\cdot N_t'U_{jt}}}\delta_{ij}ds\tag{3.42}$$

$$K^{1,Damp}_{ijlk}=\int_0^L\eta_B I\left(\frac{(N_s''U_{js})^T\cdot N_t'\dot{U}_{it}}{(N_s''U_{js})^T\cdot N_t''U_{it}}-\frac{(N_s'U_{js})^T\cdot N_t'\dot{U}_{it}}{(N_s'U_{js})^T\cdot N_t'U_{it}}\right)\frac{N_l''N_k''}{\sqrt{(N_s'U_{js})^T\cdot N_t'U_{it}}}\delta_{ij}ds\tag{3.43}$$

$$K^2_{nijlk}=\int_0^L P_n N_l'N_k'\frac{1}{\sqrt{(N_s'U_{js})^T\cdot N_t'U_{jt}}}\ \delta_{ij}ds\tag{3.44}$$

$$F^e_{il}=\int_0^L N_l\mathbf{q}(1+\varepsilon)ds\tag{3.45}$$

$$A_{mil}=\frac{1}{2}\int_0^L P_n N_l'N_k'ds\tag{3.46}$$

$$B_m=\frac{1}{2}\int_0^L P_m ds\tag{3.47}$$

$$C_{mn}=\frac{1}{EA}\int_0^L P_m P_n ds\tag{3.48}$$

$$D_{mil}=\frac{\eta_A}{E}\int_0^L P_m N_l'N_k'ds\tag{3.49}$$

$$\begin{aligned}E_{mil}(U,\dot{U})=\frac{EI}{EA}\int_0^L P_m\frac{(N_s''U_{js})^T\cdot N_t''U_{it}}{(N_s'U_{js})^T\cdot N_t'U_{it}}ds+\frac{\eta_B I}{EA}\int_0^L P_m\left(\frac{(N_s''U_{js})^T\cdot N_t'\dot{U}_{it}}{(N_s''U_{js})^T\cdot N_t''U_{it}}-\right.\\\left.\frac{(N_s'U_{js})^T\cdot N_t'\dot{U}_{it}}{(N_s'U_{js})^T\cdot N_t'U_{it}}\right)\frac{(N_s''U_{js})^T\cdot N_t''U_{it}}{(N_s'U_{js})^T\cdot N_t'U_{it}}ds\end{aligned}\tag{3.50}$$

where δ_{ij} is the Kronecker delta which ensures the independence between the DOF of the orthonormal basis of $\mathbb{R}^3$.

The derivation of Eq. (3.42)-(3.50) are more detailed in Eq.(3.51)-(3.55).

$$\int_0^L N_l \left(EI\frac{\mathbf{r}''}{\|\mathbf{r}'\|}\right)'' ds = \text{applying the chain rule: } =$$
$$\int_0^L \left(N_l \left(EI\frac{\mathbf{r}''}{\|\mathbf{r}'\|}\right)'\right)' ds - \int_0^L N_l' \left(EI\frac{\mathbf{r}''}{\|\mathbf{r}'\|}\right)' ds = \text{applying integration by parts leads to: } =$$
$$\left(EI\frac{\mathbf{r}''}{\|\mathbf{r}'\|}\right)' N_l\Big|_0^L - EI\frac{\mathbf{r}''}{\|\mathbf{r}'\|}N_l'\Big|_0^L + \int_0^L EI\, N_l''\frac{\mathbf{r}''}{\|\mathbf{r}'\|}ds$$

where the evaluated factors are related with the boundary conditions, then the resting integrated can be evaluated as: (3.51)

$$\int_0^L EI\, N_l''\frac{\mathbf{r}''}{\|\mathbf{r}'\|}ds = \sum_{i=1}^n \int_0^L \frac{EIN_l''N_k''\delta_{ij}}{\sqrt{\left(N_s'U_{js}\right)^T\cdot N_t'U_{jt}}}dsU_{jk} = K_{ijlk}^1 U_{jk}$$

$$K_{ijlk}^1 = \sum_{i=1}^n \int_0^L \frac{EIN_l''N_k''\delta_{ij}}{\sqrt{\left(N_s'U_{js}\right)^T\cdot N_t'U_{jt}}}ds$$

$$\int_0^L N_l \left(\eta_B I\left(\frac{\mathbf{r}''\cdot\dot{\mathbf{r}}''}{\mathbf{r}''\cdot\mathbf{r}''} - \frac{\mathbf{r}'\cdot\dot{\mathbf{r}}'}{\mathbf{r}'\cdot\mathbf{r}'}\right)\frac{\mathbf{r}''}{\|\mathbf{r}\prime\|}\right)'' ds = a\text{pplying derivation rules: } = \int_0^L \left(N_l \left(\eta_B I\left(\frac{\mathbf{r}''\cdot\dot{\mathbf{r}}''}{\mathbf{r}''\cdot\mathbf{r}''} - \frac{\mathbf{r}'\cdot\dot{\mathbf{r}}'}{\mathbf{r}'\cdot\mathbf{r}'}\right)\frac{\mathbf{r}''}{\|\mathbf{r}\prime\|}\right)'\right)' ds - \int_0^L N_l' \left(\eta_B I\left(\frac{\mathbf{r}''\cdot\dot{\mathbf{r}}''}{\mathbf{r}''\cdot\mathbf{r}''} - \frac{\mathbf{r}'\cdot\dot{\mathbf{r}}'}{\mathbf{r}'\cdot\mathbf{r}'}\right)\frac{\mathbf{r}''}{\|\mathbf{r}\prime\|}\right)' ds =$$
$$\text{applying integration by parts leads to: } = \left(\eta_B I\left(\frac{\mathbf{r}''\cdot\dot{\mathbf{r}}''}{\mathbf{r}''\cdot\mathbf{r}''} - \frac{\mathbf{r}'\cdot\dot{\mathbf{r}}'}{\mathbf{r}'\cdot\mathbf{r}'}\right)\frac{\mathbf{r}''}{\|\mathbf{r}\prime\|}\right)' N_l\Big|_0^L -$$
$$\left(\eta_B I\left(\frac{\mathbf{r}''\cdot\dot{\mathbf{r}}''}{\mathbf{r}''\cdot\mathbf{r}''} - \frac{\mathbf{r}'\cdot\dot{\mathbf{r}}'}{\mathbf{r}'\cdot\mathbf{r}'}\right)\frac{\mathbf{r}''}{\|\mathbf{r}\prime\|}\right) N_l'\Big|_0^L + \int_0^L \eta_B I\left(\frac{\mathbf{r}''\cdot\dot{\mathbf{r}}''}{\mathbf{r}''\cdot\mathbf{r}''} - \frac{\mathbf{r}'\cdot\dot{\mathbf{r}}'}{\mathbf{r}'\cdot\mathbf{r}'}\right) N_l''\frac{\mathbf{r}''}{\|\mathbf{r}'\|}ds$$

Where the evaluated factors are related with the boundary conditions, then the resting integrated can be evaluated as: (3.52)

$$\int_0^L \eta_B I\left(\frac{\mathbf{r}''\cdot\dot{\mathbf{r}}''}{\mathbf{r}''\cdot\mathbf{r}''} - \frac{\mathbf{r}'\cdot\dot{\mathbf{r}}'}{\mathbf{r}'\cdot\mathbf{r}'}\right) N_l''\frac{\mathbf{r}''}{\|\mathbf{r}'\|}ds = \sum_{i=1}^n \int_0^L \eta_B I\left(\frac{\left(N_s''U_{js}\right)^T\cdot N_t'\dot{U}_{it}}{\left(N_s''U_{js}\right)^T\cdot N_t''U_{it}} -$$
$$\frac{\left(N_s'U_{js}\right)^T\cdot N_t'\dot{U}_{it}}{\left(N_s'U_{js}\right)^T\cdot N_t'U_{it}}\right)\frac{N_l''N_k''}{\sqrt{\left(N_s'U_{js}\right)^T\cdot N_t'U_{it}}}\delta_{ij}ds\, U_{jk} = K_{ijlk}^{1,Damp}U_{jk}$$

$$K_{ijlk}^{1,Damp} = \sum_{i=1}^n \int_0^L \eta_B I\left(\frac{\left(N_s''U_{js}\right)^T\cdot N_t'\dot{U}_{it}}{\left(N_s''U_{js}\right)^T\cdot N_t''U_{it}} - \frac{\left(N_s'U_{js}\right)^T\cdot N_t'\dot{U}_{it}}{\left(N_s'U_{js}\right)^T\cdot N_t'U_{it}}\right)\frac{N_l''N_k''}{\sqrt{\left(N_s'U_{js}\right)^T\cdot N_t'U_{it}}}\delta_{ij}ds$$

$$\int_0^L N_l \left(\lambda\frac{\mathbf{r}'}{\|\mathbf{r}'\|}\right)' ds = \text{applying integration by parts leads to: } = \lambda N_l\frac{\mathbf{r}'}{\|\mathbf{r}'\|}\Big|_0^L - \int_0^L \lambda N_l'\frac{\mathbf{r}'}{\|\mathbf{r}'\|}ds$$

Where the evaluated factors are related with the boundary conditions, so: (3.53)

$$\int_0^L \lambda N_l'\frac{\mathbf{r}'}{\|\mathbf{r}'\|}ds = \sum_{i=1}^n \lambda_n \int_0^L P_n N_l' N_k' \frac{1}{\sqrt{\left(N_s'U_{js}\right)^T\cdot N_t'U_{jt}}}\delta_{ij}dsU_{jk} = \lambda_n K_{nijlk}^2 U_{jk}$$

$$K^2_{nijlk} = \sum_{i=1}^{n} \lambda_n \int_0^L P_n N'_l N'_k \frac{1}{\sqrt{\left(N'_s U_{js}\right)^T \cdot N'_t U_{jt}}} \delta_{ij} ds U_{jk}$$

$$F^e_{il} = \sum_x \int_0^L N_l f_x (1+\varepsilon) ds$$

where: $x = hg;\ sb;\ hd$ (3.54)

$$\int_0^L P_m \frac{1}{2}(\mathbf{r}' \cdot \mathbf{r}' - 1) ds = \frac{1}{2}\sum_{i=1}^{n} \int_0^L P_m N'_l N'_k ds U_{jl} U_{jk} - \frac{1}{2}\sum_{i=1}^{n} \int_0^L P_m ds$$

$$\int_0^L P_m \frac{\eta_A}{E}(\boldsymbol{r}' \cdot \dot{\boldsymbol{r}}') ds = \frac{\eta_A}{E}\sum_{i=1}^{n} \int_0^L P_m N'_l N'_k ds U_{jl} U_{jk} = D_{mn} U_{kl} \dot{U}_{lk}$$

$$\int_0^L P_m \left(\frac{EI}{EA} + \frac{\eta_B I}{EA}\left(\frac{\boldsymbol{r}''\cdot\dot{\boldsymbol{r}}''}{\boldsymbol{r}''\cdot\boldsymbol{r}''} - \frac{\boldsymbol{r}'\cdot\dot{\boldsymbol{r}}'}{\boldsymbol{r}'\cdot\boldsymbol{r}'}\right)\right)\kappa^2 ds = \frac{EI}{EA}\sum_{i=1}^{n} \int_0^L P_m \frac{\left(N''_s U_{js}\right)^T \cdot N''_t U_{it}}{\left(N'_s U_{js}\right)^T \cdot N'_t U_{it}} ds + \frac{\eta_B I}{EA}\sum_{i=1}^{n} \int_0^L P_m \left(\frac{\left(N''_s U_{js}\right)^T \cdot N'_t \dot{U}_{it}}{\left(N''_s U_{js}\right)^T \cdot N''_t U_{it}} - \frac{\left(N'_s U_{js}\right)^T \cdot N'_t \dot{U}_{it}}{\left(N'_s U_{js}\right)^T \cdot N'_t U_{it}}\right)\frac{\left(N''_s U_{js}\right)^T \cdot N''_t U_{it}}{\left(N'_s U_{js}\right)^T \cdot N'_t U_{it}} ds = E_{mil}\left(U, \dot{U}\right)$$

$$\int_0^L P_m \frac{\lambda}{EA} ds = \frac{1}{EA}\sum_{i=1}^{n} \int_0^L \lambda_n P_m P_n ds$$ (3.55)

3.5 STATIC PROBLEM

The initial problem of the reference configuration of the line shape is solved from the static point of view of the FEM formulation presented in section 0. Thus, the rod is supposed to be loaded from external forces such as the weight, but node accelerations and velocities are set to zero. Then, the dynamic system of equations can be expressed as Eq. (3.56) , from an *n^th^* iteration of the rod position $\left(U^{(n)}\right)$ and the Lagrange multiplier $\left(\lambda^{(n)}\right)$.

$$\left.\begin{aligned} \left(K^1_{ijlk} + \lambda_n K^2_{nijlk}\right)U^{(n)}_{jk} - F^e_{il} = 0 = G \\ A_{mil} U^{(n)}_{jl} U^{(n)}_{jk} - B_m - E_{mil}\left(U^{(n)}, 0\right) - C_{mn}\lambda^{(n)}_n = 0 = H \end{aligned}\right\} \quad (3.56)$$

To solve the equation, a Newton-Raphson's iterative method is used. Using Taylor series expansion, the equation system can be written using the first order term as:

$$\left.\begin{aligned} G^{(n+1)}_{il} = G^{(n)}_{il} + \frac{\partial G_{il}}{\partial U_{jk}}\Delta U_{jk} + \frac{\partial G_{il}}{\partial \lambda_n}\Delta\lambda_n = 0 \\ H^{(n+1)}_{m} = H^{(n)}_{m} + \frac{\partial H_{m}}{\partial U_{jk}}\Delta U_{jk} + \frac{\partial H_{m}}{\partial \lambda_n}\Delta\lambda_n = 0 \end{aligned}\right\} \quad (3.57)$$

Where:

$$\frac{\partial G_{il}}{\partial U_{jk}} = K^1_{ijlk} + \frac{\partial K^1_{ijlk}}{\partial U} U^{(n)}_{jk} + \lambda^{(n)}_n K^2_{nijlk} + \lambda^{(n)}_n \frac{\partial K^2_{nijlk}}{\partial U} U^{(n)}_{jk}$$ (3.58)

$$\frac{\partial G_{il}}{\partial \lambda_n} = K^2_{nijlk} U^{(n)}_{jk} \tag{3.59}$$

$$\frac{\partial H_m}{\partial U_{jk}} = 2A_{mkl} U^{(n)}_{jk} - \frac{\partial E_{mil}\left(U^{(n)}_{jk},0\right)}{\partial U} \tag{3.60}$$

$$\frac{\partial H_m}{\partial \lambda_n} = -C_{mn} \tag{3.61}$$

$$\frac{\partial K^1_{ijlk}}{\partial U} = \int_0^L -EIN_l'' N_k'' U^{(n)}_{jk} \frac{{U_{js}}^T {N_s'}^T \cdot N_t'}{\left(\left(N_s' U_{js}\right)^T \cdot N_t' U_{jt}\right)^{\frac{3}{2}}} \delta_{ij} ds \tag{3.62}$$

$$\frac{\partial K^2_{ijlk}}{\partial U} U^{(n)}_{jk} = \int_0^L -P_n N_l' N_k' U^{(n)}_{jk} \frac{{U_{js}}^T {N_s'}^T \cdot N_t'}{\left(\left(N_s' U_{js}\right)^T \cdot N_t' U_{jt}\right)^{\frac{3}{2}}} \delta_{ij} ds \tag{3.63}$$

$$\frac{\partial E_{mil}(U,0)}{\partial U} = \frac{EI}{EA} \int_0^L P_m \left(\frac{2 \cdot \left(N_s'' U_{js}\right)^T \cdot N_t''}{\left(N_s' U_{js}\right)^T \cdot N_t' U_{it}} - \frac{\left(N_s'' U_{js}\right)^T \cdot N_t'' U_{it} \cdot 2\left(N_s' U_{js}\right)^T \cdot N_t'}{\left(\left(N_s' U_{js}\right)^T \cdot N_t' U_{it}\right)^2} \right) ds \tag{3.64}$$

Then, the system of Eq. (3.57) can be written in matrix form as:

$$\begin{bmatrix} K^1_{ijlk} + \frac{\partial K^1_{ijlk}}{\partial U} U^{(n)}_{jk} + \lambda_n K^2_{nijlk} + \lambda_n \frac{\partial K^2_{nijlk}}{\partial U} U^{(n)}_{jk} & K^2_{nijlk} U^{(n)}_{jk} \\ 2A_{mkl} U^{(n)}_{jk} - \frac{\partial E_{mil}\left(U^{(n)}_{jk},0\right)}{\partial U} & -C_{mn} \end{bmatrix} \begin{bmatrix} \Delta U_{jk} \\ \Delta \lambda \end{bmatrix} = \begin{bmatrix} -G^{(n)}_{il} \\ -H^{(n)}_m \end{bmatrix} \tag{3.65}$$

And the next iterative solution is expressed as follows:

$$\left.\begin{aligned} U^{(n+1)}_{jk} &= U^{(n)}_{jk} + \Delta U_{jk} \\ \lambda^{(n+1)}_n &= \lambda^{(n)}_n + \Delta \lambda_n \end{aligned}\right\} \tag{3.66}$$

Then, from an initial approximation of the rod position shape (U^0) and the Lagrange multiplier (λ^0) the static values for a given loading parameter are obtained.

3.6 TIME INTEGRATION OF DYNAMIC EQUATIONS

The time integration scheme is based on an implicit generalized Newmark's method Crisfield (2000). The method is applied in a non-linear context with a corrector procedure at each time-step using the Newton algorithm.

The method has to satisfy the dynamic equilibrium in each time step by approximating the position of the $(n+1)$ step (U^{n+1}) from the previous time step (U^n). The Newmark's time integration procedure involves the next equations:

$$U_{n+1} = U_n + \Delta t \dot{U}_n + \frac{\Delta t}{2}\left((1-2\beta)\ddot{U}_n + 2\beta \ddot{U}_{n+1}\right) \tag{3.67}$$

$$\dot{U}_{n+1} = \dot{U}_n + \Delta t\left((1-\gamma)\ddot{U}_n + \gamma\ddot{U}_{n+1}\right) \tag{3.68}$$

where β and γ are the Newmark constants, and Δt is the incremental time step.

Then, the velocity and acceleration parameters of the next time step can be assessed as a function of the increment of the position $\Delta U = U_{n+1} - U_n$

$$\left.\begin{aligned}\dot{U}_{n+1} &= C_v + \frac{\gamma}{\beta\Delta t}\Delta U\\ \ddot{U}_{n+1} &= C_a + \frac{1}{\beta\Delta t^2}\Delta U\end{aligned}\right\} \tag{3.69}$$

where C_v and C_a can be defined as:

$$\begin{aligned}C_v &= \dot{U}_n + (1-\gamma)\Delta t\ddot{U}_n - \frac{\gamma\left(\Delta t\ddot{U}_n + \left(\frac{1}{2}-\beta\right)\Delta t^2\ddot{U}_n\right)}{\beta\Delta t}\\ C_a &= -\frac{\left(\Delta t\ddot{U}_n + \left(\frac{1}{2}-\beta\right)\Delta t^2\ddot{U}_n\right)}{(\beta\Delta t^2)}\end{aligned} \tag{3.70}$$

The dynamic equation can be expressed from Eq. (3.40) as follows at the $(n+1)$ time step:

$$\begin{aligned}&M_{ijlk}\ddot{U}_{jk}^{(n+1)} + F_{il}^{i(n+1)} - F_{il}^{e(n+1)} = G_{il}^{(n+1)} = 0\\ &A_{mil}U_{kl}^{(n+1)}U_{ki}^{(n+1)} - B_m + D_{mn}U_{kl}^{(n+1)}\dot{U}_{ki}^{(n+1)} - E_{mil}\left(U^{(n+1)}\dot{U}^{(n+1)}\right) -\\ &C_{mn}\lambda_n^{(n+1)}H_m^{(n+1)} = 0\end{aligned} \tag{3.71}$$

Where $F_{il}^{i(n+1)}$are the internal forces, $F_{il}^{e(n+1)}$are the external forces and $G_{il}^{(n+1)}$are the equivalent dynamic out-of-balance forces at the $(n+1)$ time step.

The internal forces and the constitutive equation can be approximate using truncated Taylor series as shown in Eq. (3.72) and Eq. (3.73).

$$\begin{aligned}F_{il}^{i(n+1)} &= F_{il}^{i(n)} + \frac{\partial F_{il}}{\partial U_{jk}}\Delta U_{jk} + \frac{\partial F_{il}}{\partial\lambda_n}\Delta\lambda_n = F_{il}^{i(n)} + \Bigg(K_{ijlk}^1 + \frac{\partial K_{ijlk}^1}{\partial U}U_{jk}^{(n)} + K_{ijlk}^{1,Damp} +\\ &\frac{\partial K_{ijlk}^{1,Damp}}{\partial U}U_{jk}^{(n)} + \lambda_n^{(n)}\frac{\partial K_{nijlk}^2}{\partial U}U_{jk}^{(n)} + \lambda_n^{(n)}K_{nijlk}^2\Bigg)\Delta U_{jk} + K_{nijlk}^2U_{jk}^{(n)}\cdot\Delta\lambda_n\end{aligned} \tag{3.72}$$

$$\begin{aligned}H_m^{(n+1)} &= H_m^{(n)} + \frac{\partial H_m}{\partial U_{jk}}\Delta U_{jk} + \frac{\partial H_m}{\partial\lambda_n}\Delta\lambda_n = H_m^{(n)} + \Big(2A_{mil}U_{kl}^{(n)} + D_{mn}\Big(\dot{U}_{ki}^{(n)} +\\ &\frac{\gamma}{\beta\Delta t}U_{kl}^{(n)}\Big) - \frac{\partial E_{mil}}{\partial U}\Big)\cdot\Delta U_{jk} - C_{mn}\Delta\lambda_n\end{aligned} \tag{3.73}$$

where:

$$\frac{\partial K_{ijlk}^{1}}{\partial U}U_{jk}^{(n)} = \int_0^L -EIN_l''N_k''U_{jk}^{(n)}\frac{{U_{js}}^T{N_s'}^T\cdot N_t'}{\left(\left(N_s'U_{js}\right)^T\cdot N_t'U_{jt}\right)^{\frac{3}{2}}}\delta_{ij}ds \tag{3.74}$$

$$\frac{\partial K_{ijlk}^{1,Damp}}{\partial U}U_{jk}^{(n)} = \int_0^L \eta_B I\frac{N_l''N_k''}{\sqrt{\left(N_s'U_{js}\right)^T\cdot N_t'U_{it}}}U_{jk}^{(n)}\left(\frac{\left(N_s''\dot{U}_{it}\right)^T\cdot N_t''+\frac{\gamma}{\beta\Delta t}\left(N_s''U_{it}\right)^T\cdot N_t''}{\left(N_s''U_{js}\right)^T\cdot N_t''U_{it}}-\right.$$

$$\frac{\left(N_s''U_{js}\right)^T\cdot N_{t_{it}''\dot{U}}\cdot 2\left(N_s''U_{it}\right)^T\cdot N_t''}{\left(\left(N_s''U_{js}\right)^T\cdot N_t''U_{it}\right)^2}-\left(\frac{\left(N_s'\dot{U}_{it}\right)^T\cdot N_t'+\frac{\gamma}{\beta\Delta t}\left(N_s'U_{it}\right)^T\cdot N_t'}{\left(N_s'U_{js}\right)^T\cdot N_t'U_{it}}-\frac{\left(N_s'U_{js}\right)^T\cdot N_t'\dot{U}_{it}\cdot 2\left(N_s'U_{js}\right)^T\cdot N_t'}{\left(\left(N_s'U_{js}\right)^T\cdot N_t'U_{it}\right)^2}\right)\Bigg)- \tag{3.75}$$

$$\eta_B I N_l''N_k''U_{jk}^{(n)}\left(\frac{\left(N_s''U_{js}\right)^T\cdot N_{t_{it}''\dot{U}}}{\left(N_s''U_{js}\right)^T\cdot N_t''U_{it}}-\frac{\left(N_s'U_{js}\right)^T\cdot N_t'\dot{U}_{it}}{\left(N_s'U_{js}\right)^T\cdot N_t'U_{it}}\right)\frac{{U_{js}}^T{N_s'}^T\cdot N_t'}{\left(\left(N_s'U_{js}\right)^T\cdot N_t'U_{jt}\right)^{\frac{3}{2}}}\delta_{ij}ds$$

$$\frac{\partial K_{ijlk}^{2}}{\partial U}U_{jk}^{(n)} = \int_0^L -P_n N_l'N_k'U_{jk}^{(n)}\frac{{U_{js}}^T{N_s'}^T\cdot N_t'}{\left(\left(N_s'U_{js}\right)^T\cdot N_t'U_{jt}\right)^{\frac{3}{2}}}\ \delta_{ij}ds \tag{3.76}$$

$$\frac{\partial E_{mil}}{\partial U} = \frac{EI}{EA}\int_0^L P_m\left(\frac{2\cdot\left(N_s''U_{js}\right)^T\cdot N_t''}{\left(N_s'U_{js}\right)^T\cdot N_t'U_{it}}-\frac{\left(N_s''U_{js}\right)^T\cdot N_t''U_{it}\cdot 2\left(N_s'U_{js}\right)^T\cdot N_t'}{\left(\left(N_s'U_{js}\right)^T\cdot N_t'U_{it}\right)^2}\right)ds+$$

$$\frac{\eta_B I}{EA}\int_0^L P_m\left(\frac{\left(N_s''\dot{U}_{it}\right)^T\cdot N_t''+\frac{\gamma}{\beta\Delta t}\left(N_s''U_{it}\right)^T\cdot N_t''}{\left(N_s''U_{js}\right)^T\cdot N_t''U_{it}}-\frac{\left(N_s''U_{js}\right)^T\cdot N_t''\dot{U}_{it}\cdot 2\left(N_s''\dot{U}_{it}\right)^T\cdot N_t''}{\left(\left(N_s''U_{js}\right)^T\cdot N_t''U_{it}\right)^2}-\right. \tag{3.77}$$

$$\left.\left(\frac{\left(N_s'\dot{U}_{it}\right)^T\cdot N_t'+\frac{\gamma}{\beta\Delta t}\left(N_s'U_{it}\right)^T\cdot N_t'}{\left(N_s'U_{js}\right)^T\cdot N_t'U_{it}}-\frac{\left(N_s'U_{js}\right)^T\cdot N_t'\dot{U}_{it}\cdot 2\left(N_s'U_{js}\right)^T\cdot N_t'}{\left(\left(N_s'U_{js}\right)^T\cdot N_t'U_{it}\right)^2}\right)\right)\frac{\left(N_s''U_{js}\right)^T\cdot N_t''U_{it}}{\left(N_s'U_{js}\right)^T\cdot N_t'U_{it}}+$$

$$P_m\left(\frac{\left(N_s''U_{js}\right)^T\cdot N_t'\dot{U}_{it}}{\left(N_s''U_{js}\right)^T\cdot N_t''U_{it}}-\frac{\left(N_s'U_{js}\right)^T\cdot N_t'\dot{U}_{it}}{\left(N_s'U_{js}\right)^T\cdot N_t'U_{it}}\right)\left(\frac{2\cdot\left(N_s''U_{js}\right)^T\cdot N_t''}{\left(N_s'U_{js}\right)^T\cdot N_t'U_{it}}-\frac{\left(N_s''U_{js}\right)^T\cdot N_t''U_{it}\cdot 2\left(N_s'U_{js}\right)^T\cdot N_t'}{\left(\left(N_s'U_{js}\right)^T\cdot N_t'U_{it}\right)^2}\right)ds$$

Then, substituting Eq. (3.69), Eq. (3.72), Eq. (3.73) into Eq. (3.71) we obtain:

$$M_{ijlk}\left(\frac{1}{\beta\Delta t^2}\Delta U+C_a\right)+F_{il}^{i(n)}+\left(K_{ijlk}^{1}+\frac{\partial K_{ijlk}^{1}}{\partial U}U_{jk}^{(n)}+K_{ijlk}^{1,Damp}+\frac{\partial K_{ijlk}^{1,Damp}}{\partial U}U_{jk}^{(n)}+\right.$$

$$\left.\lambda_n^{(n)}\frac{\partial K_{nijlk}^{2}}{\partial U}U_{jk}^{(n)}+\lambda_n^{(n)}K_{nijlk}^{2}\right)\Delta U_{jk}+K_{nijlk}^{2}U_{jk}^{(n)}\cdot\Delta\lambda_n-F_{il}^{e(n+1)}=0 \tag{3.78}$$

$$\left(2A_{mil}U_{kl}^{(n)}+D_{mn}\left(\dot{U}_{ki}^{(n)}+\frac{\gamma}{\beta\Delta t}U_{kl}^{(n)}\right)-\frac{\partial E_{mil}}{\partial U}\right)\Delta U_{jk}-C_{mn}\Delta\lambda_n=-H_m^{(n)}$$

Rearranging the terms of Eq. (3.78)

$$M_{ijlk}\frac{1}{\beta\Delta t^2}\Delta U+\left(K^1_{ijlk}+\frac{\partial K^1_{ijlk}}{\partial U}U^{(n)}_{jk}+K^{1,Damp}_{ijlk}+\frac{\partial K^{1,Damp}_{ijlk}}{\partial U}U^{(n)}_{jk}+\lambda^{(n)}_n\frac{\partial K^2_{nijlk}}{\partial U}U^{(n)}_{jk}+\right.$$
$$\left.\lambda^{(n)}_n K^2_{nijlk}\right)\cdot\Delta U_{jk}+K^2_{nijlk}U^{(n)}_{jk}\Delta\lambda_n=-M_{ijlk}C_a-F^{i(n)}_{il}+F^{e(n+1)}_{il} \tag{3.79}$$
$$\left(2A_{mil}U^{(n)}_{kl}+D_{mn}\left(\dot U^{(n)}_{ki}+\frac{\gamma}{\beta\Delta t}U^{(n)}_{kl}\right)-\frac{\partial E_{mil}}{\partial U}\right)\Delta U_{jk}-C_{mn}\Delta\lambda_n=-H^{(n)}_m$$

The above equation can be rewritten in a matrix form as follows:

$$K_{dyn}\Delta y=\Delta F_{dyn} \tag{3.80}$$

where:

$$K_{dyn}=\begin{bmatrix}M_{ijlk}\frac{1}{\beta\Delta t^2}+K^1_{ijlk}+\frac{\partial K^1_{ijlk}}{\partial U}U^{(n)}_{jk}+K^{1,Damp}_{ijlk}+\frac{\partial K^{1,Damp}_{ijlk}}{\partial U}U^{(n)}_{jk}+\cdots & K^2_{nijlk}U^{(n)}_{jk}\\ \cdots+\lambda^{(n)}_n\frac{\partial K^2_{nijlk}}{\partial U}U^{(n)}_{jk}+\lambda^{(n)}_n K^2_{nijlk} & \\ 2A_{mil}U^{(n)}_{kl}+D_{mn}\left(\dot U^{(n)}_{ki}+\frac{\gamma}{\beta\Delta t}U^{(n)}_{kl}\right)-\frac{\partial E_{mil}}{\partial U} & -C_{mn}\end{bmatrix} \tag{3.81}$$

$$\Delta F_{dyn}=\begin{bmatrix}-M_{ijlk}C_a-\left(K^1_{ijlk}+K^{1,Damp}_{ijlk}+\lambda_n K^2_{nijlk}\right)U^{(n)}_{jk}+F^{e(n+1)}_{il}\\ -H^{(n)}_m\end{bmatrix} \tag{3.82}$$

$$\Delta y=\begin{bmatrix}\Delta U_{jk}\\ \Delta\lambda_n\end{bmatrix} \tag{3.83}$$

Then, a first approach of the y^{n+1} can be assessed as $y^{n+1}=y^n+\Delta y$.

To ensure the convergence of the $(n+1)$ time step, a corrector procedure is implemented from the unbalanced residual of Eq. (3.71) by a Newton-Rapson corrector. Suppose to be j, the $j-th$ iteration of corrector procedure, Eq. (3.71) can be expressed as:

$$M_{ijlk}\ddot U^{(n+1,j)}_{jk}+F^{i(n+1,j)}_{il}-F^{e(n+1,j)}_{il}=G^{(n+1,j)}_{il}=0 \tag{3.84}$$

$$A_{mil}U^{(n+1,j)}_{kl}U^{(n+1,j)}_{ki}-B_m+D_{mn}U^{(n+1,j)}_{kl}\dot U^{(n+1,j)}_{ki}-E_{mil}\left(U^{(n+1,j)}\dot U^{(n+1,j)}\right)-$$
$$C_{mn}\lambda^{(n+1,j)}_n=H^{(n+1,j)}_m=0 \tag{3.85}$$

Then, the $(j+1)$ unbalanced term of the $(n+1)$ time step can be defined as Eq. (3.86)

$$\begin{bmatrix}G^{(n+1,j+1)}_{il}\\ H^{(n+1,j+1)}_m\end{bmatrix}=\begin{bmatrix}G^{(n+1,j)}_{il}\\ H^{(n+1,j)}_m\end{bmatrix}+K_{dyn}\Delta y^{j+1}=\begin{bmatrix}0\\0\end{bmatrix}$$
$$\Delta y^{j+1}=K^{-1}_{dyn}\begin{bmatrix}-G^{(n+1,j)}_{il}\\ -H^{(n+1,j)}_m\end{bmatrix} \tag{3.86}$$

And the $j+1-th$ approximation can be assessed as next:

$$\begin{aligned} y^{(n+1,j+1)} &= y^{(n+1,j)} + \Delta y^{j+1} \\ \dot{y}^{(n+1,j+1)} &= \dot{y}^{(n+1,j)} + \frac{\gamma}{\beta \Delta t} \Delta y^{j+1} \\ \ddot{y}^{(n+1,j+1)} &= \ddot{y}^{(n+1,j)} + \frac{1}{\beta \Delta t^2} \Delta y^{j+1} \end{aligned} \tag{3.87}$$

Where at every $(j+1)-th$ iteration the stiffness matrices, and forces are updated.

The FEM implementation presented above allows to take into account the fully dynamics of the rod system adding the rheological damping of both Axial and Bending strengths.

3.7 EQUATIONS OF THE EXTERNAL FORCES

To take into account the hydrodynamic forces, the external force per unit length $\mathbf{q}$ is defined as:

$$\mathbf{q} = \mathbf{f}_{hg} + \mathbf{f}_{am} + \mathbf{f}_{D,t} + \mathbf{f}_{D,n} + \mathbf{f}_{sb} \tag{3.88}$$

Where $\mathbf{f}_{hg}$ is the hydrostatic and gravity forces, $\mathbf{f}_{am}$ is the hydrodynamic inertia force, $\mathbf{f}_{D,t}$ and $\mathbf{f}_{D,n}$ are the hydrodynamic tangential and normal drag forces respectively, and $\mathbf{f}_{sb}$ is the seabed force. These forces per unit length can be expressed as Eq. (3.89).

$$\begin{aligned} \mathbf{f}_{hg} &= \rho_m A \mathbf{g} - \rho_w A \mathbf{g} = \gamma_w \mathbf{e}_z \\ \mathbf{f}_{am} &= -A \rho_w C_a \ddot{\mathbf{r}}^n + A \rho_w C_m \dot{\mathbf{V}}^n \\ \mathbf{f}_{D,t} &= \frac{1}{2} \rho_w C_{D,t} d |\mathbf{V}^t - \dot{\mathbf{r}}^t| (\mathbf{V}^t - \dot{\mathbf{r}}^t) \\ \mathbf{f}_{D,n} &= \frac{1}{2} \rho_w C_{D,n} d |\mathbf{V}^n - \dot{\mathbf{r}}^n| (\mathbf{V}^n - \dot{\mathbf{r}}^n) \\ \mathbf{f}_{sb,z} &= -G_k d (\mathbf{r}_z + depth) - 2 G_c \sqrt{\rho_m A G_k d} \min(\dot{\mathbf{r}}_z; 0) \qquad \text{if } \mathbf{r}_z + depth < 0 \\ \mathbf{f}_{sb,y} &= -\rho_m |\mathbf{g}| \mathrm{G}_\mu \min\left(\frac{\dot{\mathbf{r}}_{xy}}{G_{vc}}; 1\right) \end{aligned} \tag{3.89}$$

The hydrodynamic forces $\mathbf{f}_{am}$, $\mathbf{f}_{D,n}$, $\mathbf{f}_{D,t}$ are based on the Morison's equation for oscillating cylinders Laya et al. (1984). The seabed effect is set as a normal force on the flat sea-bed based on a spring-damper system. The damping force only appears when the node with seabed contact penetrates to the soil (negative velocity), nor when it is coming out. In the Eq. (3.89) the superscript *n* and *t* refer to the normal or the tangent component of the line respectively; $\mathbf{g}$ is the gravity vector, the γ_w is the wet weight per meter length; the $\mathbf{V}$ is the water particle velocity; the $\dot{\mathbf{V}}$ is the water particle acceleration; the G_K is the ballast seabed coefficient or the seabed stiffness in $\left[\frac{N}{m^3}\right]$; the depth is the sea depth; the G_C is the fraction of critical damping of ground, G_μ is the friction coefficient and G_{vc} is the cut-off velocity of friction. The

hydrodynamic coefficients are: C_D the drag coefficient, C_a the added mass coefficient and C_m the inertia coefficient.

Then, applying the Garlekin method to the forces the Eq. (3.90) and (3.91) are obtained, where the first are related to the external forces, and the second defines the added mass that will be added to the line mass.

$$F_{il}^{e} = \int_0^L N_l\left(\mathbf{f}_{hg} + \mathbf{f}_{hd} + \mathbf{f}_{sb}\right)(1+\varepsilon)ds \tag{3.90}$$

where:

$$\mathbf{f}_{hd} = \mathbf{f}_{D,t} + \mathbf{f}_{D,n} + A\rho_w C_m \dot{\mathbf{V}}^n$$

$$\begin{aligned} M_{ijlk}^{a}\ddot{U}_{jk} &= \int_0^L N_l\,(\rho_w A C_a \ddot{\mathbf{r}}^n)ds \\ &= \int_0^L N_l\left(\rho_w A C_a\left(\sum_{i=1}^{n} N_k\delta_{ij}\ddot{U}_{jk} - \sum_{i=1}^{n}(N_k N_s' N_t')U_{jt}U_{js}\delta_{ij}\ddot{U}_{jk}\right)\right)ds \end{aligned} \tag{3.91}$$

$$M_{ijlk}^{a} = \sum_{i=1}^{n}\rho_w A C_a\left(\int_0^L N_l N_k\delta_{ij} - \left(\int_0^L N_l N_k N_s' N_t' ds\right)U_{jt}U_{js}\delta_{ij}\right)$$

3.8 SLACK LINE EVENTS – NON TENSION POINTS

Chains are one of the most used elements for mooring systems. The main characteristics of the chain lines are the null bending stiffness and that compression cannot be supported.

The theory presented is suitable for chain modelling, but some modification should be implemented to avoid negative tension (compression) in the solution. Nevertheless, if no bending stiffness is considered, the theory leads to consider the rod as a rubber band, which with small compressions will easily bend. As slack events are temporally short, and the formulation used considers the bending of the line, the differences between the solutions if compression is allowed or not are very similar as shown later in this section.

The non tension events are implemented in the formulation with a corrector procedure by imposing null tension where negative tensions appear in the Lagrange multiplier λ.

$$\lambda^{(n+1,j+1)} = 0 \text{ if } \lambda_m^{(n+1,j+1)} < 0 \tag{3.92}$$

This process unbalances the constitutive equation, forcing to find a new solution where compression events are presented.

A comparative study of the influence of the slack condition is performed using the mooring line test performed by Lindahl (1985) experiments and reproduced by Palm et al. (2013). The experimental setup is shown in Figure 3-3 and a more detailed explanation is presented in section 3.10.2. The Figure 3-4 and Figure 3-5 show a slack event at two different points of the same line. One is the top end point with an arch-length of 33m, and a mid point with an arch-length of 14.85m as shown in Figure 3-3. The simulations are carried out using null bending stiffness and imposing the slack condition or allowing compression. The Figure 3-4 shows the same response for the two simulations as the slack event does no effect at the top part of the line. However, the Figure 3-5 shows the differences between both responses. The tension of the simulation with the slack condition remains zero, whereas the other accepts compression. However, even when compression is allowed, the response of the line is very similar.

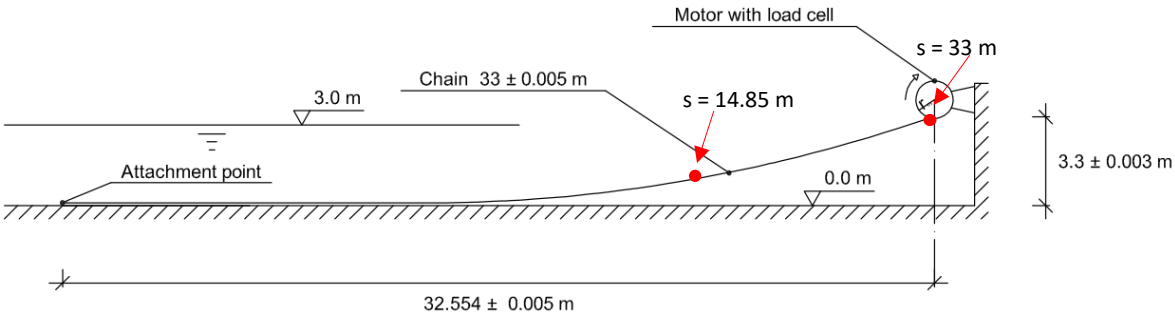

Figure 3-3: Sketch of the benchmark experiment Palm et al. (2013)

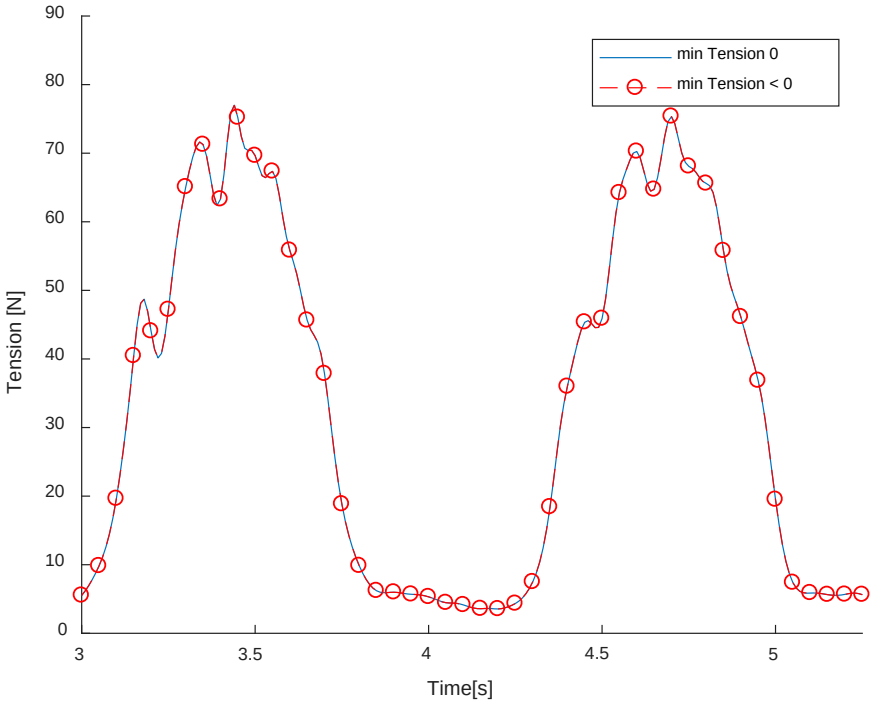

Figure 3-4: Tension at the top point of the chain

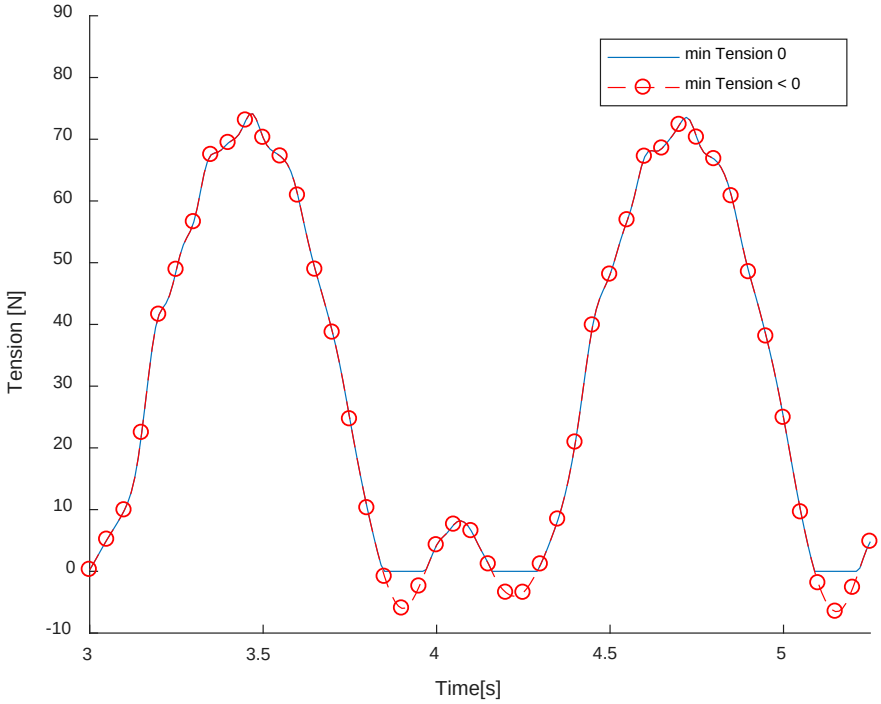

Figure 3-5: Tension at middle point of the chain

3.9 NUMERICAL VERIFICATION

The numerical verification of the model is based on two plus one examples. The first two cases mobilize the axial damping and the bending damping of the same bar, and the third case mobilizes both, axial and bending damping trough a post buckling state. All the simulations are performed for a range from 0 to 100% of the critical damping.

3.9.1 Axial and Bending Damping

The axial and bending damping verification test are a numerical simulation performed by applying an initial axial strain and bending deformation to a bar, which is allowed to move freely. The properties of the bar are shown in Table 3-1, and is discretized in 20 elements.

3.9.1.1 Axial damping

The axial case is performed by imposing an initial strain equivalent to a 500 N tension at the free end as shown in Figure 3-6. Six different axial damping viscosity ratios are used to compare the axial damping behaviour. According to section 3.3.3, the axial critical viscosity for a cantilever beam can be computed as $\eta_{A,Critic} = \frac{4L}{\pi}\sqrt{\rho_m \cdot E}$ which takes a value of $\eta_{A,Critic} = 2.576 \cdot 10^7\ \mathrm{N/(m^2 s)}$.

The time step used in the simulation is $0.5 \cdot 10^{-5}\ s$ (approximately one hundredth of the un-damped axial natural period of the bar) and the convergence of the dynamics of the rod was achieved after an average of two iterations.

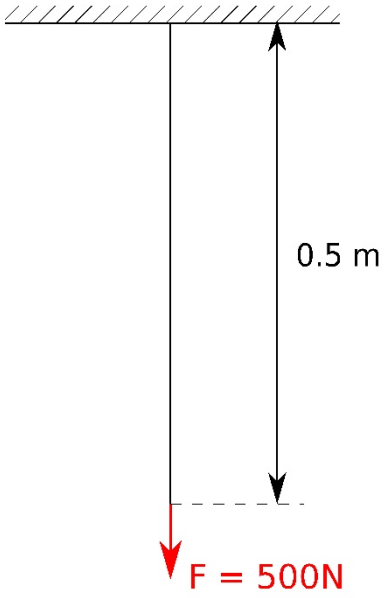

Figure 3-6: Sketch of the axial verification test

Table 3-1: Parameters of the rod for the axial and bending verification test

Length [m]	0.5
Diameter [m]	0.02
A [m²]	3.14E-04
I [m⁴]	7.85E-09
ρ [kg/m³]	7800.00
E [N/m²]	2.10E+11
Mass per meter length [kg/m]	2.46
Total mass [kg]	1.23
EA [N]	6.60E+07
EI [N·m²]	1.65E+03

The initial linear elastic displacement at the free end is $\Delta z = L \cdot \frac{F}{EA} = 3.79 \cdot 10^{-3} mm$. Figure 3-7 shows the results of the elongation at the free in the time domain, with the different ration of damping. From 0% of the axial critical damping to a 100 % ratio, the elongation of the free end varies from a sinusoidal behavior to an overdamped motion. For the intermediate damping ratios, the more axial damping ratio the more amplitude is reduced. Moreover, the natural period of the un-damped motion of the simulation can be assessed from Eq. (3.23) by $T = \frac{2\pi}{\omega_n} = \frac{2\pi}{\sqrt{k/m}} = \frac{2\pi}{\sqrt{E\beta_A^2/\rho}} = 0.000385\ \mathrm{s} = 0.385\ \mathrm{ms}$, where $\beta_A = \frac{\pi}{2L}$, which shows good agreement with the simulations.

3.9.1.2 Bending damping

The bending case is performed by imposing a bending moment at the free end of M = 172.8 N·m as is shown in Figure 3-8. According to section 3.3.3, the bending critical viscosity for a cantilever beam can be computed as $\eta_{B,Critic} = 2/\beta_B^2 \sqrt{\rho_m \cdot AE/I}$ which takes a value of $\eta_{\beta,Critic} = 2.519 \cdot 10^9\ \mathrm{N/(m^2 s)}$ for a $\beta_{B,1} = 0.59686\pi/L$.

The time step used in the simulation is $1 \cdot 10^{-4} s$ (approximately one hundredth of the natural period of the 1st bending mode) and the convergence of the dynamics of the rod was achieved after an average of three iterations.

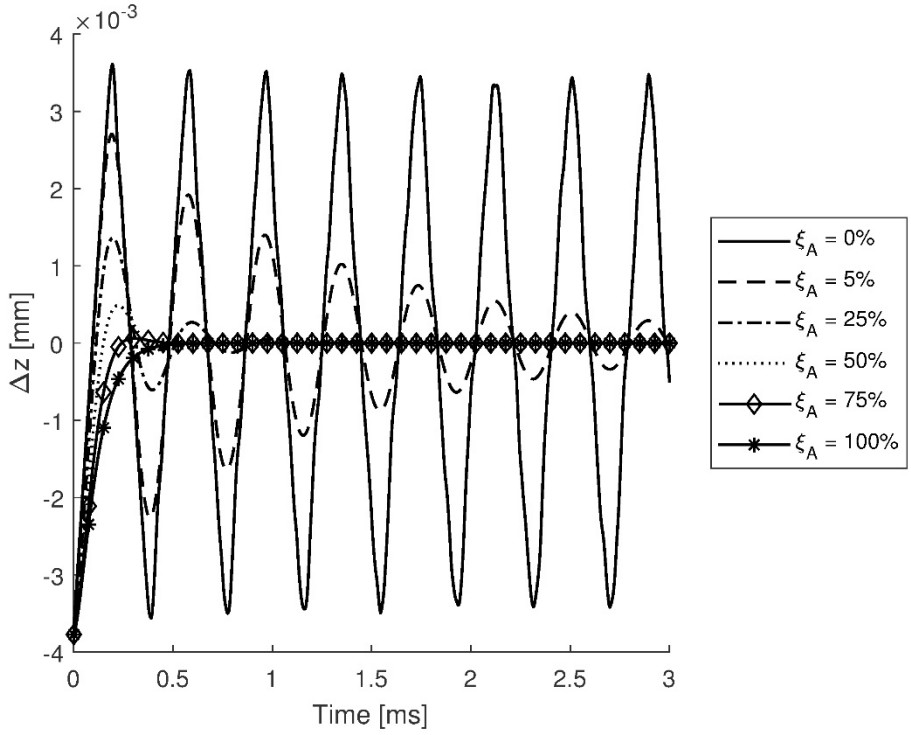

Figure 3-7: Incremental position of the free-end node of the rod

The Figure 3-9 shows the X position of the free end for the different damping ratios. For a 100 % damping ratio, the system is overdamped while for a 0 % damping ratio the motion is clearly un-damped. Moreover, the 0% damping ratio does not present a clearly sinusoidal motion as the axial damping does. The reason is that the bending motion can be composed by more than one mode, which are more likely to appear for un-damped systems.

In order to compare the natural frequencies of each node with the theoretical ones, a Fast Fourier Transform (FFT) is applied to the X motion of the free end node. Figure 3-10 shows the amplitude-frequency relation of the FFT and the main values of the peaks. The comparison of the theoretical frequency values with the values obtained through the FFT, in Table 3-2, presents a good match for all the cases and confirms the origin of the fluctuation of the motion of the free end.

The theoretical natural frequencies of the un-damped motion of the bending modes of a cantilever beam can be assessed from Eq. (3.23) by $f = \frac{\omega_n}{2\pi} = \frac{\sqrt{k/m}}{2\pi} = \frac{\sqrt{EI\beta_B^4/(\rho A)}}{2\pi}$

Table 3-2: natural frequency mode comparison

Mode\Parameter	β_n	$f_n\,[Hz]$ (theoretical)	$f_n\,[Hz]$ (FFT)
1st mode (n = 1)	3.7502	57.97	59.88
2nd mode (n = 2)	9.3882	363.29	359.3
3rd mode (n = 3)	15.7095	1017	978

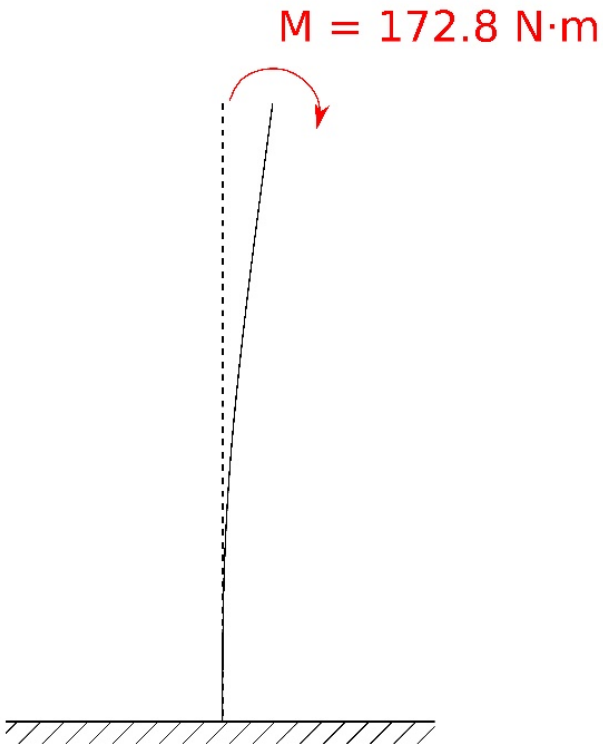

Figure 3-8: Sketch of the Bending verification test

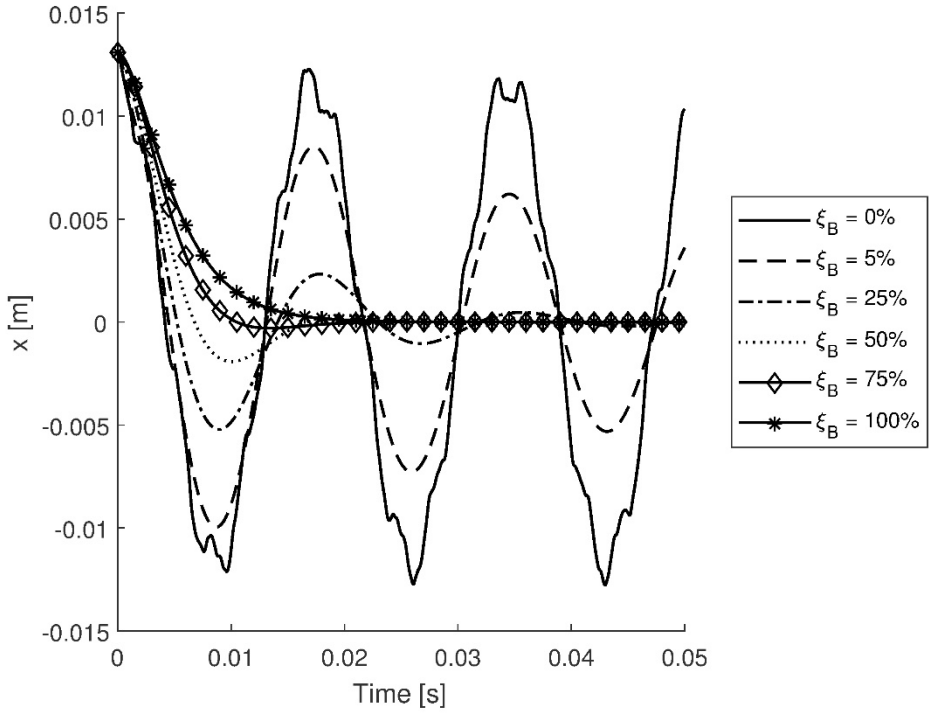

Figure 3-9: X position of the free end node

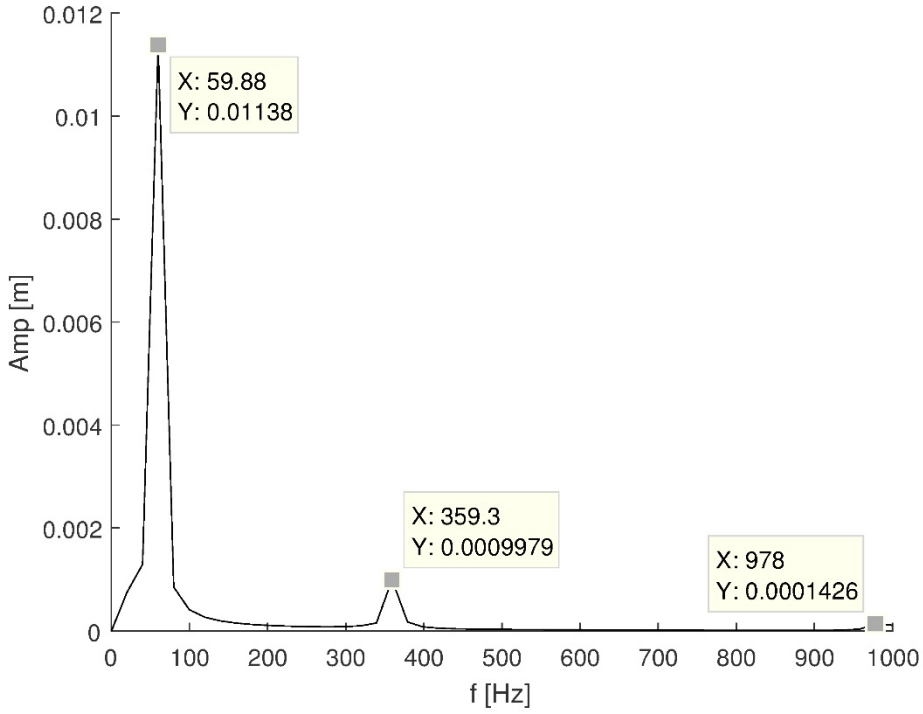

Figure 3-10: FFT of X motion of the free end node

3.9.2 Post buckling behavior – Axial and Bending coupled damping

The coupled axial and bending damping verification test is a numerical simulation performed by imposing an initial deformation of a column equivalent to a post buckling state and allowing it to move freely. The initial deformation is achieved by applying an initial axial load higher than the critical buckling load as is shown in Figure 3-11. This state causes a linear decreasing bending moment through the column with the horizontal position, which is maximum on the base and 0 at the free end. Moreover, such as an initial axial load is applied, the axial damping is also mobilized. The properties of the column and its critical buckling axial force (P_c) are shown in Table 3-3. The axial force applied is 1.0154 times the critical buckling force, that can be assessed by Eq. (3.93) Timoshenko & Gere (1963).

The critical bending damping is assessed by Eq. (3.33) with the boundary conditions of a clumped end and a free end, which leads to a $\beta_B = 0.59686\pi/L$. Herein the viscosity term for the axial damping used is the one obtained through the bending critical damping as is the main load affected. Then, the critical viscosity used takes a value of $\eta_{\beta,Critic} = 1.95 \cdot 10^6\ \mathrm{N/(m^2 s)}$

$$P_{crit} = \frac{\pi^2 EI}{4l^2} \tag{3.93}$$

The simulation was performed with 20 elements for the bar discretization, the time step used in the simulation is $0.01s$ and the convergence of the dynamics of the rod was achieved after an average of 4 iterations

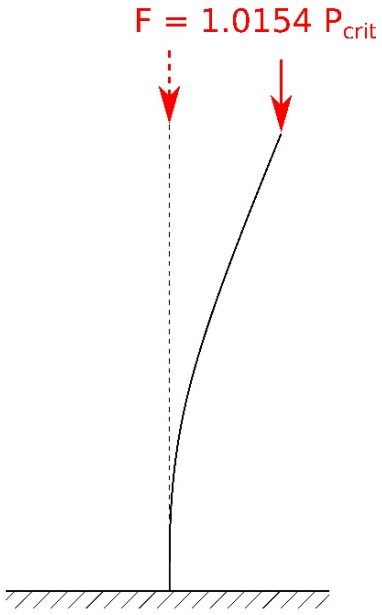

Figure 3-11: Sketch of the buckling verification test

Table 3-3: Parameters of the buckling verification test

Length [m]	1
Diameter [m]	0.08
A [m²]	5.03E-03
I [m⁴]	2.01E-06
$\boldsymbol{\rho}$ **[kg/m³]**	1430
E [N/m²]	3.14E+06
Mass per meter length [kg/m]	7.19
Total mass [kg]	7.19
EA [N]	1.54E+04
EI [N·m²]	6.021
$\boldsymbol{\eta_{B,Critic}}$ **[N/(m²s)]**	1.951e+06
$\boldsymbol{\xi_B}$**(damping ratio) [%]**	0-100
P_{crit} [N]	14.86
F [N]	15.1

The equilibrium point of the post buckling state for the initial axial force match the theoretical point Garrett (1982), shown in Table 3-4. Figure 3-12 and Figure 3-13 show the horizontal and vertical position of the free end node during the simulation, which allow to compare the motions of the free end for different bending damping ratios. By and large, the more damping ratio the more free end motion is restrained. However, it is clearly state that a 100% bending damping ratio does not produces an overdamped behavior of the column motion. This behavior can be explained by the differences between the simulation test and the differential equation used for the derivation of the critical bending damping. In the simulation the column is not purely bending loaded, but axially loaded that produces a buckling state and thus an internal bending moment. Then, when the free end is released the column does not behave as if was loaded in pure bending. Moreover, for the 0 % bending damping ratio, this phenomenon is accentuated due to the lack of damping. In both Figure 3-12 and Figure 3-13 is stated that the free end does not fit a perfect sinusoidal diagram. For this case, the deformed shape of the column in an instant, presents different curvature directions due to the superposition of different mode shapes as is shown in Figure 3-14.

The natural period of the un-damped motion of the bending simulation can be assessed from equation (3.23) by $T = \frac{2\pi}{\omega_n} = \frac{2\pi}{\sqrt{k/m}} = \frac{2\pi}{\sqrt{EI\beta_B^4/(\rho A)}} = 1.953$ s.

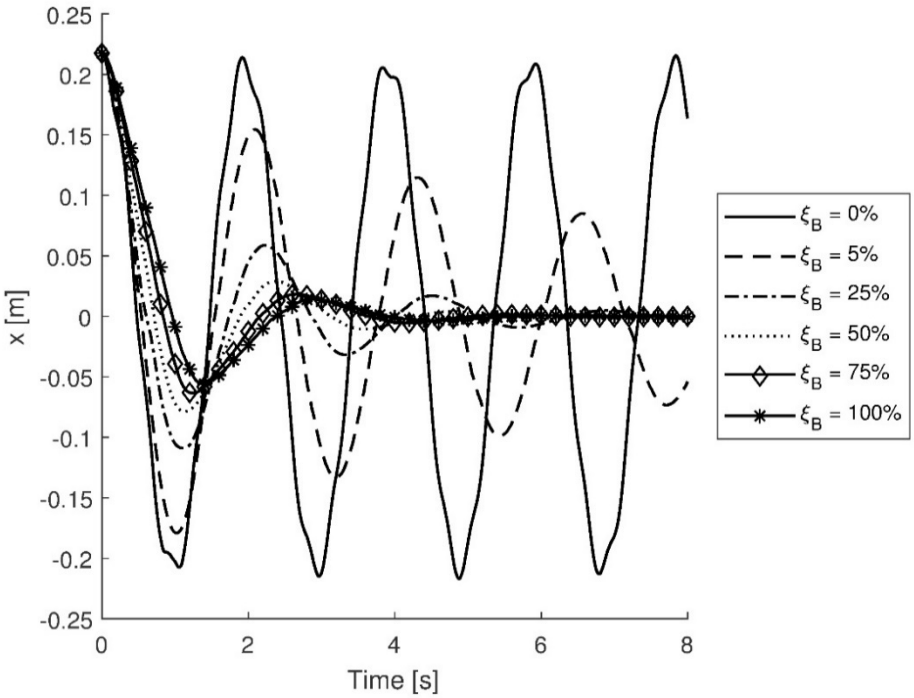

Figure 3-12: X position of the free end along the time for different damping ratios

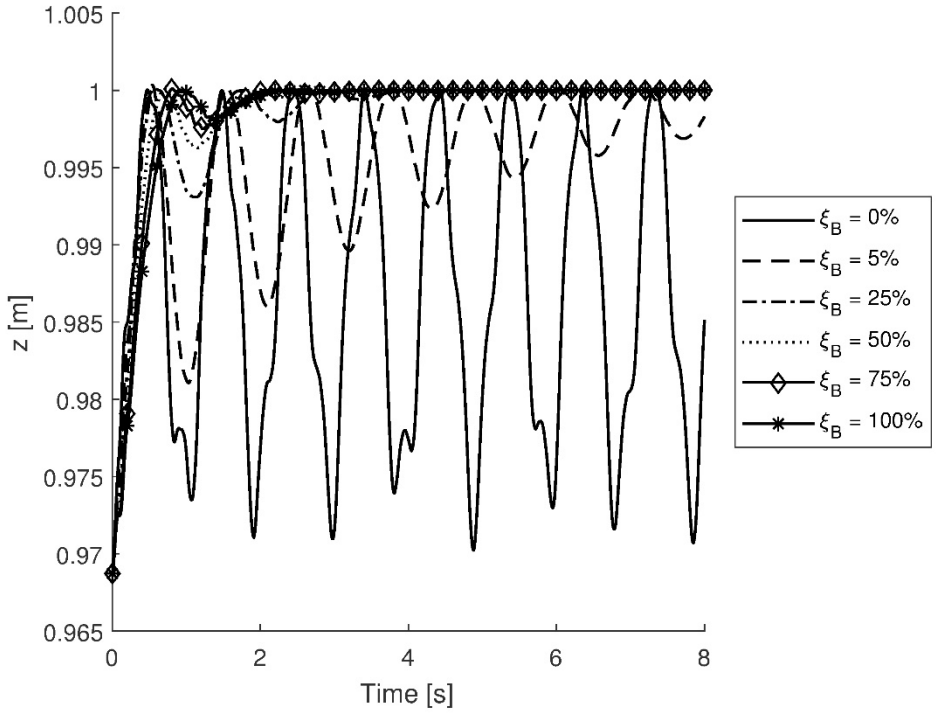

Figure 3-13: Z position of the free end along the time for different damping ratios

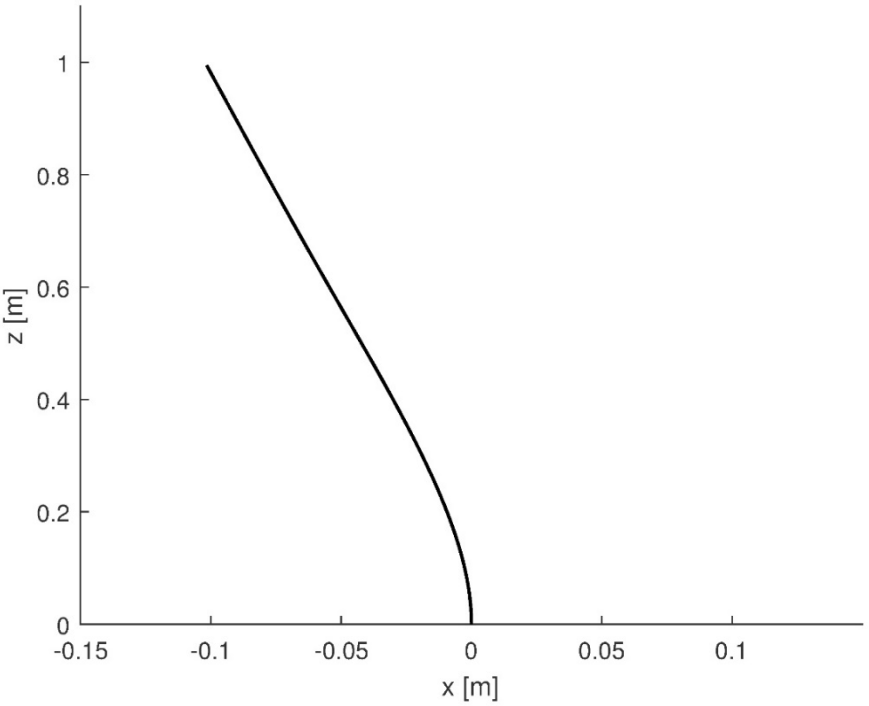

Figure 3-14:Deformed shape of the column in an instant of the motion

Table 3-4: Position of free end node for a load above the critical buckling

Model	P/P_{crit}	Z/l	X/l
Garret	1.015397	0.9697	0.2194
Proposed Model	1.015397	0.9690	0.2173

3.10 EXPERIMENTAL VALIDATION

The validation of the model is performed by the simulation of two experimental tests. The first one consists in a free fall cable presented by Koh Koh et al. (1999). The second one consists in a chain catenary mooring line with a fixed end and an imposed motion at the other end presented by Palm et al. Palm et al. (2013).

3.10.1 Free fall cable

The free fall cable test consists in a free motion of a cable hanged in one end, as a hinge, and allowing the cable to spin like a pendulum.

The rod used in the experiment was a Neoprene rubber with the properties shown in Table 3-5. The initial position of the free end of the cable is at the same height of the other end with a horizontal span of 1.8 m. Due to the length of the rod is 2.022 m, the cable bent in its initial position, as can be shown in Figure 3-15, a picture of the experimental setup. A damping ratio of 6.2 % was obtained experimentally by a pull-back test Koh et al. (1999). Then, the bending critical damping is obtained supposing a double pinned cable element, which leads to $\beta_B = \pi/L$ Inman (2001).

The simulation was performed with 20 elements for the bar discretization, the time step used in the simulation is $1 \cdot 10^{-3}\ s$ and the convergence of the dynamics of the cable was achieved after an average of three iterations.

The experimental results presented by Koh et al. (1999) include the dynamic tension of the fixed end obtained by four strain gauges placed symmetrically attached at the surface of the cable near the end, but far enough to prevent the tension concentration due to the fixed support. Figure 3-16 and 14 show the comparison of the tension between the experimental results of Koh et al. (1999) and the numerical ones obtained with the proposed model. Numerical results fit very well the experimental data. However, the proposed model presents a larger main frequency and gets less accuracy as the time increases (Figure 3-16 and 3-17), showing larger amplitudes than the experiment. Then, this could be explained by an additional damping coming from the friction of the hinge at the fixed end and the wires of the strain gages (Figure 3-15).

Table 3-5: Neoprene rubber cable properties Koh et al. (1999)

Length [m]	2.022
Diameter [m]	0.03
A	4.91E-04
I	1.92E-08
ρ [kg/m^3]	1430
E [N/m^2]	3.14E+06
Mass per meter length [kg/m]	0.702
Total mass [kg]	1.419
EA [N]	1.541E+03
EI [N·m^2]	0.06
$\eta_{B,Critic}$ $[\mathrm{N}/(\mathrm{m}^2\mathrm{s})]$	8.898E+06
ξ_B(damping ratio) [%]	6.2

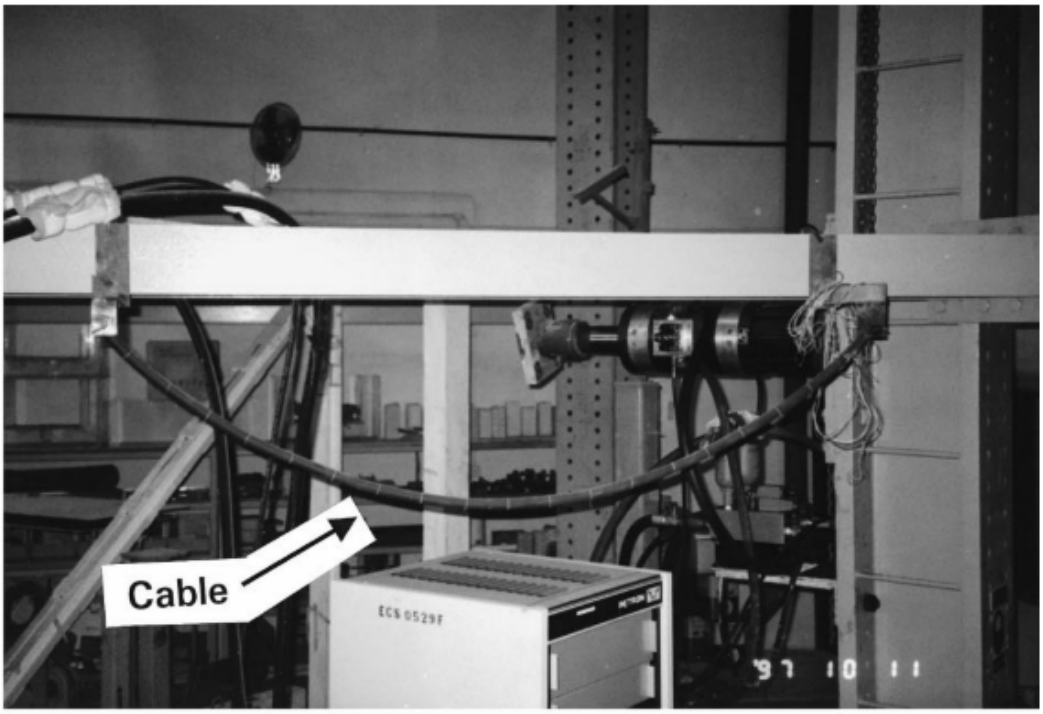

Figure 3-15: Experimental setup with the cable in its initial position Koh et al. (1999)

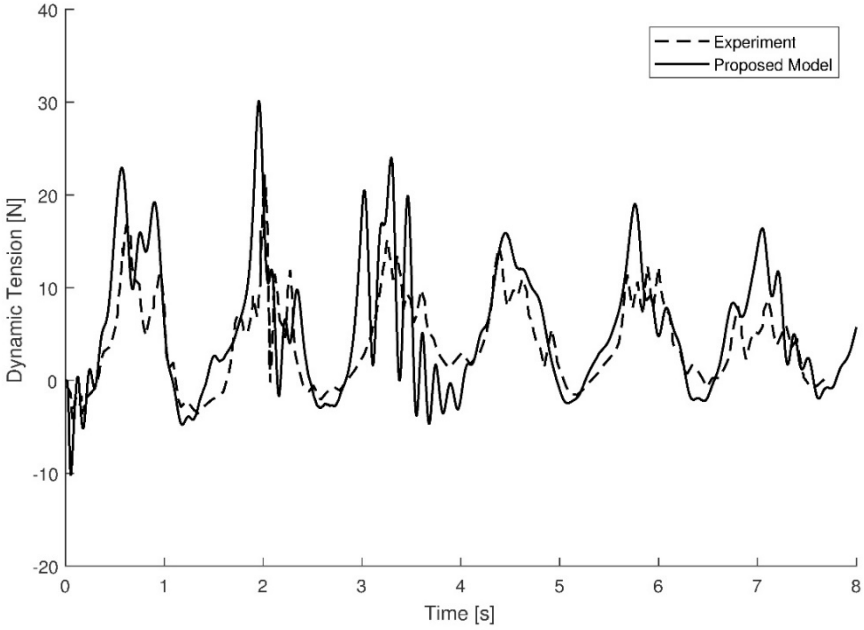

Figure 3-16: Comparison of experimental and numerical results

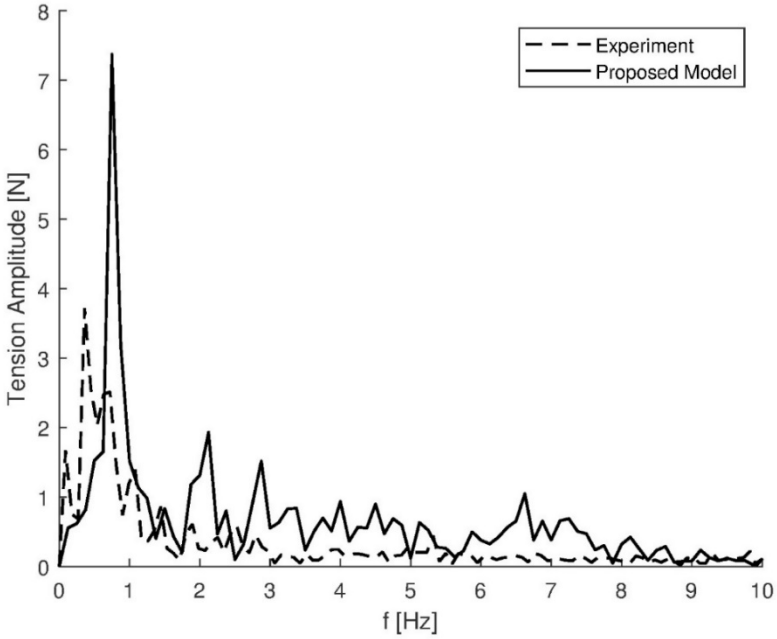

Figure 3-17: FFT comparison of experimental and numerical results

3.10.2 Mooring chain

The mooring chain validation consists in a catenary mooring chain fixed on the seabed and attached to a disk at the other end, which spins through a motor equipped with a load cell to get the mooring tension. This model test used was presented by Lindahl (1985) and recently represented by Palm et al. (2013).

The properties of the chain and main parameters of the experiment are presented in Table 3-6 and a sketch of the model test is shown in Figure 3-18. Moreover, an axial damping ratio of 3% is set to take into account the friction between links. This value has been set to avoid the use of an artificial numerical damping. The ballast seabed coefficient does not match the value provided by Palm et al. (2013), and is set to 3E+05 Pa as set Chen & Basu (2018).

The simulation was performed with 30 elements for the chain discretization. The time step used in the simulation are $0.01s$ and $0.005s$ for the T=3.5 s and T=1.25 s disk period, respectively, and the convergence of the dynamics of the chain was achieved after an average of 3 iterations

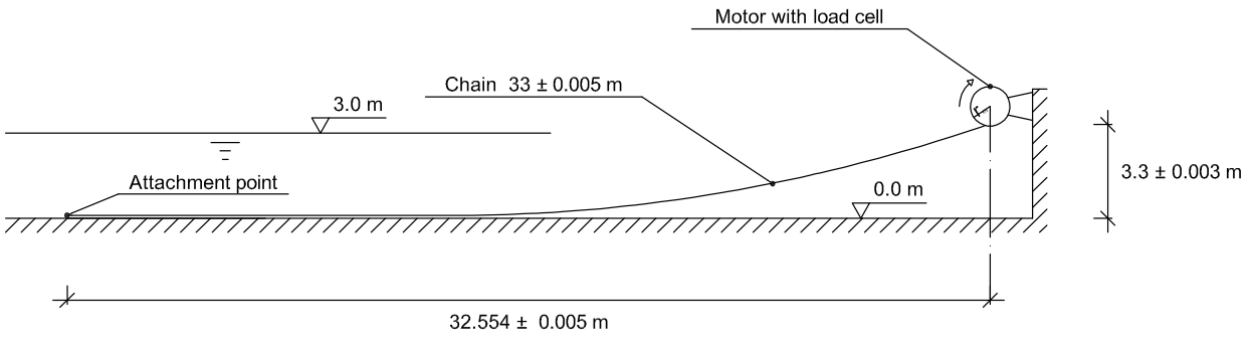

Figure 3-18: Model test sketch, Palm et al. (2013)

Table 3-6: Mooring line properties Palm et al. (2013)

Length [m]	33	**Cd_n**	2.5
Diameter [m]	0.002	**Cd_t**	0.5
Mass per meter length [kg/m]	0.0818	**Cm**	3.8
Total mass [kg]	2.7	**ρ_{water} [kg/m^3]**	1000
Wet weight per meter length [N/m]	0.699	**G_k [Pa]**	3E+05
EA [N]	1.0E+04	**G_c**	1
EI [N·m^2]	0	**G_μ**	0.3
ξ_A (damping ratio)[%]	3	**G_{vc} [m/s]**	0.01

The test is performed with two different periods of the movement of the disk: 3.5 and 1.25 s. Figure 3-19 shows the comparison between the simulations and the experimental results. Overall, the tension at the fairlead of the simulation fits the experimental data in both cases. In addition, the model also captures de loss of tension due to slack events. In the slack events, numerical instabilities can appear due to the loss of the continuity of tension between nodes, which produces snap loads. However, with the proposed

model there was no need of numerical damping to prevent these instabilities because the material damping was sufficient to avoid such instabilities. To appraise the latter, Figure 3-20 shows a cycle tension comparing the behavior of a chain with 0% and 3% of critical damping for the disk period of 1.25 s.

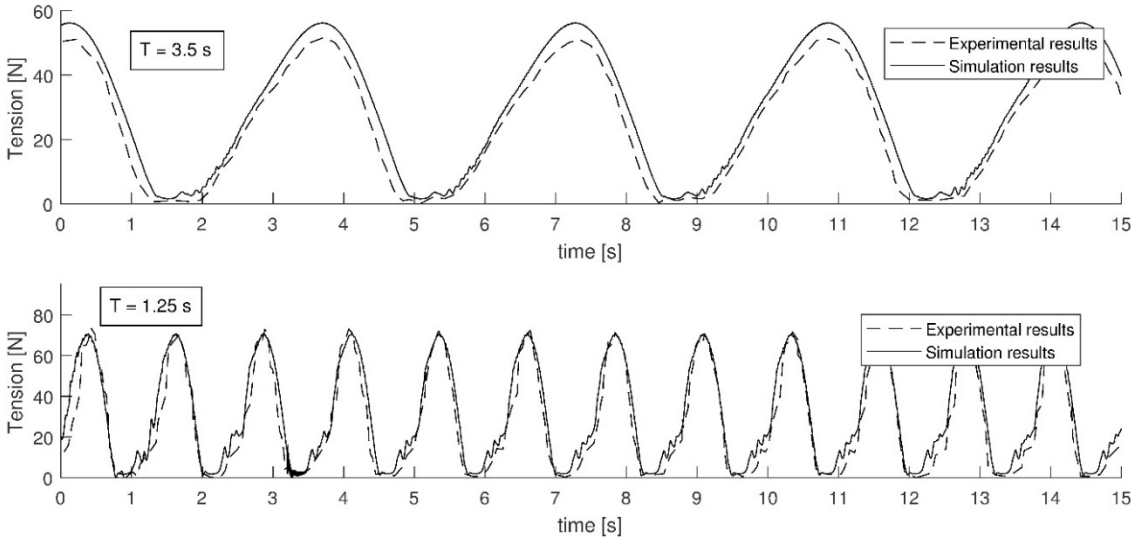

Figure 3-19: Experimental and simulation results for T = 3.5s (above) and T = 1.25s (below)

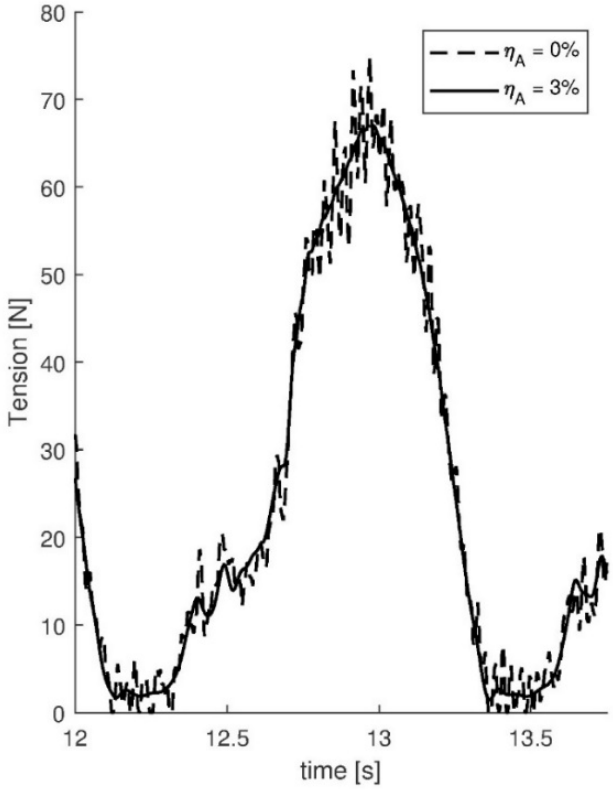

Figure 3-20: Tension cycle comparison for different values of damping ratio

3.11 CONCLUSIONS

An extension of the Garret rod model (Garrett, 1982) is developed including both the line extensibility and the axial and the bending rheological damping. Moreover, the model accounts for the bending and damping terms by a Lagrange multiplier. Extending the formulation of the Lagrange multiplier allows distinguishing between the bending and the extensional term in the constitutive equation and relating it with the equation of motion. In this way, the contributions of axial and bending damping are properly assessed and included in the formulation.

The damping of the rods, both the axial and the bending terms, are expressed using the Kelvin-Voigt rheological model. This model describes the viscoelasticity with a spring and a dashpot in parallel. The implementation of the rheological damping is introduced in both the equation of motion and the constitutive equation. Also the finite element implementation and the time integration schemes of the new model are fully described.

The proposed viscous model efficiently defines the behavior of visco-elastic materials but also can be used as an energy dissipation mechanism for other internal mechanical interactions of the dynamic system. In this case, the internal friction damping source of stranded cables has to be treated as an equivalent frequency damping.

The model is verified by means of three different tests: an axial free vibration through an initial extension of a cable, a bending free vibration through an initial pure bending state, and a post-buckling behavior of a column. The simulations produce results that coincide with the analytical ones, despite these examples are highly non-linear, appraising the capacity and the robustness of the model.

The validation of the model is based on the free fall experiment of a cable presented by Koh et al. (1999) and the experiment of a mooring chain with an imposed movement in one end presented by Lindahl (1985), with no tension episodes. The comparisons show a good agreement between the simulations and the existing experimental results, with a limited amount of iterations.

4 QUASI-DYNAMIC MOORING LINE MODEL

4.1 INTRODUCTION

The mooring dynamics have little impact on the platform dynamics and its final design. However, the mooring dynamics are a key factor to determine the actual tensions on the moorings and on the fairleads and its variation along its service life (Masciola et al., 2013; Robertson et al. , 2017). Moreover, to overcome these differences, main standards such as DNVGL (2015) require a larger safety factor on the mooring line design if quasi-static analyses are performed instead of dynamic ones. Furthermore, the mooring fatigue analysis has become a tough challenge due to the difficulties to assess the dynamics of mooring lines with a low computational cost that balances out the large number of simulations that have to be performed.

This chapter presents a novel methodology, named quasi-dynamic mooring model, which assess the mooring line tension at the fairleads and anchors with high accuracy with a computational cost equivalent to the quasi-static model. The model is proposed after a thorough study of the mooring dynamics and the

effects that modify the line tension while in motion. The study highlighted that the overall motion of a mooring line is mainly in vertical direction, either the motion of the fairlead is vertical or horizontal. Then, this motion produces also vertical inertia and hydrodynamic forces. These forces increase or decrease the distributed vertical resultant force (weight, inertia and hydro forces) of the line that leads to a variation of the tension at the fairlead different from the assumed by the static approach. Moreover, when the resultant forces tend to zero, the line gets slack. In this regard, Suhara et al. (1981) presented a method to predict slack process from the resultant of the external forces assessed at the mid-point of the suspended segment of the mooring line but only works for oscillatory constant cases and presented differences for the higher excitation ranges. The quasi-dynamic model is based on the same principium, but accounts for the variation of the vertical distributed forces along all the suspended segment to update the static tension. Accounting for all distributed forces not only produces a very good prediction of slack events but allow computing the tractions along the whole line.

The quasi-dynamic mooring model assumes that the shape of the line in each time step is the same as the static solution for the given fairlead position. Then, the quasi-dynamic tension is assessed from the static tension by multiplying it by the quasi-dynamic factor (k_{QD}), defined as the quotient of the resultant of the vertical forces over the suspended segment mooring line (the mooring weight the inertia force and the hydrodynamic forces) between the resultant of the distributed weight. However, the model does not consider the relative motion between nodes, internal vibration, neither transverse waves in the line.

The chapter is structured as follows. First, the analysis of the dynamics of a moving mooring line is presented which leads to the assumptions of the approach of the quasi-dynamic model. Second, the quasi-dynamic model approach and its implementation are presented. Third, the model is verified for a catenary line by comparing the simulations of a parametric study against a dynamic model. The parametric study consists in the analysis of the behavior of a mooring line with different line shapes, chain diameters and fairlead motion excitations. Fourth, the model is validated by comparing the simulation of the LC34 of the DeepCwind (Helder & Pietersma, 2013) experiments studied within the OC5 project (Robertson et al., 2017). Finally, the conclusions are presented which summarize the results obtained for the applicability of the quasi-dynamic model.

4.2 STUDY OF THE DNAMICS OF THE MOTION OF A MOORING LINE

The dynamics of the catenary mooring line depend on the fairlead motion which is the connection point between the line and the floating body. The fairlead position defines the catenary shape as a function of the line length and the distance to the anchor. If the fairlead is motionless, the catenary line tends to its minimum energy position, the static configuration. In this configuration, the unique external forces are the weight of the mooring line, the sea-bed contact force and the anchor and fairlead reactions. The weight per meter length is the vertical downward force that gives the catenary shape to the line in absence of bending stiffness. Then, any line subjected to a constant distributed vertical force will define a catenary shape.

If a mooring line moves from an equilibrium shape with low velocity, the line tends to follow the next static catenary shapes with the corresponding tension because the other external forces, the inertial and the hydrodynamic forces are negligible. However, the larger fairlead amplitudes or frequencies, the larger external forces for cyclic motions. These forces act on the line modifying the actual tension of the fairlead, shape and motion. If the external forces are mainly horizontally, the line will lose its catenary shape quickly, but if the acting loads are mainly vertical, the catenary equations would be a good approach.

In order to get the directions of the external forces, an approximation of the motion of the shape of the mooring line is assessed. The Figure 4-1 shows the maximum amplitudes of the vertical and horizontal components for all the points of a mooring line of 13.092 m length defined in Table 4-1 for a horizontal motion of the fairlead(left) and for a vertical motion of the fairlead (right). The figure shows clearly that the main motion of all the points of the line is in vertical direction. Moreover, the amplitude of the larger vertical motion is about 10 times larger than the larger horizontal motion, even for the horizontal fairlead motion case, unless at the fairlead when horizontal motion is applied.

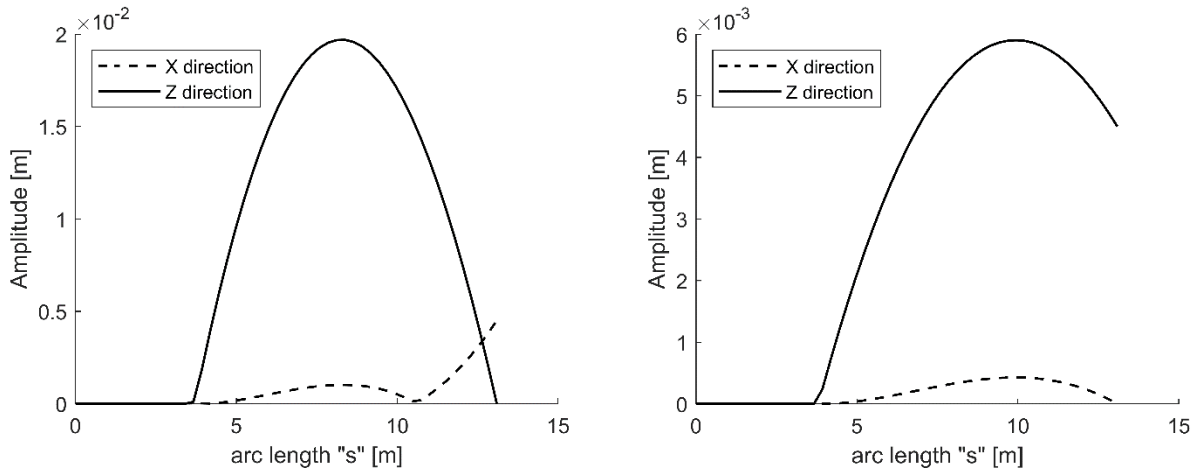

Figure 4-1: Quasi-static amplitude motion of a mooring line for a horizontal (left) and vertical (right) motion of the fairlead

To get deeply on the line dynamics, the velocity and the acceleration of the suspended segment of a mooring line are assessed for a cyclic horizontal motion with an amplitude of 0.0045 m. The properties of the mooring line are presented at Table 4-1, based on the mooring lines used for the parametric study of section 4.4. The velocity and accelerations are assessed at four critical time points of the motion of the fairlead (Figure 4-2). The time points 1, 3 and 1' are the maximum absolute velocity points, the time points 2 and 4 are the maximum absolute acceleration points. The velocity and accelerations results are assessed from a mooring line dynamic model presented in Chapter 3 and are compared with the theoretical value from the quasi-static model.

The Figure 4-3 shows the vector velocities and accelerations of the dynamic model along the suspended segment of the mooring line for each time point, (1, 2, 3 and 4). The velocity and acceleration vectors from the dynamic analysis are mainly in vertical direction, even if the motion of the fairlead is horizontal. The points closer to the fairlead present larger horizontal component, but their value is smaller than the vertical component of all the nodes.

Table 4-1: Mooring line parameters based on the parametric analysis of section 4.4

Position of Fairlead (x,y,z) [m]	(0,0,0)
Position of Anchor (x,y,z) [m]	(-12.922,0,-1.54)
Unstretched mooring line length [m]	13.092
Diameter [mm]	1.14
Wet Weight per meter length [N/m]	0.244
EA [N]	1.17E+05

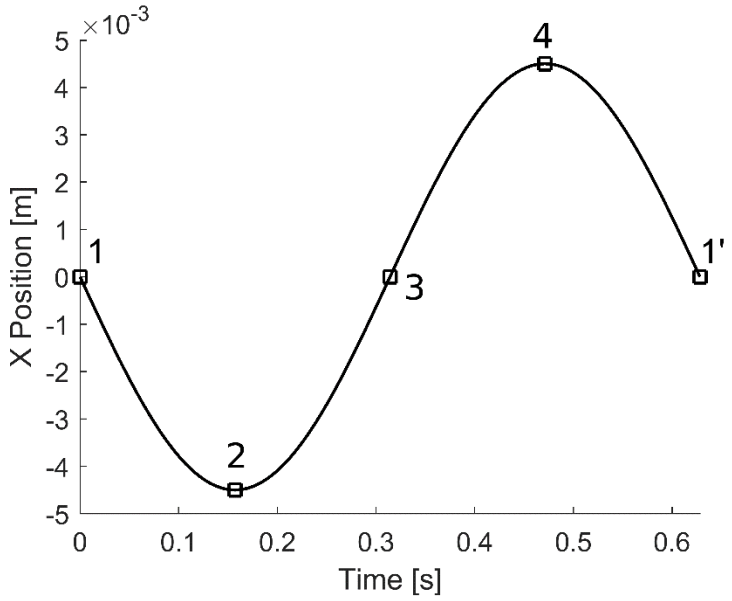

Figure 4-2:Fairlead position, velocity and acceleration assessment points

The Figure 4-3 also shows the vertical component of the velocity and the acceleration depending on the time point, which are compared with the quasi-static solution. The behavior of the quasi-static solution for the vertical component fits the dynamic one. The main differences between the simulations are found at the half of the suspended length, at the fairlead and at the touch point of the line with the seabed. These points present the maximum and minimum velocity and acceleration values. At these points are where the vertical forces differ most from the resultant mean vertical distributed load. Then, the catenary static solution is not fully fulfilled, with the largest differences at these points. Nevertheless, the mean values of the velocity and accelerations for the studied cases have little errors. The errors for the mean velocity are lower than 3.5 % while the error for the acceleration are lower than 7 %. These values support the use of the static catenary shape to approximate the velocities and accelerations of the line to assess the external forces.

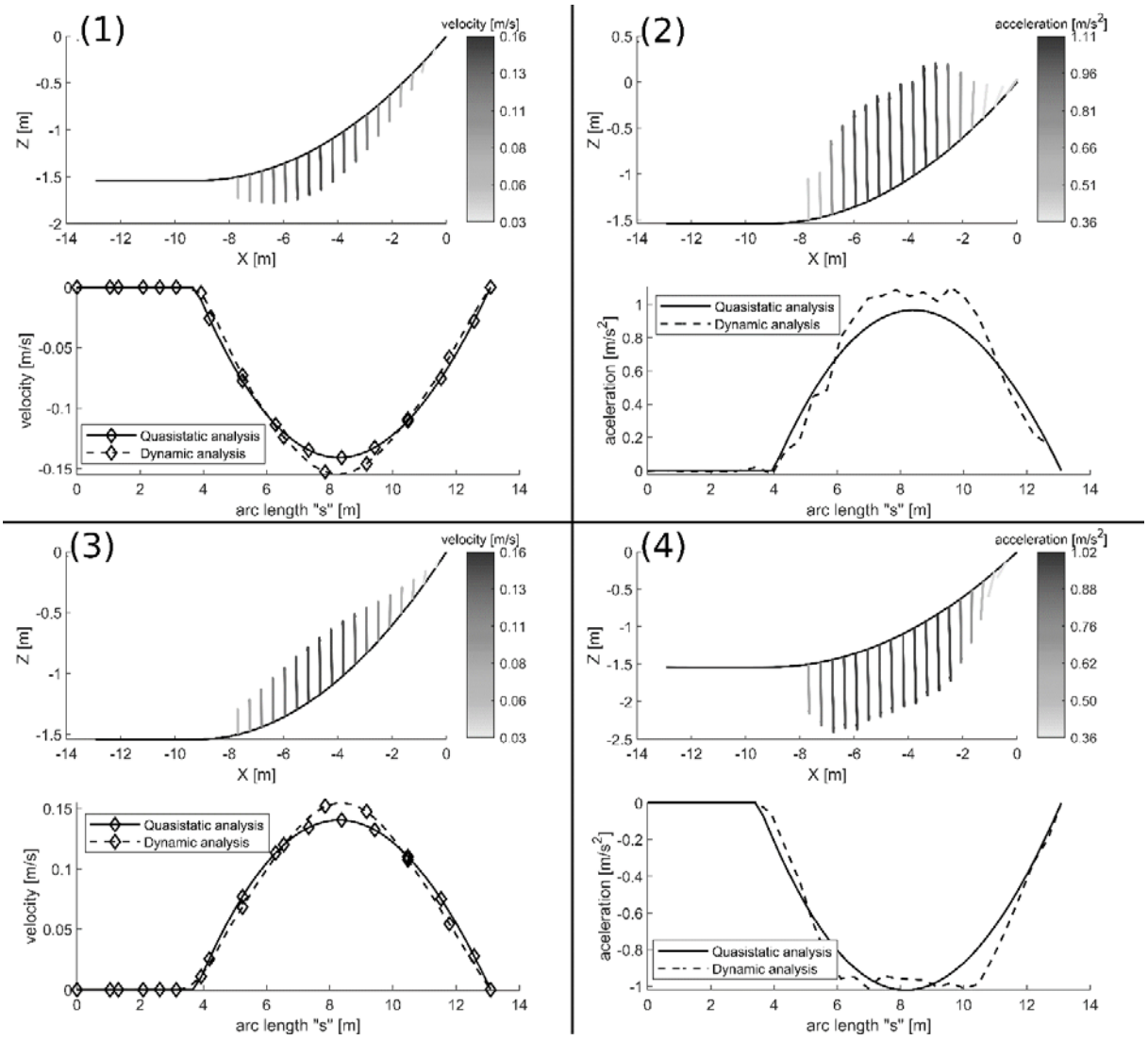

Figure 4-3: Quasi-static vs dynamic approach

4.3 MODEL APPROACH

The quasi-dynamic model approach assumes a quasi-static behavior of the mooring line by considering the catenary static shape of the line at each time step. The main difference with the quasi-static approach is that the distributed weight is updated to the apparent weight as a function of the approximation of the external forces. The apparent weight of the line is defined as the vertical distributed force of the resultant of the vertical components of the external forces (the weight, the inertial and the hydrodynamic forces).

In the proposed model, the apparent weight is applied as a quasi-dynamic factor (k_{QD}) multiplied by the static fairlead force, Eq.(4.1). Where the quasi-dynamic factor (k_{QD}) is assessed as the quotient of the resultant of the external forces in the vertical direction of the suspended segment between the weight of the suspended segment of the line as shown in Eq.(4.2). To sum up, first the static tension of the line is

assessed using the distributed weight of the line, and then is updated to the quasi-dynamic tension by multiplying it for the factor k_{QD}. When the resultant vertical force is equal or larger than zero, means that the line is in slack condition and the actual tension is zero, thus the coefficient k_{QD} may be larger or equal zero. In the following equations, the variables in bold mean they are vectors in the cartesian coordinates.

$$\boldsymbol{T}_{QD} = k_{QD}\boldsymbol{T}_S \tag{4.1}$$

$$k_{QD} = \frac{\int_{s_0}^{l}(\boldsymbol{f}_w + \boldsymbol{f}_{HD} - \boldsymbol{f}_I)\cdot \mathbf{k}\, ds}{\int_{s_0}^{l}\boldsymbol{f}_w \cdot \mathbf{k}\, ds} \geq 0 \tag{4.2}$$

Where k_{QD} is the quasi-dynamic factor, $\boldsymbol{T}_{QD}$ is the quasi-dynamic tension at the fairlead, $\boldsymbol{T}_S$ is the static tension at the fairlead, $\boldsymbol{f}_w$ is the distributed weight force per unit length, $\boldsymbol{f}_{HD}$is the distributed hydrodynamic force per unit length, $\boldsymbol{f}_I$ is the inertia force, $\mathbf{k}$ is the unitary vector in z direction, s is the arc-length parameter of the mooring line, s_0 is the arc-length value of the contact point between the mooring line and the sea-bed and l is the mooring line length

4.3.1 Model implementation

The model requires the computation of the apparent weight. To compute it, weight, drag and inertia forces are integrated along the line by using the composite Simpson's rule integration scheme. At each point, inner velocity and acceleration of the line itself during each time step are obtained from the previous static positions of the integration points. The external forces are assessed by the second law of Newton for the inertial force and by the Morison equation, Eq. (4.3), for the hydrodynamic forces as shown in Figure 4-4.

$$\begin{aligned}
\boldsymbol{f}_w &= -\omega\mathbf{k} \\
\boldsymbol{f}_I &= \rho_m A\, \mathbf{a}_i \\
\boldsymbol{f}_{HD} &= -\tfrac{1}{2}\rho_w C_{D,n} d|\mathbf{v}_i\cdot\mathbf{n}|(\mathbf{v}_i\cdot\mathbf{n})\mathbf{n} - \tfrac{\pi \mathrm{d}_{\mathrm{ap}}^2}{4}\rho_w C_{A,n}(\mathbf{a}_i\cdot\mathbf{n})
\end{aligned} \tag{4.3}$$

Where, ω is the wet weight per meter length of the line, ρ_m is the density of the mooring line material, A is the cross section of the mooring line, ρ_w is the density of the water, $C_{D,n}$ and $C_{A,n}$ are the normal drag and added mass coefficients, d is the nominal diameter of the mooring line, d_{ap} is the apparent diameter of the mooring line, $\boldsymbol{v}_i$ is the velocity of the *i-th* time step, $\boldsymbol{a}_i$ is the acceleration of the *i-th* time step, and $\mathbf{n}$ is the unitary normal vector of one point of the mooring line.

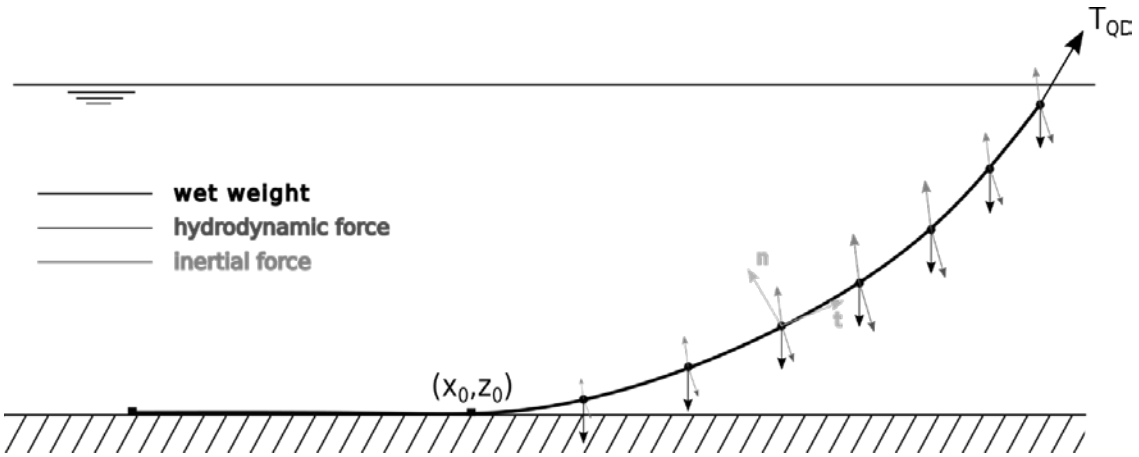

Figure 4-4: Mooring line discretized with dynamic forces

The procedure for assessing the quasi-dynamic forces is presented below:

1. The catenary equations (Faltinsen, 1990) are assessed for the updated fairlead position for the time step *"i"*, and the positions of the nodes of the mooring lines ($\boldsymbol{r_i}$) and the static tension ($\boldsymbol{T}_s$) are obtained.
2. The velocity($\boldsymbol{v_i}$) and acceleration ($\boldsymbol{a_i}$) of the suspended nodes are assessed by Eq. (4.4)
3. The external forces are evaluated
4. The quasi-dynamic factor $\left(k_{QS}\right)$ is assessed by Eq.(4.2)
5. The quasi-dynamic Tension is assessed by Eq. (4.1)
6. Compute next time step, and start again from 1

$$\mathbf{v}_i = \frac{d\boldsymbol{r}_\mathrm{i}}{dt} \cong \frac{\Delta \mathbf{r}_i}{\Delta t} = \frac{\boldsymbol{r_i} - \boldsymbol{r_{i-1}}}{\Delta t}$$
$$\mathbf{a}_i = \frac{d\mathbf{v}_i}{dt} \cong \frac{\Delta \mathbf{v}_\mathrm{i}}{\Delta t} = \frac{\boldsymbol{v_i} - \boldsymbol{v_{i-1}}}{\Delta t} \quad (4.4)$$

4.4 NUMERICAL VERIFICATION

A numerical verification is performed in order to obtain the applicability of the proposed approach. The numerical verification consists of comparing the proposed model against a validated dynamic model (Trubat & Molins, 2019). The comparison is set for the simulations of a parametric study composed for two different chain sections and three different line shapes. The simulations consist in a forced fairlead horizontal motion for different amplitudes and frequencies that ensures a combination of horizontal and vertical motion of the line.

4.4.1 Parametric study

The base of the mooring configuration for the verification test is got from the configuration of the experimental set test from Suhara et al. (1981). The variations of the mooring configurations for the

parametric study are based on the scaled DeepCwind mooring system configuration (Robertson et al., 2016), which has different shape and chain diameter.

The parametric study of the verification test is performed on six different mooring line configurations, composed by 2 chain diameters (D1 and D2), and 3 shapes (S1, S2 and S3). The sapes are obtained by varying the relation of the vertical span (h) versus the horizontal span from the seabed contact point (X_0) by modifying the anchor position. The mooring shape configurations have a h/X_0 relation of 0.17, 0.25, and 0.35 and are shown in Figure 4-5. The line characteristics with the varying parameters are presented in Table 4-3. The combination of the line shape and line dimaters are presented in Table 4-2, where the cases are named as CXY, where X is the number of the shape, and Y is the number of the chain diameter.

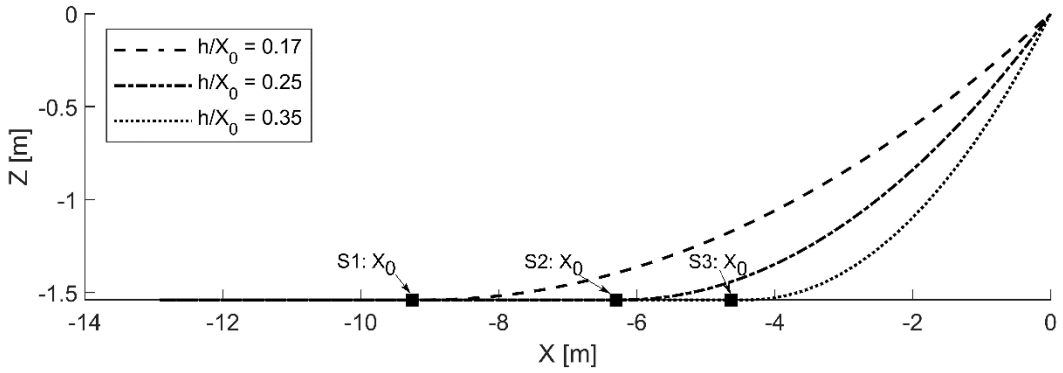

Figure 4-5: Catenary mooring shapes

Table 4-2: Parametric line shape-diameter combinations

	D1 = 1.14 mm	**D2 = 3.77 mm**
S1: h/ X_0 = 0.17	C11	C12
S2: h/ X_0 = 0.25	C21	C22
S3: h/ X_0 = 0.35	C31	C32

For each configuration five amplitudes and six dimensionless accelerations of the fairlead motion are combined to assess the line behaviour. The Table 4-4 shows the five amplitude ranges applied, equal for each mooring line shape. The amplitudes are defined from consistent ranges obtained from Suhara et al. (1981) experiments and DeepCwind tests from Robertson et al. (2017). Each amplitude is associated with the parameter Z_m, which is the maximum static vertical motion amplitude of the suspended segment of the line, shown in Table 4-4. The dimensionless acceleration (α) is defined in Eq. (4.5) from Suhara et al. (1981), and is set from 0.1 to 0.6 each 0.1. Then, the frequencies of the fairlead motion are obtained by Eq. (4.5). The range of the parameters used are common values in the reality. Assuming that the mooring analyzed is a 1:120 scaled line (about 180-200 m sea depth), the amplitudes range from 0.5 m to 4.3 m and the motion periods from 3 to 30 seconds in a real scale.

$$\alpha = \frac{\omega^2 Z_m}{g} \tag{4.5}$$

Table 4-3: Mooring line characteristics

Position of Fairlead (x,y,z) [m]		(0,0,0)
Depth of the Anchor		1.54
Anchor Horizontal Position [m]	**S1**	-12.922
	S2	-12.845
	S3	-12.75
Unstretched mooring line length [m]		13.092
Diameter [mm]	**D1**	1.14
	D2	3.77
Wet Weight per meter length[N/m]	**D1**	0.244
	D2	1.98
Mass per unit length [kg/m]	**D1**	0.028
	D2	0.23
Stiffness EA [N]	**D1**	1.17E+05
	D2	1.28E+06
Normal drag coefficient Cdn		2.5
Added mass coefficient Ca		1
Seabed stiffness [N/m^2]		1E+05
Number of nodes in the dynamic model		31
Integration points for the quasi-dynamic model		31
Time step [s]		0.0025

Table 4-4: Fairlead amplitudes for each catenary configuration

	Amplitude [m]	S1 Zm [m]	S2 Zm [m]	S3 Zm [m]
A1	0.0045	0.0280	0.0202	0.0140
A2	0.009	0.0560	0.0404	0.0280
A3	0.018	0.0840	0.0606	0.0420
A4	0.027	0.1399	0.1011	0.0700
A5	0.036	0.1959	0.1415	0.0980

4.4.2 Results and model comparison

The Figures from Figure 4-6 to Figure 4-11 show the comparison of one cycle tension range for the six different shape-diameter configurations (C11, C12, C21, C22, C31 and C32), for the each fairlead motion amplitude and for the dimensionless accelerations 0.1, 0.2, 0.4 and 0.6. Also, the static tension is shown for the smallest acceleration case. The quasi-dynamic approach fits the dynamic model with a high degree of accuracy for the low acceleration ranges. Moreover, it also predicts the slack phenomenon as seen in C11 for α values of 0.4 and 0.6. For larger dimensionless accelerations the tension presents differences less than 32.5 % on the peaks and the troughs, when the actual shape of the dynamics of the mooring lines differs to the static solution. Nevertheless, the overall shape and tension behavior is well fitted. Other differences that can be observed are the inner vibrations of the mooring line, which produce high frequency tension variations which are obviously not modelled in the quasi-dynamic approach.

An error analysis is performed in order to assess the differences between the dynamic model against the quasi-dynamic and the static models for all the simulations of verification. The error analysis consists in the assessment of the root-mean-square-error ($rmse$) of the fairlead tension for one cycle, and the assessment of the relative error (e) of the minimun and maximum peak tension at the fairlead.

The $rmse$ is computed for the relative error of the quasi-dynamic and the static solutions, which are compared with the initial static force. The initial static force is used to avoid large relative errors for very low tension ranges. The $rmse$ are presented in Eqs. (4.6) and (4.7) for the quasi dynamic and the for the static solutions respectively, where "i" is the assessed time step and "n" the total number of time steps assessed.

$$rmse_{QD} = \sqrt{\frac{1}{n}\sum_{i=1}^{n}\left(\frac{T_{dyn,i} - T_{QD,i}}{T_{S,0}}\right)^2} \tag{4.6}$$

$$rmse_{S} = \sqrt{\frac{1}{n}\sum_{i=1}^{n}\left(\frac{T_{dyn,i} - T_{S,i}}{T_{S,0}}\right)^2} \tag{4.7}$$

The results show the good accuracy of the quasi-dynamic model against the static solution in terms of both *rmse* (Figure 4-12) and the peak values (Figure 4-13). The $rmse$ of the quasi-dynamic model is less than 10 % for the 48 % of all simulations, and less than 20 % for the 84 % of all simulations. The error goes above 20 % in the case of some slack events and the maximum error in terms of rmse is 37.6 % (Figure 4-12-C11). The $rmse$ of the static solution is less than 10 % only for the 2 % of the simulations, and less than 20 % for the 18 % of the simulations.

The minum and maximum relative errors, Eqs. (4.8) and (4.9) respectively, are computed as the absolute value of the relative error of the local minimum and the local maximum, only for the quasi-dynamic model. The minimum relative error is assessed by comparing the error with the initial static tension and the maximum relative error is assessed by comparing with the dynamic local maximum tension.

$$e_{Tmin} = \left| \frac{T_{min,dyn} - T_{min}}{T_{0,static}} \right| \tag{4.8}$$

$$e_{Tmax} = \left| \frac{T_{max,dyn} - T_{max}}{T_{max,dyn}} \right| \tag{4.9}$$

The maximum and minimum relative errors of the quasi-dynamic model have an error less of the 10 % for the 67 % of the simulations, and an error less than 20 % for about the 90 % of the simulations. Again, the error goes above 20 % only in the case of large internal vibrations and the maximum error is 32.5 % (Figure 4-13-C12).

If the errors are compared depending on the mooring line shape, the lower error are for the shape S3, then the S2 and finally the S1. As was expected, the increase of the suspened length also increases the motion of the line and the external forces. The errors also increase with the amplitude of the failread motion or the dimensionless acceleration. Again, as the energy of the excitation increase, the dynamic effects increase and the response of the mooring line clearly differs from the static line shape.

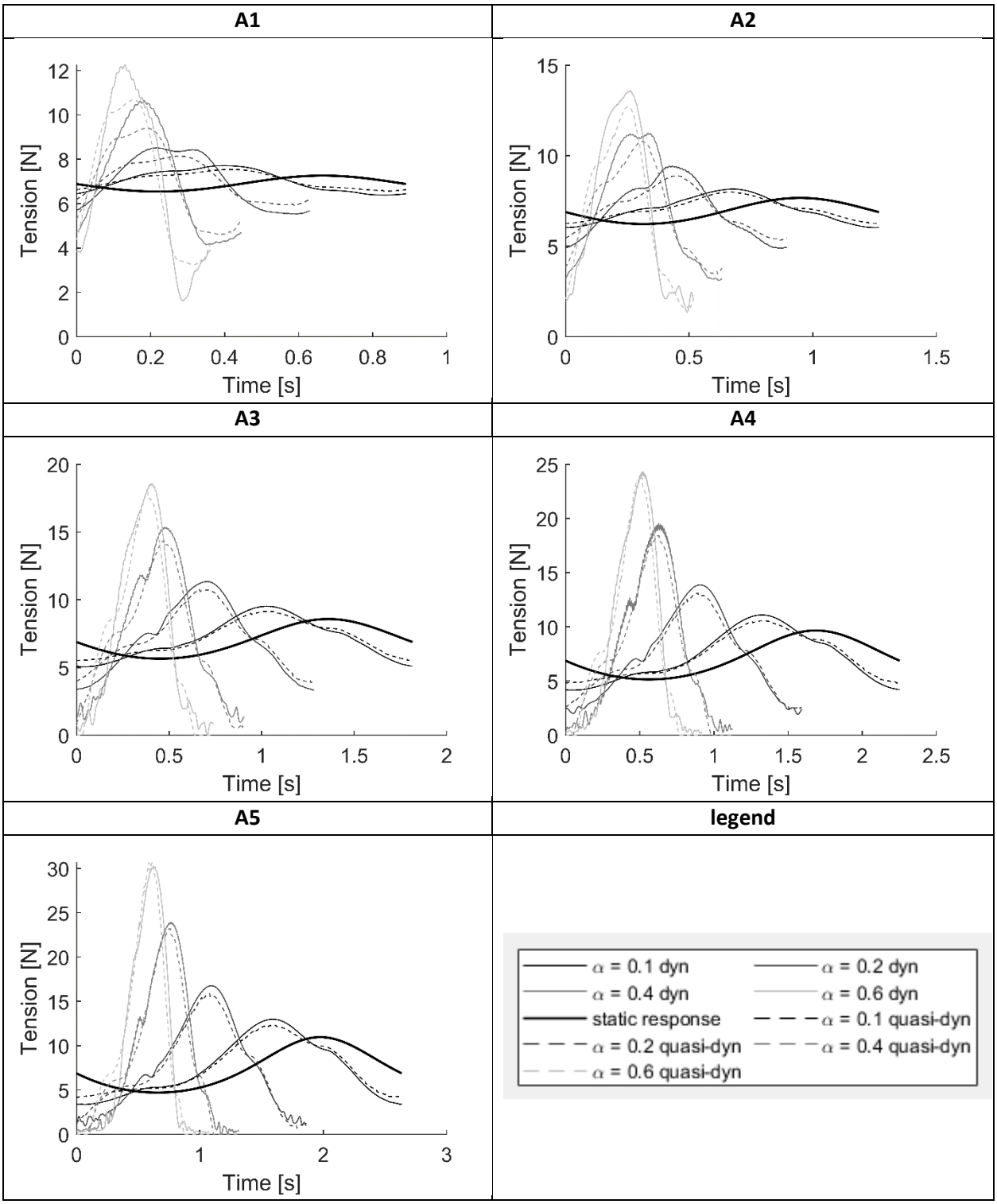

Figure 4-6: C11 verification simulations

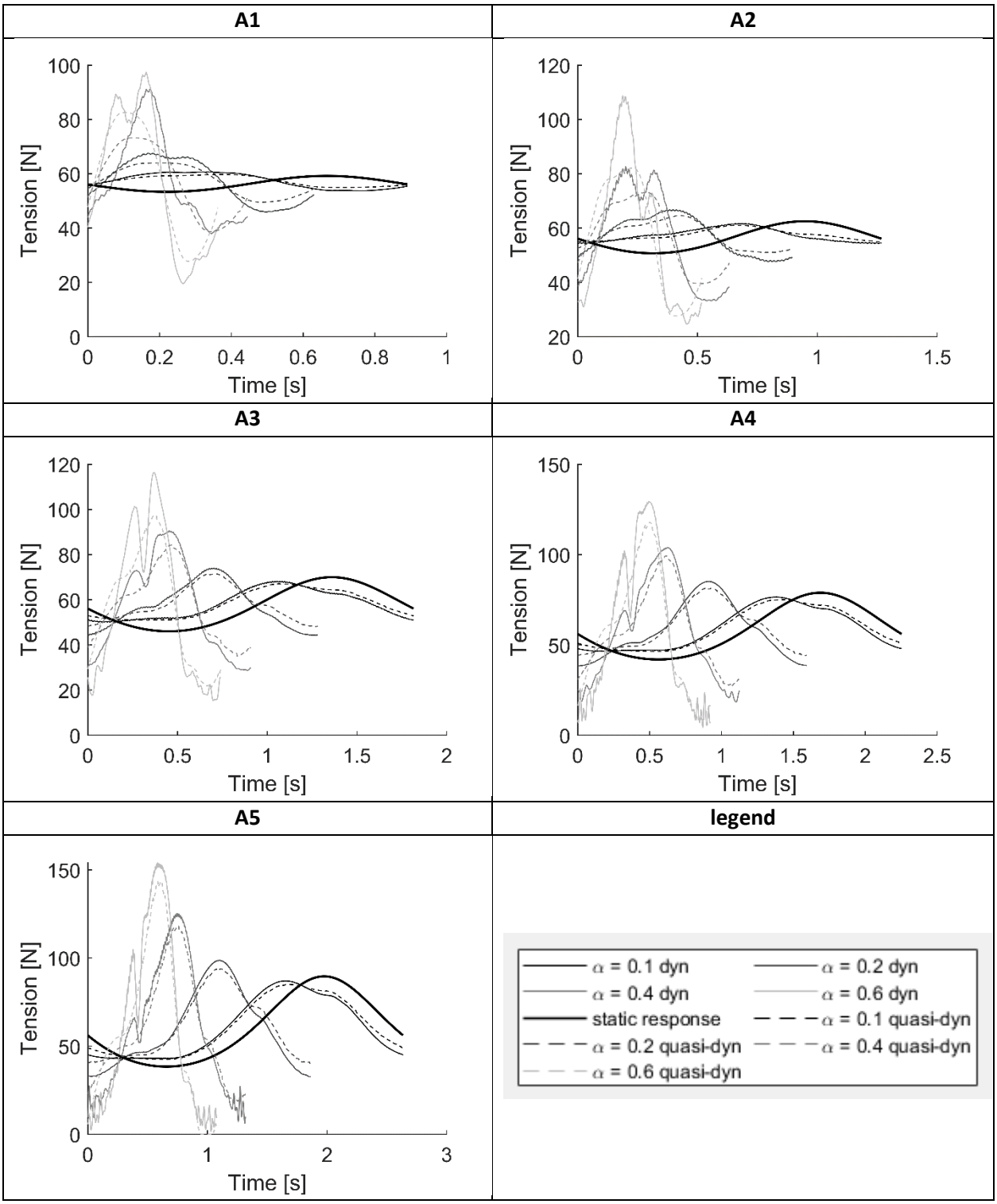

Figure 4-7: C12 verification simulations

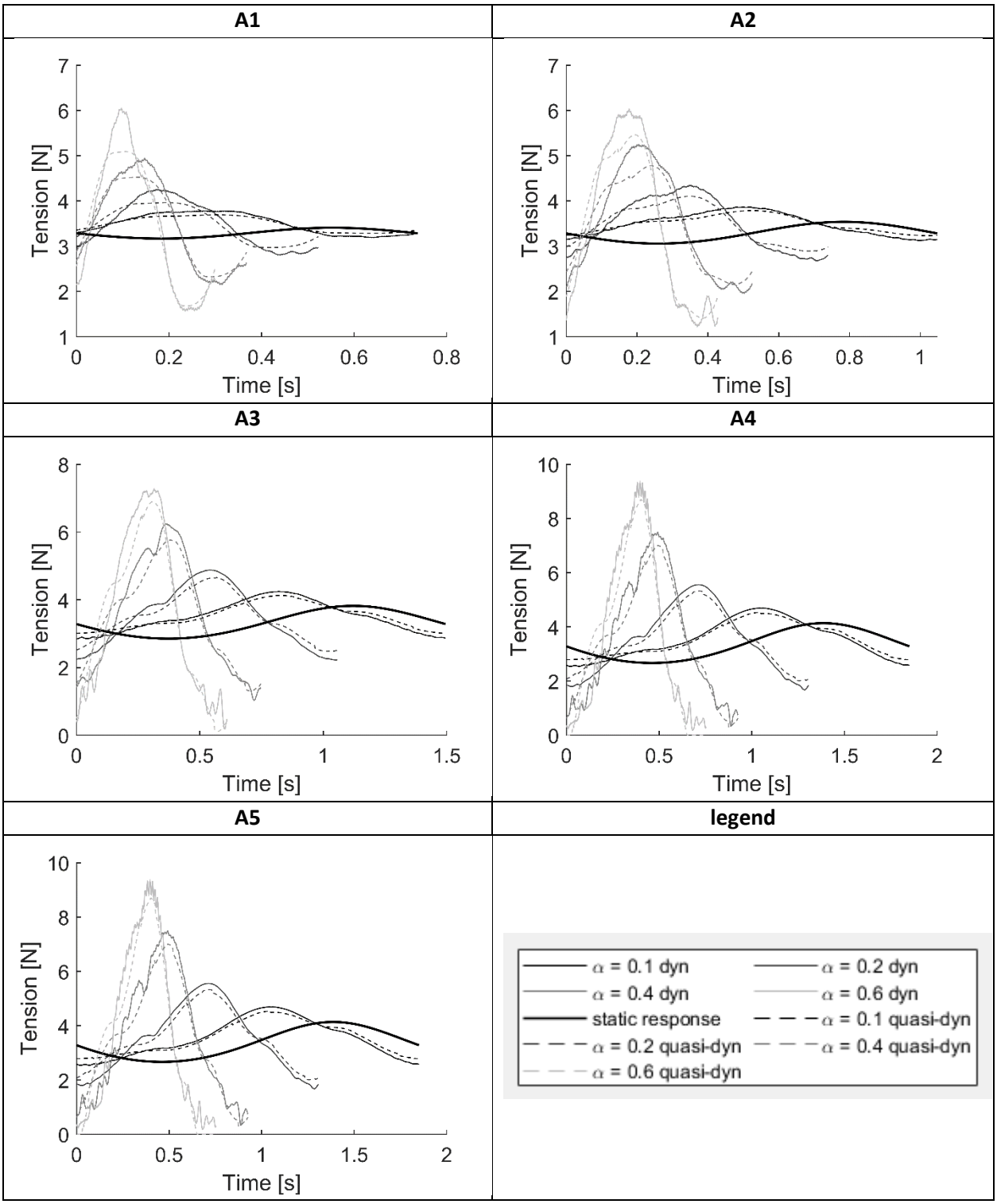

Figure 4-8: C21 verification simulations

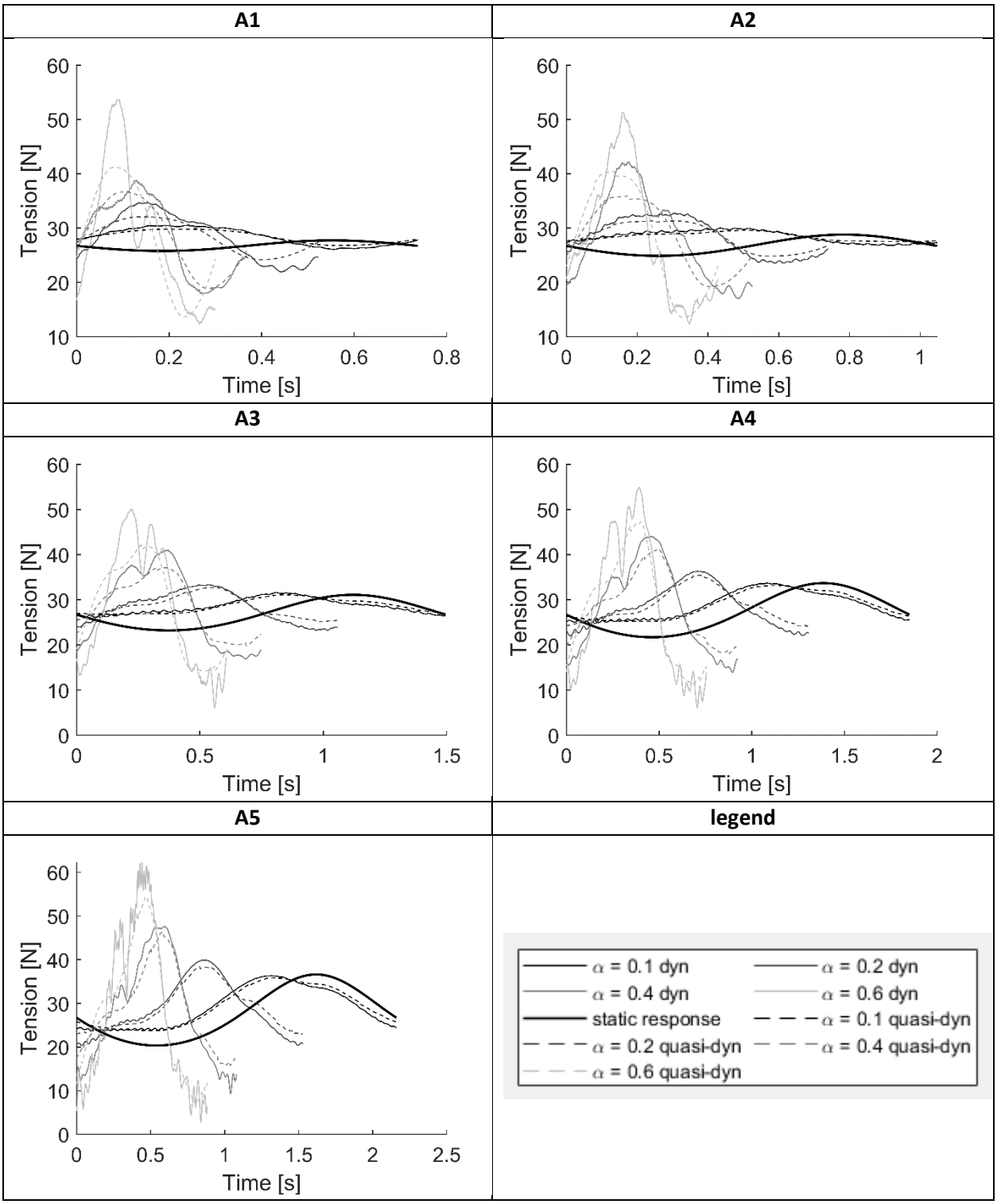

Figure 4-9: C22 verification simulations

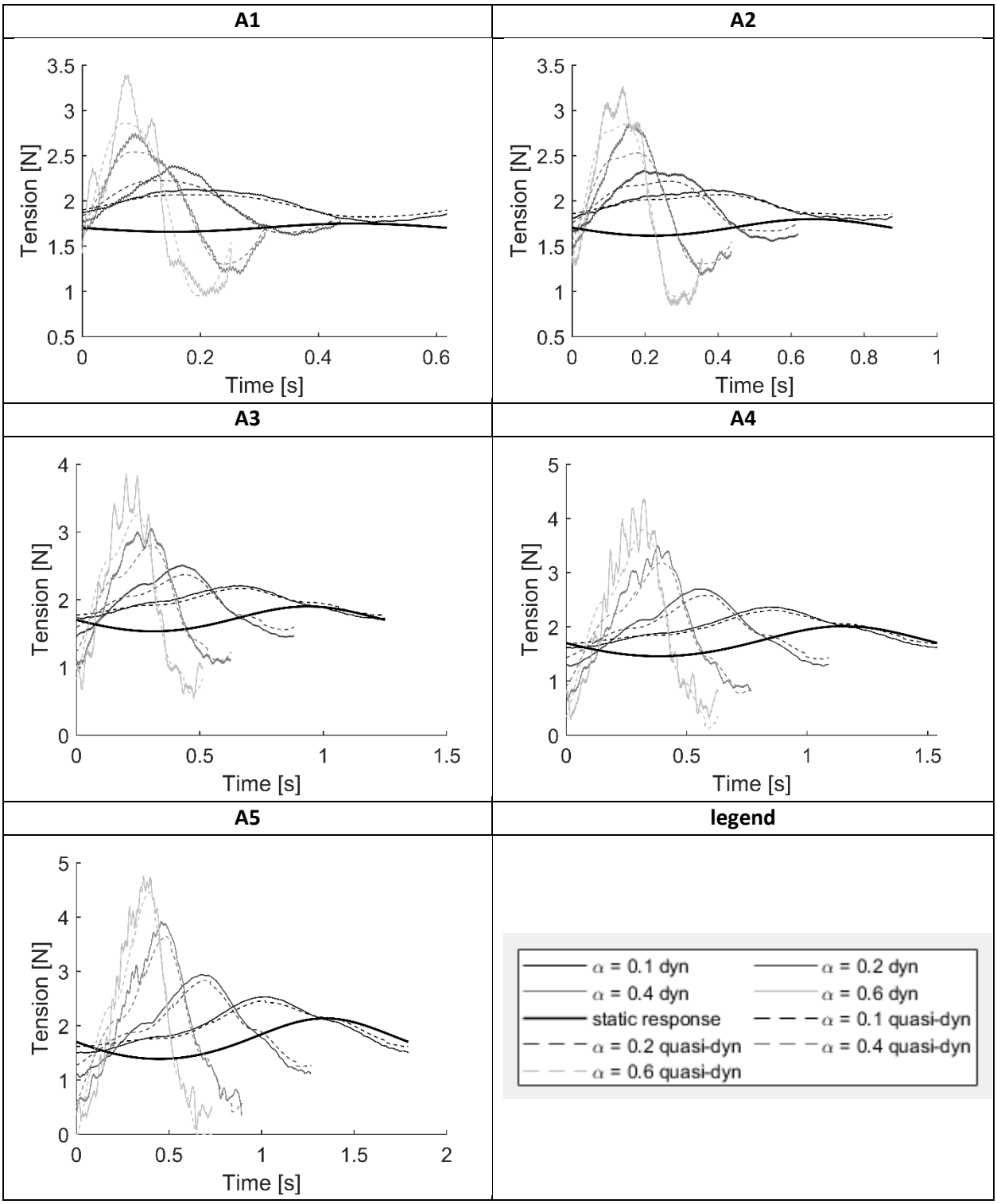

Figure 4-10: C31 verification simulations

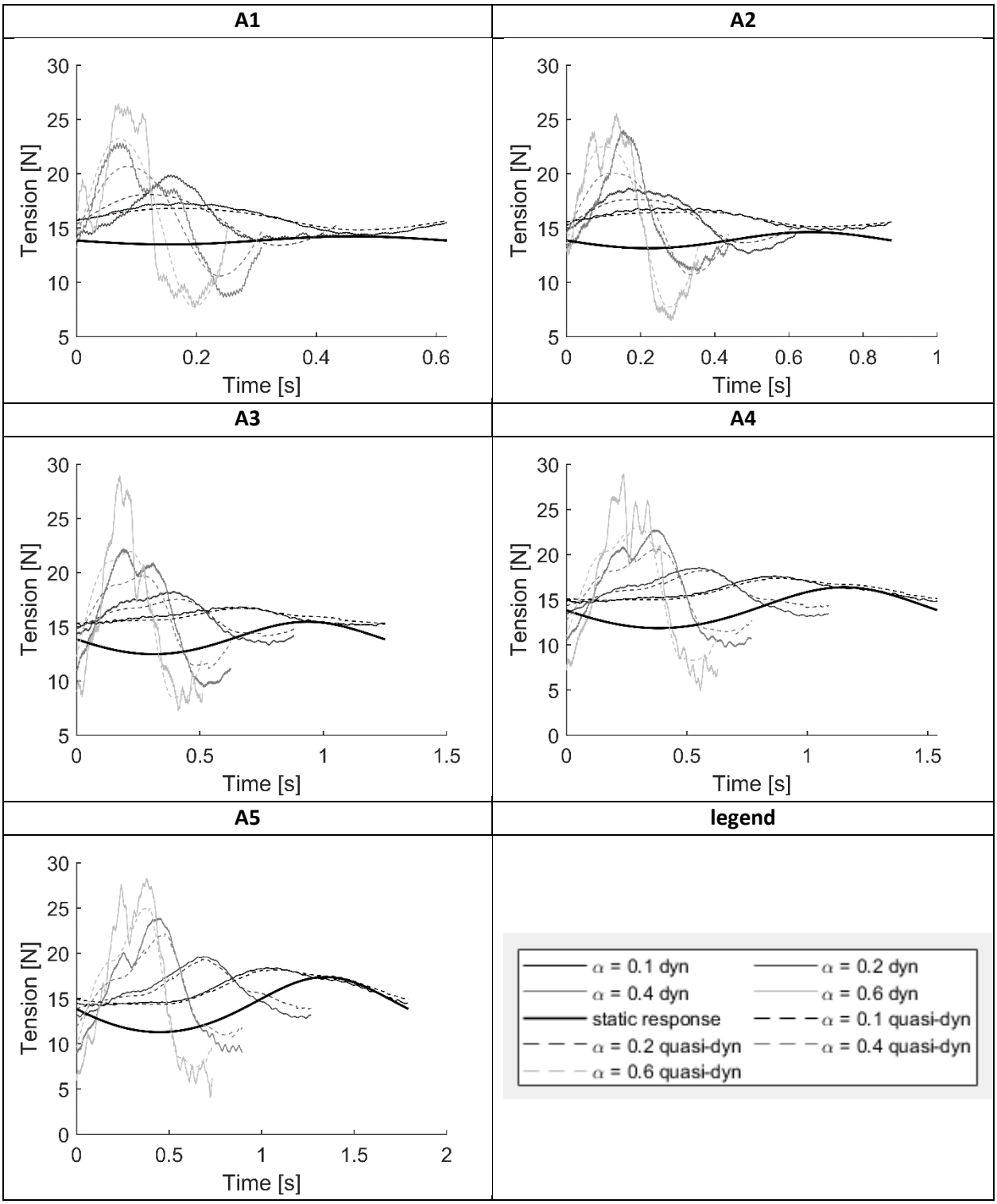

Figure 4-11: C32 verification simulations

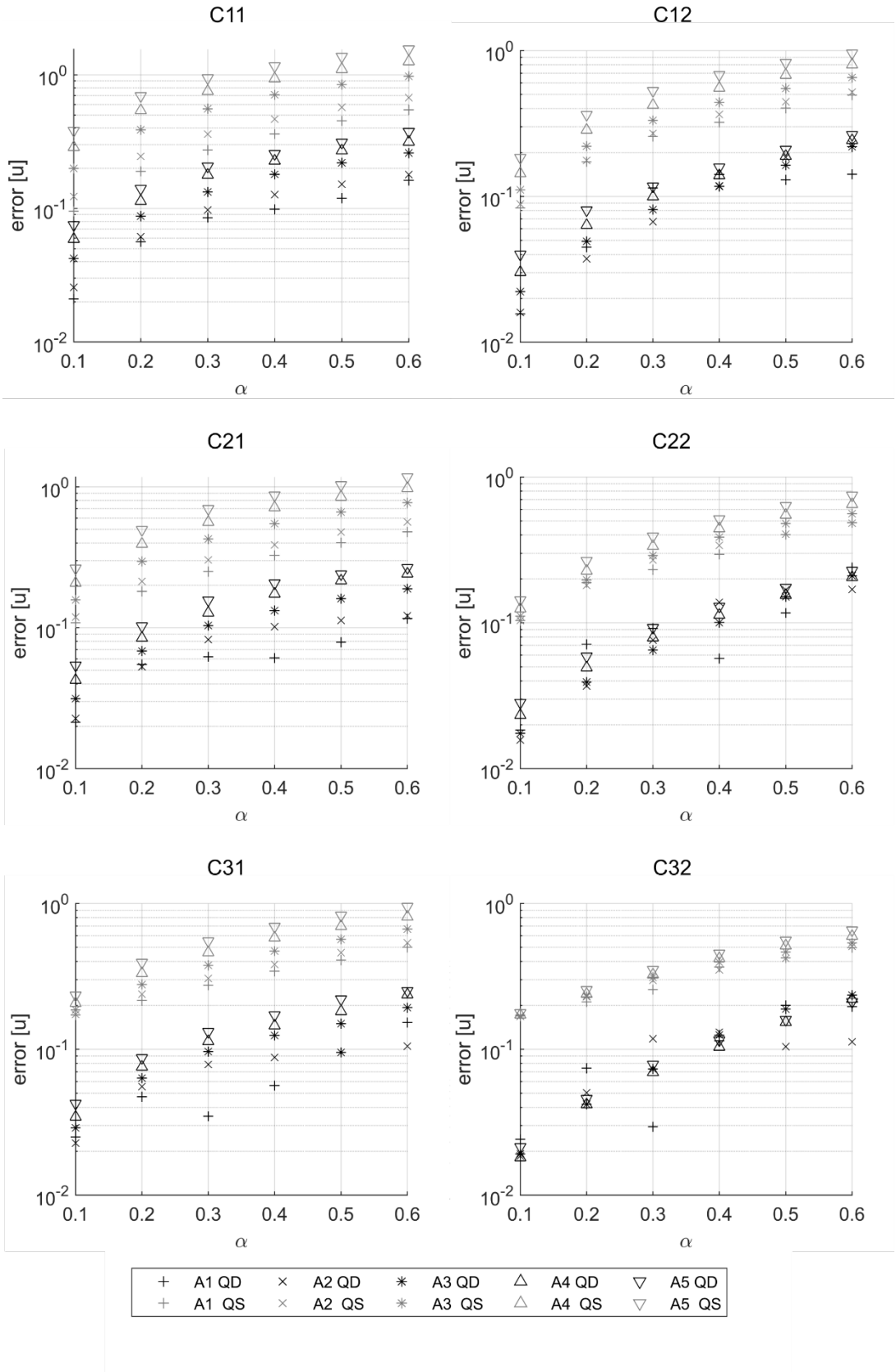

Figure 4-12: Root-mean-square-error

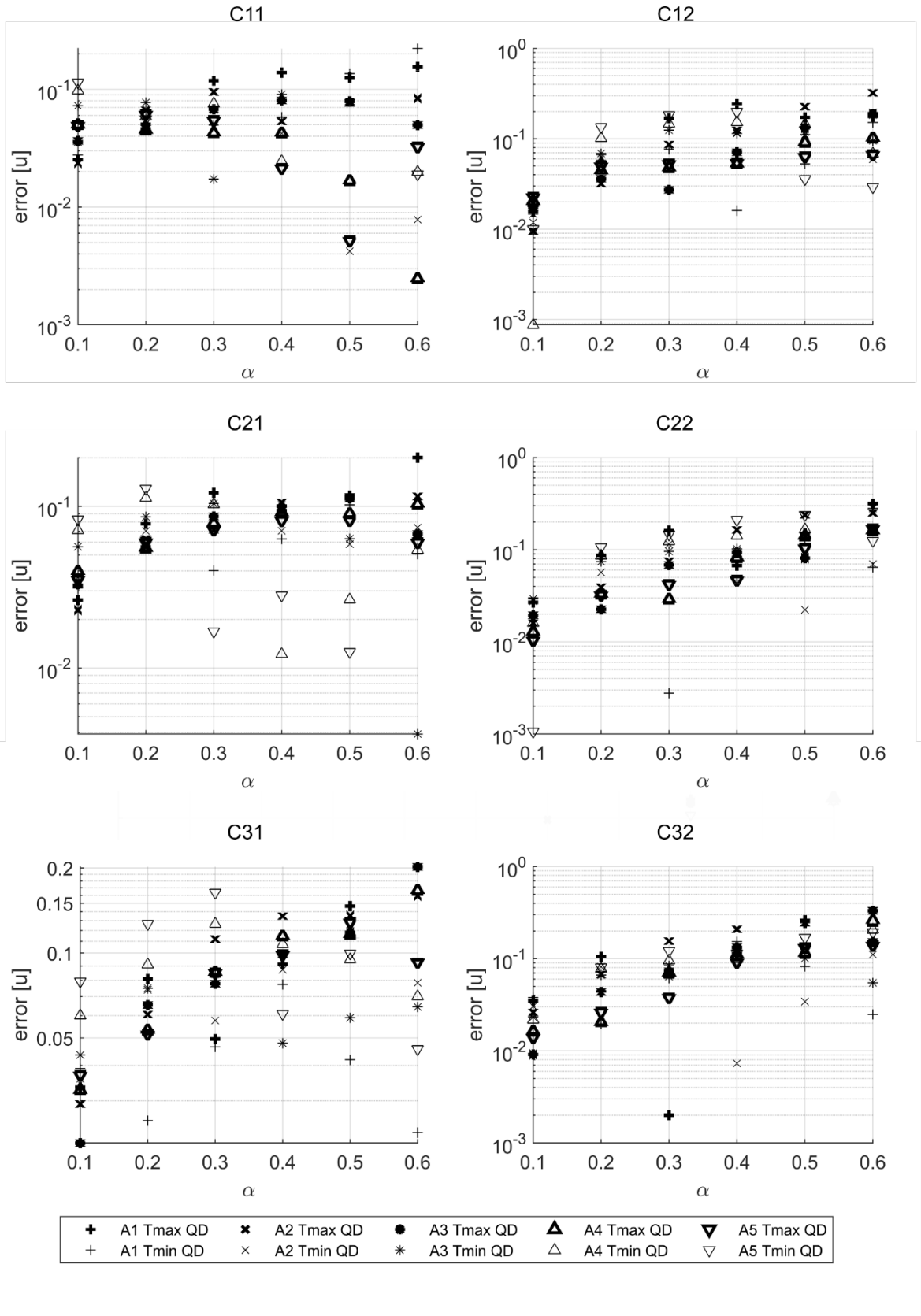

Figure 4-13: Minimum and maximum error comparison

4.5 MODEL VALIDATION

The main component for station keeping of the FOWTs is the mooring system. Although mooring systems are one of the most compliant components of a FOWT, the actual tension of the fairlead can change the motion of the platform, but normally is of little significance for the design loads of the platform. However, the actual tension of the mooring line is critical for the mooring design and can drive significant cost reductions if tension is reliably assessed.

The validation of the quasi-dynamic model is aimed to evidence the advantages, mostly improved accuracy and fast computation, of using of this approach in the coupled simulations for the mooring line design. The validation process is performed by comparing the experimental results of the DeepCwind platform with the numerical simulations using a mooring dynamic model, the quasi-dynamic proposed model and a quasi-static mooring model. The floating platform is composed by 4 steel vertical pontoons connected by trusses, from where the central tower is connected (Figure 4-14 left). The 1/50th scale model test of the concept was experimentally tested at the MARIN offshore basin (Helder & Pietersma, 2013; Goupee et al., 2014) with a specifically built scaled wind turbine for the wave tank (Ridder et al., 2014) (Figure 4-14 right). The experimental results were analyzed within the Phase II of the OC5 project Robertson et al. (2016).

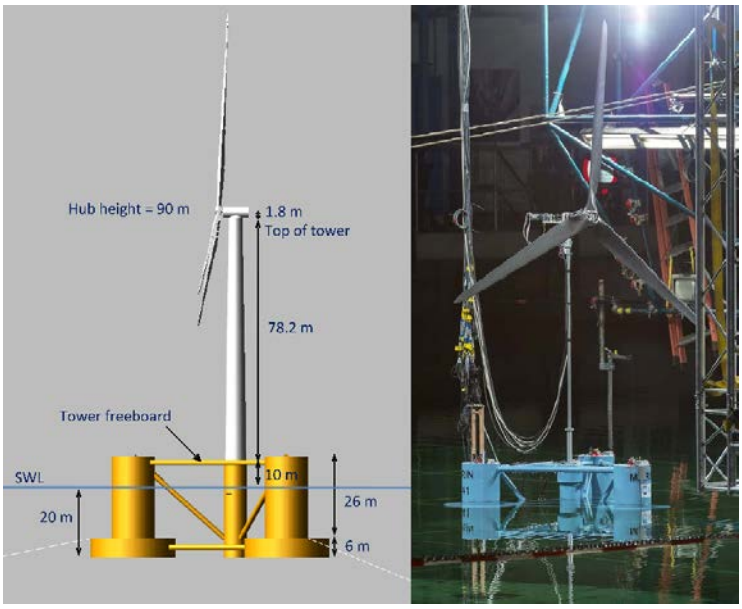

Figure 4-14:DeepCWind concept Robertson et al. (2014) *(left); OC5 task II Scale model* Helder & Pietersma (2013) *(right)*

The simulation performed corresponds to the load case LC34 of the OC5 Phase II project Robertson et al. (2017) where the platform is excited under the design wave state without wind in a 200 m sea depth. The simulation lasts 3 h to ensure a full development of the irregular wave train with a significant wave height (Hs) of 10.5 m and a peak period (Tp) of 14.3 s. The FloaWDyn model is the aero-hydro-servo-elastic tool used for the simulations. The FloaWDyn model is based on a co-rotational Finite Element Model (FEM)

developed at UPC Barcelona-Tech and is able to decouple the overall dynamics of the whole platform from its strains at each time step (Campos et al., 2017; Trubat et al. 2017).

4.5.1 DeepCwind FloaWDyn Model

The DeepCwind model used for the simulations is the model set up at UPC for the OC5 Phase II project (Trubat et al., 2017). The platform plus the tower is modeled using 112 beam elements with 138 nodes. The mooring system is discretized in 60 elements, with 20 elements per line, and a total number of 63 nodes for the dynamic and the quasi-dynamic models.

Structural properties

The FEM beam model was adjusted, by adding the required ballast mass and adding lumped masses and inertias to specific nodes, to fit the main physical properties of the tested model, converted to full scale values (Table 4-5).

Table 4-5: DeepCwind test model prototype physical properties [23]

Mass [kg]	1.3958E+7
Draft [m]	20
Displacement [m^3]	1.3917E+4
CM below SWL [m]	8.07
Roll inertia about CM [kg·m^2]	1.3947E+10
Pitch inertia about CM [kg·m^2]	1.5552E+10
Yaw inertia about CM [kg·m^2]	1.3692E+10

Hydrodynamic Properties

The hydrodynamic calibration of the model is set from the experimental free decay and regular wave tests. Since the hydrodynamics in the FloaWDyn code when using beam elements are based on the Morison's equation, the hydrodynamic coefficients to calibrate are the drag coefficients (C_d) and the inertia coefficients (C_m) for each structural member. Also, member added mass coefficients (C_a) are also adjusted to match with the total system added mass. The values used for the simulation are presented in Table 4-6.

The model takes also into account the diffraction of the waves by the MacCamy and Fuchs formulation (MacCamy & Fuchs, 1954; Trubat et al., 2018).

Table 4-6: FloaWDyn DeepCwind Hydrodynamic coefficients [27]

	C_d		C_a		C_m	
	Trans	**Long.**	**Trans**	**Long.**	**Trans**	**Long.**
Upper Columns	0.600	--	0.52	--	1.5	--
Lower Columns	0.600	1.60	0.52	0.67	1.5	0.65
Tower Column	0.663	0.80	0.51	0.88	1.5	0.87
Cross-brace members	0.564	--	0.50	--	1.5	--
Mooring elements	1.880	0.86	0.50	--	1.5	--

Mooring properties

The characteristics of the mooring lines are described in Table 4-7. The three mooring lines are considered identical, instead of using different values for each line, by averaging the characteristics of the three lines. The hydrodynamic terms used are the tangential and normal drag coefficients (C_{dt}, C_{dn}) , the added mass term (C_a) and the inertia term $C_m = 1 + C_a$. The axial damping ratio (ξ_A) is set to 3 %.

Table 4-7: Characteristics of DeepCwind mooring lines [23]

Number of mooring lines	3
Angle between adjacent lines	120º
Radius to anchors from centerline [m]	837.6
Radius to fairleads from centerline [m]	40.868
Unstretched mooring line length [m]	835.5
Volume-equivalent diameter [m]	0.1393
Mooring line mass density [kg/m]	125.6
Equiv. line extensional stiffness [N]	7.49E+8
Cdt	0.86
Cdn	1.875
Ca	0.5
ξ_A	3%
Number of nodes in the dynamic model	21
Integration points for the quasi-dynamic model	21

4.5.2 Results

4.5.2.1 Motion analysis comparison

The motions of the platform are compared by assessing the Power Spectral Density (PSD) of the surge, heave and pitch time data (Figure 4-15). The surge motion of the quasi-dynamic model produces values closer to the dynamic simulations than the quasi-static approach. However, the surge response is

underestimated in the low frequency region due to the tension hysteresis of the mooring line. The heave response of the quasi-dynamic and the dynamic models achieve a better response than the static one for the heave natural frequency at 0.057 Hz. The pitch response is quite similar for the three simulations but a close look reveals a more accurate results of the quasi-dynamic and dynamic simulations at the wave frequency range than the quasi-static response.

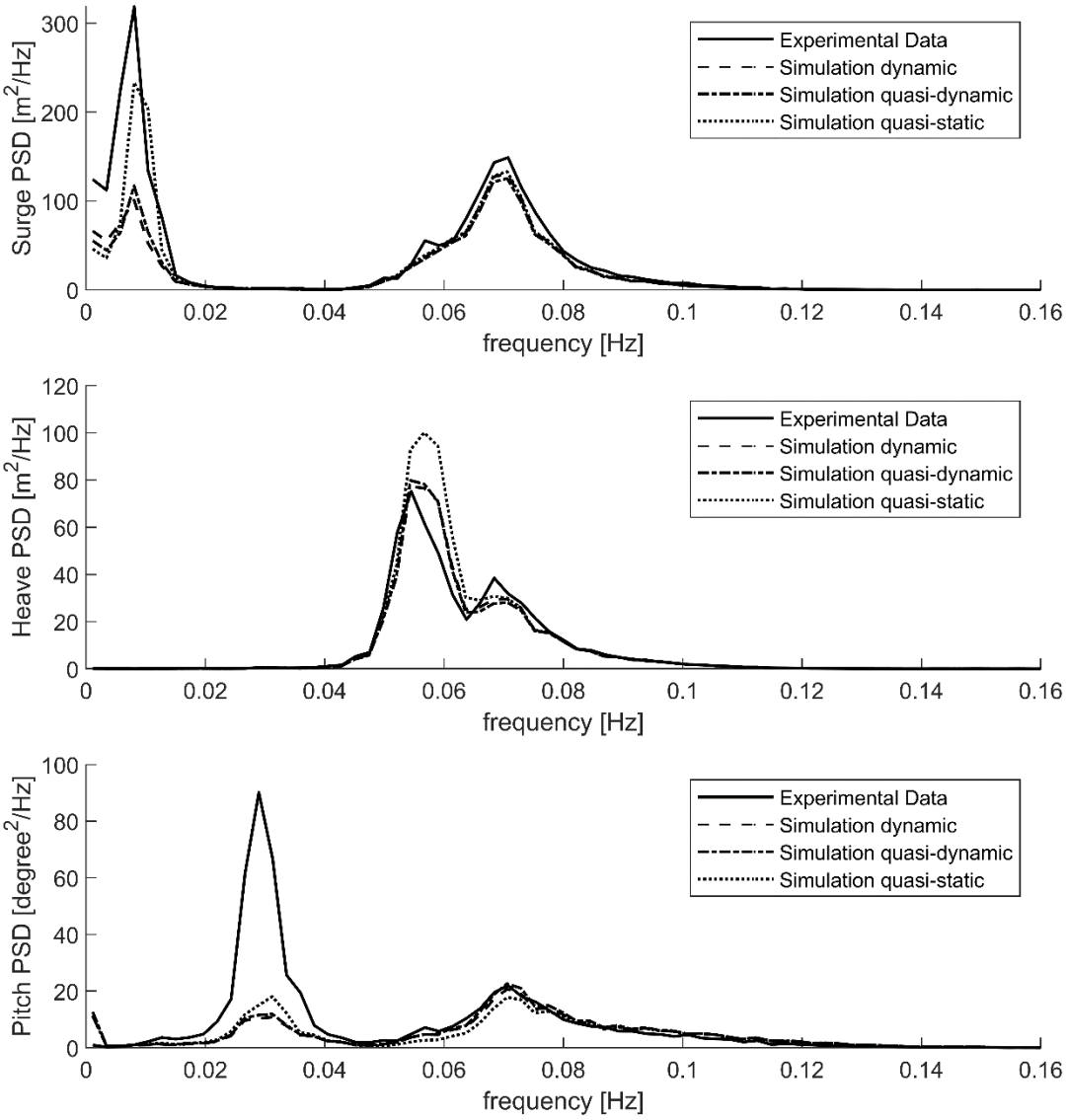

Figure 4-15: PSD the surge, heave and pitch motions of the DeepCwind

4.5.2.2 Tension analysis comparison

The analysis of the tension is performed in the frequency domain for the mooring lines 1 and 2 (Figure 4-17), and in the time domain for the tension of the mooring line 2 (Figure 4-16). Moreover, a study of the probability of exceedance of the minimum and maximum local tensions is performed and compared with the experimental data (Figure 4-18).

The Figure 4-16 shows that the quasi-dynamic model fits very well with the dynamic model and the experimental data. For the lower excitation amplitudes. At the time range of 8380-8420 seconds, three slack phenomena occur. The quasi-dynamic model catches the three phenomena perfectly. However, the dynamic mooring approach better fits the experimental results, particularly after the post slack episode. Nevertheless, if comparing with the quasi-static model, the results of the quasi-dynamic model are much better with a similar computational cost.

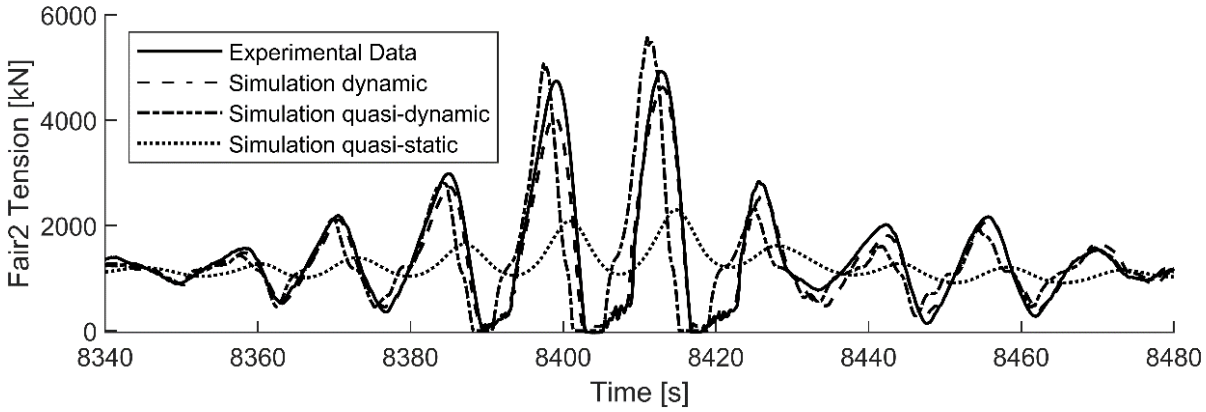

Figure 4-16: Tension time data of mooring line 2

The PSD of the tension at the fairlead of the mooring line 1 and 2 are presented in Figure 4-17. There is an evident improvement of the quasi-dynamic model compared with the quasi-static simulation in the wave frequency range. However, the energy of the PSD Tension in the wave frequency range of the quasi-dynamic model is smaller than the dynamic one. Moreover, the dynamic and the quasi-dynamic models underestimates the surge peak at low frequency range, probably due to an excess of damping produced by the lines.

The Figure 4-18 shows the probability of exceedance of the local minimum (left) and maximum (right) of the tension of the line 2. The probability of exceedance study shows clearly the underestimation of the tension computed by the quasi-static models. The quasi-dynamic model fits very well the minimum and maximum local values for the middle range values. However, the quasi-dynamic model overestimates the extreme tension values, both the minimums and maximums. This fact can be explained because these values occur at the slack phenomenon points when the mooring line reaches low tension values, and the quasi-dynamic model does not allow partial slackness of the mooring line. Moreover, after the slack events, the dynamics of the mooring line differs from the static shape, and the subsequent peaks are overestimated too.

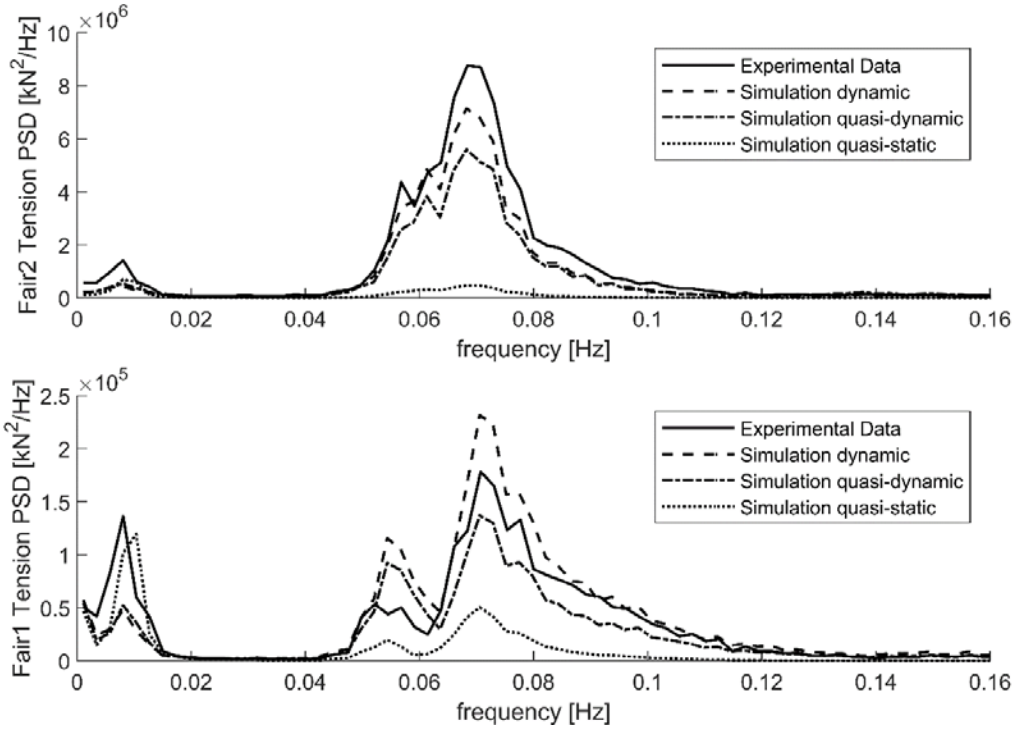

Figure 4-17:PSD of the tension at fairlead of the mooring line 1(up) and line 2 (down)

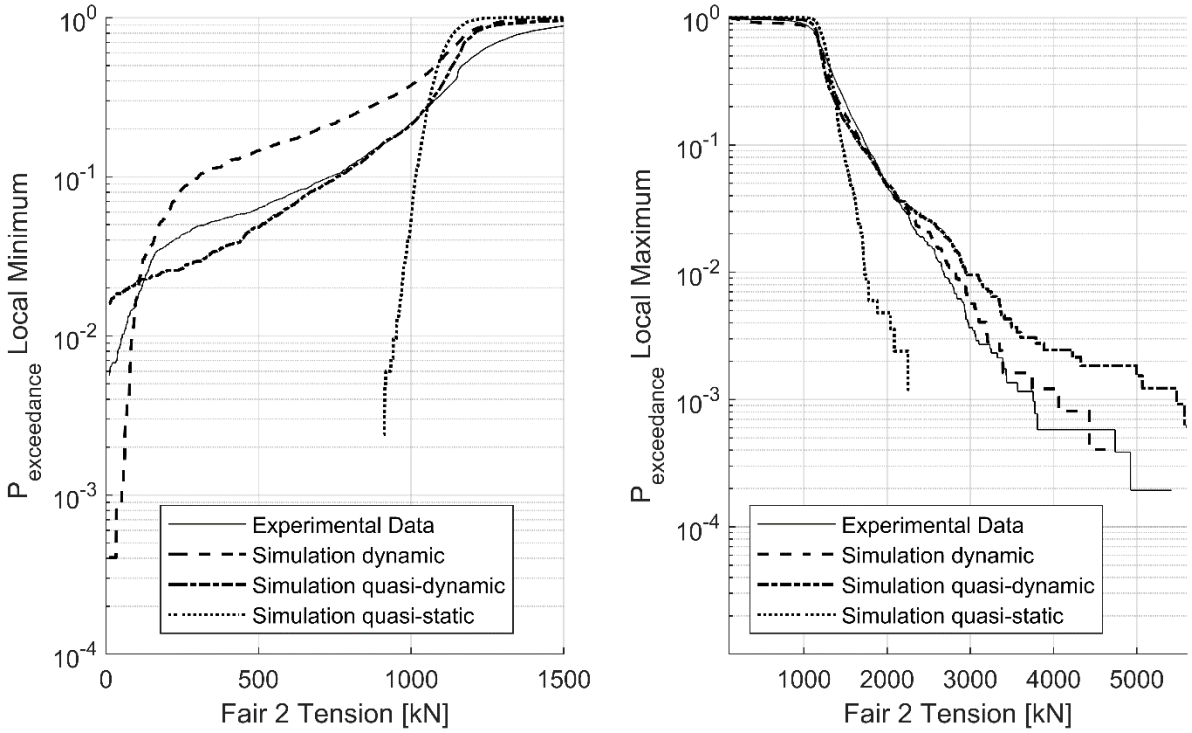

Figure 4-18: Probability of exceedance of the local minimum tension (left) and maximum tension (right) at the fairlead of the mooring line 2

4.6 CONCLUSIONS

In this chapter, the quasi-dynamic mooring model is presented, verified through a parametric study and validated by comparing it with experimental results.

The quasi-dynamic mooring model is based on the static catenary equation, where the solution is improved by applying a quasi-dynamic factor to the static tension. The quasi-dynamic factor accounts for the distributed weight, the inertial forces and the hydrodynamic forces over the suspended length of the line. The computation cost of the quasi-dynamic model is equivalent to the quasi-static ones, but is much less expensive than any dynamic mooring model.

The model fits very well the actual response of a mooring line for low and moderate fairlead excitation ranges with an error below the 10 % compared with the dynamic solution. Moreover, the model is capable to predict the slack phenomenon. However, the actual behavior can be slightly different, for example the partial slack phenomenon of the line is not captured as well as its inner vibration.

The application of the proposed model is verified for a multiple motion ranges for six different mooring line configurations. The verification is performed by a parametric study varying the amplitude and the frequency of the motion. The results of the study show a clear improvement of the model against the static solution with a root mean square tension error compared with the dynamic solution below the 20 % for the 84 % of the simulations, whereas the quasi-static model presents an error below the 20 % only for the 18 % of the simulations.

The quasi-dynamic model is validated through the simulation of the DeepCWind semisubmersible platform and compared against the experimental data. The simulation results are also compared with the simulations of the platform with a dynamic mooring model and a quasi-static mooring model. The results show a very good improvement against the quasi-static approach, but, as could be expected, the proposed model is less accurate than the dynamic model. The model fits the mooring tension for low-middle motion ranges but overestimates the slack-snap phenomenon. Then, if slack-snap phenomenon are limited, the method becomes an efficient alternative to produce comprehensive fatigue assessments of the mooring lines.

5 WAVE HYDRODYNAMIC FORCES OVER MOORING LINES ON FLOATING OFFSHORE WIND TURBINES

5.1 INTRODUCTION

This chapter aims to highlight the influence of the wave hydrodynamic forces over catenary mooring lines for FOWTs. This influence is studied through the chapter by the analyses of different cases and comparing the results with and without the waves forces on the mooring lines. The selected cases for the study are: (1) an experiment performed on a cylindrical platform attached to a catenary line, (2) the DeepCWind platform and (3) the OC3-Hywind platform. The influence of the wave hydrodynamics is analyzed in terms of the variation of the tension in the mooring line at the fairlead, in terms of the motion of the platforms and in the loads on the tower base. In all cases, the dynamic mooring model presented in chapter 3 is used.

The simulations of the experiment of a cylindrical platform connected to a longitudinal catenary mooring line subjected to a regular wave train show a non-despicable tension increment at the fairleads due to the wave loads over the mooring lines. The experiment is compared with and without the hydrodynamic

forces of the waves over the mooring lines. An increment of 6 % of the tension at the fairlead is obtained if the wave loads are applied on the line. In addition, parametric studies are performed to assess the influence of varying the ratio between the horizontal and the vertical span of the mooring and of varying the diameter and weight of the mooring line.

In order to assess the effects of the wave forces over the catenary mooring system of a FOWT, two different platforms are studied under severe and normal sea states. The FOWTs studied are the well-known DeepCWind semisubmersible platform within the OC5 project characteristics (Robertson et al., 2016) and the Marin experiments (Helder & Pietersma, 2013), and OC3 Hywind Spar platform (Jonkman, 2010). Both platforms are simulated with and without adding the wave hydrodynamic force on the mooring lines for comparison purpose. The DeepCWind platform is simulated under the LC3.4 of the OC5 project with the severe sea state and without wind. The simulation results are compared with the test data and the contribution of the increment of tension to the lines due to the wave's force is assessed. The OC3 Hywind platform is studied in a parametric study in order to analyze the importance of the depth of the fairlead position, as in deep seas, wave loads decrease exponentially. The parametric study is performed by applying four different fairlead depths, equidistantly from the actual theoretical position up to the mean sea level. The OC3 Hywind is simulated under a normal and a severe sea states, with a dynamic wind in power production state.

The chapter is structured as follows. First, the experimental test is used to validate the model and assess the contribution of the wave loads on the mooring lines. Second, the simulations models and results of the DeepCWind and OC3 Hywind Spar are presented. Finally, the conclusions summarize the obtained results from the simulations and expose the influence of the wave loads on the mooring lines.

5.2 VALIDATION OF WAVE HYDRODYNAMIC INFLUENCE

In order to assess the importance of the wave hydrodynamics over the mooring lines, a comparison between an experimental test and the simulations with and without the wave hydrodynamics on the lines is performed. In addition, the simulation is used for the validation of the model.

The experiment was presented by Paredes et al. (2013) and its setup consists in a cylindrical floater attached to one mooring line facing the wave generator and a spring attached at the other side. The experiment measures the motions of the floater excited by a regular wave train and the tension of the mooring line. The Figure 5-1 shows a sketch of the test and its main dimensions.

The buoy is defined by 560 elements to solve the Potential Flow hydrodynamics. In the dynamic analysis the buoy is treated as a rigid body, then there are 6 DOF, three for the translations and three for the rotations. The mooring line is defined by 25 elements and 26 nodes.

The regular wave train generated has a height of 0.1 meters and a period of 1.4 s. The main parameters of the floating platform, the mooring line and the spring are presented in Table 5-1 from Paredes et al. (2013). It is assumed that the scale of the experiment is 1/100, thus a regular wave of 10 m height and 14 s period, with a depth of about 100 m and a longitudinal span of the mooring line of 559m are considered.

Table 5-1: Experimental data extracted from Paredes et al. (2013)

WAVE TANK		**MOORING LINES**	
Scale	1:1	**Horizontal span [m]**	5.59
Depth [m]	1.11	**Length [m]**	5.88
TESTS		**Apparent Diameter [mm]**	2.7
H [m]	0.1	**Submerged weight per unit length [N/m]**	0.382
T [s]	1.4	**Dry weight per unit length [N/m]**	0.436
FLOATER		**Axial Stiffness (EA) [N]**	10000
Diameter [m]	0.5	**Cdt**	0.5
Height [m]	0.4	**Cdn**	2.5
CM [m] (from center of floatation)	-0.072	**Ca**	0.4129
Draft [m]	0.18	**SPRING**	
Mass [kg]	35.28	**K [N/m]**	5.36
Inertia [kg·m^2] (around center of buoyancy)	0.852	**X_0 [m]**	1.3
		T_0 [N]	1.3

The results in Figure 5-2 show good agreement between the simulations and the experimental data. The heave and the pitch motion of the buoy are the best fitted results. For the surge motion, the experimental data shows a larger mean offset than the simulations, as a possible consecuence of the mean drift force due to second order wave force. Nevertheless, the tension of the fairlead is well captured. The experimental data show a larger mooring line peak tension. Also, the trough region is deeper for the experimental data. Results including wave hydrodynamics on the moorings better adjust to the experimental peak tension at the fairlead.

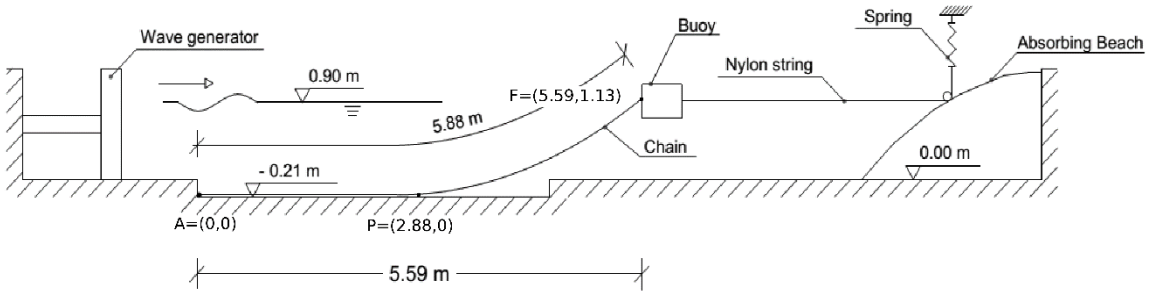

Figure 5-1: Sketch of the experimental setup developed by Paredes et al. (2013).

The platform dynamics are slightly influenced by the wave loads on the mooring lines. Very small varitions can be observed in surge, heave and pitch motions due to the inclusion of the wave forces on mooring lines. However, noticeable differences appear in the tension force at the fairlead as is shown in Figure 5-3 if waves forces on mooring line are considered or not. If wave forces are considered, the trough of the tension is wider causing the tension to increase substantially. Moreover, the maximum peak tension at the fairlead increases of 6 %. This results show the importance to inquire at the effect of wave hyrodynamics over the mooring lines. In the experimental setup, the mooring line presents a ratio about 2.5 between the horizontal projection of the suspended length and the fairlead depth, as shown in Figure 5-1. Moreover, mooring lines can also present larger ratios between the suspended horizontal and vertical span and, thus, wave hydrodynamics could have a more significant influence because the most energetic wave hydrodynamics are located near the wave surface.

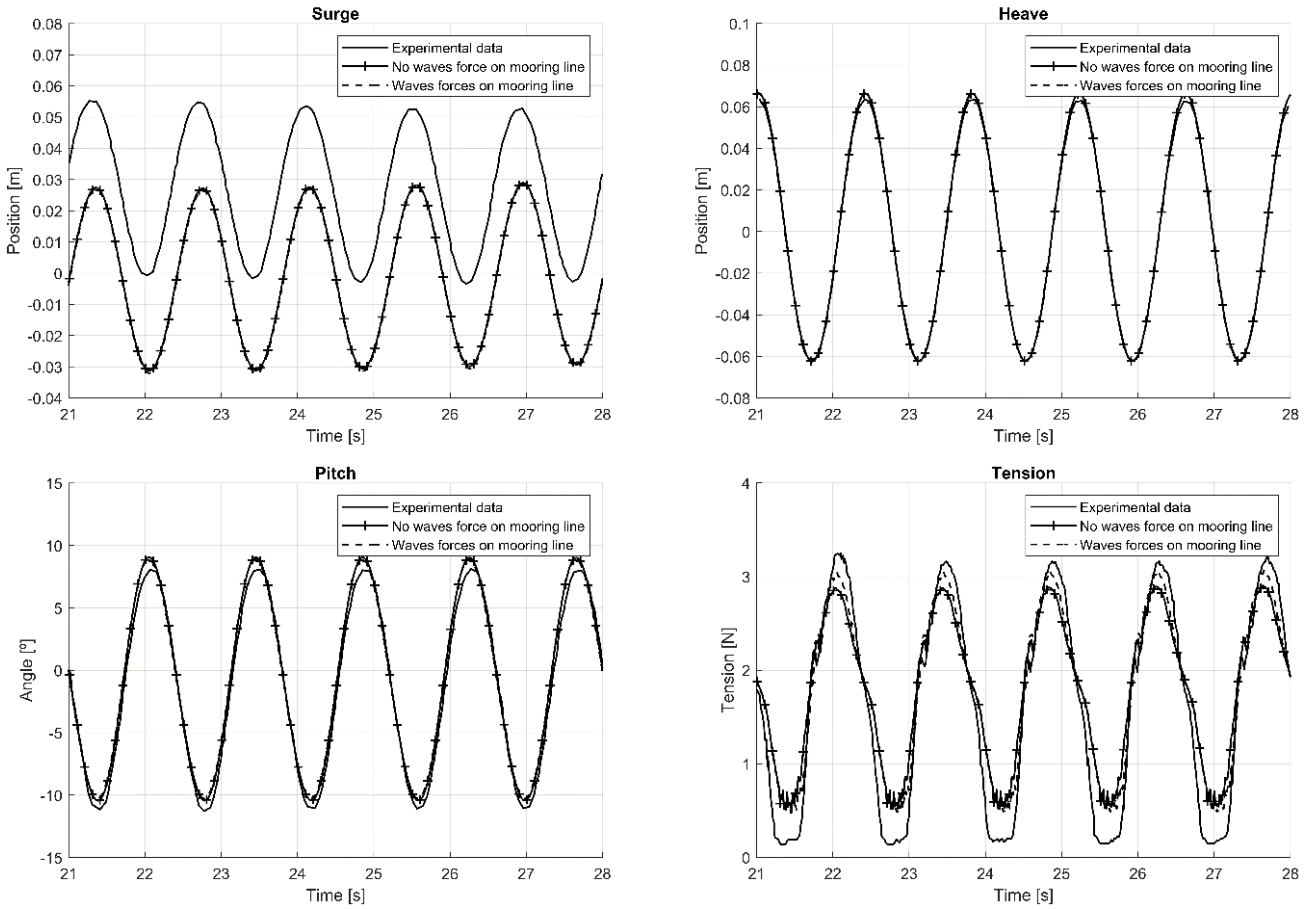

Figure 5-2: Experimental data and simulation results (T=1.4 s, H= 0.100 m)

5.2.1 Horizontal and vertical span ratio evaluation

As the wave hydrodinamics decreases with the depth, exponentially for deep waters, the effects of the hydrodynamics may be more noticeable for more flaten configurations. A comparison study between three different ratios between the horizontal span of the suspended length and the fairlead vertical distance is performed in order to assess the contribuction of the hydrodynamics over the line. The

comparison is performed assuming the same regular wave train, platform and line characteristics, but varying the total length and the anchor point position. A sketch of the initial configuration of the three studied scenarios with horizontal and vertical span of the suspended line ratios of 1.65, 2.65 and 3.65 is shown in Figure 5-4. Also the initial restoring force of the spring is modified to match the inital horizontal restoring force of the line, as the longer the suspended length the larger the tension in the mooring line.

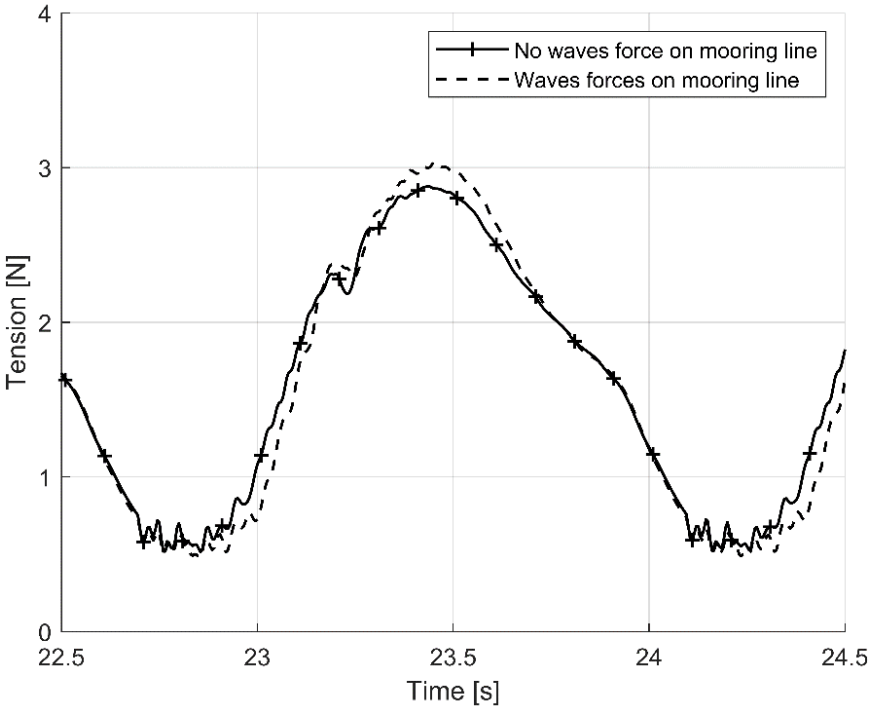

Figure 5-3: Tension of the numerical simulations (T=1.4 s, H= 0.100 m)

Figure 5-5 shows the comparison of one cycle tension of the simulations. The main difference between the simulations is the increase of the mean tension as was expected due to the longer suspended line segment. The increase of the mean tension also implies a reduction of slackness of the line during the simulation reducing internal vibrations as can be seen in the troughs of all the three simulations. Table 5-2 shows the comparison of the maximum, minimum, mean and range tensions at the fairlead of the simulations. The results show an important decrease of the minum tension of the line for the ratio H/V of 3.65 when including wave hydrodynamics on the line. The minium tensions for the H/V ratios of 1.65 and 2.65 have lower variations because they are determined by a slack event. The maximum tension increases in all three scenarios, with a maximum increment of about 0.15 N for the 2.65 scenario. The other two scenarios have a similar absoulte increase of about 0.09-0.1 N. To summarize, the ranges between the minum and maximum tension for the simulations have an increase between a 5.1 and 6.4 % if wave hydrodynamics over the mooring lines are accounted for.

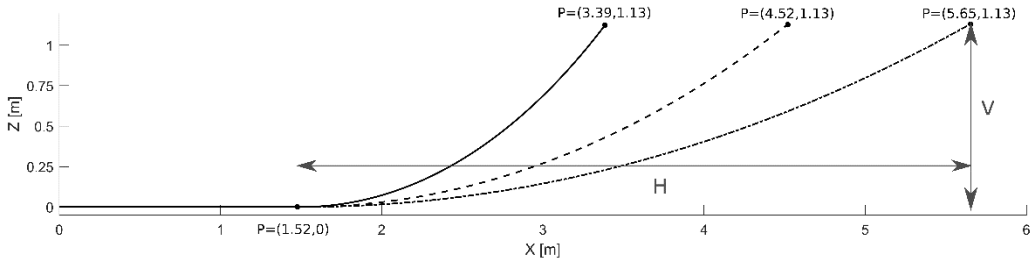

Figure 5-4: Sketch of mooring line shape of the H/V parametric study

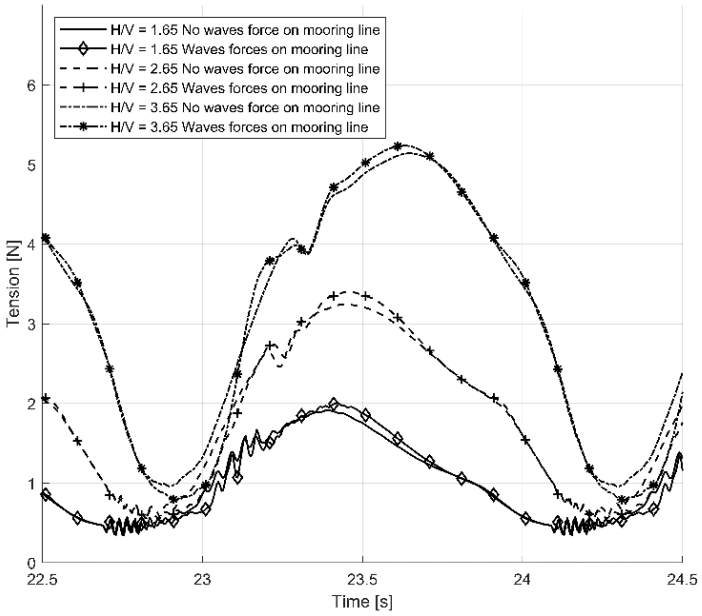

Figure 5-5: Tension of H/V parametric study (T=1.4 s, H=0.100 m)

Table 5-2: Tension comparison for the H/V parametric study (T=1.4 s, H=0.100 m)

		$\boldsymbol{min}$ $[\boldsymbol{N}]$	$\Delta\mathbf{min}$ $[\boldsymbol{N}]$	$\Delta\boldsymbol{min}$ (%)	$\mathbf{max}$ $[\boldsymbol{N}]$	$\Delta\mathbf{max}$ $[\boldsymbol{N}]$	$\Delta\boldsymbol{max}$ (%)	$\mathbf{max-min}$ $[\boldsymbol{N}]$	$\Delta(\mathbf{max-min})[\boldsymbol{N}]$	$\Delta(\mathbf{max-min})(\%)$
H/V = 1.65	No wave Hydrodynamics	0.345			1.907			1.562		
	Wave Hydrodynamics	0.352	0.007	1.9%	1.993	0.086	4.5%	1.641	0.079	5.1%
H/V = 2.65	No wave Hydrodynamics	0.558			3.263			2.704		
	Wave Hydrodynamics	0.550	-0.008	-1.4%	3.415	0.152	4.7%	2.865	0.160	5.9%
H/V = 3.65	No wave Hydrodynamics	0.959			5.142			4.184		
	Wave Hydrodynamics	0.787	-0.172	-17.9%	5.239	0.097	1.9%	4.453	0.269	6.4%

5.2.2 Chain diameter parametric study

The wave hydrodynamics, drag and wave inertial forces, also depend on the diameter of the chain. Moreover, the variation of the chain diameter also effects on the mean tension of the line due to the variation of the wet weight. Then, the influence of the hydrodynamic forces on the mooring line may vary depending on the line diameter.

To assess the influence of the line diameter on the wave hydrodynamic forces on the mooring line, the experiment presented in Section 5.2, named as case 0 (C0), is repeated by decreasing and increasing the chain diameter for case 1 (C1) and case 2(C2), respectively. The parameters that differ in these three cases are the diameter, the wet weight and the dry weight, as shown in Table 5-3. The Figure 5-6 shows the tension cycle for the C1 and C2 simulations, whereas C0 result is shown in Figure 5-3.

The Table 5-4 shows the summary of the results of the simulation for comparison purpose. The simulations show larger increments for the maximum tension in larger diameters (C2), but these are relatively smaller than in the small diameter (C1), due to the increase in the mean tension. For the minimum tension, the C1 presents larger tension, whereas for the other cases the minimum tension decreases with the increase of the diameter. Finally, the tension amplitude presents larger increments for larger diameters (C2).

Table 5-3: Chain characteristics for the diameter parametric study

Parameter	**C0**	**C1**	**C2**
Apparent diameter [mm]	2.7	1.9	3.2
Submerged weight per unit length [N/m]	0.382	0.188	0.542
Dry weight per unit length [N/m]	0.436	0.215	0.618

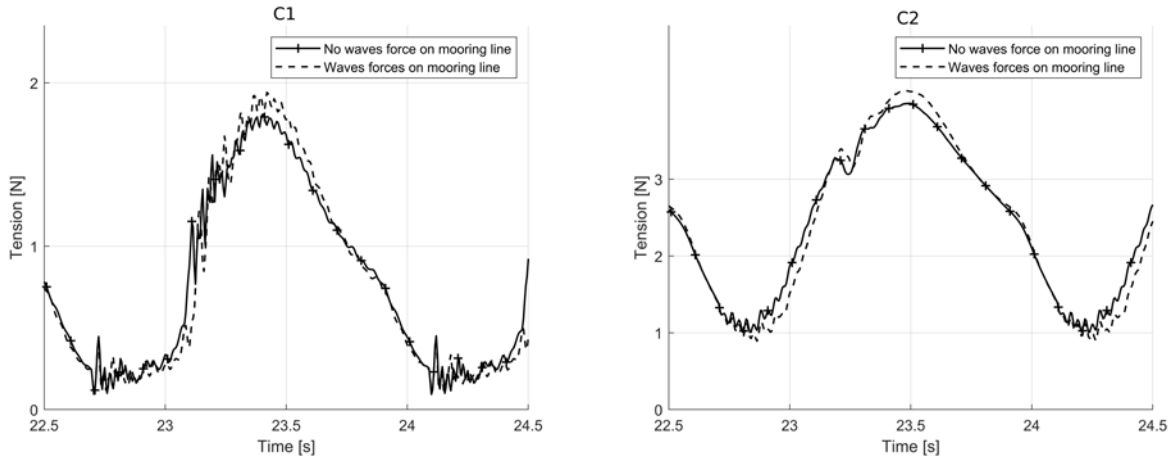

Figure 5-6: Tension cycle for C1 (left) and C2 (right) simulations

Table 5-4: Tension comparison for the diameter parametric study.

		$min\ [N]$	$\Delta\,\mathbf{min}(\%)$	$\mathbf{max}\ [\mathbf{N}]$	$\Delta\,\mathbf{max}(\%)$	$\mathbf{max-min}\ [\mathbf{N}]$	$\Delta(\mathbf{max}-\mathbf{min})(\%)$
C0 (2.7 mm)	No wave Hydrodynamics	0.485		2.964		2.478	
	Wave Hydrodynamics	0.462	-4.74%	3.121	5.30%	2.659	7.30%
C1(1.9 mm)	No wave Hydrodynamics	0.080		1.912		1.832	
	Wave Hydrodynamics	0.087	8.75%	2.040	6.69%	1.953	6.60%
C2 (3.2 mm)	No wave Hydrodynamics	0.982		4.053		3.071	
	Wave Hydrodynamics	0.876	-10.79%	4.212	3.92%	3.337	8.66%

5.3 FOWT ANALYSIS INCLUDING WAVE HYDRODYNAMICS OVER MOORINGS

FOWT mooring systems can also be subjected to an increment of the tension and tension range due to wave hydrodynamics. In order to assess the contribution of the hydrodynamic wave loads over the mooring lines, two referent floating platforms are studied by analyzing its behavior in a different sea states. These referent platforms are the DeepCWind and the OC3 Hywind platform. The DeepCWind is a semisub platform (Robertson et al., 2014) which was analyzed during the OC5 project (Robertson et al., 2016) and the results were compared with the available experimental data. This platform presents a draft of 20m and the fairleads are located at 14 m depth. In this chapter, the inclusion of wave hydrodynamics on the moorings will be compared with the available experiments. The OC3 Hywind (Jonkman, 2010) is a steel spar platform with a 120 m draft and the fairleads located at 70 m depth. Moreover, a parametric study is performed by adding three extra simulations using the same mooring system but placing the fairleads at 3 different heights above the initial one. The shift of the fairleads allows a comparison of the influence of the depth for the wave hydrodynamics on the mooring lines.

The sea state used in the simulations for both platforms is the design sea state of the OC5 Phase II project with a significant wave height (Hs) of 10.5 m and a peak period (Tp) of 14.3 s. Moreover, an operational sea state with a Hs of 7.1 m and a Tp of 12.1 s is used for the OC3 Hywind platform to assess the different contribution of the wave loads on the mooring line for different sea states.

5.3.1 DeepCWind

The OC5 phase II project is based on the scale model of the DeepCWind semisubmersible concept (Robertson et al., 2014). More details of the model can be found in section 4.5.1.

The simulation performed is the load case LC3.4 of the OC5 Phase II project (Robertson et al., 2017) where the platform is tested under the design wave state without wind (see Table 5-5 for more details). The load case lasts 3 h to ensure a full development of the irregular wave train, which was provided by the project (Robertson et al., 2016). The simulation results with and without wave hydrodynamics are also compared with the experimental data.

Table 5-5: Description of the LC 3.4 of the OC5 Task II project Robertson et al. (2017)

Load Case	Description	RPM	Blade Pitch (deg)	Wave Condition	Wind Condition	Sim. Length (min)
3.4	Design Wave	0	90	Irregular: H_s = 10.5m, T_p = 14.3s, γ=3.0, JONSWAP	N/A	180

5.3.1.1 Results

The results of the simulations of the LC3.4 are compared with the experimental data, focusing on the most affected parameters results: the surge motion of the platform and the tension of the mooring lines.

The Figure 5-7 shows the PSD of the surge motion of the platform. The results show a lower response of the simulations for the lower frequency range, but good agreement in the wave frequency. This difference is probably due again to not considering second order wave theory in wave hydrodynamics. The simulation which includes wave hydrodynamics forces on mooring lines clearly shows a higher energy peak in the mooring frequency range than without waves forces.

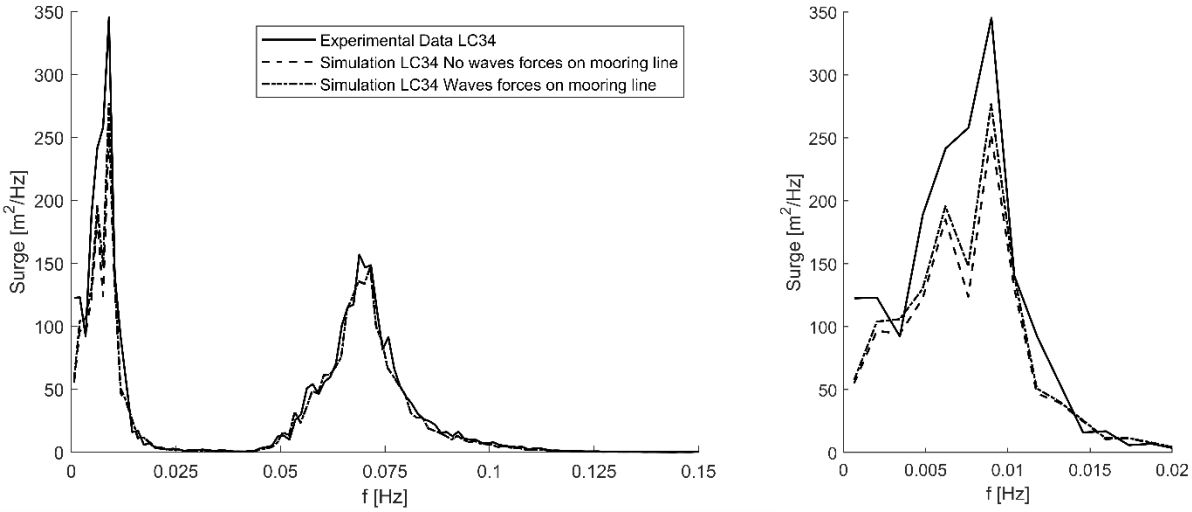

Figure 5-7: PSD of Surge motion of LC34

The tension at the fairleads also differ depending on if the hydrodynamics over the mooring lines are considered or not. The results show a reduction of the minimum tension, an increase of the maximum tension and an increase of the standard deviation (along the 10800 s simulation) of the tension at the fairleads for lines 1 and 3, the ones not aligned with the wave direction. These variations represent an increase of about 4.25 % of the standard deviation and of about 1.45 % of the maximum tension for lines 1 and 3 (Table 5-6). On the other hand, line 2 presents a larger minimum tension and a smaller maximum tension. Minimum tension events take place in the high nonlinear slack-snap phenomena. The maximum tension is only reduced by -0.19 %. However, the standard deviation of the tension of the line 2 at the fairlead also increases 1.8 %.

The Figure 5-8 shows a time series section of the tensions of Fairlead 2. An increase of the vibration of the tension due to the wave forces acting on the mooring lines is noticed. These vibrations are better noticed in the PSD plots of the tensions of the mooring lines 1 and 2 (Figure 5-9) for frequencies larger than 0.32 Hz and produce a better fitting of the experimental data.

The wave forces on the mooring lines have little influence on the forces at the tower base as shown in Table 5-6. The differences are less than 0.4 % for the maximum forces, and less than 0.55 % for the standard deviation. These differences are much lower than the differences of the tensions at the fairleads.

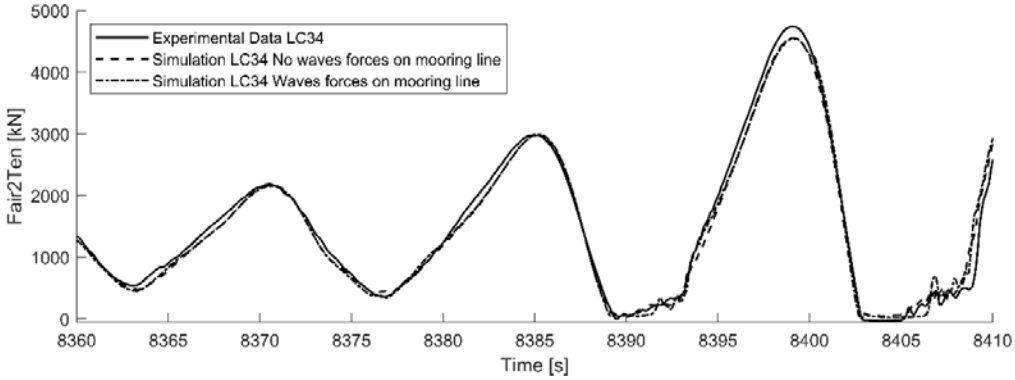

Figure 5-8: Fairlead2 tension time segment

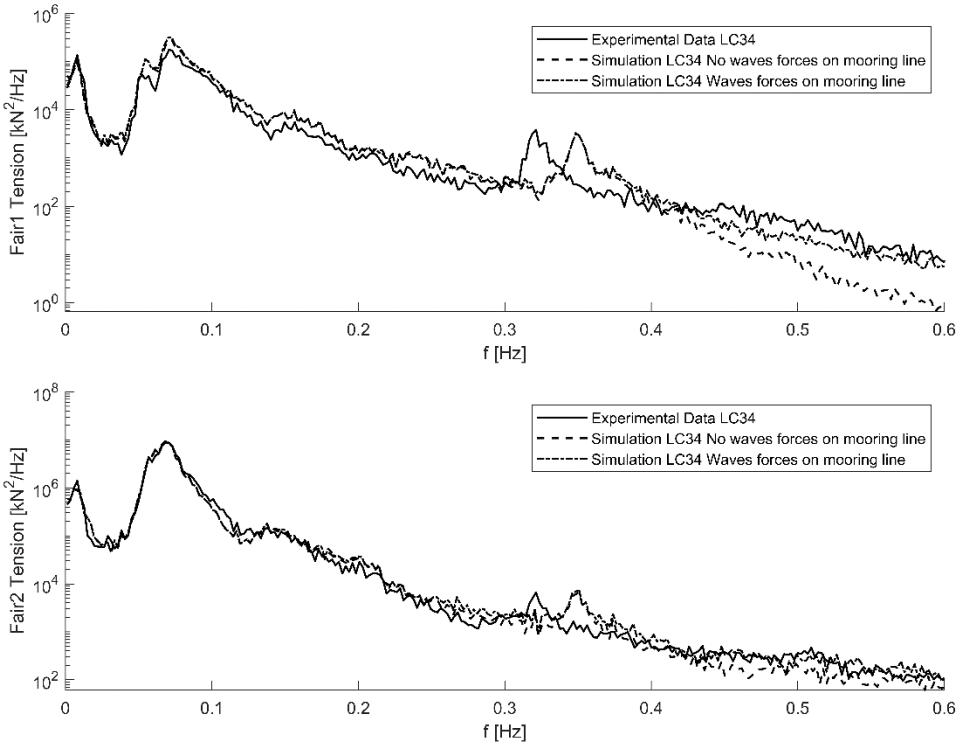

Figure 5-9: PSD of fairlead tension of the mooring line 1 (up) and of the mooring line 2(down)

Table 5-6: Tension Fairlead and Tower Base forces Summary of DeepCWind Simulations

Fairlead1	$\boldsymbol{min}$	$\boldsymbol{mean}$	$\boldsymbol{max}$	$\Delta\,\mathbf{max}(\%)$	$\boldsymbol{\sigma}$	$\Delta\boldsymbol{\sigma}(\%)$
No Mooring Hydrodynamics	390.67 kN	1031.81 kN	1533.03 kN		89.23 kN	
Mooring Hydrodynamics	367.32 kN	1030.67 kN	1554.48 kN	1.40%	92.98 kN	4.20%
Fairlead2	$\boldsymbol{min}$	$\boldsymbol{mean}$	$\boldsymbol{max}$	$\Delta\,\mathbf{max}(\%)$	$\boldsymbol{\sigma}$	$\Delta\boldsymbol{\sigma}(\%)$
No Mooring Hydrodynamics	0.4683 kN	1232.821 N	5353.26 kN		440.80 kN	
Mooring Hydrodynamics	3.4447 kN	1232.90 kN	5343.15 kN	-0.19%	448.87 kN	1.83%
Fairlead3	$\boldsymbol{min}$	$\boldsymbol{mean}$	$\boldsymbol{max}$	$\Delta\,\mathbf{max}(\%)$	$\boldsymbol{\sigma}$	$\Delta\boldsymbol{\sigma}(\%)$
No Mooring Hydrodynamics	420.61 kN	1102.61 kN	1659.80 kN		98.94 kN	
Mooring Hydrodynamics	387.32 kN	1101.46 kN	1684.55 kN	1.49%	103.17 kN	4.28%
TwrBsFxt	$\boldsymbol{min}$	$\boldsymbol{mean}$	$\boldsymbol{max}$	$\Delta\,\mathbf{max}(\%)$	$\boldsymbol{\sigma}$	$\Delta\boldsymbol{\sigma}(\%)$
No Mooring Hydrodynamics	-2315.01 kN	96.5914 kN	2220.768 kN		408.544 kN	
Mooring Hydrodynamics	-2319.6 kN	95.9656 kN	2224.82 kN	0.18%	410.7606 kN	0.54%
TwrBsMyt	$\boldsymbol{min}$	$\boldsymbol{mean}$	$\boldsymbol{max}$	$\Delta\,\mathbf{max}(\%)$	$\boldsymbol{\sigma}$	$\Delta\boldsymbol{\sigma}(\%)$
No Mooring Hydrodynamics	-190304 kN·m	-271.479 kN·m	158900.4 kN·m		31304.67 kN·m	
Mooring Hydrodynamics	-190998 kN·m	-310.272 kN·m	159523.9 kN·m	0.39%	31463.87 kN·m	0.51%

5.3.2 OC3 Hywind

The OC3·Spar Hywind platform is a steel spar platform coupled with the NREL 5MW reference wind turbine studied within the Phase IV of the OC3 project (Jonkman, 2010). The model is analyzed subjected to a normal sea state for operational condition and to a severe sea state, both in Power Production State with a dynamic wind with a mean speed of 13.05 m/s, see Table 5-7 for more details. The wave elevation are get from OC5 tsk II project (Robertson et al., 2016), but the kinematics are updated accounting for the variation of the sea depth of the OC3 Hywind.

The Hywind simulations are performed for four different fairlead positions and, again, with and without the wave hydrodynamic loads over the lines. These points are equal distributed from the actual fairlead depth to the MSL at a depths of -70, -47, -23 and 0 m. Then, in order to maintain the same mooring system shape, the seabed is also shifted as the fairlead offset. Then, the forces developed by the mooring system are equivalent. However, it is expected that the platform reduces the mean pitch rotation due to the increase of the restoring moment due to the mooring forces. Moreover, the fairlead position will be influenced by the coupling of the pitch and surge motion of the platform, and an increase of the tension range for higher fairlead positions is expected. However, the study focuses in the differences between considering or not the wave forces on the mooring line for each individual fairlead position case.

Table 5-7: Description of the LC for the OC3 Hywind analysis

Load Case	Description	RPM	Blade Pitch (deg)	Wave Condition	Wind Condition	Sim. Length (min)
OC3 Hywind Operational Case	Operational Wave	Variable	Variable	Irregular: H_s = 7.1m, T_p = 12.1s, γ=2.2, JONSWAP	NPD spectrum, μ = 13.05	180
OC3 Hywind Design Case	Design Wave	Variable	Variable	Irregular: H_s = 10.5m, T_p = 14.3s, γ=3.0, JONSWAP	NPD spectrum, μ = 13.05	180

The Figure 5-10 shows a sketch of the set-up of the OC3 Hywind model varying the fairlead position and the corresponding seabed depth. This study is intended to assess the contribution of the wave loads on the mooring lines depending on their depth. To make easier the differentiation of the models for each fairlead position, these are identified as C70 for the actual fairlead position at -70 m, C47 for the fairlead positioned at -47 m depth, C23 for the fairlead at -23 m and C0 for the fairlead depth at the MSL.

5.3.2.1 OC3 Hywind Spar Model

Structural properties

The Hywind platform wind turbine structure is discretized from -120 m up to 10 in 64 beam elements. The remaining 77 m of tower are discretized in 16 elements. A finer discretization of the submerged part is used to improve the assessment of the hydrodynamics loads. The total amount of beam elements is 80.

The density of the beam elements is set to 8500 kg/m^3 to take into account paint, bolts, welds, stiffeners and flanges of the structure. The tower is defined as presented in Jonkman (2009) with a tapered section from a base diameter of 6.5 m and 0.027 m thickness, to a top diameter of 3.87 m and 0.019 m thickness. The buoy is divided in three parts, a lower cylinder, the tapper section and the top cylinder. The draft of the buoy is 120 m, the depth of the bottom of the tapper is 12 m, the depth of the top of the tapper is 4 m, and the top cylinder ends at 10 m above the SWL. The diameter of the buoy changes at the tapper section from 9.4 m to 6.5 m, and the thickness is considered constant.

The thickness of the buoy and the height and bulk density of the ballast are deduced from an optimization problem to fit the given values of the mass, the CoG and the inertias of the OC3 Hywind shown in Table 5-8. The thickness of the platform is set to 0.0365 m, the height of the ballast to 49 m with a bulk density of 1890 kg/m^3. These values lack Yaw Inertia of 7.1703E+07 kg·m^2 that is added at the CoG.

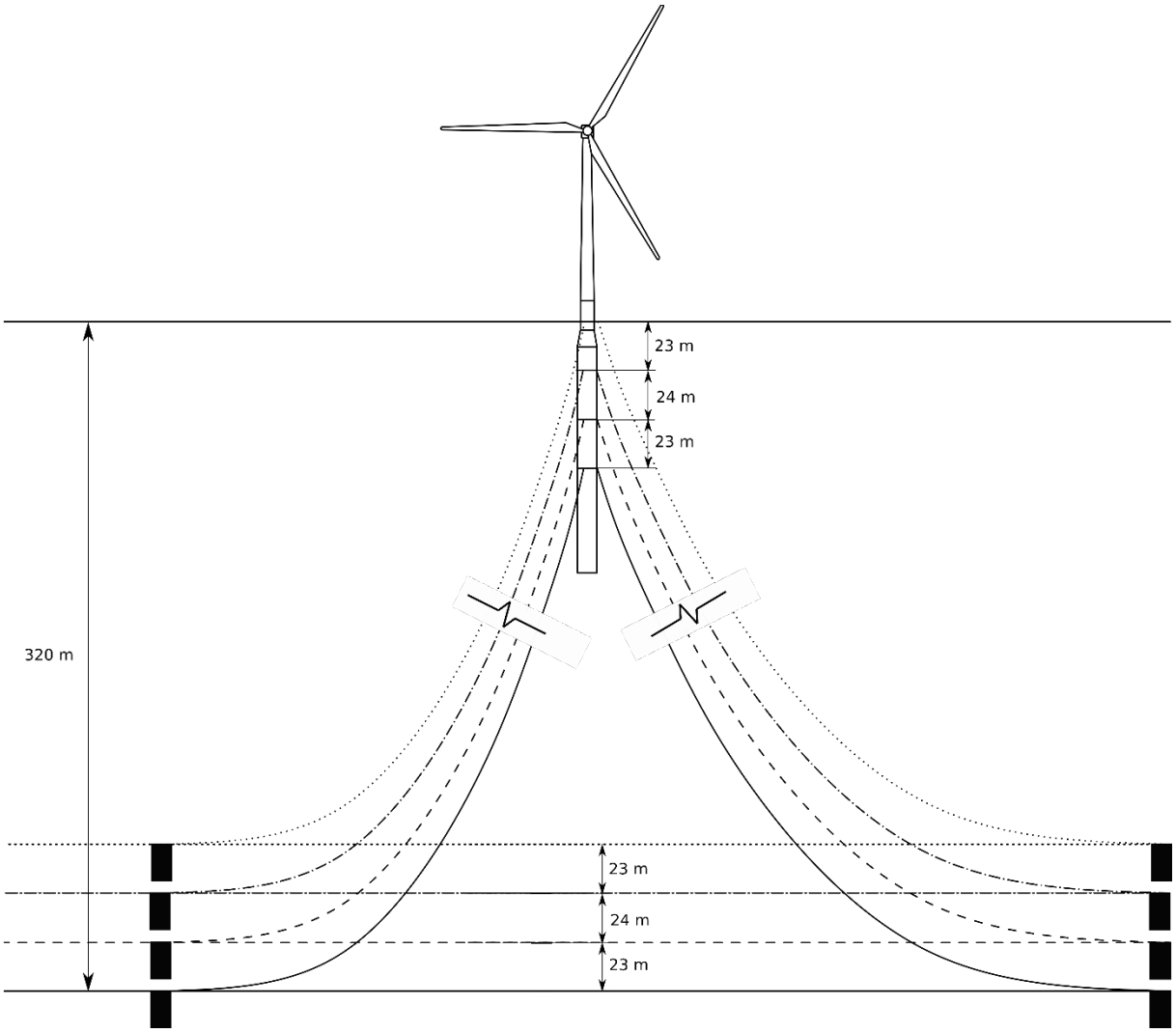

Figure 5-10: Sketch of OC3 Hywind

*Table 5-8: OC3 Hywind platform characteristics (*Jonkman, 2010)

Draft [m]	120
Platform Diameter above Taper [m]	6.5
Platform Diameter below Taper [m]	9.4
Platform Mass, including Ballast [kg]	7.466 E+06
CM Location Below SWL [m]	89.92
Platform Roll/Pitch Inertia [kg/m^2]	4.229 E+09
Platform Yaw Inertia [kg/m^2]	1.642 E+08

Hydrodynamic Properties

The hydrodynamic properties of the platform are based on the Morison equation (Morison et al., 1950) as only beam elements are considered. The hydrodynamic properties are divided in the bottom plate, the cylinders and the tapper transition as shown in Table 5-9 which are obtained from standard values used in the industry and research (Chakrabarti, 2005)

The bottom plate hydrodynamics are based on the drag normal to the plate, and the added mass proportional to volume of the half-hemisphere referent to the plate radius. The dynamic pressure is taken into account via the wave pressure. The hydrodynamics of the cylinders are defined by the transverse drag and the transverse added mass coefficient. On the other hand, the tapper section hydrodynamics accounts for the transverse drag, the transverse added mass, and the longitudinal added mass as well. However, the axial drag term of the tapper section is not considered because all longitudinal drag terms are assessed at the bottom plate.

The platform hydrodynamic coefficients are as provided in Table 5-9.:

Table 5-9: Hydrodynamic Parameters of OC3 Hywind Platform

	C_d		C_a		C_m	
	Trans	**Long.**	**Trans**	**Long.**	**Trans**	**Long.**
Bottom plate	--	2	--	1	--	--
Cylinder	0.6	--	0.97	--	1.97	--
Tapper section	0.6	--	0.97	1	1.97	1

Mooring Properties

The characteristics of the mooring lines shown in Table 5-10 are based on the same properties proposed by Jonkman (2009). The hydrodynamic properties are the same as the DeepCWind simulations of section 4.5.1 due to the lack of information and experimental results. The delta mooring system is simulated by an additional yaw spring stiffness of $98.34 \cdot 10^6$ N·m/rad at the centroid of the fairleads positions.

Wind Turbine Properties

The wind turbine used is the NREL 5 MW reference wind turbine (Jonkman et al., 2009). The blade pitch control is based on a generator-torque control strategy in the above rated torque region with a natural frequency pitch-controller-response below the platform pitch natural frequency (Jonkman & Musial, 2010).

Table 5-10: OC3 Hywind mooring line characteristics

Nº of mooring lines	3
Depth of Anchors [m]	320
Depth of Fairleads [m]	70
Radius to Anchors [m]	853.87
Radius to Fairlead [m]	5.2
Unstretched mooring line length [m]	902
Mooring line diameter [m]	0.09
Mooring line density [kg/m]	77.71
Mooring line wet weight [N/m]	698.1
Mooring line Extensional Stiffness (EA) [N]	3.842E+08
Cdt	0.86
Cdn	1.875
Ca	0.5
ξ_A	3%

5.3.2.2 Simulation Results Analysis

The effect of the hydrodynamic forces of the wave train over the mooring lines are conditioned for the depth of the fairleads as was expected. Table 5-11 and Table 5-12 show a summary of the simulation results, comparing the minimum, mean, maximum values and the standard deviation (σ) of the tension at the fairleads for the four cases with and without wave hydrodynamics over the mooring lines for the operational and design cases. However, results coming from different fairlead positions have to be compared very carefully, as the fairlead position affects clearly the tension range of the lines. Higher fairleads are more separated from the center of gravity of the structure leading to an increment of the surge motion amplitude of the fairleads, due to the platform pitch. Then, even the mean tension is almost constant for all the four cases, the lower fairlead depth, the larger tension range.

The tension results are presented for each fairlead, where the fairlead 1 is the one attached to the line placed along the wave spread direction. Fairleads 2 and 3 are attached to the lines positioned ±120º respect to the wave direction.

The results for the operational and design cases show a clear tendency to widening the mooring line tension range when the wave loads on mooring lines are considered. The minimum tension tends to decrease and the peak tension tends to increase. Then, the standard deviation of the tension also increases. Moreover, the increase of the standard deviation is larger for the higher fairlead positions, as the wave loads decrease exponentially with the depth.

The standard deviation of the tension in the operation load case increases when the wave loads on mooring lines are considered. For the lower fairlead positions, C70 and C47 the differences are less than 1 %. However, for the C0 case, the standard deviation increases 0.56 % for the fairlead 1 and about 2.8 % for the fairleads 2 and 3. However, these increments are lower than for the design load case.

The design load case presents larger hydrodynamic forces than the operational one and, then, presents larger differences between the simulations when wave loads on moorings are included. The increase of the standard deviation of the tension of the fairlead 1 goes from 0.18 % (C70) to 1.56 % (C0). For the fairleads 2 and 3, the increase of the standard deviation goes from 1.21 % (C70) to 5.53 % (C0). Taking a close look at results obtained for the design load case, the Fairlead 1 presents a slack phenomenon in C43, C32 and C0, affecting the maximum tension in the simulations.

At the C43 and C23 of the design load case, the minimum tension of fairlead 1 clearly decreases and its maximum value is almost unaltered. In these cases, the slack-snap phenomenon appears in some points of the mooring line which governs the behavior of the line, then the maximum tension does not change. However, fairleads 2 and 3 do not suffer slack events and the maximum tensions increase, as was expected.

At the C0 of the design load case also appears a slack-snap tension phenomenon on the fairlead 1 as shown in Figure 5-11. Then, the minimum tension at Fairlead 1 goes to zero. Even though this event, the maximum tension at the Fairlead 1 also increases, while in C47 and C23 changes are very small. This fact can be explained due to the line being exposed to the most energetic region close to the MSL, thus even the mooring line tension is mainly governed by this event and, as such the wave hydrodynamics cannot be despicable. Moreover, the tension of the lines are excited in the higher frequency ranges (Figure 5-11) as was also noticed in the DeepCWind mooring lines (Figure 5-9). However, the energy of these vibrations are orders of magnitude smaller than those that produce the tension changes, despite being experimentally confirmed (Figure 5-9).

5.3.2.3 Fatigue Analysis

A sensibility fatigue analysis is carried out from the data of the operational and design load cases of the fairlead tensions for each fairlead case. The aim of the analysis is to assess the contribution of the wave loads on the fatigue life of the mooring lines. The fatigue analysis is performed using DNV-GL mooring standard (DNVGL, 2015) and the rainflow count to obtain the tension range. The damage of the mooring in a state i (d_i) line is assessed by Eq.(5.1).

$$d_i = \frac{n_i}{a_D} E[S_i^m] \tag{5.1}$$

Where, n_i is the number of stress cycles, a_D is the intercept parameter of the S-N curve, m is the slope of the S-N curve, and $E[S_i^m]$ is the expected value of expected value of the nominal stress ranges raised to the power m in state i.

Supposing the mooring line is a studless chain, the a_D is set to 6.0E+10 and m is set to 3. In this case, the corrosion allowance is not taken into account, and the diameter of the chain is set to 90mm.

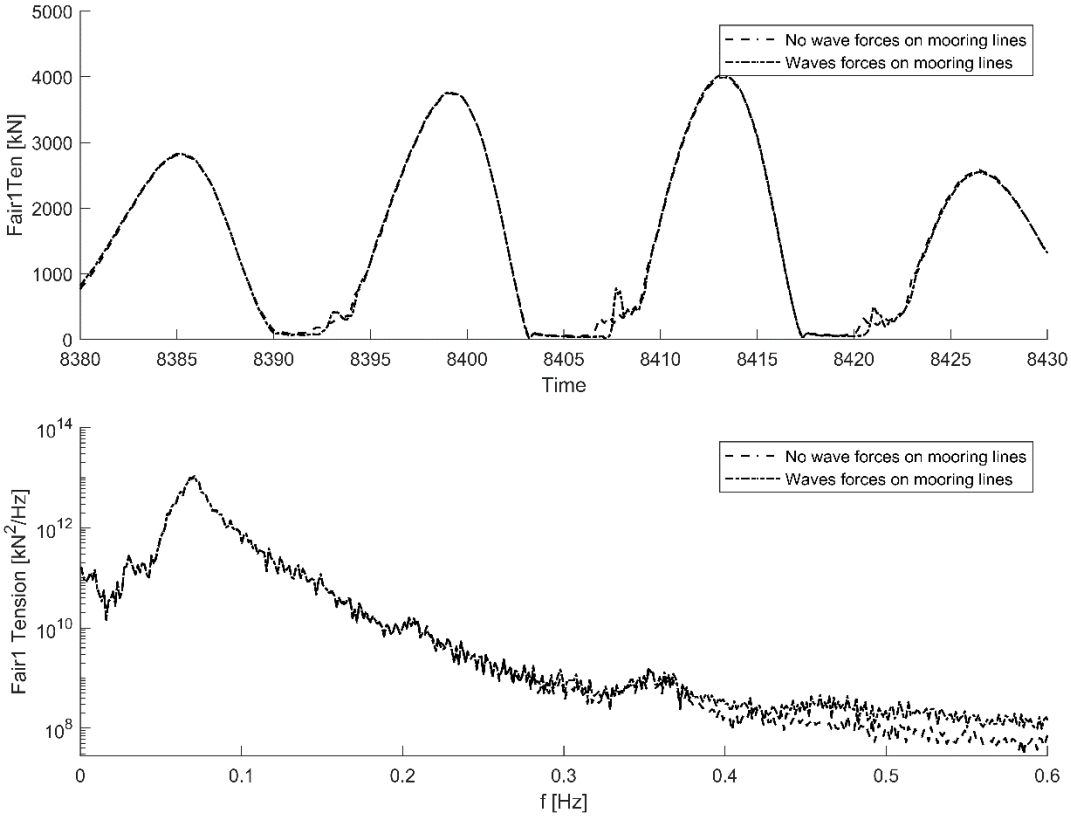

Figure 5-11: Time Series (Up) and PSD (Down) of C0 Fairlead Tension

Table 5-13 and Table 5-14 show the results of the fatigue analysis of the moorings. When the wave loads on the moorings are included, the damage of the lines increase due to the increment of the tension range at the fairleads.

Fairlead 1 is the most damaged line due to its alignment with the wave train, which implies a larger stress range. The contribution of the wave hydrodynamic forces on the damage of the line 1 is an increment from 0 % to 3 % for the operational load case and from a 1.3 % to a 5.1 % for design load case. Fairlead 2 and 3 suffer a larger percentage increment from 1 % to 9 % for the operational case and from 2.6 % to a 20.2 % for the design case. This larger percentage increase of the Fairleads 2 and 3 are due to the damage is very limited if the wave loads on mooring lines are not considered.

Table 5-11: OC3 Hywind Fairlead tension results for the operational case in kN.

C70: Fairlead depth of – 70 m						
Fairlead1	$\boldsymbol{min}$	$\boldsymbol{mean}$	$\boldsymbol{max}$	$\Delta\,\mathbf{max}(\%)$	$\boldsymbol{\sigma}$	$\Delta\boldsymbol{\sigma}(\%)$
No Mooring Hydrodynamics	916.40	1270.76	1655.75		70.11	
Mooring Hydrodynamics	914.72	1270.69	1653.70	-0.12%	70.13	0.03%
Fairlead2	$\boldsymbol{min}$	$\boldsymbol{mean}$	$\boldsymbol{max}$	$\Delta\,\mathbf{max}(\%)$	$\boldsymbol{\sigma}$	$\Delta\boldsymbol{\sigma}(\%)$
No Mooring Hydrodynamics	673.09	773.36	846.85		15.46	
Mooring Hydrodynamics	672.49	773.37	847.32	0.05%	15.49	0.23%
Fairlead3	$\boldsymbol{min}$	$\boldsymbol{mean}$	$\boldsymbol{max}$	$\Delta\,\mathbf{max}(\%)$	$\boldsymbol{\sigma}$	$\Delta\boldsymbol{\sigma}(\%)$
No Mooring Hydrodynamics	681.26	786.17	861.24		16.25	
Mooring Hydrodynamics	680.74	786.18	861.58	0.04%	16.29	0.25%
C47: Fairlead depth of – 47 m						
Fairlead1	$\boldsymbol{min}$	$\boldsymbol{mean}$	$\boldsymbol{max}$	$\Delta\,\mathbf{max}(\%)$	$\boldsymbol{\sigma}$	$\Delta\boldsymbol{\sigma}(\%)$
No Mooring Hydrodynamics	640.76	1283.11	2011.36		118.78	
Mooring Hydrodynamics	637.23	1283.04	2016.52	0.26%	118.75	-0.03%
Fairlead2	$\boldsymbol{min}$	$\boldsymbol{mean}$	$\boldsymbol{max}$	$\Delta\,\mathbf{max}(\%)$	$\boldsymbol{\sigma}$	$\Delta\boldsymbol{\sigma}(\%)$
No Mooring Hydrodynamics	616.64	776.30	891.69		21.58	
Mooring Hydrodynamics	615.05	776.28	892.63	0.11%	21.68	0.45%
Fairlead3	$\boldsymbol{min}$	$\boldsymbol{mean}$	$\boldsymbol{max}$	$\Delta\,\mathbf{max}(\%)$	$\boldsymbol{\sigma}$	$\Delta\boldsymbol{\sigma}(\%)$
No Mooring Hydrodynamics	620.52	788.91	911.18		22.75	
Mooring Hydrodynamics	619.18	788.89	912.17	0.11%	22.85	0.46%
C23: Fairlead depth of – 23 m						
Fairlead1	$\boldsymbol{min}$	$\boldsymbol{mean}$	$\boldsymbol{max}$	$\Delta\,\mathbf{max}(\%)$	$\boldsymbol{\sigma}$	$\Delta\boldsymbol{\sigma}(\%)$
No Mooring Hydrodynamics	295.58	1293.09	2503.72		165.15	
Mooring Hydrodynamics	269.13	1293.00	2503.34	-0.01%	165.39	0.14%
Fairlead2	$\boldsymbol{min}$	$\boldsymbol{mean}$	$\boldsymbol{max}$	$\Delta\,\mathbf{max}(\%)$	$\boldsymbol{\sigma}$	$\Delta\boldsymbol{\sigma}(\%)$
No Mooring Hydrodynamics	530.49	775.56	934.31		29.38	
Mooring Hydrodynamics	526.35	775.55	936.88	0.28%	29.68	0.99%
Fairlead3	$\boldsymbol{min}$	$\boldsymbol{mean}$	$\boldsymbol{max}$	$\Delta\,\mathbf{max}(\%)$	$\boldsymbol{\sigma}$	$\Delta\boldsymbol{\sigma}(\%)$
No Mooring Hydrodynamics	532.17	787.88	944.64		30.79	
Mooring Hydrodynamics	528.08	787.86	947.15	0.27%	31.11	1.01%
C0: Fairlead depth of 0m for LC33						
Fairlead1	$\boldsymbol{min}$	$\boldsymbol{mean}$	$\boldsymbol{max}$	$\Delta\,\mathbf{max}(\%)$	$\boldsymbol{\sigma}$	$\Delta\boldsymbol{\sigma}(\%)$
No Mooring Hydrodynamics	95.99	1299.39	2870.76		210.91	
Mooring Hydrodynamics	81.47	1299.51	2868.08	-0.09%	212.09	0.56%
Fairlead2	$\boldsymbol{min}$	$\boldsymbol{mean}$	$\boldsymbol{max}$	$\Delta\,\mathbf{max}(\%)$	$\boldsymbol{\sigma}$	$\Delta\boldsymbol{\sigma}(\%)$
No Mooring Hydrodynamics	495.53	776.89	997.45		33.85	
Mooring Hydrodynamics	482.70	776.87	1003.28	0.58%	34.79	2.77%
Fairlead3	$\boldsymbol{min}$	$\boldsymbol{mean}$	$\boldsymbol{max}$	$\Delta\,\mathbf{max}(\%)$	$\boldsymbol{\sigma}$	$\Delta\boldsymbol{\sigma}(\%)$
No Mooring Hydrodynamics	498.99	788.91	1006.16		35.41	
Mooring Hydrodynamics	483.10	788.88	1011.82	0.56%	36.39	2.79%

Table 5-12: OC3 Hywind Fairlead tension results for the design case in kN.

C70: Fairlead depth of – 70 m						
Fairlead1	$\boldsymbol{min}$	$\boldsymbol{mean}$	$\boldsymbol{max}$	$\Delta\,\mathbf{max}(\%)$	$\boldsymbol{\sigma}$	$\Delta\boldsymbol{\sigma}(\%)$
No Mooring Hydrodynamics	475.53	1282.31	2228.91		137.27	
Mooring Hydrodynamics	453.36	1282.36	2230.45	0.07%	137.52	0.18%
Fairlead2	$\boldsymbol{min}$	$\boldsymbol{mean}$	$\boldsymbol{max}$	$\Delta\,\mathbf{max}(\%)$	$\boldsymbol{\sigma}$	$\Delta\boldsymbol{\sigma}(\%)$
No Mooring Hydrodynamics	542.66	781.30	958.17		28.94	
Mooring Hydrodynamics	543.05	781.27	956.59	-0.17%	29.29	1.21%
Fairlead3	$\boldsymbol{min}$	$\boldsymbol{mean}$	$\boldsymbol{max}$	$\Delta\,\mathbf{max}(\%)$	$\boldsymbol{\sigma}$	$\Delta\boldsymbol{\sigma}(\%)$
No Mooring Hydrodynamics	548.49	793.28	974.65		29.82	
Mooring Hydrodynamics	548.87	793.25	972.00	-0.27%	30.18	1.21%
C47: Fairlead depth of – 47 m						
Fairlead1	$\boldsymbol{min}$	$\boldsymbol{mean}$	$\boldsymbol{max}$	$\Delta\,\mathbf{max}(\%)$	$\boldsymbol{\sigma}$	$\Delta\boldsymbol{\sigma}(\%)$
No Mooring Hydrodynamics	167.31	1289.82	2969.07		224.62	
Mooring Hydrodynamics	106.89	1289.69	2969.67	0.02%	225.50	0.39%
Fairlead2	$\boldsymbol{min}$	$\boldsymbol{mean}$	$\boldsymbol{max}$	$\Delta\,\mathbf{max}(\%)$	$\boldsymbol{\sigma}$	$\Delta\boldsymbol{\sigma}(\%)$
No Mooring Hydrodynamics	377.35	779.31	1014.72		40.69	
Mooring Hydrodynamics	372.04	779.27	1019.13	0.43%	41.53	2.06%
Fairlead3	$\boldsymbol{min}$	$\boldsymbol{mean}$	$\boldsymbol{max}$	$\Delta\,\mathbf{max}(\%)$	$\boldsymbol{\sigma}$	$\Delta\boldsymbol{\sigma}(\%)$
No Mooring Hydrodynamics	372.42	791.23	1029.27		42.21	
Mooring Hydrodynamics	366.82	791.19	1032.74	0.34%	43.07	2.02%
C23: Fairlead depth of – 23 m						
Fairlead1	$\boldsymbol{min}$	$\boldsymbol{mean}$	$\boldsymbol{max}$	$\Delta\,\mathbf{max}(\%)$	$\boldsymbol{\sigma}$	$\Delta\boldsymbol{\sigma}(\%)$
No Mooring Hydrodynamics	65.38	1299.05	3601.40		327.38	
Mooring Hydrodynamics	38.44	1298.77	3601.17	-0.01%	330.21	0.87%
Fairlead2	$\boldsymbol{min}$	$\boldsymbol{mean}$	$\boldsymbol{max}$	$\Delta\,\mathbf{max}(\%)$	$\boldsymbol{\sigma}$	$\Delta\boldsymbol{\sigma}(\%)$
No Mooring Hydrodynamics	311.18	777.57	1125.54		54.27	
Mooring Hydrodynamics	291.34	777.40	1129.93	0.39%	55.97	3.14%
Fairlead3	$\boldsymbol{min}$	$\boldsymbol{mean}$	$\boldsymbol{max}$	$\Delta\,\mathbf{max}(\%)$	$\boldsymbol{\sigma}$	$\Delta\boldsymbol{\sigma}(\%)$
No Mooring Hydrodynamics	311.87	789.51	1144.21		56.28	
Mooring Hydrodynamics	291.82	789.34	1147.19	0.26%	58.02	3.09%
C0: Fairlead depth of 0 m						
Fairlead1	$\boldsymbol{min}$	$\boldsymbol{mean}$	$\boldsymbol{max}$	$\Delta\,\mathbf{max}(\%)$	$\boldsymbol{\sigma}$	$\Delta\boldsymbol{\sigma}(\%)$
No Mooring Hydrodynamics	9.65	1309.66	4137.04		447.60	
Mooring Hydrodynamics	0.00	1309.97	4154.54	0.42%	454.59	1.56%
Fairlead2	$\boldsymbol{min}$	$\boldsymbol{mean}$	$\boldsymbol{max}$	$\Delta\,\mathbf{max}(\%)$	$\boldsymbol{\sigma}$	$\Delta\boldsymbol{\sigma}(\%)$
No Mooring Hydrodynamics	268.28	776.29	1202.46		66.50	
Mooring Hydrodynamics	220.71	775.89	1207.73	0.44%	70.18	5.53%
Fairlead3	$\boldsymbol{min}$	$\boldsymbol{mean}$	$\boldsymbol{max}$	$\Delta\,\mathbf{max}(\%)$	$\boldsymbol{\sigma}$	$\Delta\boldsymbol{\sigma}(\%)$
No Mooring Hydrodynamics	259.47	788.16	1228.10		69.07	
Mooring Hydrodynamics	209.74	787.78	1231.16	0.25%	72.44	4.87%

Table 5-13: Fatigue sensibility study for the OC3 Hywind operational load case.

		C70		C47		C23		C0	
		$\boldsymbol{d}$	$\Delta\boldsymbol{d}(\%)$	$\boldsymbol{d}$	$\Delta\boldsymbol{d}(\%)$	$\boldsymbol{d}$	$\Delta\boldsymbol{d}(\%)$	$\boldsymbol{d}$	$\Delta\boldsymbol{d}(\%)$
Fairlead1	**No Mooring Hydrodynamics**	6.22E-05		3.70E-04		1.09E-03		2.42E-03	
	Mooring Hydrodynamics	6.22E-05	0.1%	3.70E-04	0.1%	1.10E-03	0.9%	2.48E-03	2.6%
Fairlead2	**No Mooring Hydrodynamics**	7.52E-07		2.66E-06		7.14E-06		1.16E-05	
	Mooring Hydrodynamics	7.58E-07	0.8%	2.70E-06	1.3%	7.31E-06	2.4%	1.26E-05	8.3%
Fairlead3	**No Mooring Hydrodynamics**	8.51E-07		3.05E-06		8.06E-06		1.31E-05	
	Mooring Hydrodynamics	8.58E-07	0.8%	3.09E-06	1.4%	8.26E-06	2.4%	1.42E-05	8.5%

Table 5-14: Fatigue sensibility study for the OC3 Hywind design load case.

		C70		C47		C23		C0	
		$\boldsymbol{d}$	$\Delta\boldsymbol{d}(\%)$	$\boldsymbol{d}$	$\Delta\boldsymbol{d}(\%)$	$\boldsymbol{d}$	$\Delta\boldsymbol{d}(\%)$	$\boldsymbol{d}$	$\Delta\boldsymbol{d}(\%)$
Fairlead1	**No Mooring Hydrodynamics**	6.260E-04		2.684E-03		8.024E-03		1.925E-02	
	Mooring Hydrodynamics	6.341E-04	1.3%	2.766E-03	3.0%	8.403E-03	4.7%	2.024E-02	5.1%
Fairlead2	**No Mooring Hydrodynamics**	7.012E-06		1.992E-05		4.744E-05		9.045E-05	
	Mooring Hydrodynamics	7.197E-06	2.6%	2.097E-05	5.3%	5.145E-05	8.5%	1.087E-04	20.2%
Fairlead3	**No Mooring Hydrodynamics**	7.479E-06		2.181E-05		5.213E-05		1.038E-04	
	Mooring Hydrodynamics	7.682E-06	2.7%	2.295E-05	5.2%	5.645E-05	8.3%	1.147E-04	10.5%

5.4 CONCLUSIONS

The influence of the wave hydrodynamics loads over the mooring system of FOWTs is appraised through the dynamic analysis of the moorings of two different concepts of floating platforms.

First, the simulation of an experiment allows the calibration of the numerical model including the wave hydrodynamic forces on the mooring line and, second, the assessment of the potential influence of the wave hydrodynamics over the total tension at the fairleads of a floating platform is presented. The results of the parametric study based on the experiment set-up show changes in the minimum maximum tension and also a clear increase of the standard deviation of the tension. Even though, a high-power regular wave train is used in the parametric analyses, those effects could be significant in irregular wave trains in full scale FOWT models. Also, it is found that larger chain diameters cause larger tension amplitudes that can affect the fatigue design of the mooring line.

The DeepCWind and the OC3 Hywind Spar platforms are simulated through different sea states. The results of the DeepCWind simulations show an increase of the standard deviation of the tension of 1.83 % for the most loaded line, and of 4.25% for the less loaded lines.

A parametric study of the depth of the fairlead in the OC3 Hywind Spar platform allowed better analysis of the energy received from the wave loads. The study shows the effects of the increment of the wave load impact on the mooring if the fairleads are positioned closer to the MSL for an operational and a design sea state. The results show an increase of the standard deviation of the tension in the moorings, which means larger stress ranges which effects the fatigue design. The deeper the fairlead, the lower effect of the wave loads on the mooring line tensions. Moreover, a sensibility fatigue analysis is performed to assess the contribution of the wave loads on the damage of the lines. The results obtained for the OC3 Hywind Platform show an increase of 2.6 % and 5.1 % of the damage for the most loaded line for the operational and design sea states, which significantly reduce the service life of the line. Even for the actual fairlead position, a 70 m depth, the wave loads also increase the damage about 1.3 % for the design load case, whereas the damage is almost unaltered for the operational load case. For the lines not aligned to the wave train, the increment of the damage is larger than the standard deviation, but the total damaged suffered is lower due to a lower stress range.

In addition, it is stated that placing the fairleads far from the center of gravity of a floating platform may reduce the service life of the mooring system. The increment of motion of the fairleads due to the coupling of the surge and pitch motions increasing the tension range, and can double the maximum tension of the line by generating slack-snap phenomenon.

Currently, chain diameters and tendons used in FOWT are becoming larger which will make them more sensitive to wave loads. Then, there is a need to properly assess the tension on the mooring lines including the wave hydrodynamic forces on the mooring dynamics for a proper evaluation of the design life of the mooring system.

6 DESIGN OPTIMIZATION FOR A TRUNCATED CATENARY MOORING SYSTEM FOR SCALE MODEL TEST

6.1 INTRODUCTION

The physical model testing is mainly performed in the ocean engineering basins, where the environmental conditions such as waves, currents and wind can be reproduced (Tomasicchio et al., 2012, Krivtsov & Linfoot, 2014). Furthermore, there are others facilities that can reproduce the ocean situations like wave flumes that are not commonly used due to their highly restrictive dimensions. On the other hand, the usage of these installations would help the development of the offshore wind technology allowing the performance of the model tests in more places and reducing costs in that research field.

Some wind offshore platforms model tests have been performed in wave flumes despite their limited width dimension. One example is a Tension Leg Platform (TLP) prototype tested in the CEHINAV (*Canal de*

Ensayos Hidrodinámicos), (Amate et al., 2014). In this particular case, a flume is a suitable place for testing because of the inner configuration of a TLP, a buoyant platform moored with vertical tethers. Even a spread mooring system does not seem to fit well in a wave flume; Kraskowski et al. (2012) tested a spar scale model with a four line mooring system in a flume. The azimuthal angles between two adjacent mooring lines were of 90 degrees. The lines were scaled in two different ways, the lines placed in the longitudinal direction of the tank are well-scaled using proper tethers, while in the transverse direction the mooring lines are modeled as two constant forces. The forces were applied by two ropes hanging on both sides of the flume with weights on their extremes. However, this simplification does not allow changing the waves relative direction to the platform position because the scaled mooring system only works in the longitudinal direction. Furthermore, a three line mooring system could not be scaled in the same way because the different symmetry between the mooring system and the wave flume. Then, in order to perform tests with different wave directions using the same scaled mooring system, an equivalent system with shorter radius to anchor should be designed. In such a mooring system, the line length should be truncated to allow placing all mooring lines in the wave flume. Other scale models have been tested in bigger basins, Damiani et al. (2015) use truncated mooring lines attached to springs because the depth of the basin does not match the model in the selected scale. Another solution to overcome the width basin constraint was adopted by Harnois et al. (2015), where the mooring line segment, constantly resting on the seabed during the tests, was removed. This lead to a shorter radius to anchor using the well scaled prototype mooring system.

The main contribution of this chapter is the design of a truncated mooring system to replace the prototype mooring system, which cannot be installed due to basin constraints. The truncated mooring system is designed as a simple mooring line composed of two materials without any other external systems as springs. This new mooring system allows the study of several wave approaching directions to the whole structure, floater and moorings. Tests results and the comparison with numerical simulations are also presented.

First, the real model and the scale model due to the basin constrains are presented. Then, the calculation of the static mooring forces and the optimization problem are described. Finally, the optimization and the experimental results, with the comparison with numerical simulations, are discussed.

6.2 REAL MODEL

The monolithic concrete spar, the so-called Windcrete (Molins et al., 2013), is a prototype floating platform for wind turbines developed in AFOSP (Alternative Floating Platform Designs for Offshore Wind Turbines using Low Cost Materials) within a KIC-InnoEnergy innovation project (Molins et al., 2014, Campos et al., 2015).

The spasr prototype is designed as a monolithic concrete structure from the top of the tower to the bottom of the buoy, thus joints are avoided to ensure water-tightness and a good fatigue behavior. The structure, for a 5 MW wind turbine, is composed of three parts: first, the buoy, composed of a cylinder with a diameter of 13 m and a height of 120 m; second, the transition segment, which is a cone of 10 m

high, these two parts are the submerged ones, therefore the total draft of the structure is 130 m. The third part is the emerged tower that reaches 87.6 m above the SWL. A sketch of the concept and its hydrodynamic characteristics are shown in Figure 6-1 and Table 6-1. The moorings system is connected to the platform at the fairleads located 60 m above the bottom with a draft of 70 m, near the Centre of Gravity (COG) to reduce the coupling motions between the surge and pitch.

In this study, the Windcrete is considered to be placed in a 265 m depth sea location. The mooring system is configured to provide enough restoring force to maintain the platform motion in a relative offset and to prevail over the wave and wind loads. In order to achieve simplicity in the model, the prototype mooring system is composed of three equispaced chain mooring lines with the same cross section. The main characteristics of the line are defined in the Table 6-2.

6.3 SCALE MODEL

Model tests were performed in the ICTS-CIEM (Investigation flume and offshore experimentation) inside LIM (Maritime Engineering Laboratory) at the UPC (Universitat Politècnica de Catalunya—BarcelonaTech). The flume is equipped with a wave generator that can generate waves from 10 cm up to 160 cm height. The flume is 100 meters long with a cross section 3.5 m wide and 5 m high. The flume and the wave paddle are shown in Figure 6-2.

According to the prototype's sizes and the flume height, the selected scale is 1:100. Then, the scaled depth would be 2.65 m. The flume width does not allow the direct scaling of the catenary lines because the common anchor radius should be between two and four times the total depth, requiring a 10 m wide channel. Furthermore, if several wave directions are studied, the mooring system should be able to rotate in *z* direction allowing the wave to impact on the platform from different relative direction with the mooring system. Then, the mooring system should not be connected through the flume wall. For these reasons, a truncated mooring system is used in the model scale test, reducing the radius to anchor distance, and therefore the total length of the lines. The Figure 6-3 shows the cross section of the wave flume with both the scale prototype mooring system and the truncated one.

The truncated mooring system is defined by the radius to anchor, the line length and the materials that compose the different segments of the mooring line. The radius to anchor is previously defined as the maximum radius allowed by the channel width taking account the margins for a proper installation operation of the mooring system. Furthermore, if the truncated mooring line were composed of a unique cross section, the necessary weight to achieve the restoring forces of the prototype system would cause huge vertical forces on the floating platform. For this reason, two different chain sections are chosen to design the mooring line. The heaviest line section is positioned at the bottom, connected to the anchor, providing the restoring horizontal force. The upper section, a light segment connected to the platform, reduces the total line payload due to its light weight. The exact properties of the lines are obtained through an optimization problem to fit the responses between the prototype mooring system and the truncated one, which is presented in next sections.

Table 6-1: Hydrostatic characteristics of Windcrete.

Property	Value
Displaced Volume [m^3]	1.69×10^4
Draft [m]	130.0
Concrete mass [kg]	8.71×10^6
Ballast mass [kg]	8.34×10^6
Wind turbine mass [kg]	3.50×10^5
CM [m]	53.34
CB [m]	63.97
Metacentric height [m]	10.57

Table 6-2: Prototype mooring line characteristics.

Property	Value
Depth [m]	265
Draft to fairlead [m]	70
Mooring depth	195
Radius to anchor [m]	660
Line length [m]	732.93
Line mass per unit length [kg/m]	150.3

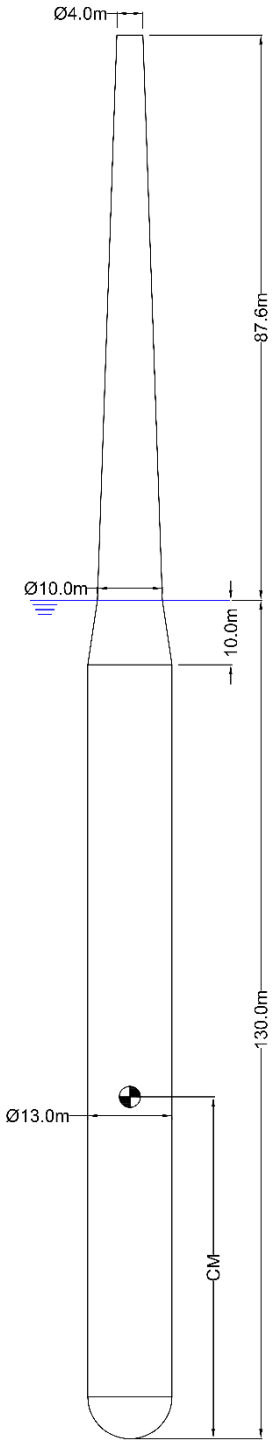

Figure 6-1:Sketch of Windcrete concept

Figure 6-2: CIEM wave paddle (left) and Wave flume (right)

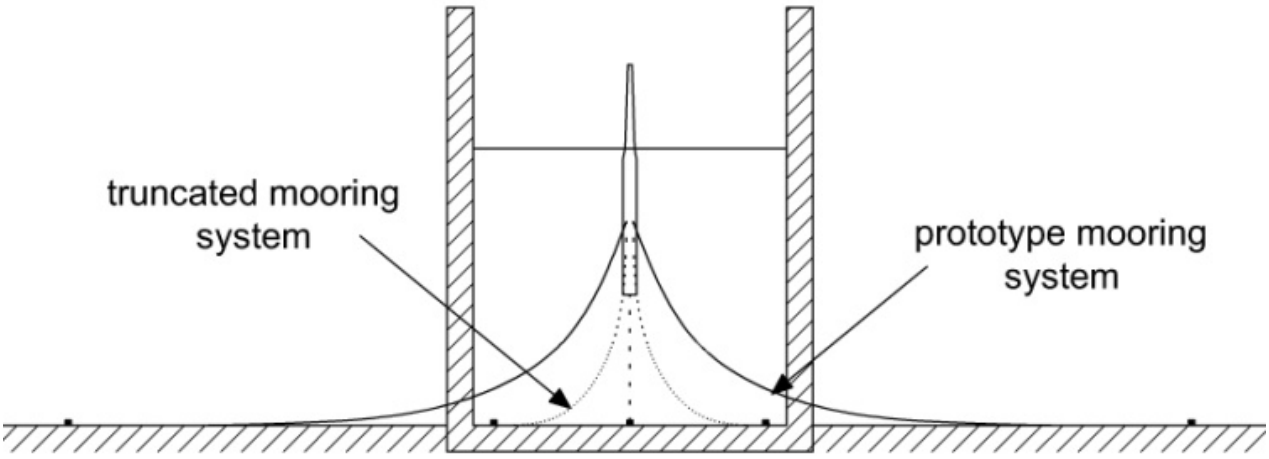

Figure 6-3: Prototype vs. truncated mooring system

6.4 OPTIMIZATION PROBLEM

The objective of the optimization problem is to determine a new catenary system presenting a similar static behavior of the prototype when the radius to anchor is reduced. This kind of problem can be expressed as a minimization problem, where the static response of the truncated mooring system has to

fit with the prototype ones in a non-scale scenario. Then the properties of the truncated mooring system will be well scaled for the tests.

The optimization problem can be expressed mathematically as Eq. (6.1):

$$\min\left[f(X)\right] \tag{6.1}$$

Subjected to the constraints expressed in Eq. (6.2) :

$$\begin{aligned} g_i(X) &\leq 0 \\ h_j(X) &= 0 \end{aligned} \tag{6.2}$$

where:

$f(X)\colon \mathbb{R}^n \longrightarrow \mathbb{R}$ is the objective function to be minimized over the variables X

$g_i(X) < 0$; $i = 1,\ldots,m$ are the inequality constraints

$h_j(X) = 0$; $j = 1,\ldots,p$ j = 1,…,p are the equality constraints

The design variables are the parameters that define the mooring line. In order to reduce the complexity of the optimization problem and the final design, the mooring truncated line would have two different segments. Each segment is defined by its lengths and chain diameter. Then, the design variables are the components of the vector X defined as $X = [d_1, d_2, l_1, l_2]$, where *d* is the diameter, *l* the segment length and the subscript defines the segment. The weight per unit length (ω) and the longitudinal stiffness (*EA*) of the segment line can be calculated from the chain diameter *(d [mm])*, using Equations (6.3) and (6.4).

$$\omega = 0.1875 d^2 \text{[N/m]} \tag{6.3}$$

$$EA = 90000 d^2 \text{[N]} \tag{6.4}$$

The objective function—to be minimized—is formulated from the prototype mooring line force responses (F_i) that have to be emulated. The objective function is evaluated in several points of the surge work range (x_j) since it is the main movement direction. The responses emulated are the horizontal and vertical restoring forces of the mooring system and the line tension. As shown in Figure 6-4, the objective function is expressed as the difference between the response of the prototype mooring system and the truncated one. This distance has to be minimized as a function of the mooring variables (X).

The objective function can be expressed as the sum of the single objective function of each property multiplied by a weight factor Eq. (6.5). The sum of all weight factors is 1: $\sum_{i=1}^{n} \omega_i = 1$.

$$f(X) = \omega_i \sum_{i=1}^{n} f_i(X) \tag{6.5}$$

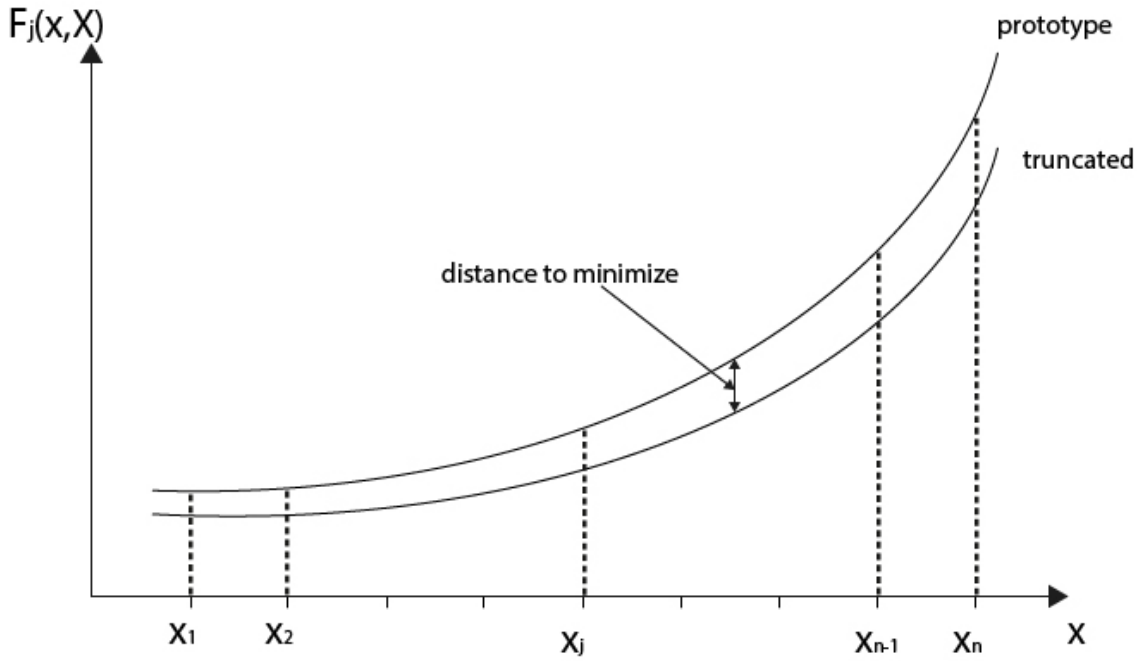

Figure 6-4: Prototype vs. truncated mooring system response

Each single objective function (Eq. (6.6)) is expressed as the root mean square value (rms) of the dimensionless difference between the prototype response and the truncated one, which are evaluated in the *n* selected surge points:

$$f_i(X) = \sqrt{\frac{1}{n}\sum_{j=1}^{n}\left(\frac{F_{i,prototype}(x_j) - F_{i,truncated}(x_j, X)}{F_{i,prototype}(x_j)}\right)^2} \tag{6.6}$$

The optimization problem is solved using the GlobalSearch Algorithm in *Matlab* (Mathworks, 2015), which uses a scatter-search mechanism for generating start points. From the starting points, GlobalSearch examines the trial points and choose the ones that can generate a better solution. Then, the chosen points are evaluated by a local minimization solver. The process ends when all the trial-points have been evaluated (Saxén & Bernander, 2014).

6.5 TRUNCATED MOORING SYSTEM DESIGN FOR WINDCRETE

The truncated mooring system was designed for a radius to anchor of 140 m. The objective function was evaluated for a surge excursion ranging from −40 to 25 m. Surge excursion is the main platform motion that depends on the mooring system response. The surge interval ensures a horizontal response for a 600 kN mean wind force. The asymmetry of the mooring system (Figure 6-5) produces an asymmetry response in surge.

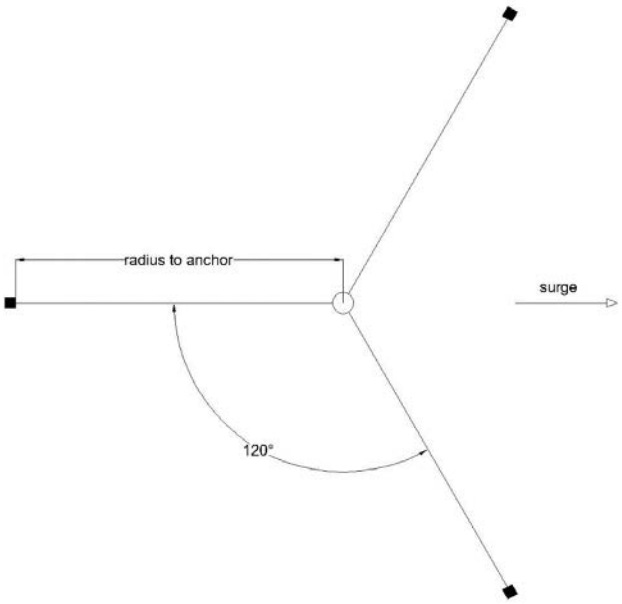

Figure 6-5: Mooring system sketch

The chosen characteristics of the prototype to be minimized in the multi-objective function are: the tension of one line, the horizontal mooring system response and the vertical mooring system response. Therefore the multi-objective function can be described as Eq. (6.7).

$$f(X) = \omega_T f_T(X) + \omega_{x,s} f_{x,s}(X) + \omega_{z,s} f_{z,s}(X)) \tag{6.7}$$

where f_T is the function to optimize the tension of a line; and $f_{x,s}$ and $f_{z,s}$ are the functions which describe the difference between the response prototype and truncated mooring system in x and $z$direction, respectively. Since the surge response is mainly depends on the mooring system, the largest weight factor $\omega_{x,s}$ is given to it. Selected weights are consistent with the references (Fan et al., 2012, Zhang et al., 2014). The weighting factors used for the multi-objective problem are 0.2, 0.6 and 0.2 for ω_T, $\omega_{x,s}$ and $\omega_{x,s}$ respectively. A sensitivity analysis of the variation of the weight factors was performed. It confirmed that low variations of the weight factors lead to a similar solution of the optimization problem.

The constraints applied to the problem are the length of the line, which is defined between its taut (Eq. (6.8)) and completely slack (Eq. (6.9)) shape. These constraints are expressed as a function of the radius to anchor and the mooring depth. Other constraints are the minimum and maximum diameter of the lines, defined by Eq. (6.10) and (6.11), respectively, which are fixed to get a feasible scalable chain for the tests.

$$l_1 + l_2 \geq \sqrt{140^2 + 195^2} = 240.1\ m \tag{6.8}$$

$$l_1 + l_2 \leq 140 + 195 = 335\ m \tag{6.9}$$

$$d_{min} > 60\ mm \tag{6.10}$$

$$d_{max} \leq 250\ mm \tag{6.11}$$

The solution of the optimization problem yields to a truncated catenary system composed by lines of two different segments with different weight per unit length. The segment *a* is the lower one and is linked to the anchor, while the segment *b* is the upper one and is connected to the platform. The segment *a* is heavier and shorter than segment *b*. With this configuration, the stiffness of the restoring force of the catenary system is mainly provided by the segment a, while the segment b contributes to reduce the suspended weight of the mooring line. The properties of each segment of the mooring line as a result of the optimization problem are shown in the Table 6-3.

Table 6-3: Truncated mooring line characteristics.

Segment a	**Diameter [mm]**	200.1
	Length [m]	80
	Line mass per unit length [kg/m]	878.6
Segment b	**Diameter [mm]**	58.4
	Length [m]	177
	Line mass per unit length [kg/m]	74.7

The response of the optimized catenary system is presented in Figure 6-6. Figure 6-6 (left) shows the comparison between the horizontal and the vertical response on both mooring systems. The horizontal response of the truncated system fits well with the prototype response. However, for large offsets, the responses start to diverge. The mooring system vertical force component is larger for the truncated one. The reduction of the radius to anchor implies an increment of the suspended weight on the platform for a similar horizontal force. Then, a deeper draft would be expected in the platform during the tests: of about 0.5 m. The line tension is well fitted along the whole surge excursion studied in the optimization problem (Figure 6-6 (right)).

6.6 EXPERIMENTAL RESULTS

The model is scaled at 1:100 factor using the Froude similitude. The platform model is made of aluminum to adjust the density of the material to be close to concrete, simplifying the fit of the rest of the platform parameters. The mooring lines are composed of two chain segments that adjusted to fit the weight per meter length computed in the optimization problem. The scale model placed inside the flume attached to the mooring system is shown in Figure 6-7.

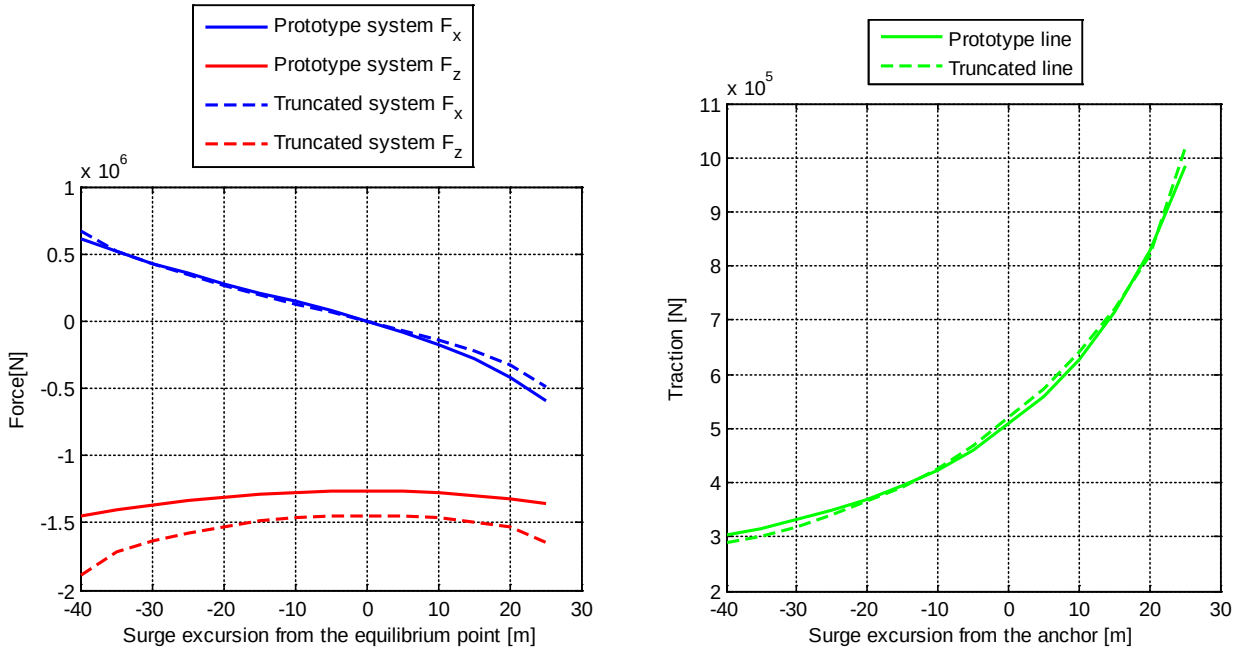

Figure 6-6: Mooring system response curves (left); Traction mooring line response (right)

Figure 6-7: Scale model inside the flume

The scaled prototype mooring line response were validated by checking the horizontal line response for a depth of 1.95 m and an excursion between 90 and 180 cm from the anchor. The results obtained in the static verification and the numerical results are plotted in Figure 6-8. The figure shows good agreement between both responses.

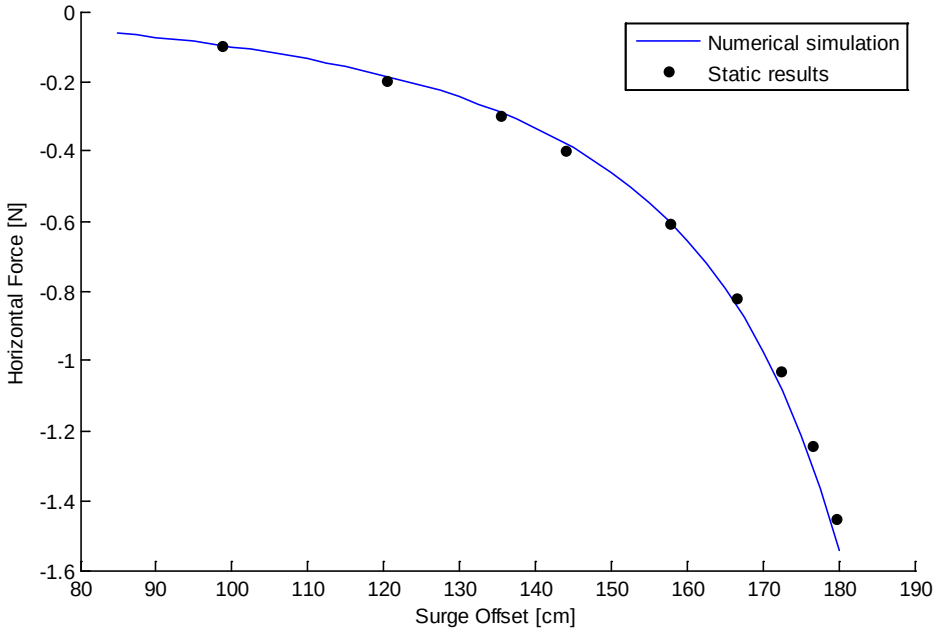

Figure 6-8: Comparative horizontal force response

Dynamic tests were carried out in several sea states with regular and irregular waves, and an almost constant wind force on the top of the nacelle. The experimental results were measured from the nacelle motion by an optical system which can track the 6 DOF (Campos, Molins, Gironella, Alarcón, et al., 2015).

Figure 6-9 shows the surge and heave response comparison between the experiment, the simulation with the truncated lines and the simulation of the platform equipped with the prototype mooring system. These responses correspond to a regular wave of 14 cm height and a period of 1.5 s, and a constant force on the top of the platform of 0.6 N to simulate the wind. The experimental results show good agreement between the test and the numeric simulation with the truncated lines in terms of mean offset, mean draft and also with the wave amplitude movement. However, some differences can be seen due to a low frequency movement that occurred during the test. This disturbance was produced by a long wave reflection in the longitudinal direction of the flume. In the transverse direction, no reflections were noticed. The simulation of the prototype mooring system shows a shorter total surge excursion than the truncated one. This difference is explained by two effects. First, the stiffness of the prototype mooring system for positive excursions is higher than the truncated ones, as is shown in Figure 6-6. Second, there is a loss of stiffness due to a draft increase of about 0.5 cm. In this situation, the lower depth of the fairlead position requires an increased excursion to achieve the same horizontal force. The draft increase can be noticed in the heave response (Figure 6-9b) as a decrease of the mean heave position of the truncated mooring compared to the prototype one.

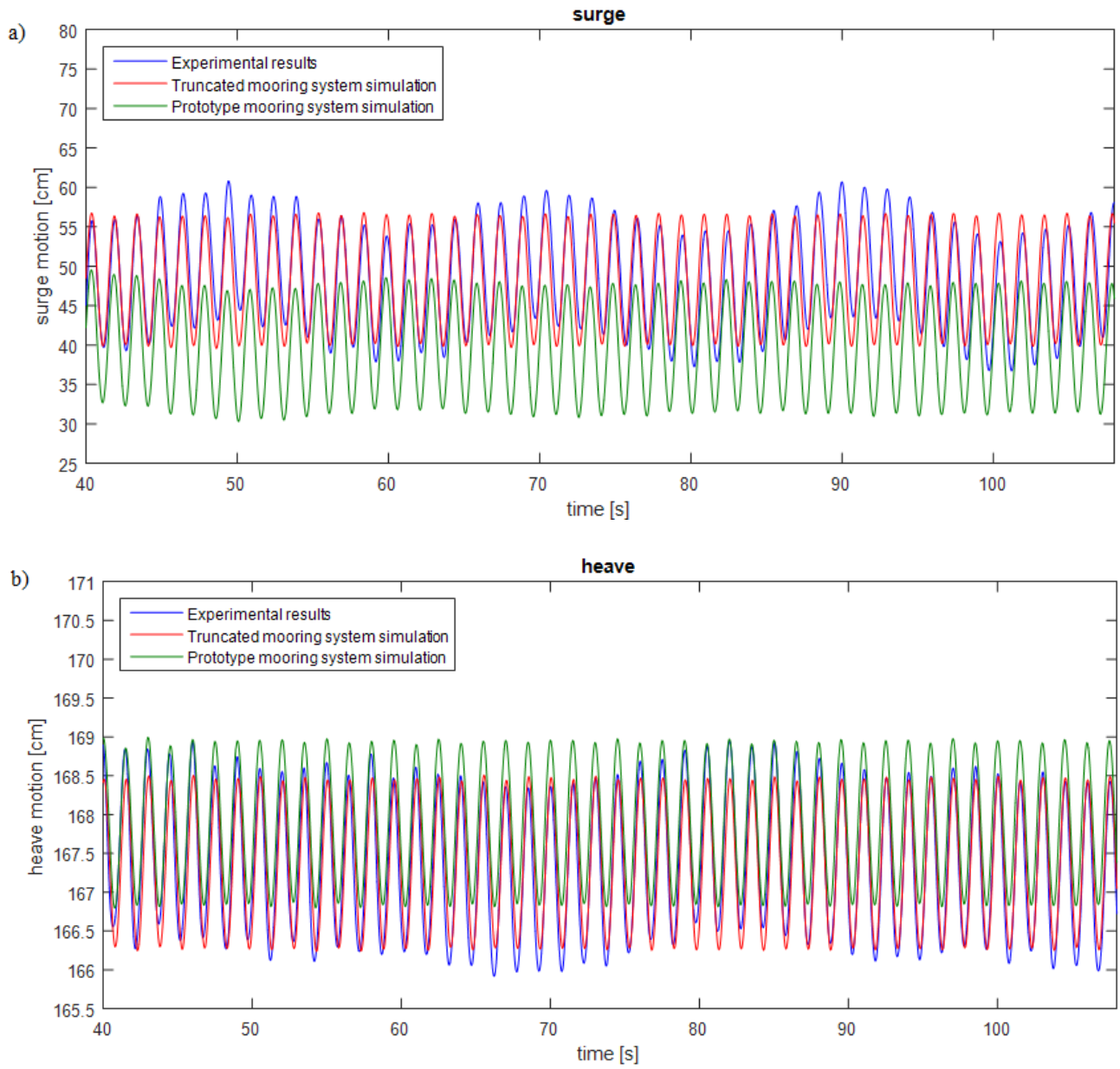

Figure 6-9: Comparison surge(a) and heave(b) nacelle motion response

The results of a Fast Fourier Transform (FFT) of the surge and heave platform responses are shown in Figure 15. Both diagrams show clearly the peak motion due to the wave excitation at a frequency of 0.66 Hz (period of 1.5 s) and the amplitudes match very well.

The main differences between the simulations and the experimental results are the excitation of the low frequency surge motion of the platform during the experiments, as already discussed. This affects the heave response, which FFT (Figure 6-10b) presents as two small peaks: at 0.05 Hz, the natural surge frequency, and at 0.337 Hz, the heave natural frequency.

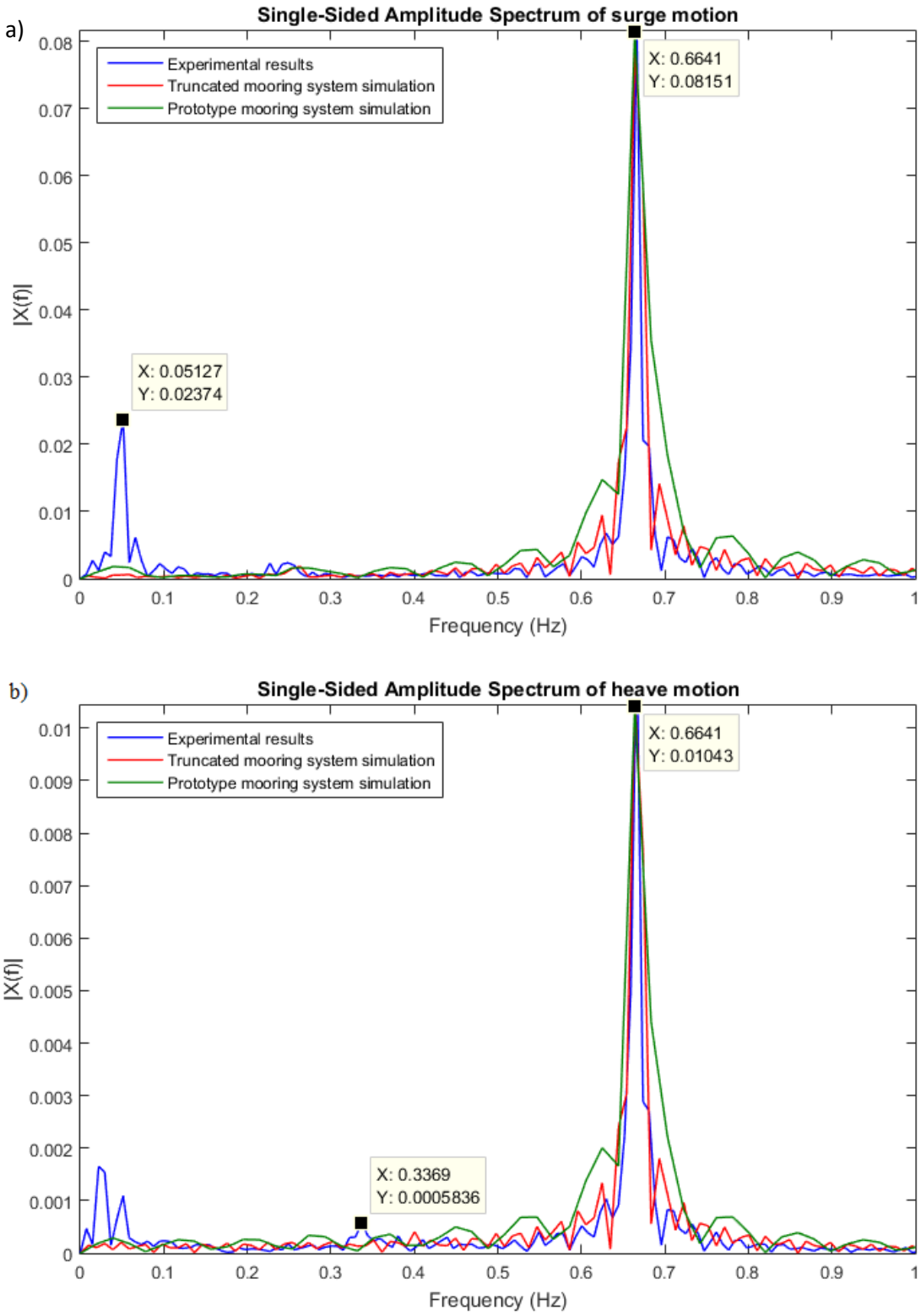

Figure 6-10: Surge(a) and heave (b) motion Fast Fourier Transform functions

6.7 CONCLUSIONS

This chapter describes and assesses the use of a truncated mooring system to emulate the real one in scaled experiments when there is a limitation of the available width in the flume. In this case, where the radius to anchor has to be reduced, an optimization problem based on the static mooring system response helped to fit the horizontal and vertical mooring responses and the traction force. The optimization problem is evaluated in the surge work range because is the main platform motion that depends on the mooring system response.

The truncated mooring line stiffness is obtained by using two different line sections: the bottom one is the heaviest and provides the horizontal mooring line stiffness. The upper section is lighter than the prototype mooring and reduces the vertical force on the platform.

The truncated catenary presents almost the same traction response as the completed prototype mooring system (differences less than 5%). On the other hand, the horizontal stiffness of the truncated system differs from the prototype, particularly for large excursions. In addition, the truncated mooring system presents a higher vertical force on the platform that lead to an increment of the draft.

Experiments are compared to numerical simulations with the real and prototype mooring system. The experimental results show good agreement with the numerical simulations. Some differences are noticed in the mean surge excursion of the truncated mooring system, which is larger. This is a consequence of the lower surge stiffness and an extra loss of stiffness due to the increase of the draft. Despite this, surge and heave responses due to wave loads are well predicted.

7 CONCLUSIONS

The present research has allowed achieving several innovative contributions to the field of station keeping analysis and design for floating offshore wind turbines. General conclusions are outlined in the following, whereas specific conclusions are given at the end of each chapter.

7.1 GENERAL CONCLUSIONS

Nowadays Finite Element Models have achieved a high degree of fidelity in the station keeping analysis. However, significant improvements can contribute to expand the applicability and accuracy of the models regarding the behavior of the use of new line types or materials like dynamic cables or synthetic lines. Furthermore, these numerical models have a high computational cost, which make difficult to perform fully fatigue assessment due to the large number of simulations required. This problem is usually dealt by using quasi-static using amplification factors to estimate the actual tension, the use of probabilistic techniques or employing large safety factors.

The design of the station keeping systems includes the verification of the response of the system against different phenomena like vortex induced motions and vibrations, slack-snap phenomenon or the direct hydrodynamic forces on the mooring lines. In addition, experimental test are required for validation purpose. However, some offshore basins are not large enough to enable the positioning of the mooring system, which has to be truncated emulating as much as possible the prototype mooring system.

This research presents two numerical models for the mooring line and station keeping system analysis that increase the applicability of the existing numerical models. The first model is a Finite Element Model based on the slender rod formulation that takes into account the rheological damping of the material in the axial and bending directions. The second model, is a novel model called quasi-dynamic model, which assess the dynamics of the mooring line from a dynamic approximation of the quasi-static response of the mooring line.

The extension of the slender rod finite element model applies the Kelvin-Voigt rheological model into the constitutive equations of the lines to implicitly consider the effects of the material damping in the dynamics simulations. The model shows good agreement with the validation cases and can predict the slack-snap phenomenon. The material damping also gives robustness to the model and can provide a damping source to prevent the propagation of the numerical errors.

The quasi-dynamic model is a new model that assesses the dynamic behavior of a catenary shape mooring line based on the quasi-static response. The quasi-static tension is updated from the theoretical dynamics of the line to obtain the quasi-dynamic tension. The verification examples performed within this research show good agreement for low and moderate excitation ranges. The model can also predict the slack-snap phenomenon but overestimates the actual tension because the high non-linearity of the problem and because there is no tension redistribution along the line. The speed up of the quasi-dynamic model is more than ten times than the dynamic model.

The quasi-dynamic model is cost computationally equivalent to the quasi-static model with only adding the estimation of the hydrodynamic and inertia forces on the integration points.

A research on the effect of the wave hydrodynamic forces over the mooring lines of FOWTs proofs that this forces cannot be despicable for certain cases. The use of large chain/wire ropes diameters and the location of fairleads close to the MSL make sensible the inclusion of the wave loads over the mooring lines for the mooring line design. The analysis performed in this research show that the damage of the most loaded line could increase a 2.6% for an operational sea state and a 5% for a design sea state.

Fairlead positions far from the center of gravity of Spar platforms could highly reduce the service life of the mooring lines due to the coupling between the surge and pitch motions at the top end of the line. The main effects of the surge and pitch coupling are the increase of the tension range of the line and the increase of the probability to produce the slack-snap phenomenon.

The research shows that optimization models are suitable to design scaled mooring systems. An optimization model is presented to design the scaled mooring system for the Windcrete platform. The optimazed truncated mooring line is formed of a heavier line segment at the seabed touchdown region and a light line in the suspended segment to be placed in a narrow flume basin. The combination of the two segments makes possible to fit the response of the prototype mooring system.

7.2 FUTURE RESEARCH

The present research has provided significant knowledge in the analysis and design of station keeping systems. However, the analysis of the results arise other interesting topics to study. Therefore, future research can investigate the following aspects.

- Deep seas over 200 m will present compromising decisions relative to mooring system design as the chain catenary system may be less cost competitive than synthetics ropes. In addition, there are few studies and models present in the literature of the FOWTs mooring system analysis and design. There are some models that account for large extensible materials, but there is a need of further research through experimental test to validate it. Furthermore, long-term assessment and performance of these types of material require further investigation due to its nonlinear behavior, like creep and its contribution to the life span of the mooring system.

- Development of a design basis to predict the slack-snap phenomenon in a predesign level stage. The increase of the knowledge of this phenomenon will allow to create tools for an easy prediction of the slack-snap behavior due to the platform excitation and avoided in the predesign.

- Development of accurate models that overcome the compromise between numerical costs and model reliability of the actual behavior of the mooring systems in FOWT parks, with shared mooring lines or anchor points to reduce the overall costs of the mooring system.

- To analyze the effects of the dynamic cable within the station keeping response. The dynamic cable connection point is a weak point that should be studied carefully to avoid large stresses that could lead to a premature failure of the connection.

BIBLIOGRAPHY

Aamo, O.M. & Fossen, T.I., 2000. Finite element modelling of mooring lines. *Mathematics and Computers in Simulation*, 53(July), pp.415–422.

Ablow, C.M. & Schechter, S., 1983. Numerical simulation of undersea cable dynamics. *Ocean Engineering*, 10(6), pp.443–457.

Airy, G.B., 1841. Tides and waves. *Hugh James Rose, et al. Encyclopædia Metropolitana. Mixed Sciences*, 3, p.396.

Allen, M.R., O.P. Dube, W. Solecki, F. Aragón-Durand, W. Cramer, S. Humphreys, M. Kainuma, J. Kala, N. Mahowald, Y. Mulugetta, R. Perez, M. Wairiu, and K. Zickfeld, 2018: Framing and Context. In: Global Warming of 1.5°C. An IPCC Special Report on the impacts of global warming of 1.5°C above pre-industrial levels and related global greenhouse gas emission pathways, in the context of strengthening the global response to the threat of climate change, sustainable development, and efforts to eradicate poverty [Masson-Delmotte, V., P. Zhai, H.-O. Pörtner, D. Roberts, J. Skea, P.R. Shukla, A. Pirani, W. Moufouma-Okia, C. Péan, R. Pidcock, S. Connors, J.B.R. Matthews, Y. Chen, X. Zhou, M.I. Gomis, E. Lonnoy, T. Maycock, M. Tignor, and T. Waterfield (eds.)]. In Press.

49Amate, J., López, V., Martín, D., García, L., Marugán, P., Gómez., A., 2014. Iberdrola Ingeniería TLPWIND " A smart way to drive costs down ." In *EWEA 2014 Posters*. p. PO.ID 270.

Aranha, J.A.P. & Pinto, M.O., 2001. Dynamic tension in risers and mooring lines: An algebraic approximation for harmonic excitation. *Applied Ocean Research*, 23(2), pp.63–81.

Argyros, A., Langley, R.S. & Ahilan, R. V, 2011. Simplifying Mooring Analysis for Deepwater Systems using Truncation. In *Proceedings of the Twenty-first (2011) International Offshore and Polar Engineering Conference*. Maui, Hawaii, USA, pp. 195–202.

Azcona, J., 2016. *Computational and experimental modelling of mooring line dynamics for offshore floating wind turbines*. E.T.S.I. Navales (UPM).

Azcona, J. Palacio, D., Munduate, X., González, L., Nygaard, T., 2017. Impact of mooring lines dynamics on the fatigue and ultimate loads of three offshore floating wind turbines computed with IEC 61400-3

guideline. *Wind Energy*, 20(5), pp.797–813.

Bai, Y. & Niedzwecki, J.M., 2018. Meshfree analysis of structures modeled as extensible slender rods. *Engineering Structures*, 156, pp.82–91.

Barrera, C., Battistella, T., Guanche, R., Losada, I., 2020. Mooring system fatigue analysis of a floating offshore wind turbine. *Ocean Engineering journal*, 195

Batchelor, G.K., 1967. *An Introduction to Fluid Dynamics* 2002nd ed. F. C. M. Library, ed., Cambridge: Cambridge University Press.

Benassai, G., Campanile, A., Piscopo, V., Scamardella, A., 2014. Ultimate and accidental limit state design for mooring systems of floating offshore wind turbines. *Ocean Engineering*, 92, pp.64–74.

Blue H Engineering, O., 2017. *Blue H Engineering*,

Borisade, F., Choisnet, T. & Cheng, P.W., 2016. Design study and full scale MBS-CFD simulation of the IDEOL floating offshore wind turbine foundation. *Journal of Physics: Conference Series*, 753(092002).

Brommundt, M, Krause, L., Merz, K., Muskulus, M., 2012. Mooring system optimization for floating wind turbines using frequency domain analysis. *Energy Procedia*, 24(January), pp.289–296.

Buckham, B.J., 2003. *Dynamics modelling of low-tension tethers for submerged remotely operated vehicles*. University of Victoria.

Campanile, A., Piscopo, V. & Scamardella, A., 2018. Mooring design and selection for floating offshore wind turbines on intermediate and deep water depths. *Ocean Engineering*, 148(November 2017), pp.349–360.

Campos, A., Molins, C., Trubat, P., Alarcón, D., 2017. A 3D FEM model for floating wind turbines support structures. In *Energy Procedia*. Elsevier B.V., pp. 177–185.

Campos, A., Molins, C., Gironella, X., Trubat, P., Alarcón, D., 2015. Experimental rao's analysis of a monolithic concrete spar structure for offshore floating wind turbines. In *Proceedings of the 34th International Conference on Ocean, Offshore and Arctic Engineering. OMAE 2015*. St. John's, NL, Canda, pp. 1–9.

Campos, A., Molins, C., Gironella, X., Alarcón, D., Trubat, P., 2015. Experiments on a scale model of a monolithic concrete spar for floating wind turbines. In *Proceedings of EWEA Offshore 2015 Copenhagen*. p. 10.

Campos, A., Molins, C., Gironella, X., Trubat, P., 2016. Spar concrete monolithic design for offshore wind turbines. *Proceedings of the Institution of Civil Engineers - Maritime Engineering*, 169(2), pp.49–63.

Chakrabarti, S., 2005. *Handbook of Offshore Engineering*, Elsevier.

Chen, L. & Basu, B., 2018. Development of an open-source simulation tool for mooring systems Development of an open-source simulation tool for mooring systems. In *Ceri-Itrn2018*.

Choisnet, T., Rogier, E.. Percher, Y., Courbois, A., Crom, I., Mariani, R., 2018. Performance and mooring qualification in Floatgen: the first French offshore wind turbine project. *16ième Journées de l'Hydrodynamique*, (1), pp.1–10.

Christensen, R.M., 1982. Chapter I - Viscoelastic Stress Strain Constitutive Relations. In R. M. Christensen, ed. *Theory of Viscoelasticity (Second Edition)*. Academic Press, pp. 1–34.

Chung, J. & Hulbert, G.M., 1993. A Time Integration Algorithm for Structural Dynamics With Improved Numerical Dissipation: The Generalized-α Method. *Journal of Applied Mechanics*.

Claren, R. & Diana, G., 1969. Mathematical Analysis of Transmission Line Vibration. *IEEE Transactions on Power Apparatus and Systems*, PAS-88(12), pp.1741–1771.

Corbetta, G., 2015. Wind energy scenarios for 2030. *EWEA Report*, pp.1–8.

Corewind, 2019. COst REduction and increase performance of floating WIND technology | COREWIND Project | H2020 | CORDIS | European Commission.

Crisfield, M.A., 2000. *Non-linear Finite Element Analysis of Solids and Structures. Volume 2 Advanced Topics*, John Wiley & Sons Ltd.

Cummins, W.E., 1962. The impulse response function and ship motions. *Schiffstechnik*.

Damiani, L., Musci, E., Tomascchio, G.R., D'Alessandro, F., 2015. Spar buoy numerical model calibration and verification. In *VI International Conference on Computational Methods in Marine Engineerint, Marine 2015*. Rome, pp. 814–825.

DNVGL, 2015. Offshore Standard DNVGL-OS-E301 Position mooring. , (July).

Driscoll, F., Jonkman, J., Robertson, A., Sirnivas, S., Skaare, B., Nielsen, F. G., 2016. Validation of a FAST Model of the Statoil-hywind Demo Floating Wind Turbine. *Energy Procedia*, 94, pp.3–19.

Equinor, 2019. Hywind - leading floating offshore wind solution - equinor.com. Available at: https://www.equinor.com/en/what-we-do/hywind-where-the-wind-takes-us.html [Accessed November 25, 2019].

European Commission, 2020. Horizon 2020 Work Programme 2018-2020. Secure , clean and efficient energy. , 2019(July 2018).

Fabry, V., Seibel, B. , Feely, R., Orr, J., 2008. Impacts of ocean acidification on marine fauna and ecosystem processes. *ICES Journalof Marine Science*, 65, pp.414–432.

Faltinsen, O.M., 1990. *Sea loads on ships and offshore structures*, Cambridge University Press.

Fan, T., Qiao, D. & Ou, J., 2012. Optimized Design of Equivalent Truncated Mooring System Based on Similarity of Static and Damping Characteristics Governing Equation of Mooring Line. In *Proceedings of the Twenty-second (2012) International Offshore and Polar Engineering Conference*. Rhodes, Greece, pp. 959–966.

Felippa, C., 2000. A systematic approach to the element-independent corotational dynamics of finite elements. *Report No. CU-CAS-00-03*, (Jaunary).

Flory, J.F., Banfield, S.P. & Petruska, D.J., 2004. Defining, Measuring, and Calculating the Properties of Fiber Rope Deepwater Mooring Lines. In *Offshore Technology Conference*. Houston, Texas U.S.A.: Society of Petroleum Engineers (SPE).

Fontana, C., Arwade, S., DeGroot, D., Myers, A., Landon, M., Aubeny, C., 2016. Efficient multiline anchor systems for floating offshore wind turbines. *Proceedings of the International Conference on Offshore Mechanics and Arctic Engineering - OMAE*, 6, pp.1–7.

Foti, F., Martinelli, L. & Perotti, F., 2016. A new approach to the definition of self-damping for stranded cables. *Meccanica*, 51(11), pp.2827–2845.

Fylling, I. & Berthelsen, P.A., 2011. WINDOPT - An optimization tool for floating support structures for deep water wind turbines. *Proceedings of the International Conference on Offshore Mechanics and Arctic Engineering - OMAE*, 5(January 2011), pp.767–776.

Garrett, D.L., 1982. Dynamic Analysis of Slender Rods. *Journal of Energy Resources Technology*, 104(4), pp.302–306.

Gobat, J.I. & Grosenbaugh, M. a., 2001. Application of the generalized-α method to the time integration of the cable dynamics equations. *Computer Methods in Applied Mechanics and Engineering*, 190(37–38), pp.4817–4829.

Gobat, Jason I. & Grosenbaugh, M.A., 2001. A simple model for heave-induced dynamic tension in catenary moorings. *Applied Ocean Research*, 23(3), pp.159–174.

Gobat, J.I. & Grosenbaugh, M.A., 2006. Time-domain numerical simulation of ocean cable structures. *Ocean Engineering*, 33(10), pp.1373–1400.

Goudreau, S. et al., 1998. Bending Energy Dissipation of Simplified Single-Layer Stranded Cable. *Journal of Engineering Mechanics*, 124(8), pp.811–817.

Goupee, A., Fowler, M., Kimball, R., Helder, J., de Ridder, E., 2014. Additional Wind/Wave Basin Testing of the DeepCwind Semi-Submersible With a Performance-Matched Wind Turbine. In *Volume 9B: Ocean Renewable Energy*. p. V09BT09A026.

Großmann, J., Dahlhaus, F., Adam, F., Schuldt, B., 2014. *The GICON ®-TLP for wind turbines: Experimental Studies and numerical Modelling of structural Behavior of a Scaled Modular TLP Structure for Offshore Wind turbines*.

Guyot, M., Connolly, A. & Le Boulluec, M., 2019. Experimental offshore floating wind turbine prototype and numerical analysis during harsh and production events. In *Proceedings of the ASME 2019 2nd International Offshore Wind Technical Conference IOWTC2019*.

Dagher, H., Viselli, A., Goupee, A., Kimball, R., Allen, ., 2017. *The VolturnUS 1:8 Floating Wind Turbine: Design, Construction, Deployment, Testing, Retrieval, and Inspection of the First Grid-Connected Offshore Wind Turbine in US*, Available at: https://www.osti.gov/servlets/purl/1375022.

Hallowell, S., Arwade, S., Fontana, C., DeGroot, D., Aubeny, C., Diaz, B., Myers, A., Landon, M., 2018. System reliability of floating offshore wind farms with multiline anchors. *Ocean Engineering*, 160(February), pp.94–104.

Hardy, C., 1990. Analysis of self-damping characteristics of stranded cables in transverse vibrations. In *Proceedings of the CSME Mechanical Engineering Forum*. Otawa (Canada), pp. 117–122.

Harnois, V., Weller, S., Johanning, L., Thies, P., Le Boulluec, M., Le Roux, D., Soulé, V., Ohana, J., 2015. Numerical model validation for mooring systems : Method and application for wave energy converters. *Renewable Energy*, 75(March), pp.869–887.

Hasselmann, K., Barnett, T., Bouws, E., Carlson, H., Cartwright, D., Enke, K., Ewing, J. A., Gienapp, H., Hasselmann, D., Kruseman, P., Meerburg, A., Muller, P., Olbers, D. J., Richter, K., Sell, W., Walden, H., 1973. Measurements of Wind-Wave Growth and Swell Decay during the Joint North Sea Wave Project (JONSWAP). *Ergnzungsheft zur Deutschen Hydrographischen Zeitschrift Reihe*, A(8)(8 0), p.p.95.

Hegseth, J.M. & Bachynski, E.E., 2019. A semi-analytical frequency domain model for efficient design evaluation of spar floating wind turbines. *Marine Structures*, 64(October 2018), pp.186–210.

Helder, J. & Pietersma, M., 2013. *DeepCwind/OC4 Semi Floating Wind Turbine Repeat Tests. MARIN Report No. 27005-1-OB*,

Hilber, H.M., Hughes, T.J.R. & Taylor, R.L., 1977. Improved numerical dissipation for time integration algorithms in structural dynamics. *Earthquake Engineering and Structural Dynamics*, (5), pp.283–292.

Howell, C.T., 1992. *Investigation of the Dynamics of Low-Tension Cables*. Massachsetts Institute of Technology.

Hsu, W. ting, Thiagarajan, K.P. & Manuel, L., 2017. Extreme mooring tensions due to snap loads on a floating offshore wind turbine system. *Marine Structures*, 55, pp.182–199.

IEA, 2018. Offshore Energy Outlook.

Inman, D.J., 2001. *Engineering vibration*, Pearson Education.

IPCC, 2014. *Climate Change 2014: Synthesis Report. Contribution of Working Groups I, II and III to the Fifth Assessment Report of the Intergovernmental Panel on Climate Change*, Geneva, Switzerland.

IPCC, 2018. *Summary for Policymakers. In: Global Warming of 1.5°C.*, IPCC.

James, R. & Costa, M., 2015. Floating Offshore Wind : Market and Technology Review. , (June), pp.1–168.

Jonkman, B. & Jonkman, J., 2016. *FAST v8.16.00a-bjj*, National Renewable Energy Laboratory.

Jonkman, J., Butterfield, S., Musial, W., Scott, G., 2009. *Definition of a 5-MW reference wind turbine for offshore system development*, National Renewable Energy Laboratory.

Jonkman, J., 2009. *Definition of the Floating System for Phase IV of OC3*, NWTC - NREL.

Jonkman, J. & Musial, W., 2010. IEA Wind Task 23 Offshore Wind Technology and Deployment Subtask 2 The Offshore Code Comparison Collaboration (OC3).

Journée, J.M.J. & Massie, W.. W., 2001. *Offshore hydromechanics*, Delft: Delft University od Technology.

Kim, Y.-B., 2003. *Dynamic Analysis of multiple-body floating platforms coupled with mooring lines and risers*. Texas A&M University.

Koh, C.G., Zhang, Y. & Quek, S.T., 1999. Low-Tension Cable Dynamics: Numerical and Experimental Studies. *Journal of Engineering Mechanics*, 125(3)(March), pp.347–354.

Komatsu, M. et al., 2016. *Development of Offshore Wind Turbine Floater that Blends into Japanese Waters - Evaluation of the Validity for Design and Applied Methods for V-shaped Semi-submersible Floating structure -*,

Kraskowski, M., Zawadzki, K. & Rylke, A., 2012. A Method for Computational and Experimental Analysis of the Moored Wind Turbine Seakeeping. In *18th Australasian Fluid Mechanics Conference*. Launceston, Australia.

Krivtsov, V. & Linfoot, B., 2014. Basin Testing of Wave Energy Converters in Trondheim: Investigation of Mooring Loads and Implications for Wider Research. *Journal of Marine Science and Engineering*, 2(2),

pp.326–335.

Laya, E.J., Connor, J.J. & Sunder, S.S., 1984. Hydrodynamic Forces on Flexible Offshore Structures. *Journal of Engineering Mechanics*, 110(3), pp.433–448..

Lenci, S. & Callegari, M., 2005. Simple analytical models for the J-lay problem. *Acta Mechanica*, 178(1–2), pp.23–39.

Lerch, M., De-prada-gil, M. & Molins, C., 2019. Collection Grid Optimization of a Floating Offshore Wind Farm Using Particle Swarm Theory. *Journal of Physics: Conference Series*, 1356, 0120.

LHEEA, 2014. *NEMOH User's manual*, Nantes (France): École Central de Nantes.

Lin, Z. & Sayer, P., 2015. An enhanced stiffness model for elastic lines and its application to the analysis of a moored floating offshore wind turbine. *Ocean Engineering*, 109, pp.444–453.

Lindahl, J., 1985. *Modellförsök med en förankringskabel. Report Series A:12*,

MacCamy, R.C. & Fuchs, R.A., 1954. Wave Forces on Piles: A Diffraction Theory. *U.S. Army coastal engineering Research Center (formerly Beach Erosion Board), Technical Memorandum No. 69*.

Manjock, A. & Starr, M.S., 2019. Loading and structural analysis of the self-aligning Hystoh floating wind turbine concept. In *Proceedings of the ASME 2019 2nd International Offshore Wind Technical Conference*. St. Julian's, Malta, pp. 1–12.

Martin, O., 2017. Nonlinear dynamic analysis of viscoelastic beams using a fractional rheological model. *Applied Mathematical Modelling*, 43, pp.351–359.

Masciola, M. et al., 2013. Assessment of the Importance of Mooring Dynamics on the Global Response of the DeepCwind Floating Semisubmersible Offshore Wind Turbine. *23th International Offshore and Polar Engineering*, 9, pp.359–368.

Matha, D. et al., 2011. Challenges in Simulation of Aerodynamics , Hydrodynamics , and Mooring-Line Dynamics of Floating Offshore Wind Turbines. *Engineering Conference*, 8(October), pp.421–428.

Mathworks, 2015. *Global Optimization Toolbox User ' s Guide R 2015 b*, Mathworks.

McCormick, M.E., 2014. *Ocean Engineering Mechanics With Applications*, Cambridge University Press.

Mezger, T.G., 2014. *The Rheology Handbook*, Vincentz Network.

Molins, C., Trubat, P., Gironella, X., Campos, A., 2014. Design optimization for a truncated catenary mooring system for scale model test. In *Asranet Conference on Offshore Renewable Energy, Glasgow*. Glasgow: ASRANET, p. 9.

Molins, C., Campos, A., Sandner, F., Matha, D., 2014. Monolithic concrete off-shore floating structure for wind turbines. In *EWEA 2014 Scientific Proceedings*. Barcelona, Spain, pp. 107–111.

Molins, C., Rebollo, J. & Campos, A., 2013. *Estructura flotante de hormigón prefabricado para soporte de aerogeneradores*, Patent WO 2013/093160 A1.

Morison, J., Johnson, J.W. & Schaaf, S.A., 1950. The Force Exerted by Surface Waves on Piles. *Journal of Petroleum Technology*, 2(05), pp.149–154.

Müller, K., Matha, D., Tiedemann, S., Proskovics, R., Lemmer, F., 2018. LIFES50+, Deliverable 7.5 Guidance

on platform and mooring line selection, installation and marine operations. , pp.1–70.

Nakajima, T., Motora, S. & FujinoM., 1982. On the dynamic analysis of multicomponent mooring lines. *OTC paper 4309*.

Niedzwecki, J.M. & Thampi, S.K., 1991. Snap loading of marine cable systems. *Applied Ocean Research*, 13(1), pp.2–11.

OECD/IEA, 2017. Renewables 2017 Executive Summary.

Oliveto, N.D. & Sivaselvan, M. V., 2015. 3D Finite-Deformation Beam Model with Viscous Damping: Computational Aspects and Applications. *Journal of Engineering Mechanics*, 141(1), p.04014103.

Palm, J., Paredes, G., Pinto, F., Bergdahl, L., 2013. Simulation of Mooring Cable Dynamics Using a Discontinuous Galerkin Method. In *International Conference on Computational Methods in Marine Engineering - MARINE*. pp. 1–12.

Palm, J., Eskilsson, C. & Bergdahl, L., 2017. An hp-adaptive discontinuous Galerkin method for modelling snap loads in mooring cables. *Ocean Engineering*, 144(August), pp.266–276.

Di Paola, M., Heuer, R. & Pirrotta, A., 2013. Fractional visco-elastic Euler-Bernoulli beam. *International Journal of Solids and Structures*, 50(22–23), pp.3505–3510.

Paredes, G., Palm, J., Eskilsson, C., Bergdahl, L., Pinto, F., 2013. Modelação Numérica de Sistemas de Amarração para Conversores Flutuantes de Energia das Ondas. In *8.as Jornadas de Hidráulica, Recursos Hídricos e Ambiente*. pp. 41–48.

Pegalajar-Jurado, A., Borg, M. & Bredmose, H., 2018. An efficient frequency-domain model for quick load analysis of floating offshore wind turbines. *Wind Energy Science*, 3(2), pp.693–712.

Peiffer, A., 2018. WindFloat : Ready for Commercial Deployment on the US West Coast . Introduction to Principle Power. In *POET Conference in Portland, OR*. POET Conference in Portland, OR.

Petrone, C., Oliveto, N.D. & Sivaselvan, M. V., 2016. Dynamic Analysis of Mooring Cables with Application to Floating Offshore Wind Turbines. *Journal of Engineering Mechanics*, 142(3), p.04015101.

Qiao, D. & Ou, J., 2014. Truncated model tests for mooring lines of a semi-submersible platform and its equivalent compensated method. *Journal of Marine Science and Technology*, 22(2), pp.125–136.

Quéau, L.M., Kimiaei, M. & Randolph, M.F., 2014. Analytical estimation of static stress range in oscillating steel catenary risers at touchdown areas and its application with dynamic amplification factors. *Ocean Engineering*, 88, pp.63–80.

Rao, S.S., 2011. *Mechanical vibrations*, Prentice Hall.

de Ridder, E., Otto, W., Zondervan, G., Huijs, F., Vaz, G., 2014. Development of a Scaled-Down Floating Wind Turbine for Offshore Basin Testing. In *Volume 9A: Ocean Renewable Energy*. ASME, p. V09AT09A027.

Robertson, A., Jonkman, J. Masciola, M., Song, H., Goupee, A., Coulling, A., Luan, C., 2014. *Definition of the Semisubmersible Floating System for Phase II of OC4*, National Renewable Energy Laboratory.

Robertson, A. & Jonkman, J., 2019. *Annex 30 – Task Extension Proposal , 2019-2022 Offshore Code Comparison Collaboration , Continued , with Correlation , and unCertainty (OC6) 1 Scope*, IEA.

Robertson, A., Jonkman, J., Wendt, F., Goupee, A., Dagher, H., 2016. *Definition of the OC5 DeepCwind Semisubmersible Floating System*, IEA.

Robertson, A, Wendt, F., Jonkman, J., Popko, W., Gueydon, S., Qvist, J., Vittori, F., Uzunoglu, E. ,Yde, A., Galinos, C., Hermans, K., Bernardus, J., Vaal, D., Bozonnet, P., Bouy, L., Bayati, I., Bergua, R., Galvan, J., Mendikoa, I., Barrera, C., Shin, H., Molins, C., Debruyne, Y., 2017. OC5 Project Phase II: Validation of Global Loads of the DeepCwind Floating Semisubmersible Wind Turbine. *Energy Procedia*, 137, pp.38–57.

Saxén, A. & Bernander, K.B., 2014. *Parallel global optimization ABB's metal process models using Matlab*, UPPSALA UNIERSITET.

Sedghi, H. & Kimiaei, M., 2018. Effects of mooring line design parameters on the line dynamics and fatigue response of subsea mooring lines. *Proceedings of the International Conference on Offshore Mechanics and Arctic Engineering - OMAE*, 1, pp.1–11.

Sharma, J.N. & Dean, R.G., 1981. SECOND-ORDER DIRECTIONAL SEAS AND ASSOCIATED WAVE FORCES. *Society of Petroleum Engineers journal*, 21(1), pp.129–140.

Stansberg, C.T., Karlsen, S.I. & Ward, E.G., 2004. OTC 16587 Model Testing for Ultradeep Waters. In *Offshore Technology Conference*. Houston, Texas, U.S.A., pp. 1–9.

Stansberg, C.T., Oritsland, O. & Ormberg, H., 2001. Challenges in Deep Water Experiments: Hybrid Approach. In *20th International Conference on Offshore Mechanics and Arctic Engineering. OMAE2001/OFT-1352*. pp. 1–9.

Suhara, T., Koterayama, W., Tasai, F., Hiyama, H., Sao, K., Watanabe, K., 1981. Dynamic behavior and tension of oscillating mooring chain. *Proceedings of the Annual Offshore Technology Conference*, 1981-May, pp.415–418.

Sumer, B.M. & Fredsoe, J., 2006. *Hydrodynamics Around Cylindrical Structures*, World Scientific.

Tahar, A. & Kim, M.H., 2008. Coupled-dynamic analysis of floating structures with polyester mooring lines. *Ocean Engineering*, 35(17–18), pp.1676–1685.

Timoshenko, S.P.S.P. & Gere, J.J.M., 1963. *Theory of elastic stability*, McGraw-Hill.

Tjavaraas, A., Zhu, Q., Liu, Y., Triantafylloy, M., Yue, D., 1998. The mechanics of highly-extensible. *Journal of Sound and Vibration*, 213(4), pp.709–737.

Tomasicchio, G., Armenio, E., Alessandro, F., Fonseca, N., Mavrakos, S., Penchev, V., Schüttrumpf, H., Voutsinas, S., Kirkegaard, J., Jensen, P., 2012. Design of a 3D physical and numerical experiment on floating off-shore wind turbines. In *Proceedings 32th International Conference on Coastal Engineering*. Santander.

Trubat, P., Molins, C., Hufnagel, P., Alarcón, D., Campos, A., 2018. Application of morison equation in irregular wave trains with high frequency waves. In *Proceedings of the International Conference on Offshore Mechanics and Arctic Engineering - OMAE*. Madrid, pp. 1–10.

Trubat, P., Campos, A., Molins, C., Alarcón, D., 2017. OC5 task II simulations with FloaWDyn numerical model. In *Proceedings of the International Offshore and Polar Engineering Conference*. San Francisco.

Trubat, P. & Molins, C., 2019. Rheological damping of slender rods. *Marine Structures*, 67.

United Nations, O., 2015. *Convención Marco sobre el Cambio Climático - Aprobación del Acuerdo de París*, UN.

Vryhof, 2015. *Vryhof Manual The guide to anchoring*, Vryhof.

Walton, T.S. & Polachek, H., 1959. *Calculation of nonlinear transient motion of cables*, Defense Documentation Center.

Wheeler, J.D., 1970. Method for Calculating Forces Produced by Irregular Waves. *Journal of Petroleum Technology*, 22, pp.359–367.

Wilcox, D.C., 1993. *Turbulence Modeling for CFD*, La Cañada, California: DWC Industries, Inc.

WindEurope, 2018. *Floating offshore wind energy, a policy blueprint for europe*, Wind Europe.

Woodward, A., 2011. DeepCwind Tirelessly Developing Floating Offshore Wind | Volumatrix Group. Available at: http://volumatrixgroup.com/?p=1258 [Accessed March 9, 2016].

X1Wind, 2019. Technology – X1 Wind. Available at: http://www.x1wind.com/x1wind-technology/ [Accessed November 25, 2019].

Young, D.G. et al., 2018. Predicting failure of dynamic cables for floating offshore wind. *Advances in Renewable Energies Offshore - Proceedings of the 3rd International Conference on Renewable Energies Offshore, RENEW 2018*, (October), pp.821–828.

Zhang, H., Huang, S. & Guan, W., 2014. Optimal design of equivalent water depth truncated mooring system based on baton pattern simulated annealing algorithm. *China Ocean Engineering*, 28(1), pp.67–80. Available at: http://link.springer.com/10.1007/s13344-014-0005-8 [Accessed May 28, 2014].

8 APPENDIX 1: FLOAWDYN MODEL

8.1 MODEL OVERVIEW

The FloaWDyn model is an aero-hydro-servo-elastic tool developed at UPC Barcelona-Tech. The FloaWDyn is based on a co-rotational Finite Element Model (FEM), able to asses the overall dynamics of the whole platform accounting for its deformations at each time step (Campos et al., 2017).

8.1.1 FEM co-rotational model

FloaWDyn FEM model allows the use of bar elements such as trusses and beams and bidimensional elements such as shells. A general element independent co-rotational formulation is used (Felippa, 2000), which in conjunction with the dynamic equilibrium equation, allows to obtain the nodal displacements field. This formulation deals with the dynamics of floating structures by allowing large rigid body motions but small strains. In general, each element places at its centroid one triad and others on the nodes defined (Figure 8-1). This technique allows to separate the element rigid motions from its internal deformations produced by the acting loads (inertial, internal and external loads). Once the internal strain field is computed, the internal stresses can be finally assessed.

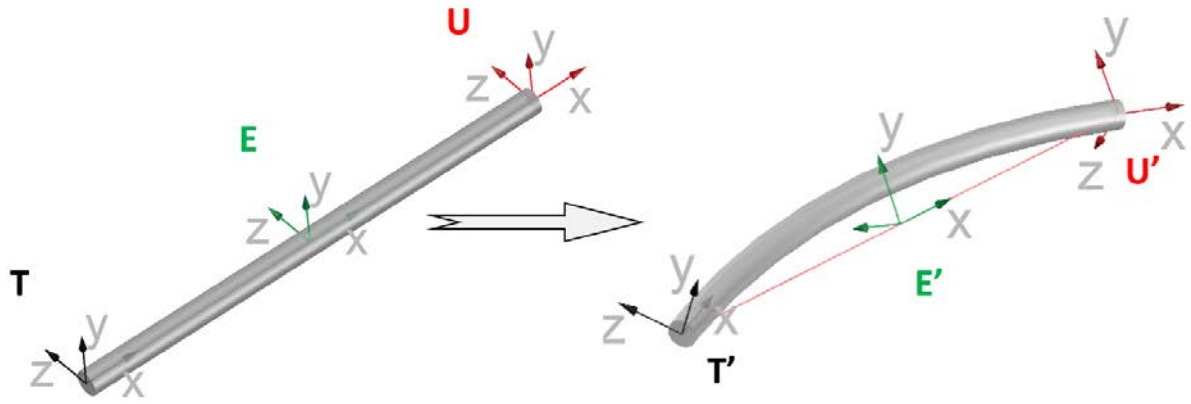

Figure 8-1: 3D Co-rotational frame for bar elements. Undeformed (left) and deformed element (right) (Campos et al., 2017)

8.1.2 Dynamic analysis

The equations of motion of the global system are obtained by applying the Newton's second law. Thus, by applying the Alembert's principle, the external, the internal and the inertia forces have to be in equilibrium at each time step.

The equations of motion are solved at each time step, by an iterative approach that updates the geometry and the internal forces. The solution of the system of equations yields to the increment of displacements between time steps in global coordinates.

For the time integration of the equations of motion, the Hilber-Hughes-Taylor (HHT) scheme is adopted (Hilber et al., 1977).

8.1.3 Aerodynamics

The aerodynamics are assessed by the FAST AeroDyn model (Jonkman & Jonkman, 2016). FAST AeroDyn is a Blade Element Momentum model which computes the aerodynamics of the rotor blades of a wind turbine. FAST AeroDyn is coupled with FloaWDyn in its standalone version. The aerodynamics consider temporal turbulence, but spatial turbulence is neglected. The wind speed is considered constant from the hub height which varies at each time step. Nevertheless, vertical wind velocity variation is considered by applying shear exponential law. Moreover, pitch and torque control models are based on FAST servo models, and the drive train is modelled as a rigid shaft.

The wind turbine forces over the yaw bearing are taken from Fast Aerodyn output results, which are updated at each time step in the tower coordinates system by accounting for the rotor azimuth, blade pitch and yaw position. Although spatial turbulence is not applied, the coupling of FAST AeroDyn allows

an assessment of the main aerodynamic effects such as the tower shadow, tip and hub losses and the power produced by the turbine.

8.1.4 Hydrostatic and Hydrodynamic Forces

The hydrostatic forces on the beam elements are computed from the buoyancy force of the submerged fraction of the element distributed according to the bar shape at each node. Thus, the hydrostatic force is split along the buoy ensuring the resultant buoyancy force will be virtually applied at the center of buoyancy. The hydrostatic forces over the shell elements are computed by the hydrostatic pressure acting at each centroid perpendicular to the shell plane. The pressure *p* is assessed by the hydrostatic law as $p = \rho_w |\boldsymbol{g}| r_z$, where ρ_w is the water density, $\mathbf{g}$ is the gravity vector, $\boldsymbol{r}$ is the vector position of the centroid of the shell element, the subscript defines the coordinate Degree Of Freedom (DOF). Then, the hydrostatic force is assessed as $f_h = -pA_s\boldsymbol{n}$, where A_s is the area of the shell element and $\boldsymbol{n}$ is the unitary normal vector of the shell element pointing to the water.

The kinematic and dynamic properties of the waves are assessed by either regular or irregular formulations. Regular wave hydrodynamics can be computed by Airy linear theory or by high order theories such as Stokes 5th order. Irregular wave kinematics are based on regular Airy linear wave theory and its components are assessed by the FFT and IFFT properties. Irregular wave trains can be defined from Jonswap spectrum or from an input wave profile.

The hydrodynamics of the beam elements are computed using the Morison equation for transversal forces. Moreover, the dynamic pressure is applied at the nodes in the axial beam direction of each element to assess the axial resultant force due to the dynamic wave pressure variation. At the free end points and cross section changing points an axial added mass term is considered based on the half sphere volume. On the other hand, the hydrodynamic forces over the shell elements are computed by the superposition of first order wave loads of the Potential Flow solution assessed by the Boundary Element Method code, Nemoh (LHEEA, 2014). The code solves the incident, diffraction and radiation waves problems for a given structure in the frequency domain for several wave directions. Using superposition of the linearization of the first order wave potential, the overall force of an irregular wave train and the radiation damping can be easily computed from the amplitude and phase of the wave and the convolution integral respectively. Herein, instead of the resultant forces, the pressure values are used and applied at each node of the shell elements of the submerged part of the structure.

8.1.5 Mooring model

The mooring numerical models implemented in the FloaWDyn model are presented in this dissertation.

8.2 WAVE HYDRODYNAMICS

8.2.1 Wave Theory

Fluid dynamics are fully described by Navier-Stokes equations. Nevertheless, solving these partial derivative equations demands large computational efforts through Computational Fluid Dynamic (CFD)

models to solve the problem. Moreover, adding the interaction with floating bodies imply that only specific problems are actually solved by these methods.

On the other hand, most marine engineering problems can assume inviscid and irrotational flow. Inviscid means that the fluid is frictionless and thus the viscous terms are neglected. This is because viscous effects are limited to a thin layer next to the body, the so-called boundary layer. Regarding the Reynolds number, marine applications have values around $1 \cdot 10^{6\sim10}$, and thus inertia terms are more important than the viscous ones. Irrotational flow mean that the water particles do not rotate, thus the vorticity of the velocity is zero ($\nabla \times \mathbf{V} = \mathbf{0}$). This condition is mostly fulfilled except when flow separation occurs (Batchelor, 1967).

- **Continuity equation**

Continuity equation can be expressed as Eq. (8.1). Supposing incompressible flow by considering the density of the fluid (ρ) remains constant $(\rho = ct)$ the Eq. (8.2) is obtained from Eq. (8.1), where the water particle velocity is expressed as $\mathbf{V} = (V_x, V_y, V_z) = (u, v, w)$, and (x, y, z) are the cartesians components of the reference system, where z points against the gravity.

$$\frac{\partial \rho}{\partial \mathrm{t}} + \nabla \cdot (\rho \mathbf{V}) = 0 \tag{8.1}$$

$$\nabla \cdot \mathbf{V} = \frac{\partial u}{\partial x} + \frac{\partial v}{\partial y} + \frac{\partial w}{\partial z} = 0 \tag{8.2}$$

- **Potential Flow**

Assuming irrotational flow, a potential function $\phi(x, y, z, t)$ can be defined to be $\nabla\phi = \boldsymbol{V}$, because by definition, $\nabla \times \nabla\phi = 0$, for potential functions. Therfore, the velocity of a sea state can be defined as de gradient of a potential function, Eq. (8.3) the velocity potential, which leads to the potential flow theory. By substitution of into Eq. (8.2), the continuity equation becomes the Laplace equation (8.4).

$$\mathbf{V} = \nabla\phi = \left(\frac{\partial \phi}{\partial \mathrm{x}}, \frac{\partial \phi}{\partial \mathrm{y}}, \frac{\partial \phi}{\partial \mathrm{z}}\right) \tag{8.3}$$

$$\nabla^2\phi = \frac{\partial^2 \phi}{\partial \mathrm{x}^2} + \frac{\partial^2 \phi}{\partial \mathrm{y}^2} + \frac{\partial^2 \phi}{\partial \mathrm{z}^2} = 0 \tag{8.4}$$

- **Euler equation**

Applying the Newton's second law to a non-viscous and incompressible fluid in a streamline the Euler equation (8.5) is obtained where g is the absolute value of the gravity and p is the pressure of the fluid.

$$\left.\begin{aligned} \frac{\partial u}{\partial t} + u\frac{\partial u}{\partial x} + v\frac{\partial u}{\partial y} + w\frac{\partial u}{\partial z} &= -\frac{1}{\rho}\frac{\partial p}{\partial x} \\ \frac{\partial v}{\partial t} + u\frac{\partial v}{\partial x} + v\frac{\partial v}{\partial y} + w\frac{\partial v}{\partial z} &= -\frac{1}{\rho}\frac{\partial p}{\partial y} \\ \frac{\partial w}{\partial t} + u\frac{\partial w}{\partial x} + v\frac{\partial w}{\partial y} + w\frac{\partial w}{\partial z} &= -\frac{1}{\rho}\frac{\partial p}{\partial z} - g \end{aligned}\right\} \tag{8.5}$$

- **Bernoulli Equation**

Rewriting the Euler equation in terms of the potential velocity, the Eq. (8.6) is obtained.

$$\left.\begin{array}{l} \frac{\partial}{\partial x}\left(\frac{\partial \phi}{\partial t}+\frac{1}{2}\left[\left(\frac{\partial \phi}{\partial x}\right)^2+\left(\frac{\partial \phi}{\partial y}\right)^2+\left(\frac{\partial \phi}{\partial z}\right)^2\right]+\frac{p}{\rho}\right)=0 \\ \frac{\partial}{\partial y}\left(\frac{\partial \phi}{\partial t}+\frac{1}{2}\left[\left(\frac{\partial \phi}{\partial x}\right)^2+\left(\frac{\partial \phi}{\partial y}\right)^2+\left(\frac{\partial \phi}{\partial z}\right)^2\right]+\frac{p}{\rho}\right)=0 \\ \frac{\partial}{\partial z}\left(\frac{\partial \phi}{\partial t}+\frac{1}{2}\left[\left(\frac{\partial \phi}{\partial x}\right)^2+\left(\frac{\partial \phi}{\partial y}\right)^2+\left(\frac{\partial \phi}{\partial z}\right)^2\right]+\frac{p}{\rho}\right)+g=0 \end{array}\right\} \quad (8.6)$$

Then, integrating Eq. (8.6) the Bernoulli equation (Eq. (8.7)) is obtained.

$$\frac{\partial \phi}{\partial t}+\frac{1}{2}\boldsymbol{V}^2+\frac{p}{\rho}+gz=C(t) \quad (8.7)$$

- **Potential Flow Theory**

Potential flow theory allows to describe a fluid motion in certain circumstances and simplifications. Moreover, potential flow can be superposed in order to achieve more complex flows due to the Laplace equation is also fulfilled for the sum of different potential flow as is shown in Eq. (8.8) and (8.9).

$$\phi_T=\phi_1+\phi_2 \quad (8.8)$$

$$\nabla^2\phi_T=\nabla^2(\phi_1+\phi_2)=\nabla^2\phi_1+\nabla^2\phi_2=0+0=0 \quad (8.9)$$

The main potential flow basic elements are the uniform flow, the source, the sink and the circulation which mean circular velocity but not spin of the particles. By the superposition of various of these elements the flow through a cylinder can be generated by the combination of a source and a sink at the same point, generating a dipole, plus an uniform flow, as is shown in Figure 8-2.

8.2.2 Incident wave potential - Regular Wave (Airy)

The regular wave theory was proposed by Airy (1841) and is wide used within the offshore community due to its simplicity and its linearity. This linearization allows to use the theory in wave superposition for random irregular wave generation and all the hydrodynamic parameters, such as velocity, acceleration and pressure taking advantage of the Fourier Transform properties for numerical assessment. The theory assumes potential flow, and assuming the water particle only moves on the x-z plane, the velocity potential can be described as shown in Eq. (6.10)(8.10). The MSL is defined at $z=0$, and k and ω are the wave number and the wave frequency.

$$\phi=\Re\left\{-jP(z)\,e^{j(kx-\omega t)}\right\}=\mathrm{P(z)}\sin(kx-\omega t) \quad (8.10)$$

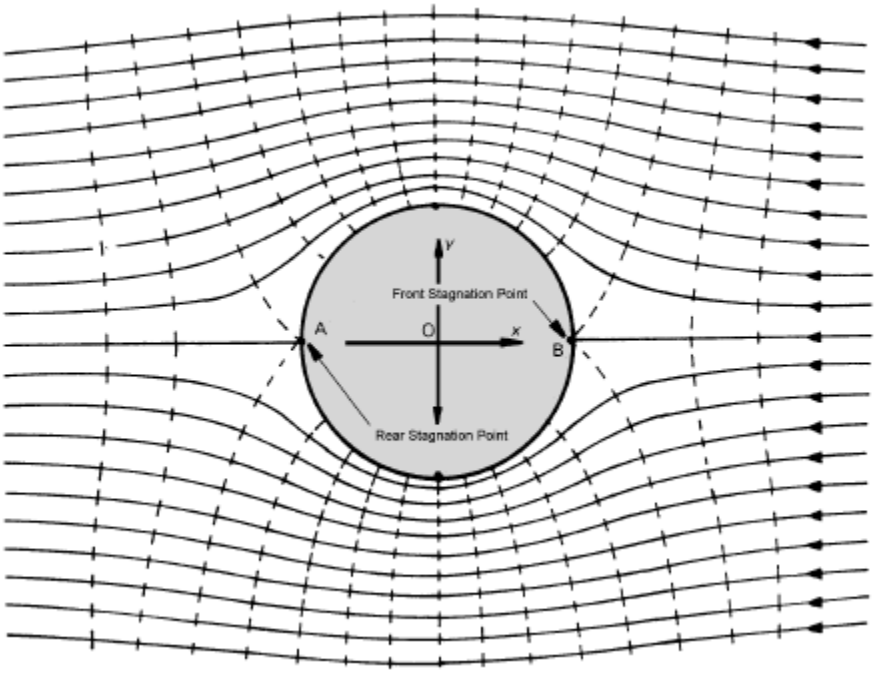

*Figure 8-2: Flow through a cylinder (*Journée & Massie, 2001)

Applying continuity by Laplace equation (8.4), $\frac{\partial^2 \phi}{\partial x^2} + \frac{\partial^2 \phi}{\partial z^2} = 0$, yields to a homogenous solution (Eq. (8.11)).

$$\frac{\partial^2 P(z)}{\partial z^2} - k^2 P(z) = 0 \tag{8.11}$$

The solution of the ordinary differential equation has the form of Eq. (8.12).

$$P(z) = C_1 e^{kz} + C_2 e^{-kz} \tag{8.12}$$

Then, the velocity potential can be expressed as Eq. (8.13).

$$\phi = \left(C_1 e^{kz} + C_2 e^{-kz}\right) \sin(kx - \omega t) \tag{8.13}$$

Applying the seabed boundary condition to ensure the vertical water velocity equal to zero, the so-called no-leak condition, $\left.\frac{\partial \phi}{\partial z}\right|_{z=-d} = 0$, the equation (8.13) becomes Eq. (8.14), where d is the depth of the sea.

$$\phi = C \cosh\left(k(z+d)\right) \sin(kx - \omega t) \tag{8.14}$$

Then, applying the free surface dynamic boundary condition by assuming atmospheric pressure at the free surface of the fluid using Bernoulli equation (8.7) leads to Eq. (8.15), where η is the wave elevation.

$$\left.\frac{\partial \phi}{\partial t}\right|_{z=\eta} + \frac{1}{2}\boldsymbol{V}^2 + \frac{p_0}{\rho} + g\eta = C \tag{8.15}$$

Considering that waves have a small steepness leads that the wave elevation and the velocity potential are sufficiently small. Then, the derivatives of these terms are small of first order, and thus, quadratic terms are small of second order and can be neglected. Furthermore, considering $C = p_0/\rho$ equation (8.15) becomes Eq. (8.16):

$$\left.\frac{\partial \phi}{\partial t}\right|_{z=\eta} + g\eta = 0 \tag{8.16}$$

Furthermore, if the velocity potential of the free surface is linearized by Taylor expansion as:

$$\phi|_{z=\eta} = \phi|_{z=0} + \eta \left.\frac{\partial \phi}{\partial z}\right|_{z=0}$$

Then, the time derivative of the velocity potential at the free surface can be expressed as:

$$\left.\frac{\partial \phi}{\partial t}\right|_{z=\eta} = \left.\frac{\partial \phi}{\partial t}\right|_{z=0} + \mathrm{O}(\varepsilon^2)$$

Thus, equation (8.16) can be rewritten as Eq. (8.17).

$$\eta = -\frac{1}{g}\left.\frac{\partial \phi}{\partial t}\right|_{z=0} \tag{8.17}$$

A substitution of equation (8.14) into (8.17), equation (8.18) is obtained.

$$\eta = -\frac{1}{g}\left.\frac{\partial \phi}{\partial t}\right|_{z=0} = \frac{\omega}{g} C \cosh(kd)\cos(kx - \omega t) = \frac{H}{2}\cos(kx - \omega t) \tag{8.18}$$

And then the velocity potential can be expressed as equation (8.19).

$$\phi = \frac{H}{2}\frac{g}{\omega}\frac{\cosh\big(k(z+d)\big)}{\cosh(kd)}\sin(kx - \omega t) \tag{8.19}$$

For deep waters, $d \to \infty$ the wave velocity potential becomes Eq. (8.20).

$$\phi = \frac{H}{2}\frac{g}{\omega} e^{kz}\sin(kx - \omega t) \tag{8.20}$$

Finally, the free surface kinematic boundary condition leads to the relationship between the ω and k, the so-called dispersion relation.

The free surface kinematic boundary condition sets that the vertical velocity of a water particle at the free surface of the fluid is identical to the vertical velocity of that free surface itself. If the boundary condition is set to $F = z - \eta(x,t) = 0$, then the time derivative of the boundary condition leads to Eq. (8.21).

$$\left.\frac{dF}{dt}\right|_{z=\eta} = \left.\frac{\partial F}{\partial t} + \mathbf{V}\cdot\nabla F\right|_{z=\eta} = \frac{\partial z}{\partial t} - \frac{\partial \eta}{\partial t} - u\left.\frac{\partial \eta}{\partial x}\right|_{z=\eta} = 0 \tag{8.21}$$

Assuming again that the wave has a small steepness the term $u\frac{\partial \eta}{\partial t}$ is of second order and can be negligible Eq. (8.22) is obtained.

$$\left.\frac{\partial z}{\partial t}\right|_{z=\eta} = \left.\frac{\partial \eta}{\partial t}\right|_{z=\eta} \tag{8.22}$$

Analogous to equation (8.17), the boundary condition can be expressed at the MSL$(z = 0)$, assuming small water elevation, thus $\eta = -\frac{1}{g}\left.\frac{\partial \phi}{\partial t}\right|_{z=0}$ and Eq. (8.23) is obtained.

$$\left.\frac{\partial z}{\partial t}\right|_{z=0} = -\frac{1}{g}\left.\frac{\partial^2 \phi}{\partial t^2}\right|_{z=0} \tag{8.23}$$

Substituting equation (8.19) into (8.23) the dispersion relation is obtained, Eq. (8.24) and (8.25) for finite and deep waters respectively

.

$$\omega^2 = kg\tanh(kd) \tag{8.24}$$
$$\omega^2 = kg \tag{8.25}$$

In the following sections the main hydrodynamic parameters of Airy regular wave theory for deep and finite waters are given in complex Euler's form and its trigonometric form.

- **Wave potential**

The wave potential can be expressed as Eq. (8.26) and (8.27) for deep waters and finite waters respectively.

$$\phi = \Re\left\{-j\frac{H}{2}\frac{g}{\omega}e^{kz}\,e^{j(kx-\omega t)}\right\} = \frac{H}{2}\frac{g}{\omega}e^{kz}\sin(kx-\omega t) \tag{8.26}$$

$$\phi = \Re\left\{-j\frac{H}{2}\frac{g}{\omega}\frac{\cosh\big(k(d+z)\big)}{\cosh(kd)}e^{j(kx-\omega t)}\right\} = \frac{H}{2}\frac{g}{\omega}\frac{\cosh\big(k(d+z)\big)}{\cosh(kd)}\sin(kx-\omega t) \tag{8.27}$$

- **Wave elevation**

The wave elevation can be expressed as $\eta = -\frac{1}{g}\left.\frac{\partial \phi}{\partial t}\right|_{z=0}$ shown in Eq. (8.28).

$$\eta = \frac{H}{2}\cos(kx-\omega t) \tag{8.28}$$

- **Water particle velocity**

The water wave velocity can be assessed by the gradient of the potential velocity as $V_x = \frac{\partial \phi}{\partial x}$, $V_z = \frac{\partial \phi}{\partial z}$ shown in Eq. (8.29) and (8.30) respectively.

Finite waters	Deep waters	
$\mathrm{V_x} = \frac{H}{2}\omega \frac{\cosh\left(k(d+z)\right)}{\sinh(kd)} \cos(kx - \omega t)$	$\mathrm{V_x} = \frac{H}{2}\omega e^{kz} \cos(kx - \omega t)$	(8.29)
$\mathrm{V_z} = \frac{H}{2}\omega \frac{\sinh\left(k(d+z)\right)}{\sinh(kd)} \sin(kx - \omega t)$	$\mathrm{V_z} = \frac{H}{2}\omega e^{kz} \sin(kx - \omega t)$	(8.30)

- **Water particle acceleration**

The water wave acceleration can be assessed by the derivative of the water wave velocity as $\dot{V}_x = \frac{\partial V_x}{\partial t}$, $\dot{V}_z = \frac{\partial V_z}{\partial t}$ expressed in Eq. (8.31) and (8.32).

Finite waters	Deep waters	
$\dot{V}_x = \frac{H}{2}\omega^2 \frac{\cosh\left(k(d+z)\right)}{\sinh(kd)} \sin(kx - \omega t)$	$\dot{V}_x = \frac{H}{2}\omega^2 e^{kz} \sin(kx - \omega t)$	(8.31)
$\dot{V}_z = -\frac{H}{2}\omega^2 \frac{\sinh\left(k(d+z)\right)}{\sinh(kd)} \cos(kx - \omega t)$	$\dot{V}_z = -\frac{H}{2}\omega^2 e^{kz} \cos(kx - \omega t)$	(8.32)

- **Water dynamic pressure**

The water wave velocity can be assessed by the gradient of the potential velocity as $p = -\rho \frac{\partial \phi}{\partial t}$ shown in Eq. (8.33).

Finite waters	Deep waters	
$p = \frac{H}{2}\rho g \frac{\cosh\left(k(d+z)\right)}{\cosh(kd)} \cos(kx - \omega t)$	$p = \frac{H}{2}\rho g e^{kz} \cos(kx - \omega t)$	(8.33)

- **Hydrodynamic stretching**

Linear Airy Wave potential is only valid for z-coordinate points at or below the MSL. Then, to consider the hydrodynamics above the MSL the common procedure is to apply a stretching to the hydrodynamics parameters.

Wheeler stretching is the most common procedure within the offshore theory to consider the water velocity and acceleration hydrodynamics above the MSL. On the other hand, dynamic pressure stretching is account in a different manner to ensure null relative pressure at the water surface (Faltinsen, 1990).

- **Wheeler stretching: Water particle velocity and acceleration**

The velocity and acceleration are stretched or compressed depending of the particle is above or below the MSL linearly by the relation of the depth and the real water height, as is shown in Figure 8-3. The conversion is performed by substituting the z variable for z' (Eq. (8.34)) in the hydrodynamic equations (Wheeler, 1970).

$$z' = \frac{(z - \eta)}{d + \eta} d \tag{8.34}$$

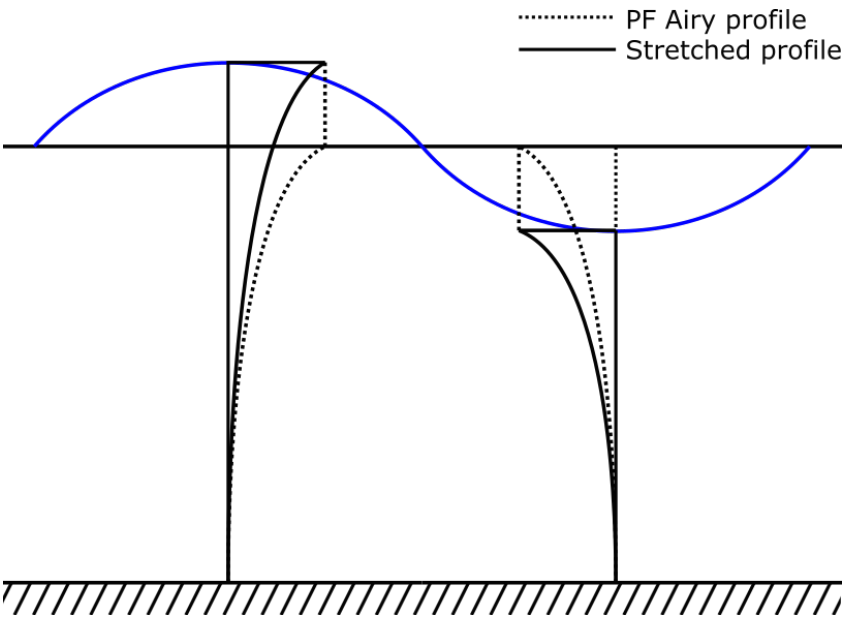

Figure 8-3: Wheeler stretching of velocity and acceleration parameters

- **Water dynamic pressure stretching**

The dynamic pressure stretching applied ensures null relative pressure at the wave surface by accounting the static pressure of the water from the MSL. Then, above the MSL the dynamic pressure is set constant and equal to the dynamic pressure at MSL, and below MSL the dynamic pressure is compressed in order to have the MSL pressure at the through. Then, the final pressures at the water surface are null as is shown in Figure 8-4, Faltinsen (1990).

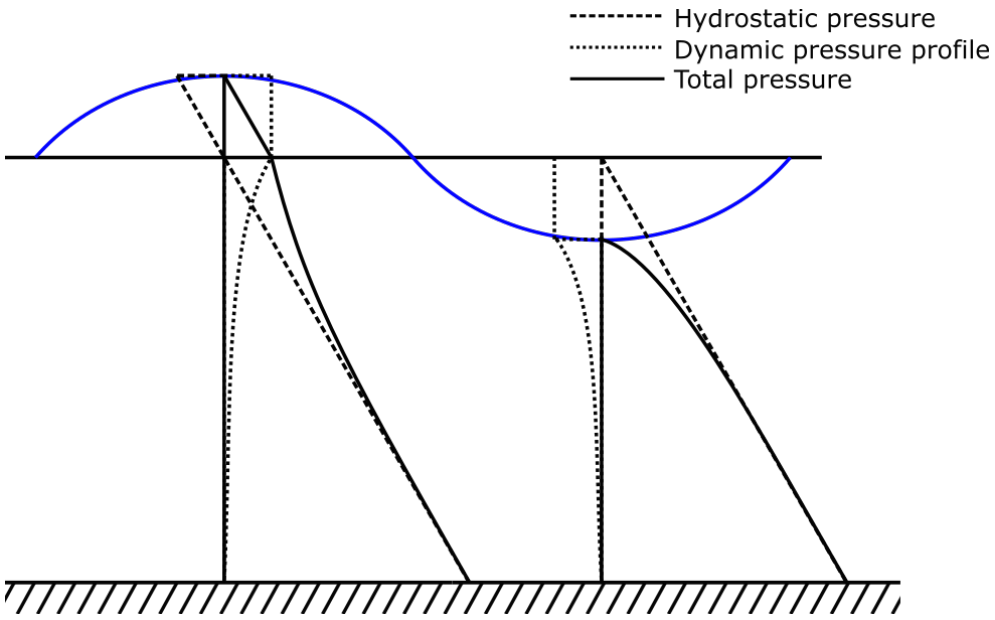

Figure 8-4: Dynamic and total pressure stretching

8.2.3 Irregular wave train

Sea states are usually irregular and can be seen as a superposition of many simple harmonic regular waves. Then, the wave elevation of an irregular sea propagating along the x-axis, can be written as the sum of a large number of regular wave components as expressed in Eq. (8.35).

$$\eta(t) = \sum_{n} \eta_n \, cos(k_n x - \omega_n t + \varepsilon_n) \tag{8.35}$$

Where for each component n, η_n is the wave amplitude component, $\omega_n$is the angular frequency component, k_n is the wave number component and ε_n is a random phase between 0 and 2π

Each wave height and its related frequency can be obtained from a wave height series time record. The data can be expressed via Fourier series, and the amplitude, frequency and phases are obtained in the frequency domain. The wave height spectrum, $S_\eta(\omega)$, can be described easily in a formula, but phases appear random (Faltinsen, 1990).

The standard wave spectra used in marine engineering are the Bretschneider and Jonswap wave spectra. These spectra are described as a function of the significant wave height ($H_s = H_{1/3}$), and average of wave periods $\bar{T}$, defined by $T_1, T_2 \text{and } T_p$. The Figure 8-5 shows a scheme of the wave record and regeneration.

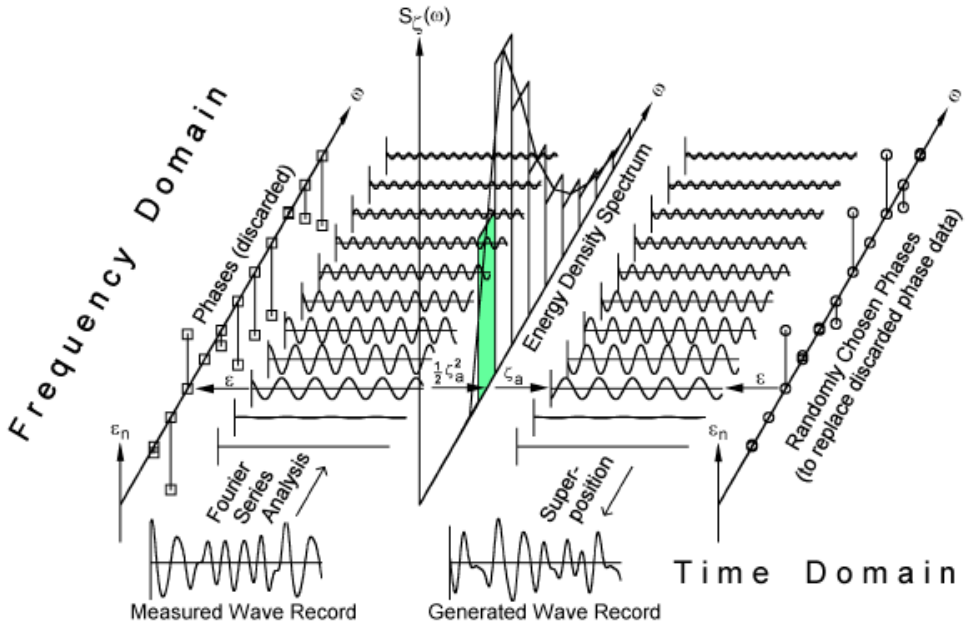

*Figure 8-5: Wave record analysis and regeneration (*Journée & Massie, 2001)

- **Jonswap Spectrum**

The expression to define the Jonswap Spectrum is shown in Eq. (8.36), (Hasselmann et al., 1973).

$$\mathrm{S}(\omega) = 320\ \mathrm{H_s^2}\frac{\omega^{-5}}{\mathrm{T_p^4}}\exp(-\frac{1950}{T_p^4}\omega^{-4})\ \gamma^{\mathrm{A}} \tag{8.36}$$

Where: $A = \exp\left(-\left(\frac{\frac{\omega}{\omega_p}-1}{\sigma\sqrt{2}}\right)^2\right)$, γ is the peakedness factor, σ is a step function of ω. If $\omega < \omega_p$: $\sigma = 0.07$, and if $\omega > \omega_p$: $\sigma = 0.09$

8.2.4 Second Order Wave Theory

The second order nonlinear boundary value problem is solved by a perturbation method that accounts for the contributions of the linear components. This method was presented by Sharma & Dean (1981).

The perturbation method adopted assumes that all variables can be expanded as a convergent power series of a small parameter, thus the Combined Surface Boundary Condition can be expanded in a Maclarurin series about the mean water level (z = 0).

The velocity potential and the surface elevation can be expressed as: Eq. (8.36)(8.37)

$$\begin{aligned}\phi(x,y,z,,t) &= \phi_1(x,y,z,,t) + \phi_2(x,y,z,,t) + \cdots \\ \eta(x,y,z,,t) &= \eta_1(x,y,z,,t) + \eta_2(x,y,z,,t) + \cdots\end{aligned} \tag{8.37}$$

Then, the Laplace equation turns to Eq. (8.38).

$$\nabla^2\phi_1 = 0 \\ \nabla^2\phi_2 = 0 \tag{8.38}$$

And the bottom boundary conditions are expressed in Eq. (8.39).

$$\left.\frac{\partial\phi_1}{\partial z}\right|_{z=-d} = 0 \\ \left.\frac{\partial\phi_2}{\partial z}\right|_{z=-d} = 0 \tag{8.39}$$

Then, according to Sharma, the Maclaurin series of the velocity potential at the free surface can be expressed as Eq. (8.40).

$$\phi(x,y,\eta,t) = \phi(x,y,0,t) + \eta\frac{\partial\phi(x,y,0,t)}{\partial z} + \frac{\eta^2}{2}\frac{\partial^2\phi(x,y,0,t)}{\partial z^2}\ldots \tag{8.40}$$

The first and second terms of Eq. (8.15) are the solution of the first-order equation, whereas the third method is the secon-order term of the velocity potential.

- **Second Order Equations**

The equations that define the second order term are the Laplace Equation (Eq. (8.41)), the seabed boundary condition (Eq. (8.42)), the free surface boundary condition (Eq. (8.43)), and the free surface equation (Eq. (8.44)).

$$\nabla^2\phi_2 = 0 \tag{8.41}$$

$$\left.\frac{\partial\phi_2}{\partial z}\right|_{z=-d} = 0 \tag{8.42}$$

$$\left.\left(\frac{\partial^2\phi_2}{\partial t^2} + g\frac{\partial\phi_2}{\partial z}\right)\right|_{z=0} = \left.\left(-\frac{\partial}{\partial t}|\nabla\phi_1|^2 - \eta_1\frac{\partial}{\partial z}\left[\frac{\partial^2\phi_1}{\partial t} + g\frac{\partial\phi_1}{\partial z}\right]\right)\right|_{z=0} \tag{8.43}$$

$$\eta_2 = \left.\left(-\frac{1}{g}\left[\frac{\partial\phi_2}{\partial t} + \frac{1}{2}|\nabla\phi_1|^2 + \eta_1\frac{\partial^2\phi}{\partial z\partial t}\right]\right)\right|_{z=0} \tag{8.44}$$

The second order solution for an irregular wave train can be expressed as Eq. (8.45).

$$\phi_2 = \frac{1}{4}\sum_{i=1}^{N}\sum_{j=1}^{N}\frac{g^2\eta_{A1,i}\eta_{A1_j}}{\omega_i\omega_j}\frac{\cosh\left(k_{ij}^{-}(z+d)\right)}{\cosh\left(k_{ij}^{-}d\right)}\frac{D_{ij}^{-}}{\omega_i-\omega_j}\sin(\psi_i-\psi_j) + \frac{1}{4}\sum_{i=1}^{N}\sum_{j=1}^{N}\frac{g^2\eta_{A1,i}\eta_{A1_j}}{\omega_i\omega_j}\frac{\cosh\left(k_{ij}^{+}(z+d)\right)}{\cosh\left(k_{ij}^{+}d\right)}\frac{D_{ij}^{+}}{\omega_i+\omega_j}\sin(\psi_i+\psi_j) \quad (8.45)$$

Where:

$k_{ij}^{-} = \left|k_i - k_j\right|$

$k_{ij}^{+} = \left|k_i + k_j\right|$

$\psi_i = k_i x - \omega_i t + \varepsilon_i$

$$D_{ij}^{-} = \frac{\left(\sqrt{R_i}-\sqrt{R_j}\right)\left[\sqrt{R_j}\left(k_i^2-R_i^2\right)-\sqrt{R_i}\left(k_j^2-R_j^2\right)\right]}{\left(\sqrt{R_i}-\sqrt{R_j}\right)^2-k_{ij}^{-}\tanh\left(k_{ij}^{-}d\right)} + \frac{2\left(\sqrt{R_i}-\sqrt{R_j}\right)^2\left(k_ik_j+R_iR_j\right)}{\left(\sqrt{R_i}-\sqrt{R_j}\right)^2-k_{ij}^{-}\tanh\left(k_{ij}^{-}d\right)}$$

$$D_{ij}^{+} = \frac{\left(\sqrt{R_i}+\sqrt{R_j}\right)\left[\sqrt{R_j}\left(k_i^2-R_i^2\right)+\sqrt{R_i}\left(k_j^2-R_j^2\right)\right]}{\left(\sqrt{R_i}+\sqrt{R_j}\right)^2-k_{ij}^{+}\tanh\left(k_{ij}^{+}d\right)} + \frac{2\left(\sqrt{R_i}+\sqrt{R_j}\right)^2\left(k_ik_j-R_iR_j\right)}{\left(\sqrt{R_i}+\sqrt{R_j}\right)^2+k_{ij}^{+}\tanh\left(k_{ij}^{+}d\right)}$$

$R_i = k_i\tanh(k_i d)$

8.3 HYDRODYNAMIC FORCES ON FLOATING BODIES

The hydrodynamic forces on floating bodies can be assessed mainly by three methods:

1) CFD methods that simplify the Navier-Stokes equations depending on the type flow, laminar or turbulent, and using time-average equations and turbulent models to solve the problem (Wilcox, 1993).

2) Potential Flow theory which solves the potential flow problem by accounting the boundary conditions of the floating body.

3) the Morison equation (Morison et al., 1950) which is valid for slender cylinders.

Engineering models are mainly based in the combination of potential flow methods and Morison equation due to its simplicity and reduced computational cost. Potential flow accounts for inertia and Froude-Krylov wave force terms as well as diffraction and radiation phenomena. Morison equation can be applied for whole wave force on cylinders but also to larger elements modelled in potential flow to account for the viscous terms.

8.3.1 Potential Flow

The potential flow method applies the potential flow theory to assess the pressure of the fluid over the floating body due to the wave incident flow, the radiated waves and the diffraction from the motion of the floating body.

The total potential ϕ can be described as Eq. (8.41).

$$\phi = \phi_w + \phi_d + \phi_r \tag{8.46}$$

where ϕ_w is the incident undistributed wave potential, ϕ_d is the diffraction potential of the waves about the restrained body and ϕ_r is the radiation potential from the oscillatory motion of the body in still water.

8.3.1.1 Incident Waves

The incident waves are the propagation of gravity waves. The incident waves are assessed as explained at 8.2.1.

8.3.1.2 Radiation

The radiation potential is associated with the oscillatory motion of a rigid body in still water.

8.3.1.3 Diffracted Waves

The wave diffraction is the phenomenon that explains the propagation of the wave energy to shadow zones, where the approaching wave is not directly in line (S. Chakrabarti, 2005).

8.3.2 Panel method solution

The panel method is a numerical method to assess the flow around a body assuming potential flow, based on the Green's theorem, which transforms a volume-integral into an easier to handle surface-integral. Then, the three-dimensional Laplace equation is transformed to a surface integral equation (Green's identity). The integral equation represents a distribution of sources (or sinks) and dipoles on the surface (Journée & Massie, 2001).

The main advantage of the panel method is the reduction from a three-dimensional problem to a two-dimensional problem. Moreover, the grid is also reduced to the surface of the floating body instead of all the volume surrounding the body, and thus, a reduction of the equations to be solved.

8.3.3 Morison Equation

Morison et al. (1950) proposed a simple equation to assess the waves forces on a fixed slender cylinders. The equation is divided in two terms, the inertia term that considers the Froude-Krylov and the scatter forces of the waves and the viscous term that account for the drag term. The Morison equation per meter length was extended for an oscillating cylinder presented in Eq. (8.47).

$$f_m = C_m \rho \pi R^2 \dot{V}_T - C_a \rho \pi R^2 \ddot{X} + \frac{1}{2} \rho C_d D \left(V_T - \dot{X}\right) \left|V_T - \dot{X}\right| \tag{8.47}$$

where C_a is the added mass term coefficient, C_m is the inertia coefficient, C_d is the drag coefficient, ρ is the fluid density, R and D are the cylinder radius and diameter respectively, V_T is the water particle velocity perpendicular to the cylinder axis, $\dot{V}_T$ is the water particle acceleration perpendicular to the cylinder axis, $\dot{X}$ and $\ddot{X}$ are the cylinder transverse velocity and the transverse acceleration.

8.3.4 MacCamy and Fuchs Theory

The hydrodynamic models only based on Morison's equation does not consider the diffraction of the waves because they only consider the incident wave hydrodynamics. This approach leads to a overpredicting the hydrodynamic wave forces at the diffraction frequency range.

MacCamy and Fuchs's proposed a formulation to assess the inertia wave forces taking into account the diffraction effect in isolated piles a single cylinder in shallow waters, but can also be expressed for deep waters. The equations given can be derived from the theory presented by MacCamy & Fuchs (1954).

If the incident velocity potential for infinite water depth is defined as Eq. (8.48).

$$\phi_i = \Re\left\{-j\frac{H_i}{2}\frac{g}{\omega}e^{kz}e^{j(kx-\omega t)}\right\} \tag{8.48}$$

Where H_i is the wave height, g is the gravity, ω is the wave frequency in [rad/s], k is the wavenumber and j is the imaginary number $\sqrt{-1}$.

Eq. (8.48) can be written in terms of polar coordinates and Bessel functions as Eq. (8.49).

$$\phi_i = -\frac{H_i}{2}\frac{g}{\omega}e^{kz}\Re\left\{\sum j^{m+1}\varepsilon_m J_m(kr)\,cos(m\beta)\,e^{-j\omega t}\right\} \tag{8.49}$$

Where:

$$\varepsilon_m = \begin{cases}1 \text{ for } m = 0\\ 2 \text{ for } m > 0\end{cases}$$

Also, the diffraction potential can be written in cylindrical coordinates and the Bessel functions as Eq. (8.50).

$$\phi_D = \frac{H_i}{2}\frac{g}{\omega}e^{kz}\Re\left\{\sum_{m=0}^{\infty} E_m\, H_m^{(1)}(kr)\,cos(m\beta)\,e^{-j\omega t}\right\} \tag{8.50}$$

where:

$H_m^{(1)}(kr) = J_m(kr) + jY_m(kr)$ is the mth-order Hankel function of the first kind

$E_m = \varepsilon_m i^{m+1}\frac{J'_m(ka)}{H'_m(ka)}, m = 0,1,2,\ldots$

Taking into account the incident and the diffracted potential, the total potential can be expressed as Eq. (8.51).

$$\phi = \frac{H_i}{2}\frac{g}{\omega}e^{kz}\Re\left\{\sum_{m=0}^{\infty}\left[-j^{m+1}\varepsilon_m J_m(kr) + E_m H_m^{(1)}(kr)\right]cos(m\beta)\,e^{-j\omega t}\right\} \tag{8.51}$$

From the dynamic pressure defined as Eq.(8.52), where a is the radius of the cylinder.

$$p|_{r=a} = -\rho \frac{\partial \phi}{\partial t}\Big|_{r=a} \tag{8.52}$$

the x-component of the force per unit length in z direction can be calculated as Eq. (8.53).

$$f_x = \int_0^{2\pi} p|_{r=a}\, cos(\beta)\, a \cdot d\beta = 2\frac{\rho g H_i}{k} e^{kz} \Lambda(ka)\, sin\big(-\omega t + \sigma(ka)\big) \tag{8.53}$$

where the amplitude function of Eq (8.53) is defined in Eq. (8.54).

$$\Lambda(ka) = \frac{1}{\sqrt{\left[J_0(ka) - \frac{1}{ka}J_1(ka)\right]^2 \left[Y_0(ka) - \frac{1}{ka}Y_1(ka)\right]^2}} \tag{8.54}$$

and the phase angle in Eq. (8.53) is defined in Eq. (8.55).

$$\sigma(ka) = arctan\left(\frac{J_0(ka) - \frac{1}{ka}J_1(ka)}{Y_0(ka) - \frac{1}{ka}Y_1(ka)}\right) \tag{8.55}$$

As is explained in McCormick (2014) and Sumer & Fredsoe (2006), the inertia term including the diffraction force can be expressed in terms of the inertia coefficient of the Morison equation. The Morison inertia term per meter length can be assessed as shown in Eq. (8.56).

$$f_i = \frac{1}{4}\rho \pi D^2 C_m \dot{\boldsymbol{V}}_{\boldsymbol{T}} \tag{8.56}$$

Then equaling Eq. (8.53) and (8.56) the Eq. (8.57) is obtained.

$$\rho \pi a^2 C_m \dot{\boldsymbol{V}}_{\boldsymbol{T}} = 2\frac{\rho g H_i}{k} e^{kz} \Lambda(ka)\, sin\big(-\omega t + \sigma(ka)\big) \tag{8.57}$$

Then, taking account the incident wave acceleration $\dot{\boldsymbol{V}}_{\boldsymbol{T}} = \frac{H_i}{2}\omega^2 e^{kz}\, sin(kx - \omega t)$, and imposing $x = 0$, the mass coefficient can be expressed as Eq. (8.58).

$$C_m = 4\frac{\Lambda(ka)}{\pi k^2 a^2} = C_{m,ME}\frac{2\Lambda(ka)}{\pi k^2 a^2} \tag{8.58}$$

Where $C_{m,ME} = 2$ is the mass coefficient of a standard cylinder for the Morison equation. Also the phase for the incident wave has to be modified using MacCamy's phase $\sigma(ka)$.

A more thorough analysis of the coefficient $\frac{2\Lambda(ka)}{\pi k^2 a^2}$as a function of the diffraction parameter ka shows that for $ka > 0.5$ the coefficient decreases from a value of 1. On the other hand, for values that ka<0.5, the coefficient remains close to 1 as can be seen in Figure 8-6. In other words, Figure 8-6 shows that Morison equation works well for $ka \leq 0.5$ while it overpredicts hydrodynamic forces for $ka > 0.5$.

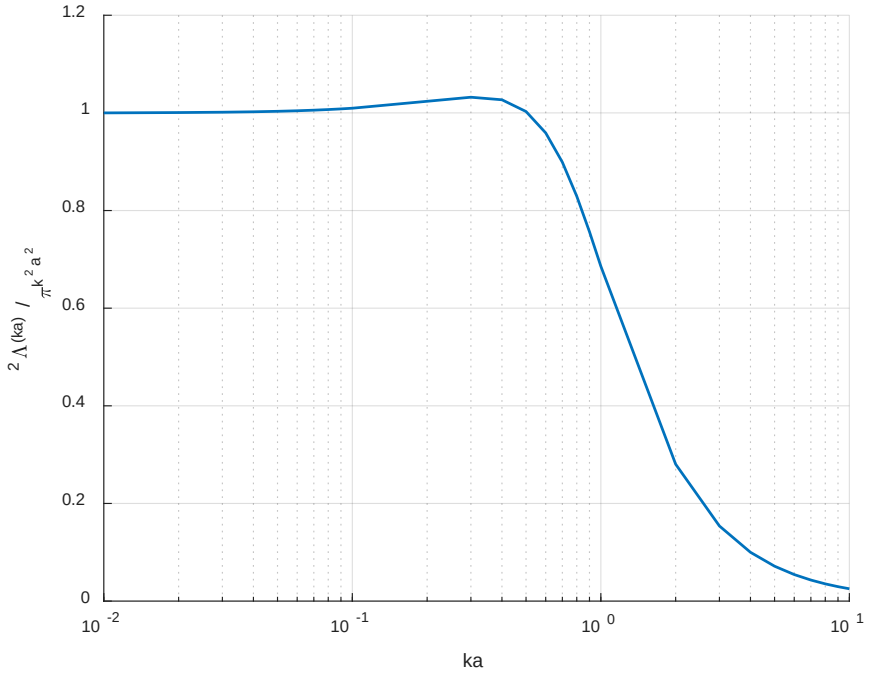

Figure 8-6: MacCamy coefficient variation

8.4 FLOWDYN HYDRODYNAMIC LOADS

8.4.1 Beam and Truss Elements

The hydro forces over the bar elements (beam and trusses) are assessed in three different approaches to consider all the effects over the structure. The first approach assesses the forces over the element and they are at the nodes of the elements. The loads assessed by this approach are the hydrostatic or buoyancy force and the transverse and the axial Morison equation terms. The second approach, assesses the dynamic pressure over each node of each element. And the third approach assesses the cap or cover hydrodynamic forces at the element endings or at node where the section of consecutive elements changes.

The input parameters are listed in the Table 8-1, and the derived parameters for the calculations are shown in Table 8-2.

Table 8-1: Input bar hydrodynamic parameters

Parameters	Units	Description
$\boldsymbol{D1}$	[m]	Diameter of Local Node 1
$\boldsymbol{D2}$	[m]	Diameter of Local Node 2
$\boldsymbol{C_{dq,T}}$		Quadratic Transversal Drag coefficient
$\boldsymbol{C_{dl,T}}$	[kg/m^{2}s]	Linear Transversal Drag coefficient
$\boldsymbol{C_{dq,Ax}}$		Quadratic Axial Drag coefficient (for tapered elements, d1≠d2)
$\boldsymbol{C_{dl,Ax}}$	[kg/m^{2}s]	Linear Axial Drag coefficient (for tapered elements, d1≠d2)
$\boldsymbol{C_{a,T}}$		Transverse Added mass coefficient
$\boldsymbol{C_{p,T}}$		Transverse FK coefficient
$\boldsymbol{C_{a,Ax}}$		Axial Added Mass Coefficient
$\boldsymbol{C_{p,Ax}}$		Axial FK Coefficient
$\boldsymbol{C_{dq,Cap}}$		Quadratic Axial Drag Coefficient of Cover
$\boldsymbol{C_{dl,Cap}}$	[kg/m^{2}s]	Linear Axial Drag Coefficient of Cover
$\boldsymbol{C_{a,Tap}}$		Axial Added Mass Coefficient of Cover
$\boldsymbol{C_{p,Tap}}$		Axial FK Coefficient of Cover

Table 8-2: Derived bar hydrodynamic parameters

Parameters	Units	Description
$\boldsymbol{R1 = D1/2}$	[m]	Radius of Local Node 1
$\boldsymbol{R2 = D2/2}$	[m]	Radius of Local Node 2
$\boldsymbol{D_{1/2} = \frac{D1 + D2}{2}}$	[m]	Diameter of the middle section
$\boldsymbol{R_{1/2} = \frac{R1 + R2}{2}}$	[m]	Radius of the middle section

8.4.1.1 Hydrostatics:

The buoyancy is assessed as the displaced volume of the conical frustum, correctly distributed at each node, as shown equation (8.59), where the volume is of the conical frustum. If the element is partially submerged, only the wet part is accounted for, as described in Eq. (8.60).

Thus, the hydrostatic restoring forces only consider the buoyancy of the elements. This means, that the heave restoring force is well calculated, but nor the pitch/roll restoring moment because the water plane inertia term of the meta centric height is not considered.

$$\mathbf{B_1} = -\rho_w \mathbf{g}\left(\frac{\pi}{12}(3R_1^2 + 2R_1R_2 + 1R_2^2)\right)l$$
$$\mathbf{B_2} = -\rho_w \mathbf{g}\left(\frac{\pi}{12}(1R_1^2 + 2R_1R_2 + 3R_2^2)\right)l \quad (8.59)$$

Where l is the length of the element

$$\mathbf{B}_{partial} = -\rho_w \mathbf{g}\left(\frac{\pi}{3}(R_s^2 + R_sR_0 + R_0^2)\right)l_s \quad (8.60)$$

where: $l_s = \frac{|\min(depth_1, depth_2)|}{|depth_1 - depth_2|}$ is the submerged length, and $depth_i = -\eta_i + z_i$, R_s is the radius of the submerged node, R_0 is the radius at wave elevation.

$$\mathbf{B_S} = \min\{\mathbf{B_i}, \mathbf{B}_{partial}\}$$
$$\mathbf{B_{NS}} = \max\{0, \mathbf{B}_{partial} - \mathbf{B}_i\}$$

Where $\mathbf{B_S}$ and $\boldsymbol{B_{NS}}$ are the buoyancy forces of the submerged and non submerged nodes respectively, i is the index (1,2) of the submerged node. (8.61)

8.4.1.2 Wave Loads and fluid –structure interaction

The parameters used to assess the wave loads are presented in Table 8-3.

Table 8-3: Wave load calculation parameters

Parameters	Units	Description
$\mathbf{V}$	[m/s]	Water particle velocity
$\dot{\mathbf{V}}$	[m/s^2]	Water particle acceleration
$\mathbf{r}$	[m]	Node position
$\dot{\mathbf{r}}$	[m/s]	Node velocity
$\ddot{\mathbf{r}}$	[m/s^2]	Node acceleration
$\mathbf{e}_x$	[u]	Axial unitary vector; $\mathbf{e}_x = (\mathbf{r}_2 - \mathbf{r}_1)/\lvert\mathbf{r}_2 - \mathbf{r}_1\rvert$

The Axial (Ax) and Transverse (T) components of a vectorial magnitude (X) respect the axial direction of an element (e_x) can be assessed as Eq. (8.62) and (8.63) respectively.

$$\mathbf{X}_{Ax} = (\mathbf{X} \cdot \mathbf{e}_x)\mathbf{e}_x \quad (8.62)$$

$$\mathbf{X}_T = \mathbf{X} - \mathbf{X}_{Ax} \quad (8.63)$$

8.4.1.3 Morison equation

The Morison equation is presented for cylinder and tapper elements. The main difference, is that tapper elements present axial components due to its shape. Then, the equation is dived in transverse and axial direction.

Transversal:

The transversal component of the Morison equation of a beam is assessed by the drag term (Eq. (8.64)), the inertia term (Eq. (8.65)) which are assessed from the integral of the Morison force per meter length, and the added mass term (Eq. (8.66)) for each local node which is assessed directly form the conical frustum. The linear drag term only takes into account the velocity of the platform in order to assess the contribution of the radiation force.

$$f_{drag,T} = \int_0^l \frac{1}{2}\rho_w C_{dq,T} D(l) |\mathbf{V}_T(l) - \dot{\mathbf{r}}_T| (\mathbf{V}_T(l) - \dot{\mathbf{r}}_T) - C_{dl,T} D(l) \dot{\mathbf{r}}_T \, dl \quad (8.64)$$

$$f_{inertia,T} = \int_0^l \left(C_{p,T} + C_{a,T}\right) A(l) \dot{\mathbf{V}}_T(l) \, dl \quad (8.65)$$

$$M_{a,T,i} = \rho_w C_{a,T} V_i [\mathrm{Id} - \mathbf{e}_x \mathbf{e}_x^T] \text{ , with } i = \{1,2\} \text{ as the local node index} \quad (8.66)$$

Where $A(l) = \pi R(l); V_1 = \frac{\pi}{12}(3R_1^2 + 2R_1R_2 + R_2^2)l; V_2 = \frac{\pi}{12}(R_1^2 + 2R_1R_2 + 3R_2^2)l$

Axial:

The axial term of the Morison equation assesses the hydrodynamic forces for tapper elements. The Eq. (8.67) is the drag term, the Eq. (8.68) is the scatter term of the inertia force and the Froude-Krylov term, and the Eq. (8.69) is the added mass term. In this case, the water added mass is assessed as the difference between the volume of the cylinder formed by the maximum radius and the volume of the truncated cone. In this case the forces are equal distributed into the local nodes.

$$f_{drag,Ax} = \frac{1}{2}\rho_w C_{dq,Ax} \left|\pi R_1^2 - \pi R_2^2\right| |\mathbf{V}_{Ax} - \dot{\mathbf{r}}_{Ax}| (\mathbf{V}_{Ax} - \dot{\mathbf{r}}_{Ax}) - C_{dl,Ax} \left|\pi R_1^2 - \pi R_2^2\right| \dot{\mathbf{r}}_{Ax} \quad (8.67)$$

$$f_{inertia,Ax} = \rho_w C_{a,Ax} (\pi R_{max}^2 - V_{tc}) l \dot{\mathbf{V}}_{Ax} + C_{p,Ax} (\pi R_1^2 - \pi R_2^2) p_{1/2} \quad (8.68)$$

$$M_{a,Ax} = \rho_w C_{a,Ax} (\pi R_{max}^2 - V_{tc}) l [\mathbf{e}_x \mathbf{e}_x^T] \quad (8.69)$$

Where $V_{tc} = \frac{l}{3}\pi(R_1^2 + R_1R_2 + R_2^2)$

8.4.1.4 Dynamic pressure

The dynamic pressure is applied at all the submerged bar elements. This dynamic pressure has to be accounted in the bar axial direction because the Morison equation is only applied in the transverse direction except for the tapper elements.

The over dynamic pressure is assessed as the difference of the resultant force of the dynamic pressure at the nodes of the elements, as show in Eq. (8.70).

$$f_{p,dyn} = C_p (p_2 \pi R_2^2 - p_1 \pi R_1^2) \boldsymbol{e}_x \quad (8.70)$$

8.4.1.5 Cap or Cover Nodes

The force on the cap or covers nodes is assessed from the exposed area of the cross section. The drag force is assessed by Eq. (8.71), the inertia force is assessed by Eq. (8.72) without the Froude-Krylov force accounted in the dynamic pressure term, and the added mass is assessed by Eq. (8.73). A half hemisphere is considered to be the reference volume for the added mass term, where R_{max} and R_{min} are the maximum and minimum radius of the two elements that meet in a node.

$$\begin{aligned} f_{drag,Ax} = {} & \frac{1}{2}\rho_w C_{dq,Cap} \left|\pi R_{max}^2 - \pi R_{min}^2\right| |\mathbf{V}_{Ax} - \dot{\mathbf{r}}_{Ax}| (\mathbf{V}_{Ax} - \dot{\mathbf{r}}_{Ax}) \\ & + \frac{1}{2}\rho_w C_{dl,Cap} \left|\pi R_{min}^2 - \pi R_{max}^2\right| (\mathbf{V}_{Ax} - \dot{\mathbf{r}}_{Ax}) \end{aligned} \quad (8.71)$$

$$f_{inertia,Ax} = \rho_w C_{a,Tap} \frac{2}{3}\pi\left(R_{max}^3 - R_{min}^3\right)\dot{\mathbf{V}}_{Ax} \tag{8.72}$$

$$M_{a,Ax} = \rho_w C_{a,Tap} \frac{2}{3}\pi\left(R_{max}^3 - R_{min}^3\right)[\mathbf{e}_x \mathbf{e}_x^T] \tag{8.73}$$

8.4.1.6 MacCamy and Fuchs modification

Since the inertia force is linearly dependent on the wave particle acceleration using Morison equation, and thus to the wave amplitude, a Fourier analysis can be used to add the diffraction term on the wave force calculation for linear wave theory. Then, the proposed application of MacCamy's theory for irregular wave trains can be done in two ways, 1) applying MacCamy and Fuchs modification directly to the Morison equations, or 2) modifying the wave surface. In the first approach, the application of the inertia wave force is done by taking a frequency-dependent inertia coefficient into account, which is the direct application of MacCamy Fuchs method. In the second approach, the application of the inertia wave force is done by modifying the amplitude of the free surface wave elevation in the diffraction area.

In the first possibility, the Morison equation is applied as follows. From the Fourier coefficients for the sea surface elevation (X_η), Eq. (8.74) a Morison inertia force Fourier coefficient $\left(X_{Cfi}\right)$ can be expressed as Eq. (8.75).

$$X_\eta(\omega) = A(\omega)\, exp(j\varphi) \tag{8.74}$$

$$\begin{aligned} X_{Cfi}(\omega) &= -jA(\omega)\omega^2 C_m(\omega)\, exp\left(j\varphi_{Cfi}\right) \\ \varphi_{Cfi}(\omega) &= \varphi_\eta - \sigma(ka) \end{aligned} \tag{8.75}$$

where $C_m(\omega)$ and $\sigma(ka)$ are defined in Eq. (8.58) and Eq. (8.55) respectively and a is the radius of the cylinder.

Then the inertia force per meter length will be calculated as Eq. (8.76).

$$\begin{aligned} f_i &= \rho\pi a^2 C_{fi} \\ C_{fi} &= IFFT\left(X_{C_{fi}}\right) \end{aligned} \tag{8.76}$$

In the second possibility, the amplitude of the wave elevation and its phase are modified in the diffraction region, in order to obtain a variation of the water particle acceleration proportional to the C_m reduction. Then, the new amplitude A_D as a function of the wave frequency, considering the relation $\omega^2 = kg$, can be expressed as Eq. (8.77).

$$\begin{aligned} X_{A_D}(\omega) &= A(\omega)\frac{2\Lambda(ka)}{\pi a^2 k^2} exp\left(j\varphi_{A_D}\right) \\ \varphi_{A_D}(\omega) &= \varphi_A - \sigma(ka) \end{aligned} \tag{8.77}$$

Also, the phase of the amplitude should be modified adding the MacCamy phase term $\sigma(ka)$. The new wave surface elevation can be calculated as Eq.(8.78).

$$\eta_D = IFFT\left(X_{A_D}\right) \tag{8.78}$$

More detailed explanation and verification and validation results can be found in Trubat et al. (2018).

8.4.2 Shell Elements

The hydro forces over the shell elements are assessed from the actual position of the platform relative to the MSL. The wave hydrodynamic forces, radiation forces and added mass terms are assessed from the potential flow solution from the software Nemoh (LHEEA, 2014).

The shell elements are defined by the position of their nodes, the position of the centroid ($\boldsymbol{r}_c = [x_c; y_c; z_c]$) and the vector perpendicular to the element pointing to the fluid $\left(n_c = \left[n_x; n_y; n_z\right]\right)$.

8.4.2.1 Hydrostatics:

The hydrostatics are assessed from the distance between the MSL and the centroid of each element. The hydrostatic force is assessed by Eq. (8.79), where A_s is the area of the shell.

$$\mathbf{f_{hydrostaic}} = -\rho_w |g| A_s z_c \boldsymbol{n} \tag{8.79}$$

8.4.2.2 Excitation Loads: Incident + diffracted

The wave excitation loads are assessed from the potential flow solution of Nemoh software (LHEEA, 2014). The pressure at the nodes of the element "i" is assessed as Eq. (8.80).

$$\mathbf{p_{i,w}} = \mathrm{A_j} p_{u,i,j} \cos(\omega_j t - k_j x_c + \phi_{j,i} + \varepsilon_j)\ \boldsymbol{n_i} \tag{8.80}$$

where A_j is the amplitude of the wave, $p_{u,i,j}$ is the pressure for an unitary wave with a frequency $\left(\omega_j\right)$, k_j is the wave number, $\phi_{j,i}$ is the phase between the wave and the pressure at the element "i", and ε_j is the phase of the wave of the irregular wave train

8.4.2.3 Radiation Loads

The radiation loads are assessed from the velocity of the reference node of the structure placed at $[0,0,0]$ from the undisturbed position.

The calculation of the radiation force is done by the convolution integral of the retardation function as presented by Cummins (1962).

$$\mathbf{p_{i,r}} = \int_{\mathrm{t}-\Delta\mathrm{T}}^{\mathrm{t}} K_{p,i}(t-\tau)\dot{\boldsymbol{r}}_c d\tau \tag{8.81}$$

with:

$$K_{p,i}(\tau) = \frac{2}{\pi}\int_0^{\infty} p_{r,i,\omega}\cos(\omega\tau)\,d\omega$$

Where $K_{p,i}$ is the retardation function of the element "*i*", $p_{r,i,\omega}$ is the frequency dependent hydrodynamic damping pressure, ω is the frequency, τ is the time, $\dot{\boldsymbol{r}}_c$ is the velocity of the reference node.

8.4.2.4 Scatter loads: Added Mass terms

The added mass terms are the frequency dependent hydrodynamic mass pressure assessed at $\omega = \infty$.